Understanding How Collective Ion Assembly Influences Electrochemical Reactivity

By

Beichen Liu

A dissertation submitted in partial fulfillment of the requirements for the degree of

Doctor of Philosophy

(Chemical Engineering)

at the

University of Wisconsin-Madison

2024

Date of final oral examination: 08/12/2024

The dissertation is approved by the following members of the final oral committee:

Matthew A. Gebbie, Assistant Professor, Chemical and Biological Engineering

Manos Mavrikakis, Professor, Chemical and Biological Engineering

Ive Hermans, Professor, Chemistry

Victor M. Zavala, Professor, Chemical and Biological Engineering

Understanding How Collective Ion Assembly Influences Electrochemical Reactivity

Abstract

Electrochemical reactions like CO_2 electroreduction offer compelling avenues to address climate change using renewable electricity by converting waste or pollutant chemicals into more useful ones. To motivate industrial scale implementation, however, we must understand the electrochemical interface and how to control it to achieve higher reaction rates, better selectivity, and reactor longevity. While significant progress is being made in electrode engineering, key knowledge gaps remain in how the electrolyte side of this interface influences local reaction environments and reaction pathways, especially in concentrated systems where nonclassical interactions are at play. Here, we present our work on addressing these knowledge gaps by systematically studying how the interfacial environment changes with electrolyte composition and how these changes ultimately affect CO_2 electroreduction.

When a potential is applied to an electrode, electrostatic interactions drive the formation of the electric double layer, which creates an ion-rich local reaction environment. In practical systems, the assumptions made in classical models of double layer formation are often not applicable and experimental measurements of this double layer confirm significant deviations from model predictions. Using electrochemical techniques in combination with interfacial spectroscopy methods, we first demonstrate non-monotonic reaction rate enhancements with concentration, which can be attributed to stronger local electric fields created by compact double layers. We then investigate double layer formation through the lens of entropy, where we show that ions with lower entropic penalties for confinement preferentially accumulate at the interface and govern electrocatalytic performance in mixed electrolytes. Finally, we assess a carbene-mediated pathway for CO_2 reduction using bulky diamondoid groups and conclude that electrochemical carbene formation plays an important role in mediating CO_2 conversion to CO.

Acknowledgments

When I first sat down to write this acknowledgments section, I foolishly thought that it would be the easiest to write. As I find myself writing, deleting, and rewriting over and over again, I have instead concluded that it is perhaps one of the most difficult. Not because it is highly technical or time-consuming, but because it is hard to convey the amount of gratitude I have for everyone who has supported and encouraged me throughout this PhD. Five years felt like such a long time at the start of this journey and yet it passed in the blink of an eye now that I am at the end. Broken down into individual moments of laughter, adventures, conversations, and challenges, it feels as if a lifetime has passed instead.

I want to begin by thanking my committee members, Professors Hermans, Mavrikakis, and Zavala, who have been generous with their guidance and support throughout my PhD. I am also indebted to my advisor, Matthew Gebbie, for his constant encouragement and unwavering optimism, even as we learned how to navigate setting up a new lab during the COVID-19 pandemic. He has always been in my corner, believing in me even when it felt hard to believe in myself and pushing me to be a better scientist. The members of the Gebbie group, both past and present, have helped mold me into the person I am today. Wenxiao Guo in particular has been a treasured mentor and fountain of knowledge. She taught me so much about how to be an exacting scientist and I am incredibly lucky to have been able to work with her on so many projects. My undergraduate mentees, Suzy W., Gene L., Megan H., and Rachel H. have been such joys to work with and I only hope that they learned as much from our time together as I did.

Madison has been a beautiful backdrop for my PhD and it's made even more so by the friends who have supported me and encouraged me from near and afar. I want to especially thank

Josh Abraham, Kevin Sánchez-Rivera, Raka Ghosh Dastidar, Ryan Cashen, Lisa Je, Harshal Bakshi, Eddie Barton, Jerrold Acdan, and Talia Cohen for being amazing colleagues, friends, and confidants. Their impact is truly indelible and my time at UW would have been severely lacking without their colorful personalities and thoughtful advice. Kamal Carter's humor and encouragement, too, have always been a welcome reprieve. I hold dear the memories we've made exploring, traveling to conferences, and trying out restaurants. As we each set off to chase our next milestones, I want to express how thankful I am that for a short five years, many of our paths converged in Madison.

Gabby Yanai deserves my sincerest gratitude for being a steadfast friend and enthusiastic cheerleader. Even though hundreds of miles separate us, she is an endless source of laughter, encouragement, and candid advice. Between our frequent phone calls, watch parties, and occasional visits, she has always reminded me about the big wide world outside of graduate school. I cannot extoll her virtues enough, so I conclude with: Gabby, from the bottom of my heart, thank you. I cannot pack the depth of my gratitude into words and express how much your friendship has meant to me but I hope this will suffice.

. And finally, I want to dedicate this dissertation to Lane Darby, who has stood by me with patience, care, and constant support. As the common refrain goes: I could not have done it without you. Your never-ending encouragement and optimism have been a guiding light over the past five years. I cherish our adventures along the way and eagerly anticipate where life takes us next.

Table of Contents

List of Figures

Chapter 1. Introduction

Electrocatalysis, and more broadly electrochemistry, offers tantalizing opportunities to address many key societal challenges using renewable electricity. Mitigating the emission of anthropogenic CO_2, for example, is a pressing problem that must be addressed to slow or reverse the major environmental and socioeconomic consequences of climate change. The electroreduction of CO_2 into value-added chemicals therefore represents an attractive solution but industrial-scale implementation remains difficult until the selectivity, reaction rates, and longevity of the reaction can be precisely controlled.[1-3]

The electroreduction of CO_2 occurs at the electrochemical interface, where the electrode and electrolyte meet. Much work has been done examining how the electrode side of this interface can be engineered to tune properties[4, 5] like adsorbate binding[6] or local reactant concentration by changing electrode compositions,[7, 8] controlling surface morphologies,[9, 10] or introducing complex electrode architectures[11, 12] and surface modifications.[13, 14] By employing a range of techniques, research groups have been able to enhance selectivity for products like CO,[8] formate,[11] or propanol[12] at high current densities.

While the reaction itself takes place on the electrode surface, the electrolyte side of the interface cannot be neglected, as the interfacial electrolyte dictates the local reaction environment. The electrochemical interface, however, is a complex and dynamic environment. Applying a potential to an electrode drives the migration of ions of the opposite charge towards the interface while ions of the same charge are driven away from the interface. This process creates the electric double layer, which screens the applied potential and forms the background upon which electrochemical reactions like CO_2 reduction occurs. Significant progress has been made in understanding how interfacial properties like local pH, local electrolyte composition, or local solvation structures impact CO_2 electroreduction. Groups have found, for example, that the choice of cation can tune local proton concentrations or otherwise buffer interfacial pH to subdue the competing hydrogen evolution reaction.[15] Others have found that the hydration radius of alkali metal cations stabilize key reaction intermediates through electric field effects.[16, 17] Anion choice too, has

been shown to impact reaction selectivity[18, 19] while the choice of solvent controls properties like CO_2 solubility and viscosity.[20]

A relatively underappreciated component of the electrochemical interface in electrocatalysis is the electric double layer itself, which is formed when a potential is applied to an electrode surface, driving the accumulation of oppositely-charged ions at the interface.[21-24] Although studies of the electrocatalytic reactions take interfacial properties into account, the long range interactions that drive the formation of the double layer are often not explicitly considered. Classical models of electric double layers assume that the ions in an electrolyte are fully solvated and hence do not interact with one another even at the interface. These assumptions are therefore inherent in predictions of double layer properties such as screening lengths.[23] While such assumptions apply at low electrolyte concentrations, even moderate electrolyte concentrations have shown significant deviations from classical models.[22, 25] These deviations from predicted behavior have been attributed to the emergence of ion-ion interactions which cause clusters and aggregates to form, leaving fewer "free" ions to screen the potential.[26]

To add further complexity, classical models of electric double layers also assume low applied potentials but reactions like CO_2 electroreduction require significantly more cathodic potentials. Additionally, there must be consistent transport of reactants to the interface and products away from the interface in order to sustain the reaction.[14] While many groups are working to improve our understanding of the electric double layer by incorporating aspects like ion-ion interactions,[22, 27] little is known about how electrocatalytic reactions impact the double layer and vice versa. Hence, there remains a significant gap between the development of an updated view of the electric double layer and our understanding of the relationship between the double layer and electrochemical reactions.

The aim of the work presented in this dissertation is to take steps toward understanding how the electric double layer influences electrocatalytic CO_2 conversion. Our findings offer new ways to view the electrochemical interface by demonstrating the importance of the electric double layer in dictating reaction rates and selectivity. By accounting for the driving forces behind double layer formation, we show how

altering the electrolyte can lead to important changes in interfacial properties like electric fields and local electrolyte compositions. Importantly, although this work focuses on CO_2 electroreduction as a model reaction, electric double layer formation is not specific to one reaction, and strategies developed in this work can be readily translated to other relevant electrocatalytic reactions.

1.1. The influence of electric double layer thickness

As electrochemical devices become more prevalent, understanding how the electric double layer changes with concentration becomes increasingly important, as practical devices often require concentrated electrolytes. Classical double layer theory predicts that the screening length should always decrease with increasing electrolyte concentration.[26-28] Experimentally, however, this is not the case, as studies of double layer thickness in neat ionic liquids, which are composed of only ions, revealed double layer thicknesses that are similar to dilute electrolytes. Furthermore, others demonstrated a non-monotonic relationship between electrolyte concentration and measured double layer thicknesses.

These results are intriguing, as the distance over which a potential is screened defines the local potential gradient and hence local electric field. That is, thicker double layers have longer screening lengths so the potential gradient is smaller and the interfacial electric field is weaker. Conversely, thin and compact double layers screen a potential over a shorter distance, leading to stronger electric fields. This concept is important, as the first step of CO_2 electroreduction, which yields CO, involves a negatively-charged polar intermediate, $CO_2^{\bullet-}$.[29] While much of the ionic liquid-mediated electrocatalysis community focuses on the role of the ionic liquid cations in stabilizing this intermediate, we anticipated that it is also possible to use electric fields to stabilize intermediates, which has been an approach highlighted in fields like enzymology.[30, 31]

Hence, we sought to study the relationship between electric double layer thickness and CO_2 electroreduction in ionic liquid-containing electrolytes. Not only do ionic liquids have high CO_2 solubility and a range of molecular structures,[32-35] but they have also been shown to facilitate the electroreduction of

CO_2 to CO. Since several exist as liquids at room temperature due to the asymmetry and bulkiness of the constituent ions, ionic liquids also allowed us to study an extended range of concentrations. Since the work of Rosen and coworkers, which reported the first instance of ionic liquid-mediated CO_2 electroreduction, imidazolium-based ionic liquids have emerged as particularly good mediators for this reaction. Thus, much of the work presented in this dissertation uses imidazolium cations as a way to demonstrate the importance of the electric double layer on CO_2 reduction kinetics and mechanisms.

In Chapter 2, we describe the general methodology employed in the experiments presented in this dissertation, which encompasses a range of electrochemical and interfacial characterization methods, as well as general ionic liquid synthesis protocols. Using these techniques, we probe interfacial electrolyte behavior as a function of concentration and electrolyte composition.

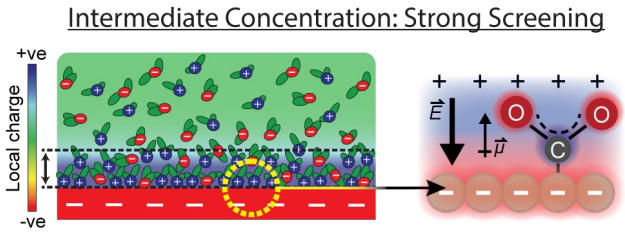

Figure 1.1. Intermediate concentrations yield compact double layers that localize electric fields to the interface, which stabilizes polar and charged intermediates**.**

Chapter 3 then describes our studies of electrolyte concentration as a proxy for double layer thickness and its effects on CO_2 reduction rates. We demonstrate a non-monotonic relationship between concentration and observed reaction rates, where intermediate concentrations yielded the highest current densities in addition to the highest faradaic efficiencies for CO. Importantly, we find that this non-monotonic trend can be observed in several kinds of ionic liquids, which suggests that there is a more generalizable cause for the trend which cannot be explained by the molecular structure of any one type of ionic liquid. Using *in situ* surface-enhanced Raman scattering spectroscopy, we conclude that the electric double layer is most compact at intermediate concentrations, which localizes a strong electric field to the interface, which stabilizes $CO_2^{\bullet-}$ (Fig. 1.1). Therefore, we highlight the importance of collective assembly

and correlations in double layer formation and electrocatalysis, as the rise of clusters and aggregates at high concentrations causes screening lengths to increase, which is detrimental to the formation of compact double layers and strong electric fields.

1.2. Approaches to controlling double layer composition

Although electrostatic interactions drive double layer formation, it is important to also consider entropic factors that oppose its formation. Confining ions from the bulk electrolyte, which is well mixed, to a condensed electric double layer comes with an entropic penalty associated with de-mixing.[36] We sought to understand how this balance between electrostatics and entropy ultimately influences the local reaction environment and allow us to control CO_2 electroreduction.

We hypothesized that decreasing the entropic penalty paid to confine charges to the interface would allow us to form more compact double layers at lower concentrations. This would have significant implications for the development of new electrolyte design strategies. In mixed electrolytes, it might be feasible to tune the entropy of one component to impart a certain property to the electric double layer. For example, creating a hydrophobic double layer might enhance selectivity by subduing the competing HER.

Work from the Koper group using mixed electrolytes offers intriguing hints that double layer composition is not simply a reflection of bulk electrolyte composition. They found that in electrolyte mixtures containing two kinds of alkali metal cations, the selectivity for certain products is dictated by the larger cation, which they attribute to an increase in concentration of larger hydrated cations at the interface.[17]

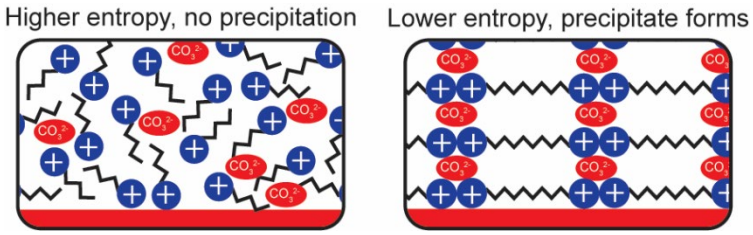

Figure 1.2 Cations with lower entropic penalty for double layer formation accumulate at electrochemical interfaces, which increases the propensity for physical processes like electrochemically-driven phase separation to occur.

In Chapter 4, we discuss how we tune the entropy of a cation while maintaining the overall chemical structure of a cation by studying dicationic ionic liquids, which are divalent, and comparing them to their monocationic counterparts. The entropic penalty to confine one charge to the electrochemical interface, which is associated with a loss in translational entropy, is smaller for the divalent cation than the monovalent one. We therefore expected the dicationic ionic liquids to facilitate CO_2 electroreduction at lower concentrations. What we found, however, was that the dicationic ionic liquids performed worse at all concentrations because of electrochemically-driven phase separation. *In situ* spectroscopy experiments showed that the dicationic ionic liquid formed structured electric double layers when CO_2 was not present in the system but that the double layer structure was disrupted when CO_2 electroreduction took place, highlighting the importance of creating models of electric double layers under reactive and non-reactive conditions. Using mixed electrolytes consisting of both the dicationic and monocationic ionic liquids, we demonstrated that the cation with the lower entropic penalty was preferentially present at the electrochemical interface, which in turn meant that interfacial processes like CO_2 reduction or precipitation are dictated by the cation with the lower entropic penalty for double layer formation (Fig. 1.2).

1.3. Examining reaction mechanisms

Electrolytes containing imidazolium-based ionic liquids often exhibit the highest reaction rates and selectivity for products like CO. The exact mechanism behind this enhancement, however, remains largely unclear. One of the first proposed mechanisms involves the ability of the imidazolium cation to form a carbene through either chemical or electrochemical deprotonation of the C2 proton. This N-heterocyclic carbene has been shown to form an adduct with CO_2, which could help stabilize the $CO_2^{\bullet-}$ intermediate.[6, 37] Other mechanisms, including hydrogen bonding as a stabilization method,[38] have since emerged and there is no consensus on which mechanism is most likely or what aspect of the imidazolium cation sets it apart from other organic cations.

The inherently unstable and reactive nature of carbenes could mean that they play other roles in the electrochemical environment. It could, for example, lead to the slow consumption of ionic liquid cations

through processes like dimerization or decyclization,[39] which is detrimental for device longevity. Or, the ability of the imidazolium to deprotonate could be beneficial for the reaction as a potential proton source. Recent work has shown that the formation of imidazolium-CO_2 adducts helps preserve local electric fields by forming a zwitterion as a conjugate base rather than $[OH]^-$ depending on the proton source.[40] A common approach to evaluating the carbene hypothesis is to methylate the C2 position and prevent deprotonation altogether. However, this method not only shuts down carbene formation, but also dramatically alters the interfacial behavior of the imidazolium cation.

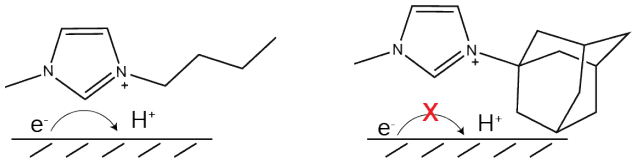

Figure 1.3 Diamondoid substituents prevent the formation of C2 carbenes through a combination of electronic and steric effects.

Persistent carbenes, which are stable carbenes isolated in 1991 by Arduengo and coworkers,[41] offer us an interesting approach to evaluating the carbene hypothesis. Chapter 5 therefore examines how tuning the substituent of the imidazolium cation allows us to study specific mechanisms by using bulky diamondoid substituents to stabilize the C2 carbene, an approach taken with the Arduengo carbenes. We sought to evaluate the role of the C2 carbene in CO_2 electroreduction. The diamondoid substituents are also hydrophobic and pay a lower entropic penalty for double layer formation than alkyl substituents due to molecular rigidity[36] so we hypothesized that diamondoid-substituted ionic liquids would form more structured and compact double layers which demonstrate enhanced reaction kinetics and selectivity. We find, however, that diamondoid-substituted ionic liquids perform worse overall due to a hindered ability to form the C2 carbene through a combination of electronic and steric effects (Fig. 1.3), suggesting that the C2 carbene formation may actually play a beneficial role in imidazolium-mediated CO_2 electrocatalysis, as preventing its formation has detrimental effects.

1.4. References

(1) Nitopi, S.; Bertheussen, E.; Scott, S. B.; Liu, X. Y.; Engstfeld, A. K.; Horch, S.; Seger, B.; Stephens, I. E. L.; Chan, K.; Hahn, C.; et al. Progress and Perspectives of Electrochemical CO_2 Reduction on Copper in Aqueous Electrolyte. *Chemical Reviews* **2019**, *119* (12), 7610-7672. DOI: 10.1021/acs.chemrev.8b00705.

(2) De Luna, P.; Hahn, C.; Higgins, D.; Jaffer, S. A.; Jaramillo, T. F.; Sargent, E. H. What would it take for renewably powered electrosynthesis to displace petrochemical processes? *Science* **2019**, *364* (6438), eaav3506 DOI: 10.1126/science.aav3506.

(3) Zhu, P.; Wang, H. T. High-purity and high-concentration liquid fuels through CO_2 electroreduction. *Nature Catalysis* **2021**, *4* (11), 943-951. DOI: 10.1038/s41929-021-00694-y.

(4) Song, R. B.; Zhu, W. L.; Fu, J. J.; Chen, Y.; Liu, L. X.; Zhang, J. R.; Lin, Y. H.; Zhu, J. J. Electrode Materials Engineering in Electrocatalytic CO_2 Reduction: Energy Input and Conversion Efficiency. *Advanced Materials* **2020**, *32* (27). DOI: 10.1002/adma.201903796.

(5) Arán-Ais, R. M.; Gao, D. F.; Roldan Cuenya, B. Structure- and Electrolyte-Sensitivity in CO_2 Electroreduction. *Accounts of Chemical Research* **2018**, *51* (11), 2906-2917. DOI: 10.1021/acs.accounts.8b00360.

(6) Fortunati, A.; Risplendi, F.; Fiorentin, M. R.; Cicero, G.; Parisi, E.; Castellino, M.; Simone, E.; Iliev, B.; Schubert, T. J. S.; Russo, N.; et al. Understanding the role of imidazolium-based ionic liquids in the electrochemical CO_2 reduction reaction. *Communications Chemistry* **2023**, *6* (1). DOI: 10.1038/s42004-023-00875-9.

(7) Vasileff, A.; Xu, C. C.; Jiao, Y.; Zheng, Y.; Qiao, S. Z. Surface and Interface Engineering in Copper-Based Bimetallic Materials for Selective CO_2 Electroreduction. *Chem* **2018**, *4* (8), 1809-1831. DOI: 10.1016/j.chempr.2018.05.001.

(8) Sheng, X. D.; Ge, W. X.; Jiang, H. L.; Li, C. Z. Engineering the Ni-N-C Catalyst Microenvironment Enabling CO_2 Electroreduction with Nearly 100% CO Selectivity in Acid. *Advanced Materials* **2022**, *34* (38). DOI: 10.1002/adma.202201295.

(9) Li, C. W.; Kanan, M. W. CO_2 Reduction at Low Overpotential on Cu Electrodes Resulting from the Reduction of Thick CuO Films. *Journal of the American Chemical Society* **2012**, *134* (17), 7231-7234. DOI: 10.1021/ja3010978.

(10) Gao, D. F.; Sinev, I.; Scholten, F.; Arán-Ais, R. M.; Divins, N. J.; Kvashnina, K.; Timoshenko, J.; Roldan Cuenya, B. Selective CO_2 Electroreduction to Ethylene and Multicarbon Alcohols via Electrolyte-Driven Nanostructuring. *Angewandte Chemie-International Edition* **2019**, *58* (47), 17047-17053. DOI: 10.1002/anie.201910155.

(11) Shi, T.; Liu, D.; Liu, N.; Zhang, Y.; Feng, H.; Li, Q. Triple-Phase Interface Engineered Hierarchical Porous Electrode for CO_2 Electroreduction to Formate. *Advanced Science* **2022**, *9* (30). DOI: 10.1002/advs.202204472.

(12) Zhuang, T. T.; Pang, Y. J.; Liang, Z. Q.; Wang, Z. Y.; Li, Y.; Tan, C. S.; Li, J.; Dinh, C. T.; De Luna, P.; Hsieh, P. L.; et al. Copper nanocavities confine intermediates for efficient electrosynthesis of C3

alcohol fuels from carbon monoxide. *Nature Catalysis* **2018**, *1* (12), 946-951. DOI: 10.1038/s41929-018-0168-4.

(13) Li, L.; Liu, Z. Y.; Yu, X. H.; Zhong, M. Achieving High Single-Pass Carbon Conversion Efficiencies in Durable CO_2 Electroreduction in Strong Acids via Electrode Structure Engineering. *Angewandte Chemie-International Edition* **2023**, *62* (21). DOI: 10.1002/anie.202300226.

(14) Bui, J. C.; Kim, C.; King, A. J.; Romiluyi, O.; Kusoglu, A.; Weber, A. Z.; Bell, A. T. Engineering Catalyst-Electrolyte Microenvironments to Optimize the Activity and Selectivity for the Electrochemical Reduction of CO_2 on Cu and Ag. *Accounts of Chemical Research* **2022**, *55* (4), 484-494. DOI: 10.1021/acs.accounts.1c00650.

(15) Marcandalli, G.; Monteiro, M. C. O.; Goyal, A.; Koper, M. T. M. Electrolyte Effects on CO_2 Electrochemical Reduction to CO. *Accounts of Chemical Research* **2022**, *55* (14), 1900-1911. DOI: 10.1021/acs.accounts.2c00080.

(16) Chen, L. D.; Urushihara, M.; Chan, K. R.; Norskov, J. K. Electric Field Effects in Electrochemical CO_2 Reduction. *ACS Catalysis* **2016**, *6* (10), 7133-7139. DOI: 10.1021/acscatal.6b02299.

(17) Resasco, J.; Chen, L. D.; Clark, E.; Tsai, C.; Hahn, C.; Jaramillo, T. F.; Chan, K.; Bell, A. T. Promoter Effects of Alkali Metal Cations on the Electrochemical Reduction of Carbon Dioxide. *Journal of the American Chemical Society* **2017**, *139* (32), 11277-11287. DOI: 10.1021/jacs.7b06765.

(18) Golru, S. S.; Biddinger, E. J. Effect of anion in diluted imidazolium-based ionic liquid/buffer electrolytes for CO_2 electroreduction on copper. *Electrochimica Acta* **2020**, *361*. DOI: 10.1016/j.electacta.2020.136787.

(19) Resasco, J.; Lum, Y.; Clark, E.; Zeledon, J. Z.; Bell, A. T. Effects of Anion Identity and Concentration on Electrochemical Reduction of CO_2. *Chemelectrochem* **2018**, *5* (7), 1064-1072. DOI: 10.1002/celc.201701316.

(20) König, M.; Vaes, J.; Klemm, E.; Pant, D. Solvents and Supporting Electrolytes in the Electrocatalytic Reduction of CO_2. *Iscience* **2019**, *19*, 135-160. DOI: 10.1016/j.isci.2019.07.014.

(21) Bard, A. J.; Faulkner, L. R. *Electrochemical Methods: Fundamentals and Applications*; John Wiley & Sons Inc. , 2000.

(22) Bazant, M. Z.; Storey, B. D.; Kornyshev, A. A. Double Layer in Ionic Liquids: Overscreening versus Crowding. *Physical Review Letters* **2011**, *106* (4), 046102(046104). DOI: 10.1103/PhysRevLett.106.046102.

(23) Damaskin, B. B.; Petrii, O. A. Historical Development of Theories of the Electrochemical Double Layer. *Journal of Solid State Electrochemistry* **2011**, *15*, 1317-1344. DOI: 10.1007/s10008-011-1562-x.

(24) Kornyshev, A. A. Double-Layer in Ionic Liquids: Paradigm change? *Journal of Physical Chemistry B* **2007**, *111* (20), 5545-5557. DOI: 10.1021/jp067857o.

(25) Gebbie, M. A.; Dobbs, H. A.; Valtiner, M.; Israelachvili, J. N. Long-Range Electrostatic Screening in Ionic Liquids. *Proceedings of the National Academy of Sciences of the United States of America* **2015**, *112* (24), 7432-7437. DOI: 10.1073/pnas.1508366112.

(26) Smith, A. M.; Lee, A. A.; Perkin, S. The Electrostatic Screening Length in Concentrated Electrolytes Increases with Concentration. *Journal of Physical Chemistry Letters* **2016**, *7* (12), 2157-2163. DOI: 10.1021/acs.jpclett.6b00867.

(27) Gebbie, M. A.; Smith, A. M.; Dobbs, H. A.; Lee, A. A.; Warr, G. G.; Banquy, X.; Valtiner, M.; Rutland, M. W.; Israelachvili, J. N.; Perkin, S.; et al. Long Range Electrostatic Forces in Ionic Liquids. *Chemical Communications* **2017**, *53*, 1214-1224. DOI: 10.1039/c6cc08820a.

(28) Gebbie, M. A.; Liu, B. C.; Guo, W. X.; Anderson, S. R.; Johnstone, S. G. Linking Electric Double Layer Formation to Electrocatalytic Activity. *ACS Catalysis* **2023**, *13* (24), 16222-16239. DOI: 10.1021/acscatal.3c04255.

(29) Hori, Y.; Wakebe, H.; Tsukamoto, T.; Koga, O. Electrocatalytic Process of CO Selectivity in Electrochemical Reduction of CO_2 at Metal-Electrodes in Aqueous-Media. *Electrochimica Acta* **1994**, *39* (11-12), 1833-1839. DOI: Doi 10.1016/0013-4686(94)85172-7.

(30) Léonard, N. G.; Dhaoui, R.; Chantarojsiri, T.; Yang, J. Y. Electric Fields in Catalysis: From Enzymes to Molecular Catalysts. *ACS Catalysis* **2021**, *11* (17), 10923-10932. DOI: 10.1021/acscatal.1c02084.

(31) Kang, K.; Fuller, J.; Reath, A. H.; Ziller, J.; Alexandrova, A.; Yang, J. Y. Installation of internal electric fields by non-redox active cations in transition metal complexes. *Chemical Science* **2019**, *10* (43), 10135-10142. DOI: 10.1039/c9sc02870f.

(32) Welton, T. Room-Temperature Ionic Liquids. Solvents for Synthesis and Catalysis. *Chemical Reviews* **1999**, *99* (8), 2071-2084. DOI: DOI 10.1021/cr980032t.

(33) Seddon, K. R. Ionic liquids for clean technology. *Journal of Chemical Technology and Biotechnology* **1997**, *68* (4), 351-356. DOI: 10.1002/(Sici)1097-4660(199704)68:4<351::Aid-Jctb613>3.0.Co;2-4.

(34) Cadena, C.; Anthony, J. L.; Shah, J. K.; Morrow, T. I.; Brennecke, J. F.; Maginn, E. J. Why is CO_2 so soluble in imidazolium-based ionic liquids? *Journal of the American Chemical Society* **2004**, *126* (16), 5300-5308. DOI: 10.1021/ja039615x.

(35) Lei, Z. G.; Dai, C. N.; Chen, B. H. Gas Solubility in Ionic Liquids. *Chemical Reviews* **2014**, *114* (2), 1289-1326. DOI: 10.1021/cr300497a.

(36) King, E. M.; Gebbie, M. A.; Melosh, N. A. Impact of Rigidity on Molecular Self-Assembly. *Langmuir* **2019**, *35* (48), 16062-16069. DOI: 10.1021/acs.langmuir.9b01824.

(37) Neyrizi, S.; Kiewiet, J.; Hempenius, M. A.; Mul, G. What It Takes for Imidazolium Cations to Promote Electrochemical Reduction of CO_2. *Acs Energy Letters* **2022**, *7* (10), 3439-3446. DOI: 10.1021/acsenergylett.2c01372.

(38) Motobayashi, K.; Maeno, Y.; Ikeda, K. In Situ Spectroscopic Characterization of an Intermediate of CO_2 Electroreduction on a Au Electrode in Room-Temperature Ionic Liquids. *Journal of Physical Chemistry C* **2022**. DOI: 10.1021/acs.jpcc.2c03012.

(39) Michez, R.; Doneux, T.; Buess-Herman, C.; Luhmer, M. NMR Study of the Reductive Decomposition of [BMIm] [NTf] at Gold Electrodes and Indirect Electrochemical Conversion of CO_2. *Chemphyschem* **2017**, *18* (16), 2208-2216. DOI: 10.1002/cphc.201700421.

(40) Guo, W. X.; Liu, B. C.; Gebbie, M. A. Suppressing Co-Ion Generation Cationic Proton Donors to Amplify Driving Forces for Electrochemical CO_2 Reduction. *Journal of Physical Chemistry C* **2023**, *127* (29), 14243-14254. DOI: 10.1021/acs.jpcc.3c04004.

(41) Arduengo, A. J.; Harlow, R. L.; Kline, M. A Stable Crystalline Carbene. *Journal of the American Chemical Society* **1991**, *113* (1), 361-363. DOI: DOI 10.1021/ja00001a054.

Chapter 2. Experimental Methods

2.1. Materials Preparation

2.1.1. Ionic liquid preparation

Commercially available ionic liquids were used as purchased and specific ionic liquid synthesis procedures are presented in each chapter. Ionic liquids that required additional processing, such as the substitution of one anion for another, were prepared by dissolving the original ionic liquid in water along with the required amount of the lithium salt containing the desired anion for anion metathesis. The mixture was stirred at room temperature for 3 hours while the desired ionic liquid formed a separate phase from the aqueous layer. The layer containing the ionic liquid with the desired anion was separated out and further purified using activated charcoal in the appropriate solvent. Once the activated charcoal was removed, the solvent was removed using rotary evaporation followed by drying *in vacuo* for 24-48 hours.

2.1.2. Electrode preparation

The working electrodes were polished to a mirror finish based on established protocols using 15 μm, 3 μm, and 1 μm diamond polish and then 0.05 μm alumina (BASi) to a mirror finish prior to sonication to remove adsorbed alumina. Geometric surface areas were calculated using either known electrode size or using ImageJ software to measure submerged electrode surface area.

2.1.3. Nafion 117 preparation

Nafion 117 membranes for chronoamperometric and chronopotentiometric studies were prepared according to literature prior to use.[1-3] In brief, as-received membranes precut to desired dimensions were immersed in 3 wt% H_2O_2 aqueous solution, Milli-Q Ultrapure water, 1 M H_2SO_4 aqueous solution, and Milli-Q Ultrapure water again in sequence. All solutions were heated to 80 °C, and each step took 1 hour. After preparation, we stored membranes in 0.1 M TBA BF_4-acetonitrile solution when not in use, and the membranes were rinsed with Milli-Q Ultrapure water and acetonitrile every time prior to use.

2.1.4. Karl Fischer measurements

Measurements of water content were carried out using a Mettler Toledo C10S Coulometric Karl Fischer Titrator. Due to the hygroscopic nature of acetonitrile, the water content of stock acetonitrile ranged from <100 ppm to 500 ppm. Water is a potential source of protons for CO_2 electroreduction, so water content is known to impact observed reactivity. To control the influence of trace water, water was systematically added to the acetonitrile to reach concentrations of 900-1100 ppm to maintain consistent electrolyte conditions between trials. In parallel experiments, we undertook extensive efforts to dry all electrolyte materials and found that CO_2 reduction is suppressed in extensively dried ionic liquid-based electrolytes, consistent with literature reports. [4-6] Hence, water is an essential proton source during ionic liquid-mediated CO_2 reduction.

2.2. Electrochemical Methods

Electrochemical measurements were using a BioLogic VSP potentiostat. Electrolyte solutions were comprised of ionic liquids dissolved in acetonitrile. The working electrodes were polished to a mirror finish based on established protocols using 15 μm, 3 μm, and 1 μm diamond polish and then 0.05 μm alumina (BASi) to a mirror finish before sonication to remove adsorbed alumina. Quantitative agreement with prior studies was achieved using this method. For all electrochemical measurements, we used an Ag/Ag^+ non-aqueous reference electrode and a coiled platinum wire as a counter electrode. Electrolyte solutions were purged for 20 minutes prior to electrochemical measurements using either Ar or CO_2 gas.

All cyclic voltammetry (CV) measurements presented were carried out at scan rates of 100 mV/s, but additional scan rates were performed. Single compartment cells were used for kinetics measurements and were composed of a 4 dram borosilicate glass vial fitted with a custom 3D-printed cap using chlorinated polyethylene elastomer filament (Prusa) to ensure reproducible cell geometry to control for effects of solution resistance across trials.

Reaction products and corresponding faradaic efficiencies during chronoamperometry studies (CA) were quantified using a custom-made gas-tight H-cell in chronoamperometry (CA) or chronopotentiometry (CP) studies. The compartments were separated using a Nafion 117 membrane and were continuously

stirred as well as purged with either Ar or CO_2. To prevent the rapid evaporation of acetonitrile, the inlet gas stream was sparged first through a pre-sparger consisting of only acetonitrile before entering the H-cell.

2.3. Product Analysis

2.3.1. Gas chromatography

Gaseous products of CA experiments were analyzed using a gas chromatograph (SRI Multiple Gas Analyzer #5) equipped with a thermal conductivity detector (TCD) and a flame-ionization detector (FID) paired with a methanizer. A HayeSep D column was connected to the TCD while the FID was connected to a HayeSep D and a Molesieve 5A column (Restek). Ultrahigh purity grade Ar (Airgas) was used as the carrier gas.

The faradaic efficiency was calculated by:[7]

$$FE(\%) = \frac{\frac{\nu}{60s/min} \times \frac{y}{24{,}000 cm^3/mol} \times N \times F}{i} \times 100\% \qquad \text{(Equation 2.1)}$$

where ν is the flow rate of CO_2 in units of sccm, y is the concentration of product measured from GC in the unit of mole fraction, N = 2 is the number of electrons consumed to convert one CO_2 molecule to one CO, F = 96500 C mol^{-1} is the Faraday constant, and *i* is the total current passing through the working electrode in the unit of A.

2.3.2. Nuclear magnetic resonance

Liquid phase products and electrolyte composition was studied using NMR spectroscopy, which was performed using a 400 MHz NMR spectrometer (Bruker Avance) with a BBFO probe. When H-D exchange was a concern, the deuterated solvent was separated from the electrolyte using a capillary tube to prevent the unwanted incorporation of deuterium in the species of interest. The spectra were analyzed using MestreNova software (Mestrelab Research).

2.4. Characterization Techniques

2.4.1. Surface-enhanced Raman scattering spectroscopy

Electrochemical surface-enhanced Raman scattering (SERS) measurements were carried out using a single-compartment PTFE electrochemical cell with a polished L-shaped Ag working electrode (Shanghai Fanyue Electronic Technology Co. Ltd) prepared by drop-casting Ag nanoparticles onto the surface to achieve enhancement or by electrochemical surface roughening techniques. Ag nanoparticles were synthesized based on a previously reported method[8] while surface roughening was performed through adaptation of another previously reported method.[9] The counter electrode was a polished and coiled Pt wire, while the reference electrode was a non-aqueous Ag/Ag^+ (0.01 M $AgNO_3$) reference. The electrolyte was purged with either Ar or CO_2 for 20 minutes prior to conducting the measurements. SERS spectra were collected using a Thermo-Fisher Scientific DXRxi Raman Imaging Microscope with a 532 nm excitation laser and at 10x magnification. Optical images of the working electrode surface were also captured using the same Raman imaging microscope in video mode.

2.4.2. Scanning electron microscopy

Scanning electron microscopy (SEM) of electrode surfaces was performed using a Zeiss Gemini 450 FESEM. SEM Images were taken using either a 5 kV or 10 kV accelerating voltage at a working distance of 8 mm to achieve the desired depth of field. Images were captured using the in-lens back-scattered electron detector.

2.5. Data management

Python scripts were used to manage the CV data generated for Chapters 3 and 4, which allowed for the compilation of cyclic voltammetry data relevant to onset potentials and current densities at various potentials into large databases. Briefly, this entailed analyzing a cyclic voltammetry curve for each cycle of each trial using a GUI that enabled a user to choose points of interest on a curve in both the anodic and cathodic sweeps. This information, along with the electrolyte composition, the scan rate, the sparging gas,

and the date of the experiment were then automatically stored in a .csv file. This data could then be extracted at a later date for specific electrolyte compositions to facilitate the analysis of data sets across experiments.

2.6. References

(1) Sun, L. Y.; Ramesha, G. K.; Kamat, P. V.; Brennecke, J. F. Switching the Reaction Course of Electrochemical CO_2 Reduction with Ionic Liquids. *Langmuir* **2014**, *30* (21), 6302-6308, Article. DOI: 10.1021/la5009076.

(2) Chae, K. J.; Choi, M.; Ajayi, F. F.; Park, W.; Chang, I. S.; Kim, I. S. Mass Transport through a Proton Exchange Membrane (Nafion) in Microbial Fuel Cells. *Energy and Fuels* **2008**, *22* (1), 169-176.

(3) Sheng, H.; Hermes, E. D.; Yang, X.; Ying, D.; Janes, A. N.; Li, W.; Schmidt, J. R.; Jin, S. Electrocatalytic Production of H_2O_2 by Selective Oxygen Reduction Using Earth-Abundant Cobalt Pyrite (CoS_2). *ACS Catalysis* **2019**, *9* (9), 8433-8442. DOI: 10.1021/acscatal.9b02546.

(4) Rudnev, A. V.; Zhumaev, U. E.; Kuzume, A.; Vesztergom, S.; Furrer, J.; Broekmann, P.; Wandlowski, T. The promoting effect of water on the electroreduction of CO_2 in acetonitrile. *Electrochimica Acta* **2016**, *189*, 38-44. DOI: 10.1016/j.electacta.2015.12.088.

(5) Rosen, B. A.; Zhu, W.; Kaul, G.; Salehi-Khojin, A.; Masel, R. I. Water Enhancement of CO_2 Conversion on Silver in 1-Ethyl-3-Methylimidazolium Tetrafluoroborate. *Journal of The Electrochemical Society* **2012**, *160* (2), H138-H141. DOI: 10.1149/2.004303jes.

(6) Figueiredo, M. C.; Ledezma-Yanez, I.; Koper, M. T. M. In Situ Spectroscopic Study of CO_2 Electroreduction at Copper Electrodes in Acetonitrile. *ACS Catalysis* **2016**, *6* (4), 2382-2392, Article. DOI: 10.1021/acscatal.5b02543.

(7) Han, N.; Wang, Y.; Yang, H.; Deng, J.; Wu, J.; Li, Y.; Li, Y. Ultrathin bismuth nanosheets from in situ topotactic transformation for selective electrocatalytic CO_2 reduction to formate. *Nature Communications* **2018**, *9* (1), 1320. DOI: 10.1038/s41467-018-03712-z.

(8) Agnihotri, S.; Mukherji, S.; Mukherji, S. Size-controlled silver nanoparticles synthesized over the range 5–100 nm using the same protocol and their antibacterial efficacy. *RSC Advances* **2014**, *4* (8), 3974-3983. DOI: 10.1039/c3ra44507k.

(9) dos Santos, D. P.; Temperini, M. L.; Brolo, A. G. Mapping the energy distribution of SERRS hot spots from anti-Stokes to Stokes intensity ratios. *Journal of The Electrochemical Society* **2012**, *134* (32), 13492-13500. DOI: 10.1021/ja305580t.

Chapter 3. Tuning Ionic Screening to Accelerate Electrochemical CO_2 Reduction in Ionic Liquid Electrolytes[1]

3.1. Introduction

Electrochemical reduction of CO_2 to CO and other products could provide opportunities to minimize the carbon footprints of industrial processes by replacing fossil fuels with waste or atmospheric CO_2. Conversion of CO_2 proceeds via mechanisms where the first step often involves a two proton, two-electron half-reaction to convert CO_2 into CO (Eq. 3.1), usually through the formation of a negative radical intermediate,[1, 2] which can then further react to wide-ranging products. Notably, the concurrent generation of H_2 by the hydrogen evolution reaction (HER) also occurs via a two proton, two-electron half-reaction at similar, often lower, onset potentials, particularly in aqueous solutions. Hence, a key challenge for the implementation of electrochemical CO_2 reduction is to devise approaches to favor CO_2 reduction, while simultaneously inhibiting electron flow into the HER pathway.

$$CO_2 + 2H^+ + 2e^- \rightarrow CO + H_2O \qquad \text{(Equation 3.1)}$$

Recently, chemical modulation of electrolyte properties, such as the inclusion of cations that stabilize CO_2 reduction transition states, has emerged as an important tool in tipping the balance away from HER and towards CO_2 reduction.[3-7] For example, ionic liquid-based electrolytes where cations are designed to selectively coordinate CO_2 have emerged as promising co-catalytic promoters of selective electro-reduction of CO_2 to CO.[3, 6-10]

Ionic liquids are salts typically composed of bulky organic cations combined with a variety of anions, which may be organic or inorganic.[11-13] While neat ionic liquids exhibit advantageous properties for CO_2 electro-reduction, including high electrochemical stability, CO_2 solubility, and intrinsic ionic

[1] Chapter adapted from: Liu B, Guo W, Gebbie MA. Tuning Ionic Screening to Accelerate Electrochemical CO_2 Reduction in Ionic Liquid Electrolytes. *ACS Catal.* 2022, **12**, 15, 9706–9716.; Supplemental information is presented in the Appendix.

conductivity, they are too viscous to facilitate high current densities needed for practical processes. As a result, ionic liquids are often blended into aqueous and non-aqueous solutions when implemented in electrocatalytic studies.

Co-catalysis of CO_2 reduction via ionic liquids was first demonstrated by Rosen and coworkers, where aqueous electrolytes with ion concentrations of 4.26 M were used in combination with silver electrodes.[3] This study showed di-alkyl imidazolium cations could serve as co-catalysts for CO_2 reduction at unprecedentedly low onset potentials for selective reduction of CO_2 to CO, despite the presence of large amounts of water. Subsequent publications delved into possible mechanisms for HER suppression and enhancement of CO_2 reduction.[4-6] Leading possibilities for enhancement of CO_2 reduction include cation hydrogen-bond stabilization of transition states[14-16] and carbene-mediated coordination of CO_2 via cation complexes to activate CO_2.[14, 17-22] HER suppression mechanisms are typically centered around exclusion of water from interfaces.[7, 23]

Despite initial reports by Rosen and colleagues of pronounced enhancement of CO_2 reduction in aqueous electrolytes with very high ion concentrations, subsequent studies proceeded to focus on understanding how ion molecular structures influence CO_2 reduction in either neat ionic liquids or low concentration ionic liquid-supporting electrolyte blends. Dilute and neat ionic liquid electrolytes appear to be emphasized because dilute electrolytes maximize CO_2 transport due to low solution viscosity and neat ionic liquids maximize CO_2 solubility. For cases when ionic liquids are blended with solvent, acetonitrile has emerged as a common choice due to low viscosity, large electrochemical window, and high CO_2 solubility.[24]

Nonetheless, current mechanistic understandings of ionic liquid-mediated CO_2 electrochemical reduction focus more on molecular interactions between single ionic liquid ions and CO_2, while the influence of collective ion correlations and self-assembly on reactivity is often overlooked. Critically, current investigations appear to avoid intermediate concentrations, especially as ion concentrations begin to exceed dilute limits, which is around 1 M for an aqueous solution. For less polar solvents, such as

acetonitrile, this crossover is shifted to lower concentrations.[25] Notably, this is the regime where ionic correlations are expected to emerge.

Therefore, we designed a systematic study of CO_2 reduction in ionic liquid solutions at varying concentrations, with a focus on intermediate concentrations, to illuminate the role of ionic correlations in electrochemical reactivity. Given that many electrochemical devices use electrolytes with ion concentrations that exceed the dilute limit, such insights will have broad implications that extend beyond CO_2 electrolysis processes.

Our core hypothesis is that ionic liquid-mediated CO_2 electrochemical reduction rates will exhibit non-monotonic scaling with electrolyte ion concentration and will be maximized at intermediate concentrations. Electrochemical reaction rates and pathways are closely related to the properties of electric double layers. Our hypothesis builds on recent findings from the surface force community showing that electric double layers often exhibit the most efficient screening, as evidenced by minimized electrostatic screening lengths, at intermediate concentrations, compared with dilute solution and high concentrations.[26-31] These observations stand in contrast to the classical Debye-Hückel theory, which predicts that increasing ion concentrations systematically increases the efficiency of electrostatic screening by decreasing screening lengths.

The non-monotonic relationship between ion concentrations and electrostatic screening lengths was interpreted as an indication that ionic correlations and clustering begin to emerge at high ion concentrations and that correlations cause many dissolved ions to become “bound” in effectively neutral aggregates.[26, 27, 32] This formation of aggregates then reduces the population of “free” ions available to screen charged surfaces. As a result, electric double layers that form in highly concentrated electrolytes are much thicker, or less efficiently screened, than would be predicted via frameworks, like Debye-Hückel theory, which assumes ions are independently “free” to screen electrodes.[25-27, 30, 31, 33] Tuning ionic correlations by varying ion concentration should influence many properties of electrode-electrolyte interfaces that dictate electrocatalytic reactivity.[34-38]

We thus envision that the modulation of ionic correlations via concentration would allow us to achieve enhanced electrostatic screening, which would aid in breaking bonds and stabilizing transition states through localizing electric field gradients to electrode surfaces. Here, we describe our proof-of-concept study of how ion correlations and screening can be used as a complementary method for controlling electrochemical reactions. We chose the electroreduction of CO_2 to CO on silver electrodes in ionic liquid/acetonitrile blends with controlled water concentrations of 900-1100 ppm as our model reaction to illustrate how a holistic approach of considering double layer formation at electrocatalytic interfaces can qualitatively transform common reactivity metrics.

Our findings demonstrate that ionic strength can alter reactivity in ways that can rival the influence of the specific chemical structures of the ionic liquid ions studied. We used electrochemical kinetics approaches, including cyclic voltammetry (CV) measurements, to conduct ion concentration sweeps and reveal non-monotonic enhancement of CO_2 electroreduction rates for both co-catalytic and non-catalytic ionic liquid-based electrolytes (Fig. 3.1). We then performed chronoamperometry (CA) and product analysis studies (Fig. 3.2) to show that steady-state current densities and faradaic efficiencies reflect enhanced kinetics measured at intermediate concentrations. To gain insight into mechanisms of this rate enhancement, we performed *in-situ* electrochemical surface-enhanced Raman scattering (SERS) spectroscopy studies, which provide clues suggesting that rate acceleration originates in the enhancement of local potential gradients at concentrations that yield maximum current densities and faradaic efficiencies (Fig. 3.3).

Finally, we describe a noteworthy case where increases in ion concentration ultimately leads to cathode passivation through the formation of (bi)carbonate resulting from the reaction between CO_2 and OH^- (Fig. 3.4). This provides key insight into the role of the imidazolium ionic liquid in enhancing CO_2 reduction rates, suggesting new strategies for mitigating electrode passivation in organic electrolytes.

3.2. Experimental Methods

Chemicals. The ionic liquids used in the preparation of the electrolytes were: 1-ethyl-3-methylimidazolium tetrafluoroborate (EMIm BF_4, >98% purity, Iolitec), 1-ethyl-2,3-dimethylimidazolium tetrafluoroborate (EMMIm BF_4, 97% purity, Alfa Aesar), 1-ethyl-1-methylpyrrolidinium tetrafluoroborate (EMPyrr BF_4, >98% purity, Iolitec), and tetrabutylammonium tetrafluoroborate (TBA BF_4, 99% purity, Sigma Aldrich). All ionic liquids were used without further purification. Ultrapure water (Milli-Q, ≥18.2 MΩcm) was used in all experiments.

Electrochemical Methods. Electrochemical measurements were performed in borosilicate glass cells and were carried out using a BioLogic VSP potentiostat. Electrolyte solutions were comprised of ionic liquids dissolved in acetonitrile. In parallel experiments, we undertook extensive efforts to dry all electrolyte materials and found that CO_2 reduction is suppressed in extensively dried ionic liquid-based electrolytes, consistent with literature reports. [4, 39, 40] Hence, water is an essential proton source during ionic liquid-mediated CO_2 reduction, and our results substantiate this conclusion, as elaborated in the Results and Discussion.

For cyclic voltametric (CV) and chronoamperometric (CA) measurements, the working electrode was a polycrystalline Ag electrode (BASi) with a geometric surface area of 0.071 cm^2. For all electrochemical measurements, we used an Ag/Ag^+ non-aqueous reference electrode and a coiled platinum wire as a counter electrode. A ferrocene/ferrocenium redox couple was used initially to confirm the applicability of a Ag/Ag^+ (0.01 M $AgNO_3$) non-aqueous reference previously described for acetonitrile-containing electrolytes. Since the silver surface readily oxidizes in the potential range near the ferrocene/ferrocenium redox couple, all potentials used in this work are referenced to the Ag/Ag^+ (0.01 M $AgNO_3$) reference.[41] Electrolyte solutions were purged for 20 minutes prior to electrochemical measurements using either Ar or CO_2 gas. All CV measurements were carried out at scan rates of 100 mV/s.

Product Analysis. We studied the products of electrolysis and determined corresponding faradaic efficiencies using a custom-made gas-tight 2-compartment cell in CA studies. The compartments were

separated using a Nafion 117 membrane and were continuously stirred and purged with CO_2 at 9.2 sccm. Potentials of -2.5 V were held for 3 hours, where steady state was reached after 1 hour and gas samples were taken every 20 minutes.

We performed NMR spectroscopy using a 400 MHz NMR spectrometer (Bruker Avance) with a BBFO probe to evaluate the electrolyte composition before and after CA experiments through ^{1}H NMR and ^{13}C NMR. DMSO-d6 was used as the solvent.

3.3. Results

3.3.1. Cyclic Voltammetry

We first analyzed the electrochemical behavior of ionic liquid solutions of varying concentrations separately under Ar- and CO_2-saturated solution conditions. Using 1-ethyl-3-methylimidazolium tetrafluoroborate (EMIm BF_4) in combination with a common supporting electrolyte salt tetrabutylammonium tetrafluoroborate (TBA BF_4) (Scheme 3.1), we examined ionic liquid-derived electrolytes with ions dissolved in acetonitrile at low concentrations that are commonly described in literature. We observed cyclic voltammetry (CV) results in agreement with prior studies for 25 mM EMIm BF_4 containing 0.1 M TBA BF_4, and neat EMIm BF_4 (Fig. 1A).[14, 19, 35, 42-44]

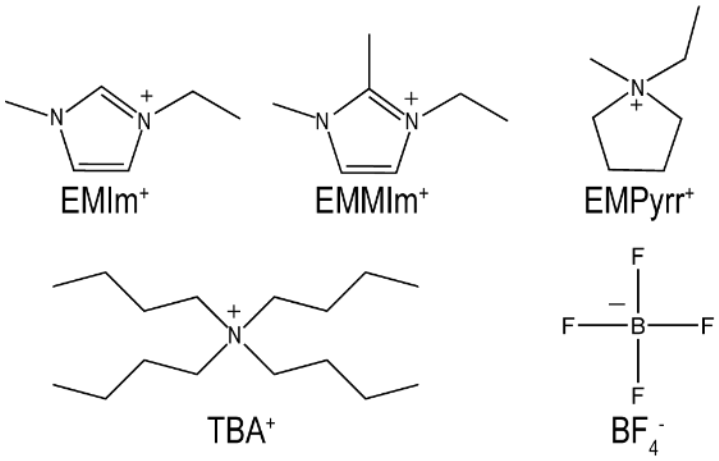

Scheme 3.1. Chemical structures of ionic liquid cations and anions used in this work.

We then studied how the chemical structures of ions influence interfacial properties. Interestingly, the CV response of 125 mM EMIm BF_4 solution was comparable to that of 25 mM EMIm BF_4 + 0.1 M TBA BF_4 solution, exhibiting very similar onset potentials and current densities. Onset potentials are dictated by charge transfer activation energies, while current densities provide an indication of reaction rates.

Typically, EMIm BF_4 is thought to be a co-catalyst for the CO_2 electroreduction reaction, while TBA BF_4 is used as a supporting electrolyte to mitigate solution resistance losses. If the co-catalytic nature of EMIm BF_4 is critical at these lower solution concentrations, then electrolytes with higher concentrations of EMIm BF_4 should yield higher current densities. The similarities in both onset potential and current density suggest that the total ion concentration has a larger influence on reactivity than the identity of the dissolved cations in the low concentration regime. Within the low concentration regime for these electrolytes, we conclude that CO_2 reduction is largely independent of specific ion properties but is instead proceeding via an outer-sphere mechanism, or direct electrode-CO_2 electron transfer.

Another notable finding from our work is that the onset potentials and current densities measured for neat EMIm BF_4 and the dilute (25 mM, no TBA BF_4) EMIm BF_4 solutions are similar. This surprising result, which is also observed for EMPyrr BF_4 and TBA BF_4 (Fig. A1.4, A1.6), raises the possibility that reaction environments exhibited by some neat liquids may share analogies to reaction environments present in dilute electrolyte solutions, as ion clustering can dramatically suppress the availability of "free ions" to screen charged surfaces and localize potential gradients. Such an interpretation is consistent with discussions from the surface force community, where it is proposed that large electrostatic screening lengths present in ionic liquids cause them to behave analogously to dilute electrolytes, where very few "free" ions are available to redistribute and screen charged surfaces.[25, 26, 30, 33]

Most importantly, we observed a remarkable increase in CO_2 reduction rates, in the form of enhanced current densities, as we increased the concentration of EMIm BF_4 to exceed dilute limits (ca. 150 mM). At intermediate concentrations, such as 0.5 M EMIm BF_4 (Fig. 3.1A), we observed current densities

that were almost double that of more dilute concentrations. Such high current densities were absent when electrolytes were purged with Ar. Notably, onset potentials for CO_2 reduction did not vary greatly within this intermediate concentration regime. Hence, our concentration-dependent measurements indicate that the activation energy for CO_2 reduction reaction is similar across varied concentrations, but the reaction rate was substantially enhanced at intermediate concentration, as compared to the dilute and neat concentrations.

Small differences in onset potentials may be observed if an iR correction is used to account for solution resistance potential drops, where there is an associated potential drop required for current to flow in an electrochemical cell. In electrolytes with low conductivity, the potential experienced by reactants and products at the working electrode can be much smaller in magnitude than the potential applied by the potentiostat, and resulting voltammetry curves would appear linear rather than exponential with an increase in potential due to solution resistance.[45] As seen in Figure 3.1, the key intermediate concentration regimes that are the focus of our work exhibit CV curves that are more exponential in nature than linear, and accounting for iR drops would further increase the pronounced rate enhancement we observed.

Nevertheless, the 25 mM and neat EMIm BF_4 electrolytes do exhibit characteristics of solution resistance-limited rates (Fig. 3.1A), indicating that solution resistance plays a larger role at these two extreme concentrations. Solution resistance is dependent on cell geometry, so we maintained consistent distances and orientations between working and reference electrodes for all experiments.[45] To account for the solution resistance component of CV measurements, an iR correction can be applied, where solution resistance-related potential drop is calculated or measured and subtracted from the reported potential. When this data transformation is implemented, CV curves appear exponential. We present the untransformed data in the main text as we found that applying iR corrections will not change the trends and core features that we observe and present in this work.

In addition to solution conductivity, the identity of the proton donor involved in CO_2 reduction can have a large influence on reaction rates. In many cases, water is the only proton donor available to participate in CO_2 reduction, particularly when water is doped into aprotic solvents, like acetonitrile. In

EMIm BF_4 solutions, imidazolium cations can also donate the acidic 2-site proton, which can cause EMIm cations to become the primary proton donor in intermediate-to-high concentration solution studied here. Future work evaluating how water concentration and the presence or absence of proton donors other than water influences reactivity would be illuminating in light of the universal enhancement of reaction rate with ion concentration we report here.

Overall, we conclude that changes in solution resistance and water activity are unlikely to be primary reasons for the rate enhancements we observe. By keeping the initial concentration of water constant among samples, we see variations in current density and faradaic efficiencies solely through changing cation structures (Fig. 3.1, Figs. A1.4, A1.6). If water activity or solution resistance were the dominant factor, we would expect to observe reactivity that was largely independent of cation structure. Notably, our results support recent works in the field, which increasingly suggest that cations play a leading role in determining CO_2 reduction activity[5, 46-48] and the likelihood that water activity or solution resistance could have higher order effects on observed reactivity would complement our key findings and conclusions.

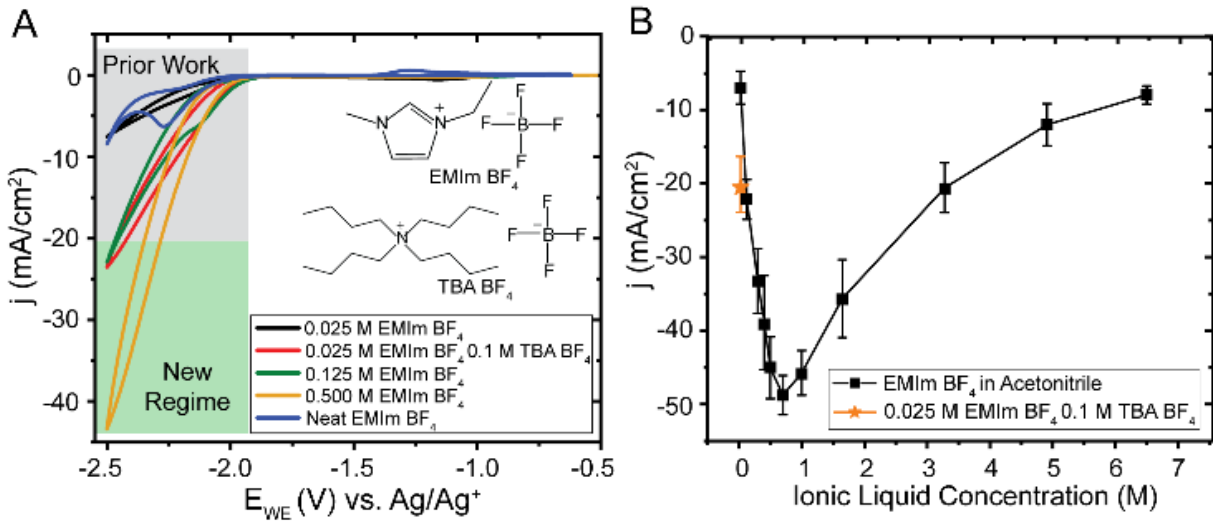

Figure 3.1 Non-monotonic concentration-dependent reactivity of CO2 electrochemical reduction CO_2-saturated acetonitrile solutions of EMIm BF4 at varying concentrations. (A) Compared to the dilute and neat ionic liquid limits typically used in electrocatalysis studies, intermediate concentrations display a significant increase in current densities from CO_2 electrochemical reduction. (B) Non-monotonic concentration dependence of current densities. At -2.5 V vs. Ag/Ag^+, we observe pronounced increases in reactivity at intermediate concentrations of EMIm BF_4 in acetonitrile. Using the current densities at -2.5 V

vs. Ag/Ag^+ as a representative value for a relatively high polarization, we find a remarkable average current density of 48.6 ± 3.0 mA/cm^2 at 0.7 M EMIm BF_4, which is more than double that of more traditional concentrations, such as neat EMIm BF_4 or 25 mM EMIm BF_4 + 0.1 M TBA BF_4. Each data point and error bar represent three independent trials, from which two representative CVs were used for each trial for a total of at least six values.

We also note that rigorous discussion of overpotentials for practical electrolysis of a complete electrochemical cell necessitates an understanding of both the cathodic and anodic reactions of interest. Conventionally, the cathodic reaction is depicted in Eq. 3.1, where CO_2, two protons, and two electrons react to form CO and H_2O. The corresponding anodic reaction, particularly in aqueous electrolytes, is the oxidation of water into two protons and one oxygen atom (Eq. 3.2).

$$H_2O \rightarrow 2H^+ + \tfrac{1}{2}O_2 + 2e^- \qquad \text{(Equation 3.2)}$$

Using these two half-reactions, the overall thermodynamic potential is -1.33 V.[3, 41] As written, water should be neither generated nor consumed between the two half-reactions. During our trials, we observed a consistent increase in water content in the anolyte after CA, suggesting the circuit was completed by anodic reactions other than water oxidation.[16, 49] Prior works indicate that -1.5 V vs. Ag/Ag^+ is the onset potential for the cathodic reaction shown in Eq. (3.1) in acetonitrile solutions of ionic liquids,[49] and we find this value to be the appropriate potential to use for calculating overpotentials. Taken together, we conclude that the onset potentials we report in this work are comparable to prior studies.

We then conducted a study on a wide concentration range of EMIm BF_4 with a particular focus on the intermediate concentrations. We observed a non-monotonic enhancement of reaction rate with concentration, with a maximum average current density at 0.7 M EMIm BF_4 (Fig. 3.1B). CV is used primarily to study electrochemical reaction kinetics, so our results suggest that the maximum reaction rate enhancement of CO_2 reduction occurs at 0.7 M EMIm BF_4. Beyond this concentration, however, the reactivity decreased such that current densities of the neat ionic liquid became similar to that of the 25 mM electrolyte.

3.3.2. Chronoamperometry

Figure 2 shows results from 3-hour-long electrolysis experiments under well-mixed conditions. Generally, the trends observed in CA experiments align well with the CV results. The steady-state current densities and corresponding faradaic efficiencies for CO reached a maximum at 0.9 M EMIm BF_4 rather than the 0.7 M suggested by CV. In addition to CA experiments, we used nuclear magnetic resonance (NMR) to compare changes in electrolyte composition before and after experiments. For EMIm BF_4, we observed formation of a carboxylate adduct in catholytes that has previously been reported in literature.[19, 50, 51] The abundance of this adduct was positively correlated with the current density of corresponding electrolytes and was the most pronounced in electrolytes with intermediate concentrations (Fig. A1.3 and Table A1.1).

Reduction of CO_2 with water as the proton donor is known to generate HCO_3^- through reaction between CO_2 and OH^- anions and is a major contributor to low faradaic efficiencies for CO_2 reduction reactions in alkaline or near-neutral pH media.[46, 52-54] Meanwhile, prior studies suggested that the carboxylate adduct spontaneously forms when EMIm cations and HCO_3^- coexist in acetonitrile.[49] We conclude that the formation of adduct at the C2 position of the imidazolium cation ring in our study is more likely a byproduct of the reduction of CO_2 through the full reaction:

$$3CO_2 + 2EMIm^+\text{-}H + 2e^- \rightarrow CO + 2EMIm^+\text{-}COO^- + H_2O \qquad \text{(Equation 3.3)}$$

Indeed, the water content in catholytes increased by 1000 to 2000 ppm after 3-hour electrolysis, matching the trend predicted by the equation and suggesting that imidazolium cations serve as a primary proton donor for CO_2 reduction in EMIm BF_4 electrolytes.

We observed a similar non-monotonic trend in steady-state current densities and faradaic efficiencies for 1-ethyl-1-methylpyrrolidinium tetrafluoroborate (EMPyrr BF_4), an ionic liquid that is not considered a co-catalyst for CO_2 electroreduction and cannot act as a proton donor (Fig. 3.2). In CA studies for EMPyrr BF_4, we found that the steady-state current densities and faradaic efficiencies reach a maximum

at 0.5 M EMPyrr BF_4, instead of the maximum at 0.9 M observed for EMIm BF_4. Using CV, we measured the largest current densities for the 125 mM EMPyrr BF_4 solution (Fig. A1.4), which may be due to both electrochemical cell setup, as well as electrode cycling history. For practical considerations, CA results are more directly applicable to electrolysis applications. NMR results indicated no significant change in the composition of the electrolyte after the electrolysis experiments.

In both EMIm BF_4 and EMPyrr BF_4, acetonitrile decomposition accounts for the reduced faradaic efficiency at low concentrations,[55] since H_2 production was absent and ^{1}MR showed similar impurity peaks for catholytes with different contents (Figs. A1.3, A1.5). At high concentrations, drops in steady-state current densities and faradaic efficiencies likely arise from ionic liquid decomposition[44, 51] since significant H_2 production was not observed, nor was the formation of carbonate species. Yet, due to the low current densities corresponding to these concentrations, ionic liquid decomposition products are not abundant enough to be detected by NMR of bulk electrolyte.

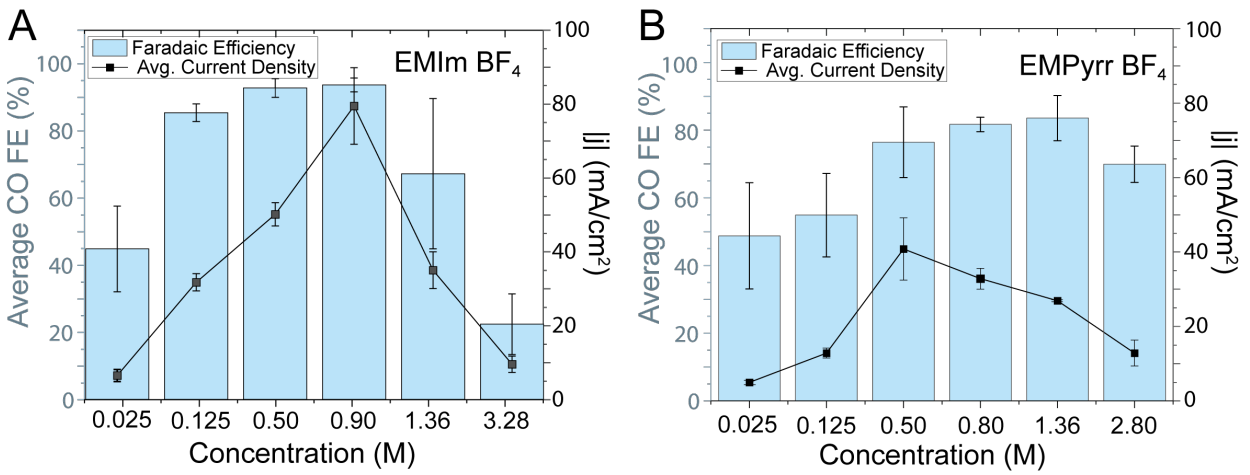

Figure 3.2 Steady-state faradaic efficiencies (FE) for CO production and current densities (j) obtained over the course of hours 1-3 of chronoamperometry at -2.5 V vs. Ag/Ag^+ on Ag electrodes for varying concentrations of (A) EMIm BF_4, and (B) EMPyrr BF_4 in acetonitrile solvent. While EMIm BF_4 displayed higher steady-state current densities and faradaic efficiencies at intermediate concentrations, EMIm BF_4 and EMPyrr BF_4 share a similar non-monotonic enhancement of both current densities and faradaic efficiencies along with concentrations, suggesting that this enhancement is not ion-specific. Each data point represents an average and standard deviation obtained from seven time points collected for each sample.

We then tested the supporting electrolyte to further evaluate its role in the reduction reaction. CV trials with TBA BF_4 exhibited very similar reactivity trends (Fig. A1.6) as EMIm BF_4 and EMPyrr BF_4, where the peak current density is achieved at concentrations lower than 1 M. Prior works concluded that tetraalkylammonium-based salts are not co-catalysts for CO_2 electroreduction and mediate the reaction via an outer-sphere mechanism,[24, 56] which may explain the lower current densities for TBA BF_4 when compared with EMIm BF_4.

3.3.3. Surface-enhanced Raman spectroscopy (SERS)

With our observation of a concentration-dependent reactivity for TBA BF_4, we posit that the role of TBA BF_4 both reduces solution resistance and impacts CO_2 electroreduction by influencing interfacial properties. The higher current densities and faradaic efficiencies we observed for EMIm BF_4 still strongly point to imidazolium-based ionic liquids functioning as a co-catalyst, where the non-monotonic behavior is amplified by the co-catalytic nature of EMIm cations. The non-monotonic trend that we observe for both co-catalytic and non-catalytic ionic liquids provides evidence suggesting that this behavior is generalizable to different ion structures. We propose that difference in electric potential gradients mediated by the collective assembly of ions is a likely mechanism influencing reactivity. Thus, we used *in situ* SERS to gain molecular level insights into the potential-modulated assembly of ions in the electric double layer and determine how electric potential gradients depend on the concentration of ionic liquid ions (Fig. 3.3).

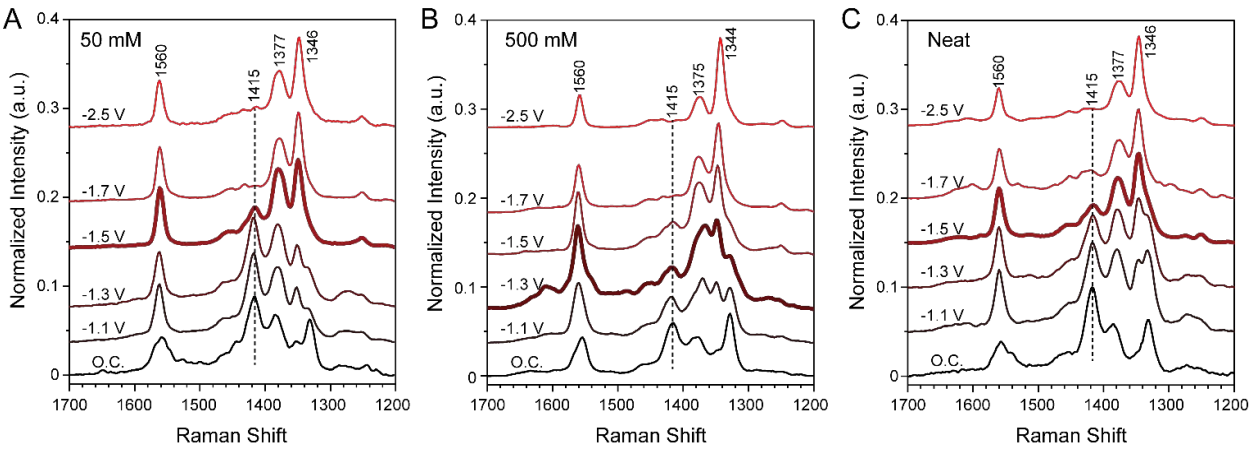

Figure 3.3 *In situ* SERS spectra of (A) 50 mM EMIm BF_4, (B) 500 mM EMIm BF_4, and (C) neat EMIm BF_4 in the ring deformation region in forward potential sweeps. Intensities of peaks at 1560, 1375, and 1344 cm^{-1} gradually increase, and the peak at 1415 cm^{-1} gradually decreases when the potential is decreased from open-circuit potential to -2.5 V vs. Ag/Ag^+ in all three cases. Nonetheless, the 500 mM EMIm BF_4 exhibits more rapid changes in relative peak intensities compared with 50 mM and neat EMIm BF_4. While the intensity ratio of the 1344 cm^{-1} peak over the 1415 cm^{-1} peak is initially smaller than 1, it is inverted before the applied potential reaches -1.3 V for 500 mM EMIm BF_4. In contrast, at least -1.5 V was required to observe a similar inversion in the peak ratio for 50 mM and neat EMIm BF_4. At each concentration, the SERS spectrum from the potential required to invert the peak ratio between 1344 and 1415 cm^{-1} is bolded for a clearer comparison. O.C. stands for open-circuit potential.

For EMIm BF_4 solutions, the intensity of SERS peaks at 1560, 1376, and 1344 cm^{-1} in the imidazolium ring fingerprint region increase during cathodic potential sweeps,[57, 58] which is accompanied by a decrease in the intensity of a peak at 1415 cm^{-1}. Identical spectral changes occurred in both CO_2-saturated (Fig. 3.3) and Ar-purged solutions (Fig. A1.9), which can be interpreted as reorientation of $EMIm^+$ in response to the electric fields.[50, 59] We use the intensity ratio of the peak at 1344 cm^{-1} to the peak at 1415 cm^{-1} as an indicator of the extent of $EMIm^+$ reorientation. This ratio shows a more rapid increase with the applied potential and reaches a higher value at -2.5 V for 500 mM EMIm BF_4 compared with 50 mM and neat EMIm BF_4 (Fig. 3.3, Figs. A1.8, A1.10). This indicates a more pronounced reorientation of EMIm cations in 500 mM solution as a function of applied potential, indicating stronger local electric fields exist in solutions with intermediate ionic concentrations.

We also studied the concentration-dependent behavior of 1-ethyl-2,3-dimethylimidazolium tetrafluoroborate (EMMIm BF_4), an ionic liquid that was reported to display higher reactivity than EMIm BF_4 at low concentrations due to the methylation of the C2 site that prevents carbene formation.[14, 19, 44] We

found that solution ion concentration critically determines if methylation enhances or detracts from reactivity. We successfully reproduced the high activity of CO_2 reduction using EMMIm BF_4 at a low concentration (25 mM) with 0.1 M TBA BF_4 supporting electrolyte. However, increasing the concentration of EMMIm BF_4 to 125 mM and higher resulted in significantly lower current densities and faradaic efficiencies in 3-hour electrolysis (Fig. 3.4A).

Upon further examination, we found that the CVs associated with higher concentrations of EMMIm BF_4 yielded vastly different shapes between the initial and subsequent cycles (Figs. A1.12- A1.15), unlike EMIm BF_4 which maintained the same shape between cycles (Fig. A1.11). Although the initial cycles for EMMIm BF typically yielded current densities greater than -20 mA/cm^2 and displayed the same non-monotonic enhancement as EMIm BF_4 (Fig. A1.16), the following cycles appeared to allow little or no CO_2 electroreduction. Steady-state current densities also showed quick drops in current density upon initial polarization, and faradaic efficiencies reached a maximum at 125 mM EMMIm BF_4 (Fig. 3.4).

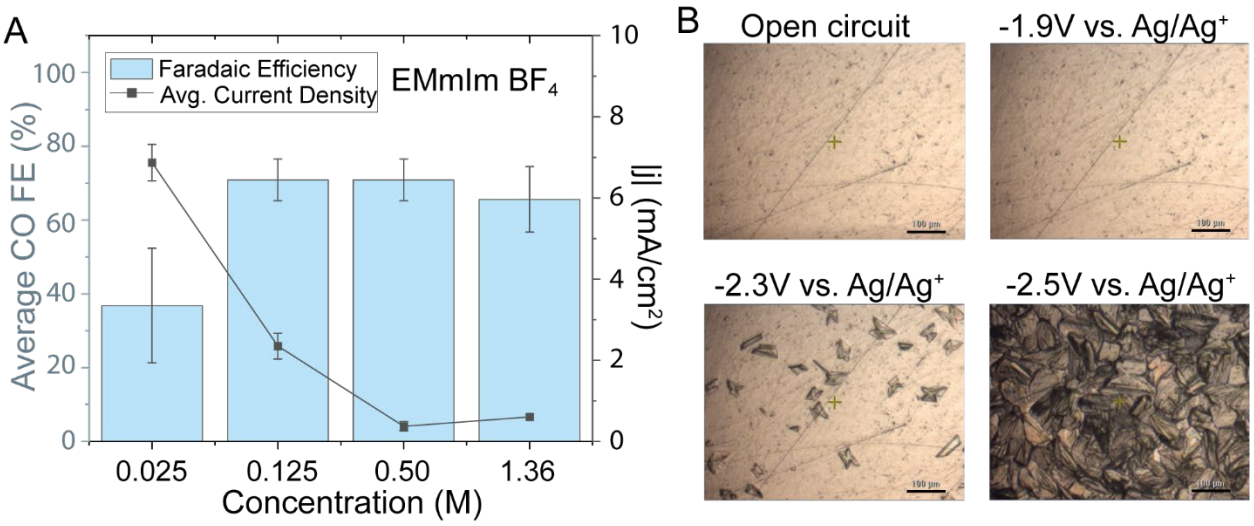

Figure 3.4 CA and FE results for CO_2-saturated acetonitrile solutions of EMMIm BF_4 at different concentrations and representative images of electrode passivation via the formation of EMMIm HCO_3. (A) CA and FE results. EMMIm BF_4 is considered a better co-catalyst than EMIm BF_4 in previous literature at dilute concentrations. However, EMMIm BF_4 displays an unexpected decrease in steady-state current densities at concentrations beyond 125 mM, while faradaic efficiencies at these concentrations are near constant. (B) Nucleation and growth of EMMIm HCO_3 crystals in a CO_2-saturated acetonitrile solution of 0.125 M EMMIm BF_4 at 10x magnification. Crystals started to form at potentials exceeding -2.3 V. These crystals likely limit mass transport of reactants and products across interfaces, accounting for the decrease

in reactivity at relatively higher concentrations shown in (A). Interestingly, onset potentials for crystallization, crystal morphology, and crystal growth rate vary drastically with solution conditions (Figs. A1.18- A1.21). Scale bars in (B) stand for 100 μm.

To understand this surprising drop in reactivity, we used *in situ* SERS and optical microscopy to observe electrode surfaces as reactions proceeded. When electrolyte solutions were saturated with CO_2, we observed the potential-dependent nucleation and growth of crystals even when the concentration of EMMIm BF_4 was as low as 50 mM (Figs. 3.4B, A1.18, and A1.19). Interestingly, similar crystals formed in CO_2-saturated solutions of EMMIm Br and EMMIm TSFI at potentials close to the onset potential for CO_2 reduction (Figs. A1.20, A1.21), suggesting that the crystallization was independent of anion identity and was derived from processes related to CO_2 reduction. Indeed, NMR analysis indicates that the crystals are EMMIm HCO_3, which is insoluble in acetonitrile (Figs. A1.22, A1.23). Therefore, we deduce that initial CO_2 reduction in EMMIm BF_4 electrolytes quickly built up HCO_3^- at electrode-electrolyte interface, which then precipitates with EMMIm cations to rapidly passivated electrode surfaces.

Electrode passivation, along with carbonate or bicarbonate formation, are major hurdles that must be overcome to achieve efficient CO_2 electroreduction. The onset potential and rate of crystal nucleation and growth varied with the corresponding anion or when we added supporting electrolytes such as TBA BF_4. These changes in rate of electrode passivation suggest promising pathways towards combatting the issue of electrode passivation by disrupting crystal formation via tuning interfacial assembly. Further, these results offer an explanation for the high activity of EMIm BF_4 – it is able to form a carboxylate with HCO_3^- in solution, decreasing the bicarbonate concentration near the electrode surface. In doing so, EMIm BF_4 appears to mitigate the problem of bicarbonate formation to an extent, a pathway that was unavailable to the other ionic liquids we examined.

3.4. Discussion

The general nature of non-monotonic concentration-dependent reactivity in different ionic liquid-derived electrolytes, together with *in situ* SERS results on EMIm BF_4, indicate that differences in CO_2 reduction rates originate from changes in screening efficiency as a non-monotonic function of ion

concentration (Fig. 3.5). To substantiate the plausibility of this mechanism, we performed a mean-field scaling theory analysis of how the Debye screening length for ionic liquid-acetonitrile blends depends on solution concentration.

Briefly, dilute electrolyte theory, such as Debye-Hückel theory, predicts that electrostatic screening lengths, and correspondingly, double layer thicknesses, arise from competition between ion entropy of mixing, which favors thicker double layers, and ion-surface Coulomb interactions that favor thinner double layers. In the dilute limit, the key length scale associated with screening is the Debye screening length, which can be calculated from knowledge of ion concentration, ion valence, and solution permittivity. The Debye screening length is a classical length scale associated with the efficiency of ionic screening and is defined as the distance where the local potential is 1/e of the surface potential of the electrode, or approximately 63.2% of the surface potential is screened. The Debye length is given by the following expression:

$$\lambda_D = \sqrt{\frac{\varepsilon_r \varepsilon_0 k_B T}{2q^2 n}} \qquad \text{(Equation 3.4)}$$

where ε_0 (F m^{-1}) is the permittivity of free space, ε_r is the dielectric constant of the solution, k_B is the Boltzmann constant (J K^{-1}), T (K) is the temperature, $q = ze$ (Coulombs) is the ion charge, z is the ion valence, e (Coulombs) is the elementary charge, and n (m^{-3}) is the number density of ions. The Debye screening length is often used interchangeably with the full electrostatic screening length, which is the distance over which the potential gradient is almost entirely screened. In contrast, the Debye-Hückel model predicts that 99% screening is not reached until about 5 Debye lengths away from a charged surface. Using the Debye length as a proxy for the electric double layer thickness, dilute theory predicts that electrostatic screening lengths and double layer thicknesses always decrease, indicating enhanced screening, as ion concentration increases.

Yet, dilute electrolyte theories neglect ion-ion interactions, leading to predicted Debye lengths that become smaller than any plausible dimension of individual ions as concentration is increased (Fig. A1.24).

Given the $\frac{1}{\sqrt{n}}$ dependence of the Debye length on ion concentration, this classical framework predicts that increasing the ion concentration of an electrolyte will always enhance screening efficiency. In the concentrated limit, ion-ion interactions drive ion clustering into charge-neutral aggregates as the ion concentration is further increased. Cluster formation decreases the concentration of "free ions" available to participate in screening, leading to a disparity between the "free ion" concentration and total number of ions per unit volume. Indeed, recent work on ionic liquid-solvent blends and aqueous electrolytes from the surface forces community indicates that a primary signature of ion-ion correlations is deviation of measured electrostatic screening lengths from calculated Debye length, which arises at around 1 M.[25, 27]

Taken together, we propose that ionic liquid electrolytes with either dilute or high concentrations can have relatively long screening lengths at the order of several nanometers due to a scarcity of ions and the clustering of ions to neutral aggregates, respectively, leading to inefficient screening.[28-30] At intermediate concentrations, the transition between dilute and correlated regimes should yield double layers with much shorter screening lengths, as there are sufficient ions to efficiently screen surface potentials without the presence of excessive impeding ion clusters.

More broadly, thin double layers yield steeper potential gradients as applied potentials are screened within short distances, and the magnitude of the local potential gradient is key in determining electrochemical reaction rates.[46, 60, 61] In strongly-screening cases, large potential gradients will enhance reactivity by creating polarized environments that require less energy for bonds to bend or break. Similar themes of electric field gradients enhancing reactivity are found in biology, where potential gradients in enzyme active sites orient and break chemical bonds or stabilize important reaction intermediates.[60-63]

In CO_2 electroreduction, a key intermediate is $CO_2^{\bullet-}$, an unstable and bent negative radical with a permanent dipole. Therefore, a compact and strongly-screening double layer achieved at intermediate concentrations would more effectively stabilize $CO_2^{\bullet-}$, leading to the maximum rate of CO_2 electroreduction. In contrast, electrolytes in dilute and correlated regimes, where ionic screening lengths

are longer, would be expected to form an environment that is less amenable to stabilizing charged or polar intermediates and lead to lower reactivity.

Overall, our scaling theory analysis links the regime of highest expected reactivity with that of the most efficient double layer screening and suggests that intermediate ion concentration may be a generally advantageous electrolyte regime for electrocatalytic processes. Yet, we caution that the electric double layer is a dynamic and complex environment during electrochemical reactions that cannot be comprehensively described using classical electrolyte theory, especially at high ionic liquid concentrations where ionic liquid assembly plays a major role.[64] Future refinement of this proposed mechanism would require new ways of measuring electrolyte structure and potential distributions at interfaces, molecular dynamics simulations, or other approaches that yield further molecular detail on the role of ionic correlations.

Our interpretation explains the concentration-dependent reactivity trend we observe, where reaction rates are non-monotonic with ion concentration. Specifically, intermediate concentrations create local reaction environments that better facilitate the formation of intermediates and turnover to products. Importantly, this characteristic of compact and thin double layers is not restricted to only co-catalytic ionic liquids, as evidenced by the EMPyrr BF_4 studies. We anticipate that our findings have applications extending far beyond CO_2 electroreduction and may prove useful in both understanding, as well as controlling energy-intensive electrochemical reactions such as nitrogen fixation.

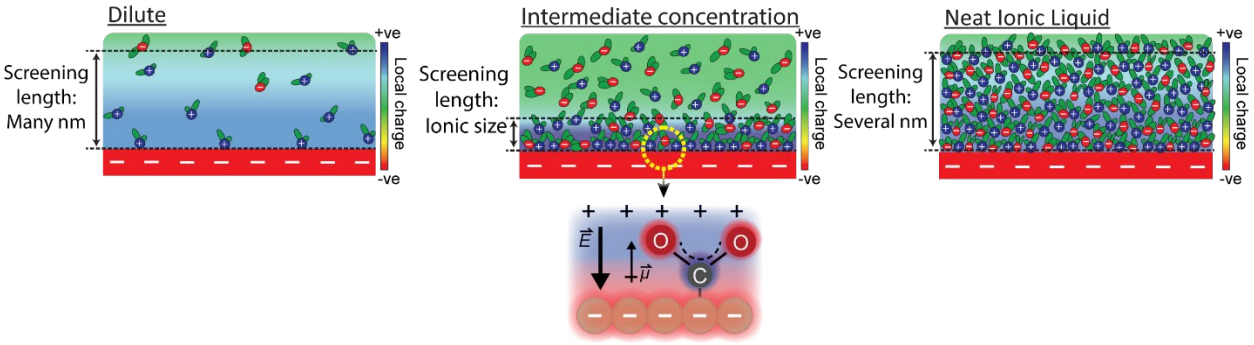

Figure 3.5 We propose that by changing concentration as a proxy for changing ionic correlations, we can drastically enhance CO_2 electroreduction rates by modulating the double layer thicknesses and electrostatic screening lengths. For dilute and concentrated regimes, a lack of ions and excessive ionic correlations,

respectively, induce the formation of thick double layers. At the crossover between the dilute and correlated regimes, intermediate concentrations facilitate formation of thin double layers, which can screen electrode potentials across molecular level distances and sustain large gradients in electric field strength. At these intermediate concentrations, the screening length approaches ionic sizes, forming a double layer that is more efficient at electrostatic screening and creating a large potential gradient. This large potential gradient near electrode surfaces would stabilize intermediates and transition states.

3.5. Conclusions

In this work, we show that ionic liquid-based electrolytes exhibit pronounced non-monotonic reactivity-concentration scaling for electrochemical CO_2 reduction to CO. Our conclusions are supported by cyclic voltammetry studies of reaction kinetics as well as steady-state electrolysis experiments. Notably, our findings are general for multiple classes of ionic liquids and should also extend to other solvents.

To substantiate our conclusions, we performed SERS and found that more strongly screening environments were formed near electrode surfaces at intermediate concentrations, where we observed higher reactivity. This is evidenced by more pronounced changes to potential-dependent ring deformation at intermediate concentrations, observed as shifts in the Raman scattering exhibited by imidazolium ring structure.

We interpret our data set to indicate that electrostatic screening is more efficient at intermediate concentrations, leading to thinner electric double layers, which facilitate CO_2 reduction via near-surface localization of potential gradients. While EMMIm BF_4 does exhibit a non-monotonic concentration-reactivity trend based on CV data, chronoamperometry measurements are hindered by precipitation of an insulating crystalline layer over time, which inhibits further CO_2 electrochemical reduction. We determined that this crystalline precipitate occurs due to formation of HCO_3^- species, which drive the nucleation and growth of a crystalline insulating EMMIm HCO_3^- film under reaction conditions. This important result suggests that the EMIm BF_4 reactivity is partially owed to the ability of the C2 position to coordinate HCO_3^- and also offers potential strategies to combat electrode passivation.

In summary, our findings have important implications for understanding how tuning electric double layer assembly, and in turn, local reaction environments, could enhance or enable better control over

reactivity in important electrochemical reactions. We show that tuning EDL screening efficiency can significantly influence the electrocatalytic reaction both in terms of current density and faradaic efficiency. Our preliminary scaling analysis suggests that the Debye screening length can be a simple and useful metric for analyzing screening efficiency by showing that the range of concentrations in which the Debye screening length approaches ion sizes is an ideal regime to explore for enhanced reactivity. Notably, our proposed theory is not ion or solvent specific, and can be generalized to electrochemical processes requiring different electrolyte compositions or more energy-intensive electrocatalytic reactions. Our findings show that the liquid side of electrode-electrolyte interfaces can be used to sculpt reaction landscapes in ways that can rival the influence of the solid side of electrochemical interfaces.

3.6. References

(1) Chandrasekaran, K.; Bockris, J. O. M. In-situ spectroscopic investigation of adsorbed intermediate radicals in electrochemical reactions - CO_2^-. *Surface Science* **1987**, *185*, 495-514.

(2) Hori, Y.; Wakebe, H.; Tsukamoto, T.; Koga, O. Electrocatalytic process of CO selectivity in electrochemical reduction of CO_2 at metal electrodes in aqueous media. *Electrochimica Acta* **1993**, *94*, 1833-1839.

(3) Rosen, B. A.; Salehi-Khojin, A.; Thorson, M. R.; Zhu, W.; Whipple, D. T.; Kenis, P. J. A.; Masel, R. I. Ionic Liquid–Mediated Selective Conversion of CO_2 to CO at Low Overpotentials. *Science* **2011**, *334*.

(4) Rosen, B. A.; Zhu, W.; Kaul, G.; Salehi-Khojin, A.; Masel, R. I. Water Enhancement of CO_2 Conversion on Silver in 1-Ethyl-3-Methylimidazolium Tetrafluoroborate. *Journal of The Electrochemical Society* **2012**, *160* (2), H138-H141. DOI: 10.1149/2.004303jes.

(5) Bondue, C. J.; Graf, M.; Goyal, A.; Koper, M. T. M. Suppression of Hydrogen Evolution in Acidic Electrolytes by Electrochemical CO_2 Reduction. *Journal of the American Chemical Society* **2021**, *143* (1), 279-285. DOI: 10.1021/jacs.0c10397.

(6) Rosen, B. A.; Haan, J. L.; Mukherjee, P.; Braunschweig, B.; Zhu, W.; Salehi-Khojin, A.; Dlott, D. D.; Masel, R. I. In Situ Spectroscopic Examination of a Low Overpotential Pathway for Carbon Dioxide Conversion to Carbon Monoxide. *The Journal of Physical Chemistry C* **2012**, *116* (29), 15307-15312. DOI: 10.1021/jp210542v.

(7) Wang, Y.; Hayashi, T.; He, D.; Li, Y.; Jin, F.; Nakamura, R. A reduced imidazolium cation layer serves as the active site for electrochemical carbon dioxide reduction. *Applied Catalysis B: Environmental* **2020**, *264*. DOI: 10.1016/j.apcatb.2019.118495.

(8) Faggion, D., Jr.; Goncalves, W. D. G.; Dupont, J. CO_2 Electroreduction in Ionic Liquids. *Front Chem* **2019**, *7*, 102. DOI: 10.3389/fchem.2019.00102.

(9) Appel, A. M.; Bercaw, J. E.; Bocarsly, A. B.; Dobbek, H.; DuBois, D. L.; Dupuis, M.; Ferry, J. G.; Fujita, E.; Hille, R.; Kenis, P. J.; et al. Frontiers, opportunities, and challenges in biochemical and chemical catalysis of CO_2 fixation. *Chemical Reviews* **2013**, *113* (8), 6621-6658. DOI: 10.1021/cr300463y.

(10) Alvarez-Guerra, M.; Albo, J.; Alvarez-Guerra, E.; Irabien, A. Ionic liquids in the electrochemical valorisation of CO_2. *Energy & Environmental Science* **2015**, *8* (9), 2574-2599. DOI: 10.1039/c5ee01486g.

(11) Welton, T. Ionic liquids: a brief history. *Biophysical Reviews* **2018**, *10* (3), 691-706. DOI: 10.1007/s12551-018-0419-2.

(12) Rogers, R. D.; Seddon, K. R. Ionic Liquids— Solvents of the Future? *Science* **2003**, *302*, 792-793.

(13) Sheldon, R. Catalytic reactions in ionic liquids. *Chemical Communications* **2001**, (23), 2399-2407. DOI: 10.1039/b107270f.

(14) Lau, G. P. S.; Schreier, M.; Vasilyev, D.; Scopelliti, R.; Gratzel, M.; Dyson, P. J. New Insights Into the Role of Imidazolium-Based Promoters for the Electroreduction of CO_2 on a Silver Electrode. *Journal of the American Chemical Society* **2016**, *138* (25), 7820-7823. DOI: 10.1021/jacs.6b03366.

(15) Ratschmeier, B.; Braunschweig, B. Cations of Ionic Liquid Electrolytes Can Act as a Promoter for CO_2 Electrocatalysis through Reactive Intermediates and Electrostatic Stabilization. *The Journal of Physical Chemistry C* **2021**, *125* (30), 16498-16507. DOI: 10.1021/acs.jpcc.1c02898.

(16) Wang, Y.; Hatakeyama, M.; Ogata, K.; Wakabayashi, M.; Jin, F.; Nakamura, S. Activation of CO_2 by ionic liquid EMIM-BF4 in the electrochemical system: a theoretical study. *Physical Chemistry Chemical Physics* **2015**, *17* (36), 23521-23531. DOI: 10.1039/c5cp02008e.

(17) Vasilyev, D. V.; Shyshkanov, S.; Shirzadi, E.; Katsyuba, S. A.; Nazeeruddin, M. K.; Dyson, P. J. Principal Descriptors of Ionic Liquid Co-catalysts for the Electrochemical Reduction of CO_2. *ACS Applied Energy Materials* **2020**, *3* (5), 4690-4698. DOI: 10.1021/acsaem.0c00330.

(18) Dupont, J.; Simon, N. M.; Zanatta, M. The Nature of Carbon Dioxide in Bare Ionic Liquids. *ChemSusChem* **2020**, *13* (12), 3101-3109. DOI: 10.1002/cssc.202000574.

(19) Sun, L. Y.; Ramesha, G. K.; Kamat, P. V.; Brennecke, J. F. Switching the Reaction Course of Electrochemical CO_2 Reduction with Ionic Liquids. *Langmuir* **2014**, *30* (21), 6302-6308, Article. DOI: 10.1021/la5009076.

(20) Gu, L. Z., Y. Unexpected CO_2 Splitting Reactions To Form CO with N-Heterocyclic Carbenes as Organocatalysts and Aromatic Aldehydes as Oxygen Acceptors. *Journal of the American Chemical Society* **2010**, *132* (3), 914-915.

(21) Noack, K.; Schulz, P. S.; Paape, N.; Kiefer, J.; Wasserscheid, P.; Leipertz, A. The role of the C2 position in interionic interactions of imidazolium based ionic liquids: a vibrational and NMR spectroscopic study. *Physical Chemistry Chemical Physics* **2010**, *12* (42), 14153-14161. DOI: 10.1039/c0cp00486c.

(22) Whipple, D. T.; Kenis, P. J. A. Prospects of CO_2 Utilization via Direct Heterogeneous Electrochemical Reduction. *The Journal of Physical Chemistry Letters* **2010**, *1* (24), 3451-3458. DOI: 10.1021/jz1012627.

(23) Kemna, A.; Braunschweig, B. Potential-Induced Adsorption and Structuring of Water at the Pt(111) Electrode Surface in Contact with an Ionic Liquid. *Journal of Physical Chemistry Letters* **2020**, *11* (17), 7116-7121. DOI: 10.1021/acs.jpclett.0c02037.

(24) König, M.; Vaes, J.; Klemm, E.; Pant, D. Solvents and Supporting Electrolytes in the Electrocatalytic Reduction of CO_2. *Iscience* **2019**, *19*, 135-160. DOI: 10.1016/j.isci.2019.07.014.

(25) Smith, A. M.; Lee, A. A.; Perkin, S. The Electrostatic Screening Length in Concentrated Electrolytes Increases with Concentration. *The Journal of Physical Chemistry Letters* **2016**, *7* (12), 2157-2163, Article. DOI: 10.1021/acs.jpclett.6b00867.

(26) Gebbie, M. A.; Valtiner, M.; Banquy, X.; Fox, E. T.; Henderson, W. A.; Israelachvili, J. N. Ionic liquids behave as dilute electrolyte solutions. *Proceedings of the National Academy of Sciences* **2013**, *110* (24), 9674-9679. DOI: 10.1073/pnas.1307871110.

(27) Gebbie, M. A.; Smith, A. M.; Dobbs, H. A.; Lee, A. A.; Warr, G. G.; Banquy, X.; Valtiner, M.; Rutland, M. W.; Israelachvili, J. N.; Perkin, S.; et al. Long range electrostatic forces in ionic liquids. *Chemical Communications* **2017**, *53* (7), 1214-1224, Article. DOI: 10.1039/c6cc08820a.

(28) Bazant, M. Z.; Storey, B. D.; Kornyshev, A. A. Double layer in ionic liquids: overscreening versus crowding. *Physical Review Letters* **2011**, *106* (4), 046102. DOI: 10.1103/PhysRevLett.106.046102.

(29) Kornyshev, A. A. Double-Layer in Ionic Liquids: Paradigm Change? *The Journal of Physical Chemistry B* **2007**, *111* (20), 5545-5557.

(30) Lee, A. A.; Perez-Martinez, C. S.; Smith, A. M.; Perkin, S. Scaling Analysis of the Screening Length in Concentrated Electrolytes. *Physical Review Letters* **2017**, *119* (2), 026002. DOI: 10.1103/PhysRevLett.119.026002.

(31) de Souza, J. P.; Bazant, M. Z. Continuum Theory of Electrostatic Correlations at Charged Surfaces. *The Journal of Physical Chemistry C* **2020**, *124* (21), 11414-11421. DOI: 10.1021/acs.jpcc.0c01261.

(32) Gebbie, M. A.; Dobbs, H. A.; Valtiner, M.; Israelachvili, J. N. Long-range electrostatic screening in ionic liquids. *Proceedings of the National Academy of Sciences of the United States of America* **2015**, *112* (24), 7432-7437. DOI: 10.1073/pnas.1508366112.

(33) Han, M.; Kim, H.; Leal, C.; Negrito, M.; Batteas, J. D.; Espinosa-Marzal, R. M. Insight into the Electrical Double Layer of Ionic Liquids Revealed through Its Temporal Evolution. *Advanced Materials Interfaces* **2020**, *7* (24). DOI: 10.1002/admi.202001313.

(34) García Rey, N.; Dlott, D. D. Structural Transition in an Ionic Liquid Controls CO2 Electrochemical Reduction. *The Journal of Physical Chemistry C* **2015**, *119* (36), 20892-20899. DOI: 10.1021/acs.jpcc.5b03397.

(35) Lim, H.-K.; Kwon, Y.; Kim, H. S.; Jeon, J.; Kim, Y.-H.; Lim, J.-A.; Kim, B.-S.; Choi, J.; Kim, H. Insight into the Microenvironments of the Metal–Ionic Liquid Interface during Electrochemical CO_2 Reduction. *ACS Catalysis* **2018**, *8* (3), 2420-2427. DOI: 10.1021/acscatal.7b03777.

(36) Hahn, C.; Jaramillo, T. F. Using Microenvironments to Control Reactivity in CO_2 Electrocatalysis. *Joule* **2020**, *4* (2), 292-294. DOI: 10.1016/j.joule.2020.01.017.

(37) Hansen, K. U.; Jiao, F. Creating the right environment. *Nature Energy* **2021**, *6* (11), 1005-1006. DOI: 10.1038/s41560-021-00930-6.

(38) Kim, C.; Bui, J. C.; Luo, X.; Cooper, J. K.; Kusoglu, A.; Weber, A. Z.; Bell, A. T. Tailored catalyst microenvironments for CO_2 electroreduction to multicarbon products on copper using bilayer ionomer coatings. *Nature Energy* **2021**, *6* (11), 1026-1034. DOI: 10.1038/s41560-021-00920-8.

(39) Rudnev, A. V.; Zhumaev, U. E.; Kuzume, A.; Vesztergom, S.; Furrer, J.; Broekmann, P.; Wandlowski, T. The promoting effect of water on the electroreduction of CO_2 in acetonitrile. *Electrochimica Acta* **2016**, *189*, 38-44. DOI: 10.1016/j.electacta.2015.12.088.

(40) Figueiredo, M. C.; Ledezma-Yanez, I.; Koper, M. T. M. In Situ Spectroscopic Study of CO_2 Electroreduction at Copper Electrodes in Acetonitrile. *ACS Catalysis* **2016**, *6* (4), 2382-2392, Article. DOI: 10.1021/acscatal.5b02543.

(41) Pavlishchuk, V. V.; Addison, A. W. Conversion constants for redox potentials measured versus different reference electrodes in acetonitrile solutions at 25°C. *Inorganica Chimica Acta* **1999**, *298*, 97-102.

(42) Zhao, S.-F.; Horne, M.; Bond, A. M.; Zhang, J. Is the Imidazolium Cation a Unique Promoter for Electrocatalytic Reduction of Carbon Dioxide? *The Journal of Physical Chemistry C* **2016**, *120* (42), 23989-24001. DOI: 10.1021/acs.jpcc.6b08182.

(43) Tanner, E. E. L.; Batchelor-McAuley, C.; Compton, R. G. Carbon Dioxide Reduction in Room-Temperature Ionic Liquids: The Effect of the Choice of Electrode Material, Cation, and Anion. *The Journal of Physical Chemistry C* **2016**, *120* (46), 26442-26447. DOI: 10.1021/acs.jpcc.6b10564.

(44) Vasilyev, D. V.; Dyson, P. J. The Role of Organic Promoters in the Electroreduction of Carbon Dioxide. *ACS Catalysis* **2021**, *11* (3), 1392-1405. DOI: 10.1021/acscatal.0c04283.

(45) Bard, A. J.; Faulkner, L. R. *Electrochemical Methods: Fundamentals and Applications*; Wiley, 2001.

(46) Gu, J.; Liu, S.; Ni, W.; Ren, W.; Haussener, S.; Hu, X. Modulating electric field distribution by alkali cations for CO_2 electroreduction in strongly acidic medium. *Nature Catalysis* **2022**. DOI: 10.1038/s41929-022-00761-y.

(47) Monteiro, M. C. O.; Dattila, F.; Lopez, N.; Koper, M. T. M. The Role of Cation Acidity on the Competition between Hydrogen Evolution and CO2 Reduction on Gold Electrodes. *Journal of the American Chemical Society* **2022**, *144* (4), 1589-1602. DOI: 10.1021/jacs.1c10171.

(48) Marcandalli, G.; Goyal, A.; Koper, M. T. M. Electrolyte effects on the faradaic efficiency of CO_2 reduction to CO on a gold electrode. *ACS Catalysis* **2021**, *11* (9), 4936-4945. DOI: 10.1021/acscatal.1c00272.

(49) Matsubara, Y.; Grills, D. C.; Kuwahara, Y. Thermodynamic Aspects of Electrocatalytic CO_2 Reduction in Acetonitrile and with an Ionic Liquid as Solvent or Electrolyte. *ACS Catalysis* **2015**, *5* (11), 6440-6452. DOI: 10.1021/acscatal.5b00656.

(50) Santos, V. O.; Leite, I. R.; Brolo, A. G.; Rubim, J. C. The electrochemical reduction of CO_2 on a copper electrode in 1-n-butyl-3-methyl imidazolium tetrafluoroborate (BMI.BF4) monitored by surface-enhanced Raman scattering (SERS). *Journal of Raman Spectroscopy* **2016**, *47* (6), 674-680. DOI: 10.1002/jrs.4871.

(51) Michez, R.; Doneux, T.; Buess-Herman, C.; Luhmer, M. NMR Study of the Reductive Decomposition of [BMIm][NTf_2] at Gold Electrodes and Indirect Electrochemical Conversion of CO_2. *ChemPhyschem* **2017**, *18* (16), 2208-2216. DOI: 10.1002/cphc.201700421.

(52) Monteiro, M. C. O.; Philips, M. F.; Schouten, K. J. P.; Koper, M. T. M. Efficiency and selectivity of CO_2 reduction to CO on gold gas diffusion electrodes in acidic media. *Nature Communications* **2021**, *12* (1), 4943. DOI: 10.1038/s41467-021-24936-6.

(53) Li, T.; Lees, E. W.; Goldman, M.; Salvatore, D. A.; Weekes, D. M.; Berlinguette, C. P. Electrolytic Conversion of Bicarbonate into CO in a Flow Cell. *Joule* **2019**, *3* (6), 1487-1497. DOI: 10.1016/j.joule.2019.05.021.

(54) Rabinowitz, J. A.; Kanan, M. W. The future of low-temperature carbon dioxide electrolysis depends on solving one basic problem. *Nature Communications* **2020**, *11* (1), 5231. DOI: 10.1038/s41467-020-19135-8.

(55) Foley, J.; Korzeniewski, C.; Pons, S. Anodic and cathodic reactions in acetonitrile/tetra- n -butylammonium tetrafluoroborate: an electrochemical and infrared spectroelectrochemical study. *Canadian Journal of Chemistry* **1988**, *66* (1), 201-206.

(56) Berto, T. C.; Zhang, L.; Hamers, R. J.; Berry, J. F. Electrolyte Dependence of CO_2 Electroreduction: Tetraalkylammonium Ions Are Not Electrocatalysts. *ACS Catalysis* **2014**, *5* (2), 703-707. DOI: 10.1021/cs501641z.

(57) Dhumal, N. R.; Noack, K.; Kiefer, J.; Kim, H. J. Molecular Structure and Interactions in the Ionic Liquid 1-Ethyl-3-methylimidazolium Bis(Trifluoromethylsulfonyl)imide. *The Journal of Physical Chemistry A* **2014**, *118* (13), 2547-2557. DOI: 10.1021/jp502124y.

(58) Sanchora, P.; Pandey, D. K.; Rana, D.; Materny, A.; Singh, D. K. Impact of Size and Electronegativity of Halide Anions on Hydrogen Bonds and Properties of 1-Ethyl-3-methylimidazolium-Based Ionic Liquids. *The Journal of Physical Chemistry A* **2019**, *123* (23), 4948-4963. DOI: 10.1021/acs.jpca.9b04116.

(59) Santos, V. O.; Alves, M. B.; Carvalho, M. S.; Suarez, P. A. Z.; Rubim, J. C. Surface-Enhanced Raman Scattering at the Silver Electrode/Ionic Liquid ($BMIPF_6$) Interface. *The Journal of Physical Chemistry B* **2006**, *110* (41), 20379-20385. DOI: 10.1021/jp0643348.

(60) Siddiqui, S. A.; Dubey, K. D. Can the local electric field be a descriptor of catalytic activity? A case study on chorismate mutase. *Physical Chemistry Chemical Physics* **2021**, *24*, 1974-1981. DOI: 10.1039/d1cp03978d.

(61) Léonard, N. G.; Dhaoui, R.; Chantarojsiri, T.; Yang, J. Y. Electric Fields in Catalysis: From Enzymes to Molecular Catalysts. *ACS Catalysis* **2021**, *11* (17), 10923-10932. DOI: 10.1021/acscatal.1c02084.

(62) Resasco, J.; Chen, L. D.; Clark, E.; Tsai, C.; Hahn, C.; Jaramillo, T. F.; Chan, K.; Bell, A. T. Promoter Effects of Alkali Metal Cations on the Electrochemical Reduction of Carbon Dioxide. *Journal of the American Chemical Society* **2017**, *139* (32), 11277-11287. DOI: 10.1021/jacs.7b06765.

(63) Lee, G.; Li, Y. C.; Kim, J.-Y.; Peng, T.; Nam, D.-H.; Sedighian Rasouli, A.; Li, F.; Luo, M.; Ip, A. H.; Joo, Y.-C.; et al. Electrochemical upgrade of CO_2 from amine capture solution. *Nature Energy* **2020**, *6* (1), 46-53. DOI: 10.1038/s41560-020-00735-z.

(64) Fedorov, M. V.; Kornyshev, A. A. Ionic liquids at electrified interfaces. *Chemical Reviews* **2014**, *114* (5), 2978-3036. DOI: 10.1021/cr400374x.

Chapter 4. Exploring how cation entropy influences electric double layer formation and electrochemical reactivity[2]

4.1. Introduction

Electrochemical interfaces are a core area of research in the soft matter community[1-3] for advanced energy storage[4, 5] and electrocatalytic systems[6, 7] that provide opportunities to offset anthropogenic CO_2 emissions.[8-10] For example, converting CO_2 into useful chemical products through electrocatalysis offers a way to not only mitigate the effects of CO_2, but also to sustainably produce chemicals for industrial processes.[10, 11] However, achieving this vision will require considerable advancements in fundamental electrolyte and interface science as well as overall electrochemical systems design.

To date, the electrocatalysis community has demonstrated that CO_2 can be reduced to a variety of potentially useful products by judiciously tuning catalyst materials[12-15] and electrolyte properties.[12, 16-18] The formation of CO is typically the first reduction step for the production of more complex C_{2+} products.[19, 20] However, reducing CO_2 to CO requires significant energy input due to the relative stability of the CO_2 double bonds,[21, 22] making electrocatalytic reduction of CO_2 to CO an especially relevant model reaction for fundamental studies.

In most cases, CO_2 reduction to CO proceeds through a two-electron, two-proton reduction process (Eq. 4.1), where the intermediate has been reported to be a negatively-charged radical, $CO_2^{\bullet-}$.[21, 22] The formation of this intermediate, as well as the transformation of CO_2 from a nonpolar molecule to the polar CO molecule, means that this reaction is particularly sensitive to potential gradients and therefore presents a unique avenue for the study of electric double layers.

$$CO_2 + 2H^+ + 2e^- \rightarrow CO + H_2O \qquad \text{(Equation 4.1)}$$

[2] Chapter adapted from Liu B, Guo W, Anderson SR, Johnstone SG, Wu S, Herrington MC, Gebbie MA. Exploring how cation entropy influences electric double layer formation and electrochemical reactivity. *Soft Matter* 2024, **20**, 351-364.; Supplemental information, including a more detailed description of the ionic liquid synthesis procedure, is presented in the Appendix.

Notably, CO_2 electroreduction is carried out at high cathodic potentials, often exceeding -1 V below open circuit potential.[23] These intense electrode polarizations induce the formation of nanostructured electric double layers,[24-29] where ion-ion correlations and excluded volume effects play defining roles in determining local potential gradients and reaction microenvironments.[30, 31] Hence, electric double layer formation at electrocatalytic interfaces often hinges on collective ion self-assembly, which is not considered in classical electric double layer theories, such as the Gouy-Chapman-Stern model, where ion size, ion shape, and ion-ion interactions are neglected.[32-35]

In this work, we aim to expand our understanding of how cation entropy influences ion assembly, electric double layer formation, and ultimately local reaction microenvironments under conditions of high applied bias that are inherent to CO_2 electrocatalytic reduction. We selected ionic liquid-mediated CO_2 reduction to CO on an Ag electrode as a model system, as ionic liquid molecular structures can be systematically modulated via synthetic protocols.[36]

Ionic liquids, which are salts that are often composed of weakly coordinating organic cations and anions, have been heavily studied as excellent promoters of CO_2 reduction in both aqueous[37-40] and nonaqueous electrolytes.[30, 41, 42] Imidazolium-based salts are the prototypical class of ionic liquids used for mediating CO_2 electroreduction due to their propensity to donate protons and coordinate CO_2.[37] Increasingly, however, studies are highlighting how other organic cations which cannot donate protons or form coordination interactions can also effectively promote CO_2 electroreduction,[43, 44] leaving many open questions surrounding how and why organic cations can facilitate electrocatalytic reactions.

We hypothesize that cation entropy provides an important and underexplored element in explaining why ionic liquids can facilitate efficient CO_2 electroreduction. Electric double layer formation hinges on both entropic and electrostatic interactions,[45] where the large size and irregular shape of ionic liquid ions can lead to additional dielectric fluctuations and responses which can contribute to electrostatic screening and enhance interfacial potential gradients.[32, 46, 47] An ion confined to the double layer not only experiences electrostatic interactions, but also incurs entropic penalties.[48] However, the degree to which the entropic

penalty that is incurred to confine ions to the interface influences double layer formation, and subsequently electrostatic screening, remains poorly understood.

Here, we systematically isolate the influence of entropy on electric double layer formation by comparing electric double layer properties and electrocatalytic CO_2 reduction rates in two ionic liquids which are structurally identical, except for a covalent linkage that forms a dimer analogue of a common monovalent ionic liquid. Specifically, we examine the role of entropy in double layer formation by comparing the interfacial behavior and reactivity of 1-butyl-3-methylimidazolium bis(trifluoromethanesulfonyl)imide ([BMIm][TFSI]) and its dicationic analogue, 1,8-bis(3-methylimidazolium-1-yl)octane bis(trifluoromethanesulfonyl)imide ([BisMImO][TFSI]$_2$) (Fig. 4.1).

Ions confined to the interface must pay an entropic penalty due to the loss of translational motion of $\frac{3}{2}k_BT$, where k_B and T represent the Boltzmann constant and temperature in Kelvin, respectively. As this entropic penalty pertains to any single molecule regardless of size or shape, $[BisMImO]^{2+}$ pays an entropic penalty of $\frac{3}{2}k_BT$ while $[BMIm]^+$ must pay an entropic penalty of $\frac{6}{2}k_BT$ to confine two charges to the interface. Therefore, $[BisMImO]^{2+}$ pays a lower entropic penalty and it is more thermodynamically favorable to confine the $[BisMImO]^{2+}$ cation to the double layer than 2 $[BMIm]^+$ ions for the same amount of charge screening.

We hypothesized that salts with lower entropic penalties, such as [BisMImO][TFSI]$_2$, will preferentially accumulate at interfaces, generally leading to thinner and more efficiently-screening double layers. However, the effects of a thinner double layer may be tempered with the additional electrostatic interactions between the imidazolium rings of the $[BisMImO]^{2+}$ cation, as well as the imposed constraint on the number of positions the imidazoliums can adopt relative to each other in $[BisMImO]^{2+}$ when compared to $[BMIm]^+$. We evaluated the electrochemical reactivity and interfacial structure of [BisMImO][TFSI]$_2$ and [BMIm][TFSI] in acetonitrile to avoid the competing hydrogen evolution reaction,[49] and on Ag working electrodes for its selectivity for CO.[50]

Our findings demonstrate that entropic contributions to double layer formation can dominate interfacial ion assembly and govern reaction rates. Using cyclic voltammetry (CV), we show that [BisMImO][TFSI]$_2$ generally exhibits lower current densities than [BMIm][TFSI], but that current densities begin to converge in more concentrated electrolytes. We then use chronoamperometry (CA) and product analysis such as gas chromatography (GC) to show that CO_2 electroreduction [BisMImO][TFSI]$_2$-containing electrolytes lead to noticeable precipitation of the bicarbonate salt at the electrode surface, which compromises steady state reactivity, while [BMIm][TFSI] does not.

To better understand the structure within the double layer and how it is related to the reaction rate, we performed *in situ* electrochemical surface-enhanced Raman scattering (SERS) spectroscopy and found that [BisMImO][TFSI]$_2$ more readily forms ordered double layers, especially under inert gas-sparging conditions. Furthermore, in a mixture of the two ionic liquids, we provide evidence that electrocatalytic performance and interfacial structuring are dominated by the ionic liquid with the lower entropic penalty of de-mixing from the bulk electrolyte.

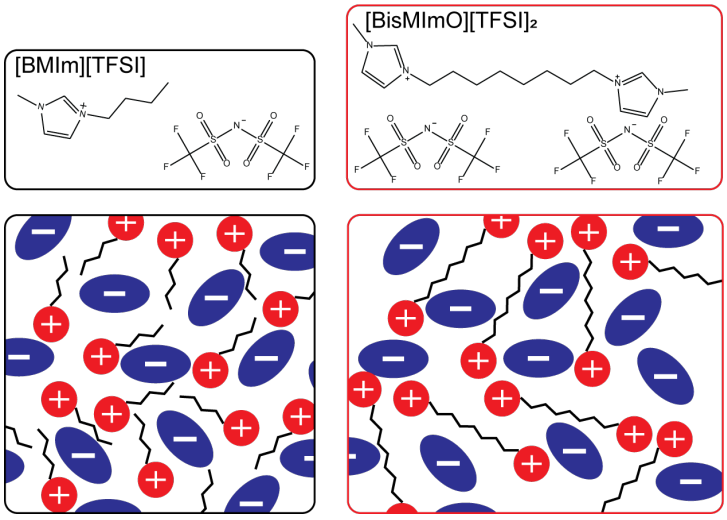

Figure 4.1 Chemical structures of the ionic liquids (top) and cartoon schematic (bottom) of the neat ionic liquids. The 1-butyl-3-methylimidazolium bis(trifluoromethanesulfonyl)imide ([BMIm][TFSI], black) ionic liquid contain monovalent cations and anions. The dicationic ionic liquid, 1,8-bis(3-methylimidazolium-1-yl)octane bis(trifluoromethanesulfonyl)imide ([BisMImO][TFSI]$_2$, red), consists of a divalent cation and monovalent anions. The introduction of a single covalent bond on the N3 substituents of the $[BMIm]^+$ cation yields the $[BisMImO]^+$ cation, which has lower entropy of confinement within the double layer. Thus, at the same total concentration of ionic liquid, the $[BisMImO]^+$ cations hold 2 positive charges while the $[BMIm]^+$ cation holds only one.

4.2. Experimental Methods

Chemicals. 1-Butyl-3-methylimidazolium bis(trifluoromethanesulfonyl)imide ([BMIm][TFSI], >98% purity, Iolitec) was used as purchased.

The dicationic ionic liquid, 1,8-bis(3-methylimidazolium-1-yl)octane bis(trifluoromethanesulfonyl)imide ([BisMImO][TFSI]$_2$) was synthesized according to established literature procedures.[51, 52] Briefly, 1-methylimidazole (99%, Thermo Scientific) and 1,8-dibromooctane (98%, Sigma-Aldrich) were added to a round-bottom flask in a 2:1 molar ratio and allowed to react for 24 hours at room temperature to make 1,8-bis(3-methylimidazolium-1-yl)octane dibromide ([BisMImO][Br]$_2$). The [BisMImO][Br]$_2$ was then washed with acetone and dried, resulting in a dry and white powder.

To conduct the anion exchange, [BisMImO][Br]$_2$ and [Li][TFSI] (>98%, TCI) in a 1:2 molar ratio were added to a round bottom flask and fully dissolved in MilliQ H_2O. The mixture was stirred at room temperature for 3 hours. The water layer was decanted off and the resulting ionic liquid was washed with MilliQ H_2O. After several washes, the water layer was tested with the silver nitrate halide test to confirm the removal of halides.

The crude [BisMImO][TFSI]$_2$ was then purified by first dissolving it in acetonitrile and then stirring it with activated charcoal (Sigma-Aldrich) for 2-3 days. After removing the activated charcoal, the solution was dried using first a rotary evaporator (BUCHI R-300M Rotavapor) followed by a vacuum drying oven (Yamato ADP200C) at 80 °C for 2 days. The resulting [BisMImO][TFSI]$_2$ was a viscous and colorless oil that slowly began to solidify upon storage.

The water content of HPLC grade acetonitrile (>99.9%, Sigma-Aldrich) was adjusted to be 900-1000 ppm according to our previous protocol to ensure that protons were available for the reaction.[30] Potassium bromide was purchased from MP Biomedicals and silver nitrate was from Alfa Aesar.

Electrochemical Methods.

A VSP potentiostat from BioLogic was used for all electrochemical experiments. In electrochemical measurements, a Ag/Ag^+ non-aqueous reference electrode containing 0.1 M [TBA][BF_4] and 0.01 M [Ag][NO_3] in acetonitrile was prepared[53] and a coiled platinum wire was used as the counter electrode.

For cyclic voltammetry and steady-state electrolysis, we used a 3 mm polycrystalline Ag electrode (geometric surface area of 0.071 cm^2) purchased from BASi as the working electrode, which was polished to a mirror finish using 15 μm, 3 μm, and 1 μm diamond polish followed by 0.05 um alumina (BASi) before ultrasonication in water. All electrolytes were purged with either Ar or CO_2 prior to electrochemical measurements. All presented CV measurements were carried out at a scan rate of 100 mV/s.

Product Analysis.

CA measurements were conducted in a custom two-compartment H-cell separated by a Nafion 117 membrane. The Nafion 117 membranes were activated according to prior established protocols[54, 55] and stored in a solution of 0.1 M [TBA][BF_4] in acetonitrile. They were rinsed thoroughly with acetonitrile prior to use. Potentials of -2.5 V vs. Ag/Ag^+ were held for 1 hour, where steady state was typically reached after 10 minutes.

The cells were continuously stirred with Teflon stir bars (VWR) and CO_2 was continuously purged through the cathode compartment at 10sccm. The resulting gas stream outlet fed directly into the gas chromatograph (Multiple Gas Analyzer #5, SRI Instruments). We also used NMR spectroscopy to identify products in the catholyte after electrolysis. The NMR (400 MHz, Bruker Avance) was equipped with a BBFO probe.

SERS Measurements.

Electrochemical surface-enhanced Raman scattering (SERS) spectroscopy measurements were carried out in a single-compartment PTFE electrochemical cell. A polycrystalline L-shaped Ag working electrode (Shanghai Fanyue Electronic Technology Co. Ltd) was first polished and then electrochemically roughened following reported methods in literature with modifications.[56]

Briefly, the electrode was submerged in an aqueous solution of 0.1 M KBr under continuous Ar purging. The electrode was then cycled between -0.3 V and +0.3 V vs. open-circuit potential (OCP) for 4 cycles. The electrode was then held at -0.3 V vs. OCP for 10 seconds to desorb bromide from the silver surface. The electrode was thoroughly rinsed with water after roughening and dried prior to use. A mechanically polished and coiled Pt wire was the counter electrode and a non-aqueous Ag/Ag^+ (0.01 M $AgNO_3$) reference electrode was used.

The electrolytes were purged with either Ar or CO_2 for 20 minutes at 10 sccm prior to measurement. SERS spectra were collected using a Thermo-Fisher Scientific DXRxi Raman Imaging Microscope with 532 nm excitation laser at 10x magnification. The laser power was 8.0 mW, the acquisition time was 0.125 seconds, and 25 scans were collected for each spectrum. The potential was swept from -0.5 V to -2.5 V vs. Ag/Ag^+ and then back to -0.7 V vs. Ag/Ag^+ at intervals of 0.2 V. Only the forward scans are presented in this work, as the trends were reversible.

4.3. Results and Discussion

4.3.1. Cation Entropy Influences Reaction Rate and Selectivity

Using a polycrystalline Ag working electrode, we systematically conducted CV scans on a series of ionic liquid concentrations in acetonitrile under continuous CO_2 sparging. The current density at -2.5 V vs Ag/Ag^+ was used for comparison among different concentrations.

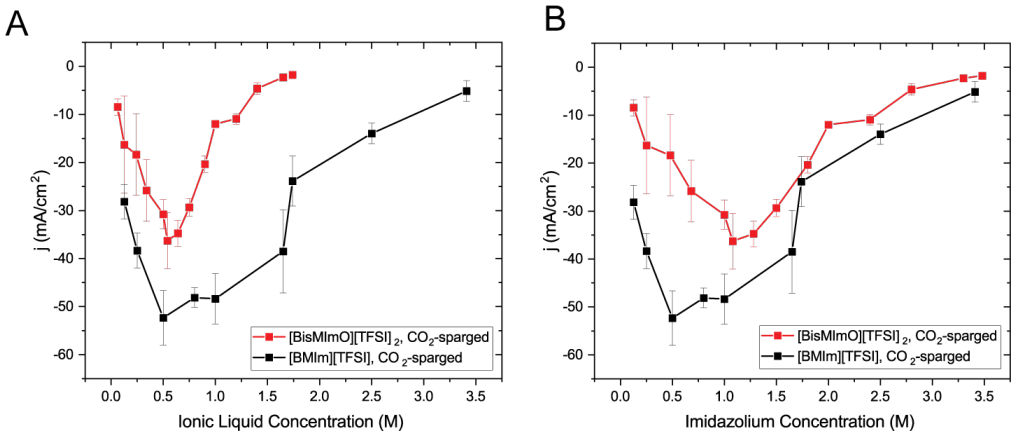

Figure 4.2 Electrochemical behavior of $[BisMImO][TFSI]_2$ and [BMIm][TFSI]. CV experiments show that $[BisMImO][TFSI]_2$-acetonitrile electrolytes (red) always yield lower current densities than [BMIm][TFSI]

(black). (A) Accounting for total ionic liquid concentration, we find that [BisMImO][TFSI]$_2$ electrolytes reach a maximum current density at a lower concentration than [BMIm][TFSI]. (B) If total imidazolium concentrations are considered, however, we find that current densities begin to converge at higher concentrations. Datapoints and standard deviations were calculated by averaging the current density at -2.5 V vs Ag/Ag$^+$ for 2 cycles of CV at 100 mV/s for 3 separate electrolyte samples at each concentration.

We found that the [BisMImO][TFSI]$_2$ electrolytes display a maximum current density at similar salt concentrations as [BMIm][TFSI] but that the current densities of [BisMImO][TFSI]$_2$-containing electrolytes are lower than that of [BMIm][TFSI] at all concentrations (Fig. 4.2). More interestingly, after accounting for the total number of charge-carrying imidazoliums in each cation, we observe that the discrepancies in current densities between the two ionic liquids are larger at lower concentrations (<1 M) but converge to similar current densities as concentration increases (Fig. 4.2B).

We attribute the discrepancy in CO_2 reduction rates at lower imidazolium concentrations to the reorientation of the cations in the double layer and their corresponding role in the reaction. The imidazolium cation is thought to stabilize the $CO_2^{\bullet-}$ intermediate through either complexing with the C2 position,[37, 57] or through hydrogen bonding between $CO_2^{\bullet-}$ and the C4 and C5 protons.[42, 58] The covalent link between two imidazolium rings in the [BisMImO]$^{2+}$ cation serves to further constrain the imidazolium ring orientation relative to the $CO_2^{\bullet-}$ intermediate. As such, the imidazoliums in [BisMImO]$^{2+}$ have fewer degrees of freedom and hence fewer stabilizing conformations compared to the [BMIm]$^+$ cation. Additionally, at low concentrations, the [BMIm]$^+$ cations remain fully solvated and "free" while the imidazoliums in the [BisMImO]$^{2+}$ cations experience enhanced interactions due to the covalent linkage, which could promote the formation of electrode-blocking precipitates containing (bi)carbonate anions. The imposed constraint and corresponding entropic limitations are likely the reason behind the attenuated reactivity of the [BisMImO][TFSI]$_2$ at concentrations lower than 1 M of imidazolium cation.

As concentration increases past 1 M, however, the emergence of bulk ion-ion correlations and the formation of multi-ion aggregates makes screening less efficient than the predictions of classical double layer theory.[59] At these concentrations, ion-ion interactions between [BMIm]$^+$ cations also serve to decrease screening efficiency such that correlations within [BMIm]$^+$ electrolytes become similar to those in

$[BisMImO]^{2+}$ electrolytes. As a result, increasing concentration towards the neat limit yields converging current densities for the two ionic liquids as double layer screening efficiency decreases and the double layer thickness increases.

We then conducted chronoamperometry (CA) studies combined with product analysis techniques to evaluate the two ionic liquids for steady-state electrolysis performance. CA experiments were conducted using polycrystalline Ag working electrodes in a well-mixed H-cell with continuous CO_2 sparging at 10 sccm. The outlet gas was directed into the sample loop of a gas chromatograph to identify gaseous products.

We notice that within 10-15 minutes of applying a potential of -2.5 V vs Ag/Ag^+, the current density and faradaic efficiency of CO_2 conversion to CO for all $[BisMImO][TFSI]_2$ electrolytes drop and remain at a low level for the remainder of the experiment (Fig. 4.3A). In contrast, the [BMIm][TFSI] electrolytes maintain a relatively constant current density and faradaic efficiency (Fig. 4.3B). Upon inspection of the working electrode after electrolysis with the dicationic analogue, we observed that a solid precipitate had formed on the surface and completely occluded the working electrode. This precipitate was not observed after electrolysis in [BMIm][TFSI], suggesting that covalently joining the two imidazoliums together has the effect of inducing precipitate formation.

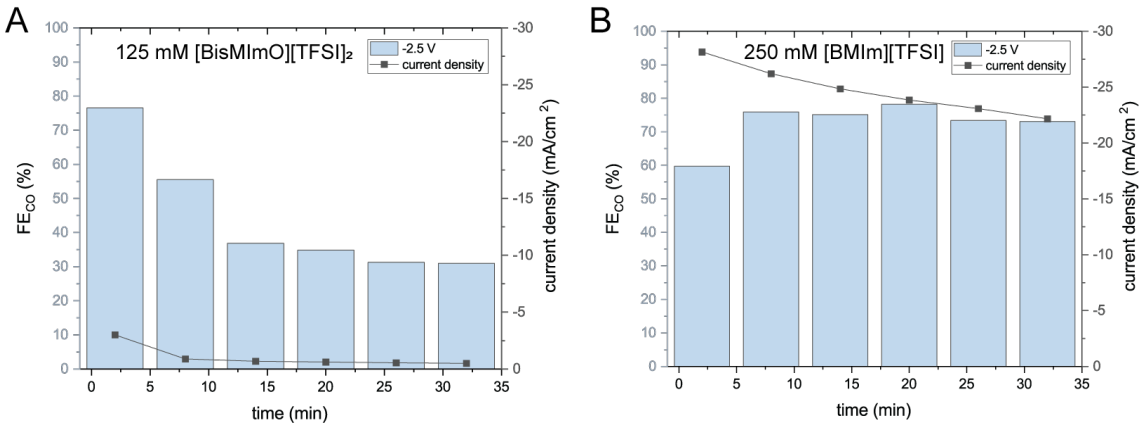

Figure 4.3 Representative CA and GC results show that within a few minutes of applying a -2.5 V vs. Ag/Ag^+ potential, the current density and faradaic efficiencies drop for 125 mM $[BisMImO][TFSI]_2$ (A) but remain relatively stable for 250 mM [BMIm][TFSI] (B). This is due to the formation of (bi)carbonate species at the interface, leading to the growth of a solid precipitate.

The formation of the obstructing precipitate on the electrode under CO_2-sparged and its absence under Ar-sparged conditions indicates that the formation of byproducts during CO_2 reduction is the likely cause of the precipitate. Indeed, (bi)carbonate formation and subsequent precipitation of (bi)carbonate salts, which is caused by the reaction between interfacially-generated $[OH]^-$ and dissolved CO_2, is a common issue in CO_2 electrocatalysis.[10, 60] The precipitate that is formed lowers the current density and the subsequent concentration of gaseous products, which can approach or fall below the detection limits of our instrumentation and makes rigorous analysis of product distributions challenging. Analysis of the carbonate precipitate suggests that the precipitate can trap products like formate at the electrode-electrolyte interface, which can further decrease the faradaic efficiency for CO (Fig. 4.4). Carbonate salt precipitate formation is also observed in inorganic electrolytes and remains a common source of diminishing reactor performance in steady state CO_2 electrolysis.[61, 62] Our observations are also consistent with our prior work,[30, 31] where we previously reported the formation of a solid precipitate in electrolytes with 1-ethyl-2,3-dimethylimidazolium tetrafluoroborate, where the bicarbonate anion paired with the imidazolium cation was insoluble in acetonitrile.

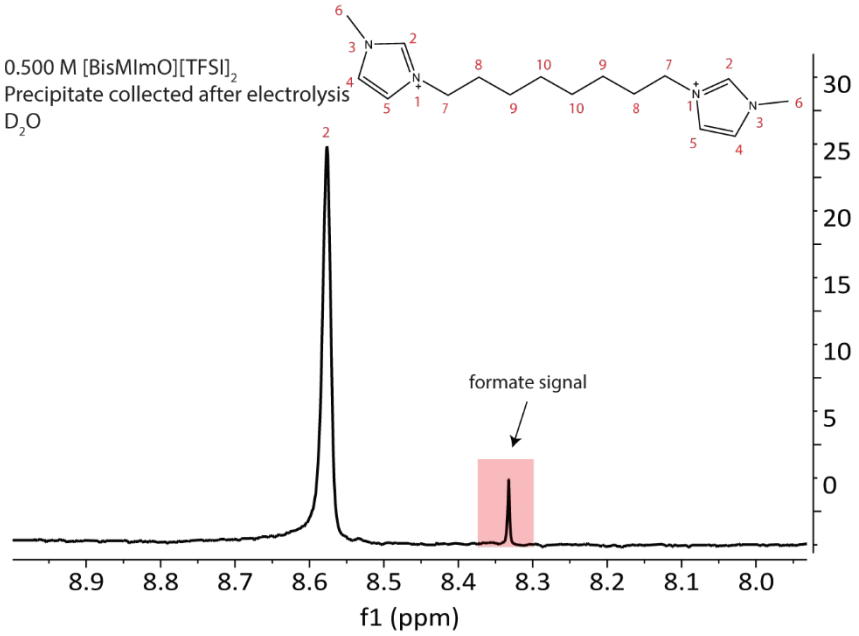

Figure 4.4 1H NMR results of the precipitate that forms in $[BisMImO][TFSI]_2$ electrolytes under CO_2-sparged conditions, indicating the formation of formate.

Hence, simply joining two imidazolium rings together dramatically alters the steady-state electrocatalytic behavior. It is difficult to overstate the importance of ion molecular structure and how it impacts both double layer formation and reactivity. Prior works have demonstrated significant cation effects in both aqueous[63] and non-aqueous systems,[64] which often focus on how changing the cation structure or size can enhance local concentration gradients[65] or the availability of protons.[66] Here, we show that cation entropy can have similarly drastic effects on CO_2 electroreduction by preserving the inherent structure of the imidazolium cation but introducing an entropic constraint. To further investigate the double layer that is formed when the cation is entropically-constrained, we used surface-enhanced Raman scattering (SERS) spectroscopy to examine the structure of the double layer at various applied potentials.

4.3.2. Electrochemical Reactions Disrupt Interfacial Ion Organization

We collected *in situ* SERS spectra at low and intermediate concentrations of the two ionic liquids to probe the structure of the double layer. Our experiments were conducted in one-compartment SERS cells with surface-roughened Ag working electrodes.[56] All solutions were sparged with either Ar or CO_2 for 20 minutes prior to data collection. Our group has previously used this method to interrogate the orientation of the imidazolium ring in the double layer as cathodic potentials were applied.[30, 31]

In the alkyl substituent region, we observed the rise of a peak at 1003 cm^{-1}, which is particularly pronounced in [BisMImO][TFSI]$_2$ electrolytes and is observed primarily in Ar-sparged conditions (Fig. 4.5). Upon the reverse potential scan in Ar-sparged electrolytes, the intensity of the 1003 cm^{-1} peak diminishes. Interestingly, we found that there was a marked difference in the growth of the 1003 cm^{-1} peak when the electrolyte had been sparged with Ar compared to CO_2 (Fig. 4.5). Additionally, while we do observe peaks that may be assigned to Raman-active modes of carbonate, these peaks overlap with those associated with the alkyl chain region of the cation and definitive assignment of these peaks in CO_2-sparged solutions is challenging.

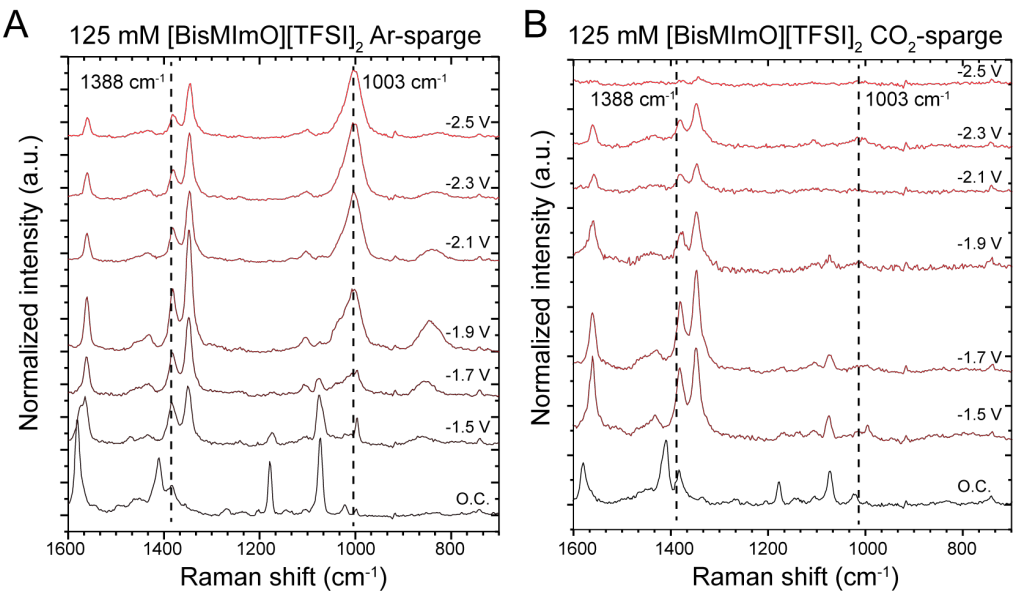

Figure 4.5 *In situ* SERS spectra of 125 mM [BisMImO][TFSI]$_2$ under Ar- and CO_2-sparged conditions highlight the differences in double layer structure in a capacitive and reactive double layer, respectively. In the presence of Ar (A), the rise of a peak ca. 1003 cm^{-1} associated with the alkyl chain substituents that appears at -1.7 V demonstrates potential-dependent restructuring of the alkyl domains of the cation. When CO_2 is present (B), however, the 1003 cm^{-1} peak is not observed. We hypothesize that this could be due to the transport of reactants and products through the double layer and the formation of negatively charged byproducts that disrupt double layer ordering. The formation of a precipitate at the surface at -2.5 V vs. Ag/Ag$^+$ hinders Raman spectra collection under CO_2-sparged conditions.

To analyze the growth of the 1003 cm^{-1} peak, we took the ratio of the peak intensity of the 1003 cm^{-1} peak relative to the peak intensity of the 1388 cm^{-1} peak, which is associated with the stretching mode of the imidazolium ring structure and remains largely unchanged with applied potential. We find that the peak intensity of the 1003 cm^{-1} peak surpasses that of the 1388 cm^{-1} peak at -1.9 V vs. Ag/Ag$^+$ (Fig. 4.6). After reaching this potential, the intensity of the 1003 cm^{-1} peak becomes several times larger than the 1388 cm^{-1} peak in Ar-sparged solutions. A similar trend is observed in [BMIm][TFSI] solutions, but the growth of the 1003 cm^{-1} peak in Ar-sparged solutions is much more subdued (Fig. 4.7).

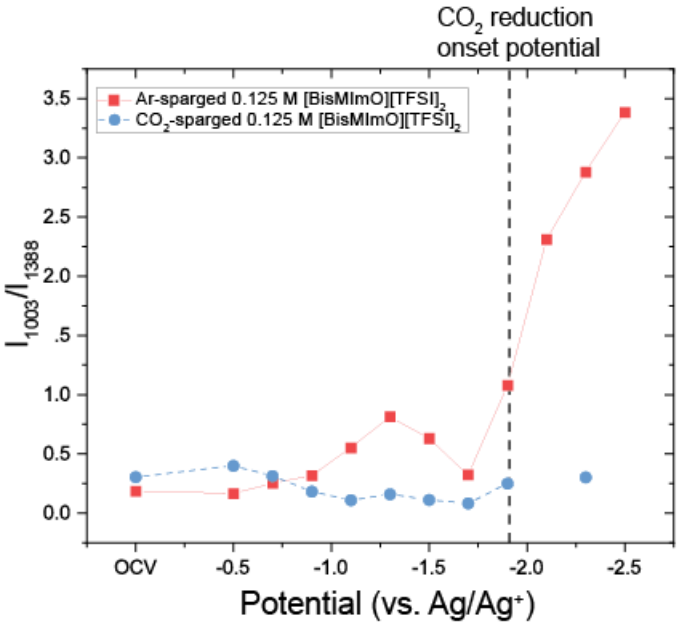

Figure 4.6 *In situ* SERS of 0.125 M [BisMImO][TFSI]$_2$ under Ar-sparged (red) and CO_2-sparged (blue) conditions. Peak ratios of 1003 cm^{-1} and 1388 cm^{-1} were taken to denote extent of alkyl chain organization. We note that the disappearance of the 1003 cm-1 peak under CO_2-sparged conditions indicates the alkyl chain aggregation behavior we observe under Ar is disrupted due to the dynamic nature of the CO_2 reduction double layer.

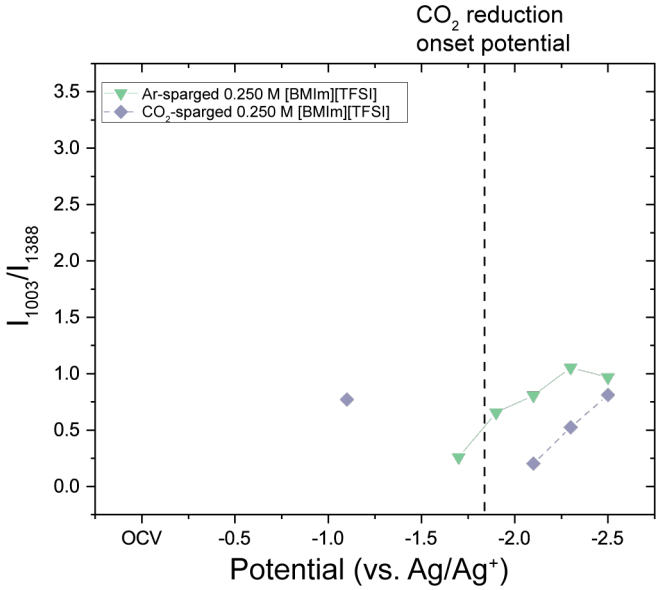

Figure 4.7 Potential-dependent *in situ* SERS of 0.250 M [BMIm][TFSI] under Ar- (green) and CO_2-sparged (purple) conditions. The noticeable lack of the 1003 cm^{-1} peak indicates that there is no significant aggregation of the alkyl chain in [BMIm][TFSI] electrolytes.

The 1003 cm^{-1} peak is associated with the alkyl substituents on the imidazolium and has been previously shown to correspond to C-C stretching.[67, 68] The pronounced 1003 cm^{-1} peaks likely arise from interfacial segregation of the alkyl chains from the imidazolium ring structures given that the alkyl chains, especially for $[BisMImO]^{2+}$, are less polar than the positively charged imidazolium ring. Additionally, the formation of segregated alkyl chain domains have previously been observed in monovalent imidazolium ionic liquid systems.[28, 69] There was also a greater enhancement of the 1003 cm^{-1} signal in $[BisMImO]^{2+}$, suggesting that the connecting alkyl chain imparts more organization to the double layer. Notably, the peak at 1003 cm^{-1} disappeared altogether after -1.9 V vs. Ag/Ag^+ under CO_2-sparged conditions, which is approximately the onset potential for CO_2 electroreduction.

The CO_2 reduction process requires the transport of molecules across the double layer and forms primarily CO but can also generate unwanted byproducts such as $[OH]^-$ (Eq. 4.2) and, by recombination of the $[OH]^-$ with CO_2, (bi)carbonate.[31, 60]

$$CO_2 + H_2O + 2e^- \rightarrow CO + 2OH^- \qquad \text{(Equation 4.2)}$$

Transporting CO_2 towards the electrode and transporting products and byproducts away from the electrode can disrupt the structure that would have formed when there is no reaction in the double layer. Furthermore, the formation of negatively charged products like the $CO_2^{\bullet-}$ intermediate or (bi)carbonates can electrostatically balance the charge of the cations already in the double layer, therefore negating the screening effect of the cation. As a result, more cations are recruited to the double layer as the neutral clusters of ions diffuse away from the surface, thus creating a more dynamic and disrupted double layer structure.

We find that the increase in the intensity of the 1003 cm^{-1} peak under Ar-sparged conditions was also observed in N_2-sparged electrolytes (Fig. 4.8). Combined with the CO_2-sparged results, this suggests that the double layer under inert conditions is fundamentally different from an active double layer in which the transport of reactants and (by)products creates a more dynamic interface. This finding has far-reaching implications, the most significant of which is that double layer models developed for inert conditions, or capacitive double layers, are not directly applicable to dynamic reactive double layers.

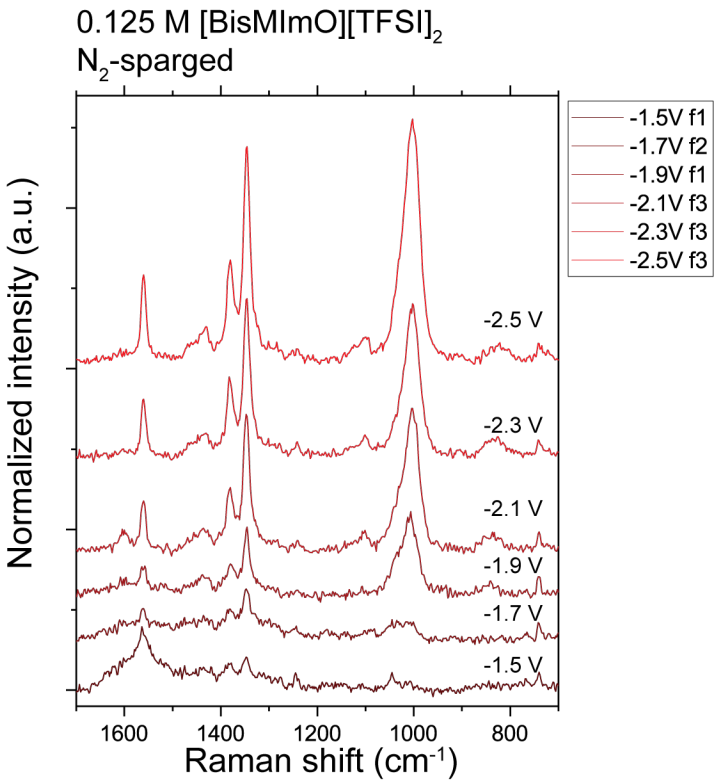

Figure 4.8 Potential-dependent *in situ* SERS of 0.125 M [BisMImO][TFSI]$_2$ under N_2-sparged conditions, which demonstrates the emergence of the 1003 cm^{-1} peak at -1.9 V vs. Ag/Ag$^+$ under inert conditions and suggests that there is a noticeable difference between interfaces in which a reaction such as CO_2 electroreduction occurs, and an inert interface.

4.3.3. Cation Reorientation Occurs at Similar Potentials for Mono- and Dicationic Imidazolium Species

Imidazolium rings have been shown to adopt an orientation parallel to the electrode surface at high cathodic potentials, leading to enhanced cation packing and therefore more efficient screening.[30, 70] To determine if concentration had a significant impact on cation orientation when CO_2 was present, we collected SERS data for low concentrations (0.125 M [BisMImO][TFSI]$_2$ and 0.250 M [BMIm][TFSI]) and concentrated electrolytes (0.825 M [BisMImO][TFSI]$_2$ and 1.65 M [BMIm][TFSI]). These concentrations were chosen to keep the total number of imidazoliums consistent between the two ionic liquids.

The ring deformation region of 1344 to 1580 cm^{-1} can be used to qualitatively understand the reorientation of the imidazolium ring due to the development of an electric field as a potential is applied to

the electrode. In SERS spectroscopy, the vibration modes with tensors perpendicular to the electrode plane are enhanced so trends in signal intensities can be used to gauge the strength of the Raman mode. We observed the red-shifting of the 1580 cm^{-1} peak to 1561 cm^{-1}, which is indicative of increased proximity between the C4 and C5 protons with the surface[71-73] (Fig. 4.9). We also observed a decrease in the intensity of the 1415 cm^{-1} peak, which is associated with the in-plane stretching mode of the imidazolium,[73, 74] and a corresponding increase in the intensity of the 1344 cm^{-1} peak, associated with CH_2(N) stretching,[73-75] as the potential becomes more cathodic for both [BisMImO][TFSI]$_2$ and [BMIm][TFSI] electrolytes. Taken together, these trends in ring Raman modes as a function of applied potential suggests that the imidazolium ring begins to adopt an orientation parallel to the electrode surface,[72, 74, 75] likely with the alkyl substituents roughly also parallel to the electrode.

We used the ratio of the intensity of the 1344 and 1415 cm^{-1} peaks as a metric for assessing the strength of the electric field, as stronger electric fields can reorient an imidazolium ring at lower potentials than weaker electric fields (Fig. 4.9B). Although we observe the same general trend of diminishing 1415 cm^{-1} peak intensities between the two ionic liquids, the potentials at which the ratio of the peak intensities become greater than 1 are quite different at various concentrations.

For example, the intensity inversion for 0.125 M [BisMImO][TFSI]$_2$ and 0.250 M [BMIm][TFSI] are very similar and occur at approximately -1.0 V and -0.9 V vs. Ag/Ag^+, respectively. At higher concentrations, however, we observed a delayed inversion potential of -1.6 V vs. Ag/Ag^+ for the 1.65 M [BMIm][TFSI] electrolyte. The inversion potential for 0.825 M [BisMImO][TFSI]$_2$ occurs at approximately -1.0 V vs. Ag/Ag^+, indicating little difference between the low and intermediate concentrations of [BisMImO][TFSI]$_2$.

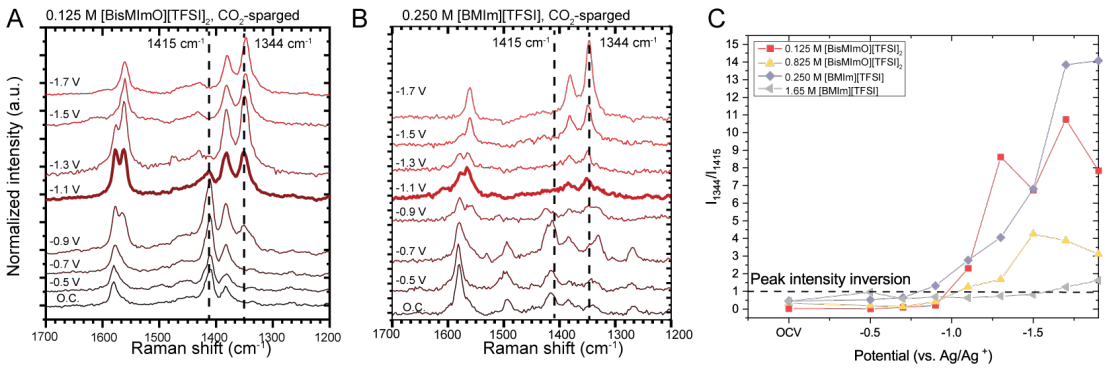

Figure 4.9 *In situ* SERS spectra of 0.125 M [BisMImO][TFSI]$_2$ (A) and 0.250 M [BMIm][TFSI] (B) under CO_2-sparged conditions. The potential at which the 1344 cm^{-1} peak intensity surpasses the 1415 cm^{-1} peak is bolded. The relative intensities of the 1344 and 1415 cm^{-1} peaks are used to determine the extent of imidazolium reorientation (C). The normalized peak intensity of the 1344 cm^{-1} peak surpasses that of the 1415 cm^{-1} peak at -1.1 V vs. Ag/Ag$^+$ for both samples. Comparing the ratios of the peak intensities of the 1344 to 1415 cm^{-1} peaks, we find that the 1.65 M [BMIm][TFSI] inversion potential is more negative than the other ionic liquid concentrations. The inversion potential for the 0.825 M [BisMImO][TFSI]$_2$ remains similar to the lower concentration electrolytes, which suggests that the covalent link provides a "pre-structuring" effect between the two imidazoliums of the [BisMImO]$^+$ cation.

The imidazolium ring reorientation inversion potential allows us to gauge how bulk ion-ion correlations impact double layer formation. For the lower concentrations of [BisMImO][TFSI]$_2$ and [BMIm][TFSI], the intensity inversion occurs at similar potentials, as ion-ion correlations have not yet begun to dominate. In the 1.65 M [BMIm][TFSI] electrolyte, we observed a delayed inversion potential, which can be explained by ion-ion interactions, as well as the formation of clusters and aggregates in the bulk electrolyte that decrease screening efficiency and thus lower the strength of the interfacial electric field. Although there are the same number of charges, 0.825 M [BisMImO][TFSI]$_2$ did not have such a delay and the potential of peak intensity inversion was more similar to lower concentration electrolytes, indicating a stronger electric field in 0.825 M [BisMImO][TFSI]$_2$ than 1.65 M [BMIm][TFSI.

One explanation for this is that the linkage between the two imidazoliums in [BisMImO]$^{2+}$ can help with the potential-dependent reorientation through a decrease in accessible orientations of imidazolium rings relative to [BMIm]$^+$, hence imparting a "pre-structure" to the double layer. The ratio of the 1344 cm^{-1} and 1415 cm^{-1} peaks, however, were smaller than that of the lower concentrations especially at potentials

more cathodic than -1.5 V vs. Ag/Ag^+. Thus, the SERS results indicate that the extent of this reorientation is smaller in more concentrated electrolytes and is likely hindered by ion-ion interactions.

4.3.4. Divalent Cations are Surface Active

We also aimed to understand how lower entropic penalties impacted ion availability in the double layer using mixtures of $[BisMImO][TFSI]_2$ and [BMIm][TFSI]. Additionally, we expected that mixing ionic liquids would help mitigate the precipitation issue, as having multiple types of cations present could disrupt the crystal structure needed to make the solid (bi)carbonate salt. We evaluated the mixtures of the two ionic liquids using CA, GC, and SERS spectroscopy. For simplicity, we kept the total ionic liquid concentration at 125 mM.

First, we find that by adding 5 mM $[BisMImO][TFSI]_2$ to 120 mM [BMIm][TFSI], the steady-state current density drops to 25% of the current density observed for the 125 mM [BMIm][TFSI] electrolyte. As the ratio of $[BisMImO][TFSI]_2$ increases, the steady state current density decreases until it becomes less than -2.5 mA/cm^2 in a mixture of 25 mM $[BisMImO][TFSI]_2$ and 100 mM [BMIm][TFSI]. Notably, faradaic efficiency for CO decreases gradually until it reaches approximately 50% at 125 mM $[BisMImO][TFSI]_2$ (Fig. 4.10).

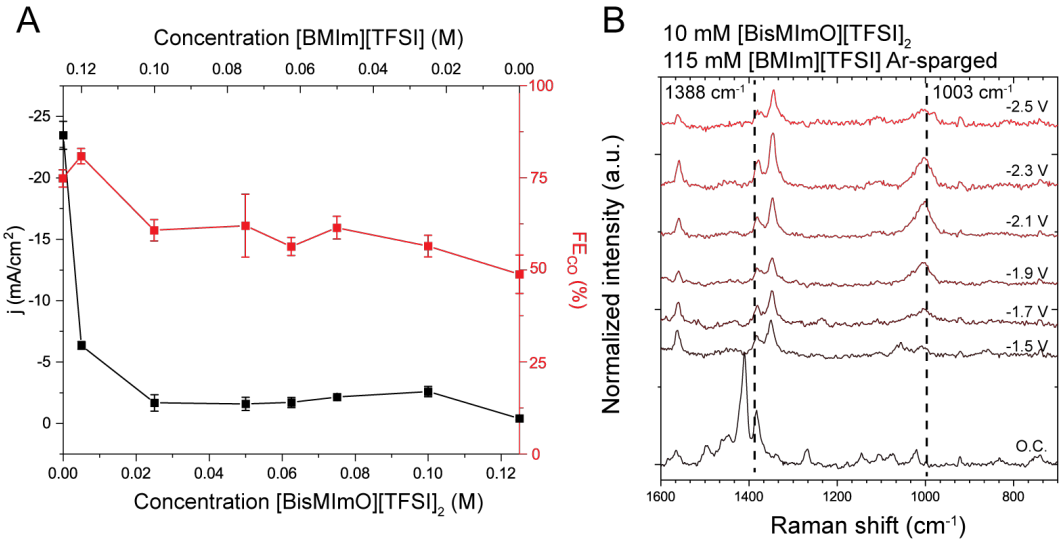

Figure 4.10 Results of mixed electrolytes demonstrate the preferential accumulation of the $[BisMImO]^{2+}$ cation. Steady state electrolysis (A), where current density (black) and faradaic efficiency for CO (red) in mixtures of $[BisMImO][TFSI]_2$ and [BMIm][TFSI] show that the addition of 5 mM $[BisMImO][TFSI]_2$ to

120 mM [BMIm][TFSI] results in a decrease in current density and the formation of an occluding phase on the electrode surface. The faradaic efficiency for CO decreases steadily with increasing concentration of $[BisMImO][TFSI]_2$. SERS spectra of 10 mM $[BisMImO][TFSI]_2$ and 115 mM [BMIm][TFSI] under Ar-sparged conditions reveal the presence and growth of the 1003 cm^{-1} peak that was observed in $[BisMImO][TFSI]_2$ electrolytes and not in [BMIm][TFSI] electrolytes. Due to the drop in current density and the formation of an occluding phase on the electrode surface, our interpretation is that the $[BisMImO]^{2+}$ cation accumulates within the double layer and thus has an outsized effect on reactivity.

We observed a pronounced decrease in current density with the addition of relatively small amounts of $[BisMImO][TFSI]_2$ as well as precipitate formation, which together indicates that a distinct [BisMImO]-enriched phase forms on the electrode surface. Interestingly, the potential applied to the electrode surface dictated the physical appearance of the precipitate in solutions containing only $[BisMImO][TFSI]_2$. For instance, a solid white crystal nucleated and propagated on the surface when a potential of -2.5 V vs Ag/Ag^+ was held under CO_2-sparged conditions. If the potential was quickly stepped to -2.7 V vs Ag/Ag^+ and held, however, a dynamic precipitate formation process was observed that occurred in two steps. First, evidence of liquid-liquid phase separation was observed as islands of a liquid phase formed on the electrode surface and began to coalesce. Within these liquid droplets, solid precipitates began to form, ultimately resulting in the formation of an orange gel-like film spanning the entire electrode surface, likely composed of the (bi)carbonate salt and decomposed imidazolium (Fig. 4.11). These same trends were observed in mixtures of $[BisMImO][TFSI]_2$ and [BMIm][TFSI].

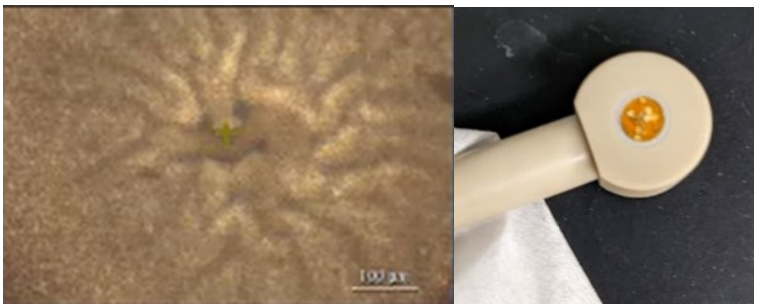

Figure 4.11 Picture of the electrode surface when a potential is stepped to -2.7 V vs. Ag/Ag^+ (left) showing the formation of solid precipitate that, when exposed to ambient humidity, forms an orange film (right).

Hence, we find that decreasing the entropic penalty of constraining cations within electric double layers appears to amplify driving forces for electrochemically induced phase separation. Electrochemically

induced phase separation has been previously demonstrated by Leibler and coworkers to be possible in binary mixtures of silicone oil and paraffin oil,[76] and followed up with a theoretical model for electric field gradient-induced phase separation in ion-containing mixtures.[77] In experiments by Lahiri and coworkers, the mechanism for potential-dependent phase separation in ionic liquid-containing electrolytes was through the formation of unstable bonds resulting in the eventual decomposition of the electrolyte into two phases.[78]

Even more interestingly, electrolytes containing only 10 mM $[BisMImO][TFSI]_2$ (with 115 mM [BMIm][TFSI]) formed a clear liquid phase on the electrode surface that was distinguishable from the bulk electrolyte under CO_2-sparged conditions but not in Ar-sparged conditions. We hypothesize that this is due to the formation of the $[BisMImO]^{2+}$ (bi)carbonate salt, where the concentration of the salt is not sufficient to induce precipitation. Additionally, the presence of $[BMIm]^+$ could disrupt the formation of a solid crystal since the (bi)carbonate salt of $[BMIm]^+$ does not precipitate out of solution, leading to the metastable liquid-liquid phase separation process.

To the best of our knowledge, liquid-liquid phase separation due to the active electrocatalytic processes in ionic liquid electrolytes has not been reported in literature. This separate liquid phase was fluid and moved when the cell was lightly disturbed before reverting to its original state. A white crystal began to nucleate and grow after more than 30 minutes of applied potential of -2.7 V vs. Ag/Ag^+. Further increases in the ratio of $[BisMImO][TFSI]_2$ to [BMIm][TFSI] in the electrolyte mixtures began to yield precipitates that were indistinguishable from that of electrolytes containing only $[BisMImO][TFSI]_2$. Hence, we conclude that the formation of solid precipitates in these mixed electrolytes appears to pass through a nonclassical multistep nucleation and growth process, as explained by De Yoreo and colleagues for carbonate precipitation in biological systems.[79]

The low concentration required to observe this phase separation indicates that the $[BisMImO][TFSI]_2$ preferentially accumulates in the double layer but crystal formation is suppressed or delayed due to the presence of $[BMIm]^+$ cations with lower propensity to form solid (bi)carbonate crystals. Although the full mechanism is the subject of ongoing work, the potential-dependent liquid-liquid phase separation we observe in these mixed ionic liquids appears to have intriguing connections to the process of

coacervate formation in biology, where changes in pH and ionic strength drive formation of distinct liquid phases.[79] We therefore expect that the interface would contain higher concentrations of [BisMImO][TFSI]$_2$ than the bulk.

To investigate the composition of the double layer, we collected SERS spectra of the electrolyte mixtures, focusing on the electrolyte compositions with low ratios of [BisMImO][TFSI]$_2$:[BMIm][TFSI]. Given that even mixtures of low concentrations of [BisMImO][TFSI]$_2$ exhibited electrochemical behavior more like that of [BisMImO][TFSI]$_2$-only electrolytes, we expected that the SERS spectra of the interface would reflect an enhanced abundance of interfacial [BisMImO][TFSI]$_2$ in these mixed electrolytes.

Under Ar-sparged conditions, we indeed found that the electrolytes containing small amounts of the [BisMImO][TFSI]$_2$ behaved more like the electrolyte containing primarily [BisMImO][TFSI]$_2$. In short, the 1003 cm^{-1} peak outgrew the 1388 cm^{-1} peak in intensity in all solutions containing [BisMImO][TFSI]$_2$ regardless of whether [BMIm][TFSI] was also present. We observed the appearance of the 1003 cm^{-1} peak under Ar-sparged conditions in a mixture of 10 mM [BisMImO][TFSI]$_2$ and 115 mM [BMIm][TFSI]. This suggests the organization of the alkyl chain domains of the cations and the enhanced presence of the [BisMImO]$^+$ cation at the interface. In other mixtures, the ratio of the peak intensities in the mixed electrolytes began to approach that of the 125 mM [BisMImO][TFSI]$_2$ solution as the concentration of [BisMImO][TFSI]$_2$ increased (Fig. 4.12). This suggests that the [BisMImO]$^{2+}$ concentrates within the double layer. Otherwise, the low ratio of [BisMImO][TFSI]$_2$ to [BMIm][TFSI] should yield SERS spectra more like an electrolyte containing only [BMIm][TFSI].

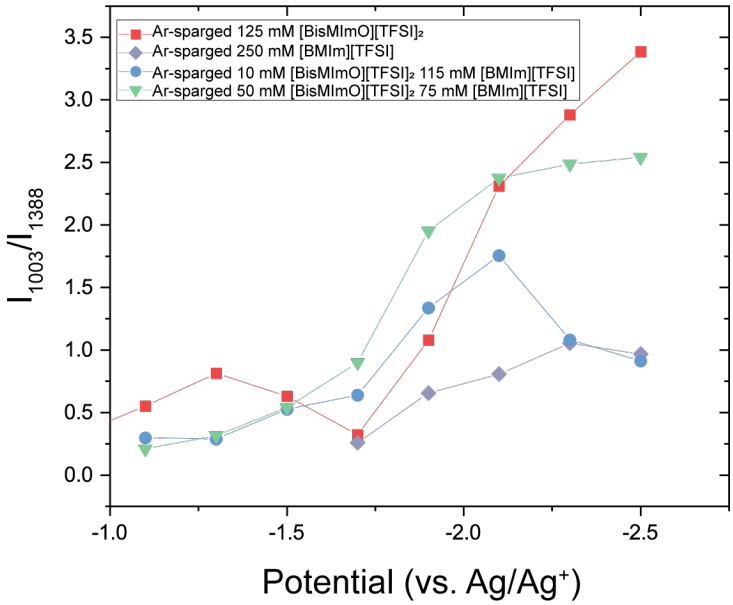

Figure 4.12 Peak ratios of 1003 cm^{-1} and 1388 cm^{-1} peaks of ionic liquid mixtures containing $[BisMImO][TFSI]_2$ under Ar-sparged conditions. Compared to 125 mM $[BisMImO][TFSI]_2$ (red) and 250 mM [BMIm][TFSI] (purple), electrolytes containing a mixture of the two show that as the concentration of $[BisMImO][TFSI]_2$ increases from 10 mM (blue) to 50 mM (green), the potential-dependent ratio of the two peaks becomes more like that of the $[BisMImO][TFSI]_2$-only electrolyte, suggesting enhanced accumulation of the $[BisMImO][TFSI]_2$ at the interface.

These findings, combined with the electrolysis data, point to the preferential accumulation of the lower entropic penalty ionic liquid, $[BisMImO][TFSI]_2$, at the electrode/electrolyte interface. In short, the electrochemical behavior of a mixed electrolyte is dictated by the salt with the lowest entropic penalty for double layer formation (Fig. 4.13). Intriguingly, our results on entropic considerations of double layer formation may also help explain observations made in aqueous studies of mixed alkali metal salts, where the reactivity of mixed electrolytes containing dilute Li^+ and larger alkali metal cations is dominated by the reactivity of the larger alkali metal cation,[80] or the enhancement of CO_2 electroreduction in the presence of multivalent ions.[60]

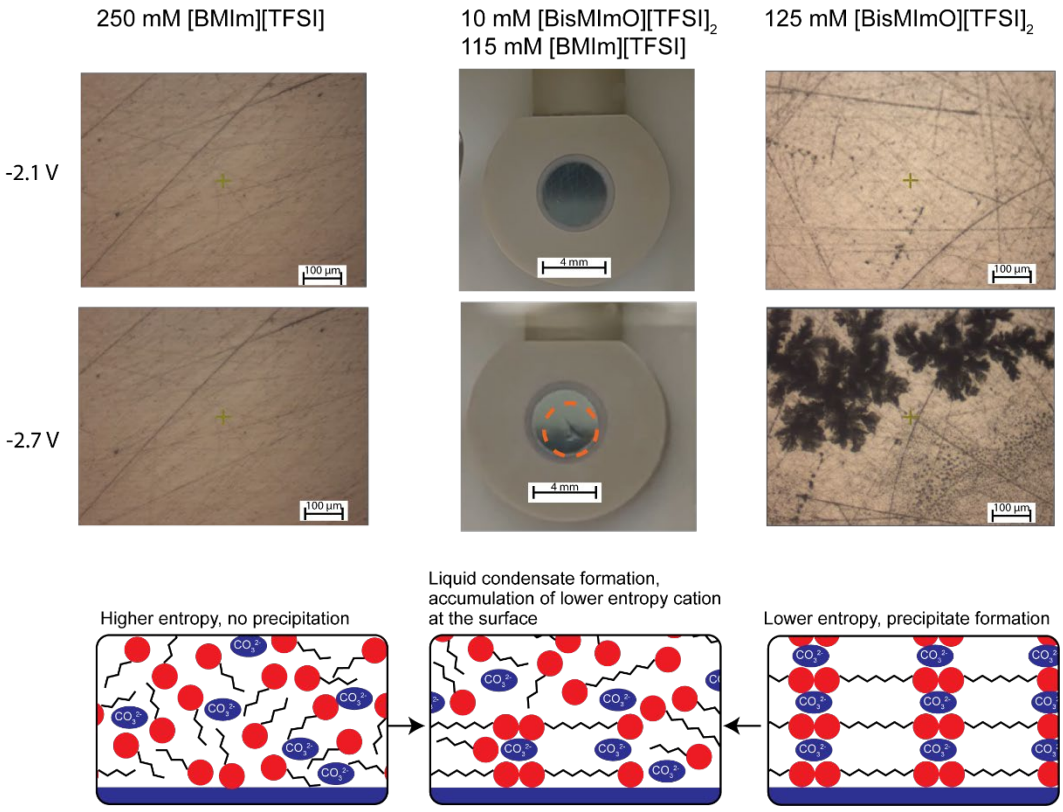

Figure 4.13 Ionic liquids with higher entropic penalties of confinement form fluid interfaces (left column) while those with lower entropic penalties for confinement within the double layer preferentially accumulate at the interface but can lead to electrode-blocking precipitation formation (right column). Mixtures of ionic liquids exhibit electrocatalytic behavior that depend on the ion with the lower entropic penalty and can yield liquid-liquid phase separated interfaces (middle column).

4.3.5. Cation Entropy Governs Interfacial Reactivity

Our findings comparing [BisMImO][TFSI]$_2$ and [BMIm][TFSI] highlight the importance of cation entropy in dictating interfacial electroreduction in a manner that can rival that of changing the overall cation structure. Although the core imidazolium structure remains constant, imposing an entropic constraint through the covalent bond leads to decreases in CO_2 reduction rates due to the formation of a precipitate layer on the electrode surface. By tethering two $[BMIm]^+$ ions together to make the $[BisMImO]^{2+}$ ion, the primary change is in the orientational degrees of freedom of the cation, as the basic $[BMIm]^+$ structure is preserved.

When confined within the double layer, the $[BMIm]^+$ ion has more orientational degrees of freedom. The imidazoliums in the $[BisMImO]^{2+}$ ion, on the other hand, have a reduced number of available orientations available relative to one another. The covalent bond in $[BisMImO]^{2+}$ also serves to impose an additional layer of ion correlations, resulting in smaller current densities at lower concentrations due to the formation of precipitates. These effects become less pronounced at high concentrations, however, as the emergence of ion-ion correlations in $[BMIm]^+$ attenuates the difference between CO_2 reduction in $[BisMImO]^{2+}$ and $[BMIm]^+$, leading to converging reaction rates in the neat ionic liquid limit.

Analysis of SERS results in $[BisMImO][TFSI]_2$ electrolytes also point towards a fundamental difference in the structure of the double layer under inert or reactive conditions. We found that under inert conditions, the long alkyl chains of the $[BisMImO]^{2+}$ formed segregated domains or local nanostructures. When CO_2 is present, however, the double layer structure becomes disrupted, which can be attributed to the dynamic nature of a reactive double layer, in which the transport of reactants and products disturbs the interfacial structure, and formation of charged byproducts disrupts the local electric field. This difference in double layer structure under two different gas sparging conditions highlights the complex nature of double layers and suggests that conventional models of double layers, which assume no faradaic reactions, may not be directly applicable to reactive double layers.

In $[BisMImO][TFSI]_2$ electrolytes, we observed solid precipitate formation, which passivated the electrode surface and prevented further CO_2 electroreduction from occurring. These phase separations only occurred under CO_2-sparged conditions, suggesting that byproducts of the CO_2 reduction reaction facilitate the phase separation. Additionally, the overall appearance of the solid precipitate differs at different applied potentials, indicating that the presence of other electrochemical products, such as those made by the deactivation of imidazolium, can also modify for surface passivation processes.

The inclusion of an ion like $[BMIm]^+$ in mixed electrolytes disrupted the solid [BisMImO]-(bi)carbonate precipitate crystal structure, thus leading to the liquid-liquid separation observed in the 10 mM $[BisMImO][TFSI]_2$ 115 mM [BMIm][TFSI] solutions. Precipitate formation poses a serious hurdle in the adoption of CO_2 electrolysis cells, as formation of solid (bi)carbonate salts creates a passivating layer

on the electrode surface, ultimately leading to electrolytic cell failure.[10, 60] Our mixed electrolyte experiments show that this precipitation process occurs via a multistep mechanism, in which liquid-liquid phase separation first occurs and is followed by precipitate nucleation. Multistep nucleation processes have been demonstrated to have much lower energy barriers than classical nucleation,[79] which may explain the prevalence of the precipitate problem and also offer methods for prevention. We have shown that mixing two salts can have a stabilizing effect on the metastable liquid formed at the electrode surface, but higher compositional complexity may be a more suitable approach for completely suppressing nucleation.

4.4. Conclusion

We compared a dicationic ionic liquid, [BisMImO][TFSI]$_2$, with its monovalent counterpart [BMIm][TFSI] to investigate the role of entropy in double layer formation. We found that differences in cation entropy can fundamentally alter reaction rates and selectivity during steady-state electrolysis. SERS spectroscopy results show a pronounced difference between reactive and non-reactive double layers for both the monocationic and dicationic species. We also found that when CO_2 was present, the reorientation of the imidazolium rings of $[BisMImO]^{2+}$ and $[BMIm]^{+}$ were similar at low concentrations but had more pronounced differences at higher concentrations. In mixtures of the two ionic liquids, we concluded that the cation that pays the lowest entropic penalty accumulates within the double layer and dictates reactivity.

Our findings highlight the key role entropy plays in determining interfacial potential gradients and electrochemical reactivity. We also demonstrate that entropy-reactivity relationships offer a new approach to tuning electrocatalytic reactions, in which the design of an electrochemical system must account for both ion entropy of confinement to the double layer, as well as the ability of ions to reorient at the interface. Double layer models must take both entropic considerations and reactive conditions into account to understand the dynamic nature of the reactions occurring in double layers. Ions at the interface can facilitate or hinder a reaction, as evidenced by the onset of liquid-liquid phase separation followed by solid precipitate formation in [BisMImO][TFSI]$_2$ electrolytes.

Our observation of multi-step nucleation processes of solid precipitates in mixed electrolytes also warrants a reexamination of electrochemically induced phase separation and its pertinence for electrolyte engineering. Multistep nucleation mechanisms, akin to those described by De Yoreo and coworkers for biological carbonate precipitation,[79] have much lower energy barriers than classical nucleation. It is possible that (bi)carbonate salts of $[BMIm]^+$ undergo classical nucleation with high energy barriers, while $[BisMImO]^{2+}$ salts tend to undergo multi-step nucleation pathways and are therefore more prone to precipitate formation. Thus, understanding how entropy governs double layer formation can offer fundamentally new ways to leverage entropy as an additional parameter for double layer engineering and can offer an exciting opportunity to reexamine precipitate nucleation and growth mechanisms.

4.5. References

(1) Maggs, A. C.; Podgornik, R. General theory of asymmetric steric interactions in electrostatic double layers. *Soft Matter* **2016**, (4), 1219-1229.

(2) Silkina, E. F.; Molotilin, T. Y.; Maduar, S. R.; Vinogradova, O. I. Ionic equilibria and swelling of soft permeable particles in electrolyte solutions. *Soft Matter* **2020**, *16* (4), 929-938. DOI: 10.1039/c9sm01602c.

(3) Kjellander, R. The intimate relationship between the dielectric response and the decay of intermolecular correlations and surface forces in electrolytes. *Soft Matter* **2019**, *15* (29), 5866-5895. DOI: 10.1039/c9sm00712a.

(4) Ryu, C. H.; Lee, H.; Lee, H.; Ren, H. Learning from the Heterogeneity at Electrochemical Interfaces. *Journal of Physical Chemistry Letters* **2022**, *13* (33), 7838-7846. DOI: 10.1021/acs.jpclett.2c02009.

(5) Shin, H.; Yoo, J. M.; Sung, Y.-E.; Chung, D. Y. Dynamic Electrochemical Interfaces for Energy Conversion and Storage. *JACS Au* **2022**, *2* (10), 2222-2234. DOI: 10.1021/jacsau.2c00385.

(6) Groß, A. Grand-Canonical Approaches To Understand Structures And Processes At Electrochemical Interfaces From An Atomistic Perspective. *Current Opinion in Electrochemistry* **2021**, *27*, 100684. DOI: 10.1016/j.coelec.2020.100684.

(7) Stamenkovic, V. R.; Strmcnik, D.; Lopes, P. P.; Markovic, N. M. Energy and Fuels from Electrochemical Interfaces. *Nature Materials* **2017**, *16*, 57-69. DOI: 10.1038/nmat4738.

(8) Chen, L. D.; Urushihara, M.; Chan, K.; Nørskov, J. Electric Field Effects in Electrochemical CO_2 Reduction. *ACS Catalysis* **2016**, *6* (10), 7133-7139. DOI: 10.1021/acscatal.6b02299.

(9) Su, H.; Zhou, W.; Zhang, H.; Zhou, W.; Zhao, X.; Li, Y.; Liu, M.; Cheng, W.; Liu, Q. Dynamic Evolution of Solid–Liquid Electrochemical Interfaces over Single-Atom Active Sites. *Journal of the American Chemical Society* **2020**, *142* (28), 12306-12313. DOI: 10.1021/jacs.0c04231.

(10) Birdja, Y. Y.; Pérez-Gallent, E.; Figueiredo, M. C.; Göttle, A. J.; Calle-Vallejo, F.; Koper, M. T. M. Advances and Challenges in Understanding the Electrocatalytic Conversion of Carbon Dioxide to Fuels. *Nature Energy* **2019**, *4*, 732-745. DOI: 10.1038/s41560-019-0450-y.

(11) Zhu, P.; Wang, H. High-Purity and High-Concentration Liquid Fuels Through CO_2 Electroreduction. *Nature Catalysis* **2021**, *4*, 943-951. DOI: 10.1038/s41929-021-00694-y.

(12) Gao, D.; Arán-Ais, R. M.; Jeon, H. S.; Cuenya, B. R. Rational Catalyst and Electrolyte Design for CO_2 Electroreduction Towards Multicarbon Products. *Nature Catalysis* **2019**, *2*, 198-210. DOI: 10.1038/s41929-019-0235-5.

(13) Tomboc, G. M.; Choi, S.; Kwon, T.; Hwang, Y. J.; Lee, K. Potential Link between Cu Surface and Selective CO_2 Electroreduction: Perspective on Future Electrocatalyst Designs. *Advanced Materials* **2020**, *32* (17), 1908398. DOI: 10.1002/adma.201908398.

(14) Niu, Z.-Z.; Gao, F.-Y.; Zhang, X.-L.; Yang, P.-P.; Liu, R.; Chi, L.-P.; Wu, Z.-Z.; Qin, S.; Yu, X.; Gao, M.-R. Hierarchical Copper with Inherent Hydrophobicity Mitigates Electrode Flooding for High-Rate CO_2 Electroreduction to Multicarbon Products. *Journal of the American Chemical Society* **2021**, *143* (21), 8011-8021. DOI: 10.1021/jacs.1c01190.

(15) Ge, W.; Chen, Y.; Fan, Y.; Zhu, Y.; Liu, H.; Zong, L.; Liu, Z.; Lian, C.; Jiang, H.; Li, C. Dynamically Formed Surfactant Assembly at the Electrified Electrode–Electrolyte Interface Boosting CO_2 Electroreduction. *Journal of the American Chemical Society* **2022**, *144* (14), 6613-6622. DOI: 10.1021/jacs.2c02486.

(16) Yang, K.; Kas, R.; Smith, W. A. In Situ Infrared Spectroscopy Reveals Persistent Alkalinity near Electrode Surfaces during CO_2 Electroreduction. *Journal of the American Chemical Society* **2019**, *141*, 15891-15900. DOI: 10.1021/jacs.9b07000.

(17) Kas, R.; Kortlever, R.; Yılmaz, H.; Koper, M. T. M.; Mul, G. Manipulating the Hydrocarbon Selectivity of Copper Nanoparticles in CO_2 Electroreduction by Process Conditions. *ChemElectroChem* **2014**, *2* (3). DOI: 10.1002/celc.201402373.

(18) Xu, A.; Govindarajan, N.; Kastlunger, G.; Vijay, S.; Chan, K. Theories for Electrolyte Effects in CO_2 Electroreduction. *Accounts of Chemical Research* **2022**, *55* (4), 495-503. DOI: 10.1021/acs.accounts.1c00679.

(19) Kortlever, R.; Shen, J.; Schouten, J. P.; Calle-Vallejo, F.; Koper, M. T. M. Catalysts and Reaction Pathways for the Electrochemical Reduction of Carbon Dioxide. *Journal of Physical Chemistry Letters* **2015**, *6* (20), 4073-4082. DOI: 10.1021/acs.jpclett.5b01559.

(20) Hori, Y.; Murata, A.; Yoshinami, Y. Adsorption of CO, Intermediately Formed in Electrochemical Reduction of CO_2, at a Copper Electrode. *Journal of the Chemical Society, Faraday Transactions* **1991**, *87* (1), 125-128. DOI: 10.1039/FT9918700125.

(21) Chadrasekaran, K.; Bockris, J. O. M. In-situ Spectroscopic Investigation of Adsorbed Intermediate Radicals in Electrochemical Reactions: CO_2^- on Platinum. *Surface Science* **1987**, *185* (3), 495-514. DOI: 10.1016/S0039-6028(87)80173-5.

(22) Bockris, J. O. M.; Wass, J. C. On the Photoelectrocatalytic Reduction of Carbon Dioxide. *Materials Chemistry and Physics* **1989**, *22* (3-4), 249-280. DOI: 10.1016/0254-0584(89)90001-1.

(23) Hori, Y. Electrochemical CO_2 Reduction on Metal Electrodes. In *Modern Aspects of Electrochemistry*, Vayenas, C. G., White, R. E., Gamboa-Aldeco, M. E. Eds.; Vol. 42; Springer, 2008; pp 89-189.

(24) Mariano, R. G.; Kang, M.; Wahab, O. J.; McPherson, I. J.; Rabinowitz, J. A.; Unwin, P. R.; Kanan, M. W. Microstructural Origin of Locally Enhanced CO_2 Electroreduction Activity on Gold. *Nature Materials* **2021**, *20*, 1000-1006. DOI: 10.1038/s41563-021-00958-9.

(25) Merlet, C.; Limmer, D. T.; Salanne, M.; van Roij, R.; Madden, P. A.; Chandler, D.; Rotenberg, B. The Electric Double Layer Has a Life of Its Own. *Journal of Physical Chemistry C* **2014**, *118* (32), 18291-18298. DOI: 10.1021/jp503224w.

(26) Zhang, Y.; Ye, T.; Chen, M.; Goodwin, Z. A. H.; Feng, G.; Huang, J.; Kornyshev, A. A. Enforced Freedom: Electric-Field-Induced Declustering of Ionic-Liquid Ions in the Electrical Double Layer. *Energy & Environmental Materials* **2020**, *3* (3), 414-420. DOI: 10.1002/eem2.12107.

(27) de Souza, J. P.; Goodwin, Z. A. H.; McEldrew, M.; Kornyshev, A. A.; Bazant, M. Z. Interfacial Layering in the Electric Double Layer of Ionic Liquids. *Physical Review Letters* **2020**, *125* (11). DOI: 10.1103/PhysRevLett.125.116001.

(28) Perkin, S.; Crowhurst, L.; Niedermeyer, H.; Welton, T.; Smith, A. M.; Gosvami, N. N. Self-assembly in the electrical double layer of ionic liquids. *Chemical Communications* **2011**, *47* (23), 6572-6574. DOI: 10.1039/c1cc11322d.

(29) Goodwin, Z. A. H.; McEldrew, M.; de Souza, J. P.; Bazant, M. Z.; Kornyshev, A. A. Gelation, clustering, and crowding in the electrical double layer of ionic liquids. *Journal of Chemical Physics* **2022**, *157* (9). DOI: 10.1063/5.0097055.

(30) Liu, B.; Guo, W.; Gebbie, M. A. Tuning Ionic Screening To Accelerate Electrochemical CO_2 Reduction in Ionic Liquid Electrolytes. *ACS Catalysis* **2022**, *12* (15), 9706-9716. DOI: 10.1021/acscatal.2c02154.

(31) Guo, W.; Liu, B.; Gebbie, M. A. Suppressing Co-Ion Generation via Cationic Proton Donors to Amplify Driving Forces for Electrochemical CO_2 Reduction. *Journal of Physical Chemistry C* **2023**, *127* (29), 14243-14254. DOI: 10.1021/acs.jpcc.3c04004.

(32) Kornyshev, A. A. Double-Layer in Ionic Liquids: Paradigm Change? *Journal of Physical Chemistry B* **2007**, *111* (20), 5545-5557. DOI: 10.1021/jp067857o.

(33) Fedorov, M. V.; Kornyshev, A. A. Towards Understanding the Structure and Capacitance of Electrical Double Layer in Ionic Liquids. *Electrochimica Acta* **2008**, *53* (23), 6835-6840. DOI: 10.1016/j.electacta.2008.02.065.

(34) Bazant, M. Z.; Storey, B. D.; Kornyshev, A. A. Double Layer in Ionic Liquids: Overscreening versus Crowding. *Physical Review Letters* **2011**, *106* (4). DOI: 10.1103/PhysRevLett.106.046102.

(35) Gebbie, M. A.; Smith, A. M.; Dobbs, H. A.; Lee, A. A.; Warr, G. G.; Banquy, X.; Valtiner, M.; Rutland, M. W.; Israelachvili, J. N.; Perkin, S.; et al. Long range electrostatic forces in ionic liquids. *Chemical Communications* **2017**, *53* (7), 1214-1224. DOI: 10.1039/c6cc08820a.

(36) Koutsoukos, S.; Becker, J.; Dobre, A.; Fan, Z. J.; Othman, F.; Philippi, F.; Smith, G. J.; Welton, T. Synthesis of Aprotic Ionic Liquids. *Nature Reviews Methods Primers* **2022**, *2* (1). DOI: 10.1038/s43586-022-00129-3.

(37) Rosen, B. A.; Salehi-Khojin, A.; Thorson, M. R.; Zhu, W.; Whipple, D. T.; Kenis, P. J. A.; Masel, R. I. Ionic Liquid-Mediated Selective Conversion of CO_2 to CO at Low Overpotentials. *Science* **2011**, *334* (6056), 643-644. DOI: 10.1126/science.1209786.

(38) Rey, N. G.; Dlott, D. D. Structural Transition in an Ionic Liquid Controls CO2 Electrochemical Reduction. *Journal of Physical Chemistry C* **2015**, *119* (36), 20892-20899. DOI: 10.1021/acs.jpcc.5b03397.

(39) Rey, N. G.; Dlott, D. D. Effects of water on low-overpotential CO2 reduction in ionic liquid studied by sum-frequency generation spectroscopy. *Physical Chemistry Chemical Physics* **2017**, *19* (16), 10491-10501. DOI: 10.1039/c7cp00118e.

(40) Yang, X. H.; Papasizza, M.; Cuesta, A.; Cheng, J. Water-In-Salt Environment Reduces the Overpotential for Reduction of CO_2 to CO_2^- in Ionic Liquid/Water Mixtures. *ACS Catalysis* **2022**, *12* (11), 6770-6780. DOI: 10.1021/acscatal.2c00395.

(41) Sun, L. Y.; Ramesha, G. K.; Kamat, P. V.; Brennecke, J. F. Switching the Reaction Course of Electrochemical CO_2 Reduction with Ionic Liquids. *Langmuir* **2014**, *30* (21), 6302-6308, Article. DOI: 10.1021/la5009076.

(42) Lau, G. P. S.; Schreier, M.; Vasilyev, D.; Scopelliti, R.; Grätzel, M.; Dyson, P. J. New Insights Into the Role of Imidazolium-Based Promoters for the Electroreduction of CO_2 on a Silver Electrode. *Journal of the American Chemical Society* **2016**, *138* (25), 7820-7823. DOI: 10.1021/jacs.6b03366.

(43) Zhao, S. F.; Horne, M.; Bond, A. M.; Zhang, J. Is the Imidazolium Cation a Unique Promoter for Electrocatalytic Reduction of Carbon Dioxide? *Journal of Physical Chemistry C* **2016**, *120* (42), 23989-24001. DOI: 10.1021/acs.jpcc.6b08182.

(44) Tanner, E. E. L.; Batchelor-McAuley, C.; Compton, R. G. Carbon Dioxide Reduction in Room-Temperature Ionic Liquids: The Effect of the Choice of Electrode Material, Cation, and Anion. *Journal of Physical Chemistry C* **2016**, *120* (46), 26442-26447. DOI: 10.1021/acs.jpcc.6b10564.

(45) Theodoor, J.; Overbeek, G. The Role of Energy and Entropy in the Electrical Double Layer. *Colloids and Surfaces* **1990**, *51*, 61-75. DOI: 10.1016/0166-6622(90)80132-N.

(46) Wang, Y. F.; Adhikari, L.; Baker, G. A.; Blanchard, G. J. Cation structure-dependence of the induced free charge density gradient in imidazolium and pyrrolidinium ionic liquids. *Physical Chemistry Chemical Physics* **2022**, *24* (32), 19314-19320. DOI: 10.1039/d2cp01066f.

(47) Ma, K.; Jarosova, R.; Swain, G. M.; Blanchard, G. J. Modulation of an Induced Charge Density Gradient in the Room-Temperature Ionic Liquid BMIM+BF4-. *Journal of Physical Chemistry C* **2018**, *122* (13), 7361-7367. DOI: 10.1021/acs.jpcc.8b02345.

(48) Lindner, J.; Weick, F.; Endres, F.; Schuster, R. Entropy Changes upon Double Layer Charging at a (111)-Textured Au Film in Pure 1-Butyl-1-Methylpyrrolidinium Bis[(trifluoromethyl)sulfonyl]imide Ionic Liquid. *Journal of Physical Chemistry C* **2020**, *124* (1), 693-700. DOI: 10.1021/acs.jpcc.9b09871.

(49) Figueiredo, M. C.; Ledezma-Yanez, I.; Koper, M. T. M. In Situ Spectroscopic Study of CO_2 Electroreduction at Copper Electrodes in Acetonitrile. *ACS Catalysis* **2016**, *6* (4), 2382-2392. DOI: 10.1021/acscatal.5b02543.

(50) Peterson, A. A.; Nørskov, J. K. Activity Descriptors for CO_2 Electroreduction to Methane on Transition-Metal Catalysts. *Journal of Physical Chemistry Letters* **2012**, *3* (2), 251-258. DOI: 10.1021/jz201461p.

(51) Liu, Q. B.; van Rantwijk, F.; Sheldon, R. A. Synthesis and Application of Dicationic Ionic Liquids. *Journal of Chemical Technology and Biotechnology* **2006**, *81* (3), 401-405. DOI: 10.1002/jctb.1411.

(52) Anderson, J. L.; Ding, R. F.; Ellern, A.; Armstrong, D. W. Structure and properties of high stability geminal dicationic ionic liquids. *Journal of the American Chemical Society* **2005**, *127* (2), 593-604. DOI: 10.1021/ja046521u.

(53) Pavlishchuk, V. V.; Addison, A. W. Conversion constants for redox potentials measured versus different reference electrodes in acetonitrile solutions at 25°C. *Inorganica Chimica Acta* **1999**, *298* (1), 97-102. DOI: 10.1016/S0020-1693(99)00407-7.

(54) Chae, K. J.; Choi, M.; Ajayi, F. F.; Park, W.; Chang, I. S.; Kim, I. S. Mass Transport through a Proton Exchange Membrane (Nafion) in Microbial Fuel Cells. *Energy Fuels* **2008**, *22* (1), 169-176. DOI: 10.1021/ef700308u.

(55) Sheng, H.; Hermes, E. D.; Yang, X.; Ying, D.; Janes, A. N.; Li, W.; Schmidt, J. R.; Jin, S. Electrocatalytic Production of H_2O_2 by Selective Oxygen Reduction Using Earth-Abundant Cobalt Pyrite (CoS_2). *ACS Catalysis* **2019**, *9*, 8433-8442. DOI: 10.1021/acscatal.9b02546.

(56) dos Santos, D. P.; Temperini, M. L. A.; Brolo, A. G. Mapping the Energy Distribution of SERRS Hot Spots from Anti-Stokes to Stokes Intensity Ratios. *Journal of the American Chemical Society* **2012**, *134* (32), 13492-13500. DOI: 10.1021/ja305580t.

(57) Rosen, B. A.; Haan, J. L.; Mukherjee, P.; Braunschweig, B.; Zhu, W.; Salehi-Khojin, A.; Dlott, D. D.; Masel, R. I. In Situ Spectroscopic Examination of a Low Overpotential Pathway for Carbon Dioxide Conversion to Carbon Monoxide. *Journal of Physical Chemistry C* **2012**, *116* (29), 15307-15312. DOI: 10.1021/jp210542v.

(58) Motobayashi, K.; Maeno, Y.; Ikeda, K. In Situ Spectroscopic Characterization of an Intermediate of CO_2 Electroreduction on a Au Electrode in Room-Temperature Ionic Liquids. *Journal of Physical Chemistry C* **2022**, *126* (29), 11981-11986. DOI: 10.1021/acs.jpcc.2c03012.

(59) Smith, A. M.; Lee, A. A.; Perkin, S. The Electrostatic Screening Length in Concentrated Electrolytes Increases with Concentration. *Journal of Physical Chemistry Letters* **2016**, *7* (12), 2157-2163. DOI: 10.1021/acs.jpclett.6b00867.

(60) Marcandalli, G.; Monteiro, M. C. O.; Goyal, A.; Koper, M. T. M. Electrolyte Effects on CO_2 Electrochemical Reduction to CO. *Accounts of Chemical Research* **2022**, *55* (14), 1900-1911. DOI: 10.1021/acs.accounts.2c00080.

(61) Sassenburg, M.; Kelly, M.; Subramanian, S.; Smith, W. A.; Burdyny, T. Zero-Gap Electrochemical CO_2 Reduction Cells: Challenges and Operational Strategies for Prevention of Salt Precipitation. *ACS Energy Letters* **2023**, *8* (1), 321-331. DOI: 10.1021/acsenergylett.2c01885.

(62) Kash, B. C.; Gomes, R. J.; Amanchukwu, C. V. Mitigating Electrode Inactivation during CO_2 Electrocatalysis in Aprotic Solvents with Alkali Cations. *Journal of Physical Chemistry Letters* **2023**, *14* (4), 920-926. DOI: 10.1021/acs.jpclett.2c03498.

(63) Qin, X.; Vegge, T.; Hansen, H. A. Cation-Coordinated Inner-Sphere CO_2 Electroreduction at Au-Water Interfaces. *Journal of the American Chemical Society* **2023**, *145* (3), 1897-1905. DOI: 10.1021/jacs.2c11643.

(64) Chu, A. T.; Surendranath, Y. Aprotic Solvent Exposes an Altered Mechanism for Copper-Catalyzed Ethylene Electrosynthesis. *Journal of the American Chemical Society* **2022**, *144* (12), 5359-5365. DOI: 10.1021/jacs.1c12595.

(65) Ren, W.; Xu, A.; Chan, K.; Hu, X. A Cation Concentration Gradient Approach to Tune the Selectivity and Activity of CO_2 Electroreduction. *Angewandtie Chemie International Edition* **2022**, *61* (49), e202214173. DOI: 10.1002/anie.202214173.

(66) Ma, Z.; Yang, Z.; Lai, W.; Wang, Q.; Qiao, Y.; Tao, H.; Lian, C.; Liu, M.; Ma, C.; Pan, A.; et al. CO_2 electroreduction to multicarbon products in strongly acidic electrolyte via synergistically modulating the local microenvironment. *Nature Communications* **2022**, *13* (1), 7596. DOI: 10.1038/s41467-022-35415-x.

(67) Moumene, T.; Belarbi, E. H.; Haddad, B.; Villemin, D.; Abbas, O.; Khelifa, B.; Bresson, S. Vibrational Spectroscopic Study of Imidazolium Dicationic Ionic Liquids: Effect of Cation Alkyl Chain Length. *Journal of Applied Spectroscopy* **2016**, *83* (2), 165-171. DOI: 10.1007/s10812-016-0264-7.

(68) Paschoal, V. H.; Faria, L. F. O.; Ribeiro, M. C. C. Vibrational Spectroscopy of Ionic Liquids. *Chemical Reviews* **2017**, *117* (10), 7053-7112. DOI: 10.1021/acs.chemrev.6b00461.

(69) Smith, A. M.; Lovelock, K. R. J.; Gosvami, N. N.; Licence, P.; Dolan, A.; Welton, T.; Perkin, S. Monolayer to Bilayer Structural Transition in Confined Pyrrolidinium-Based Ionic Liquids. *Journal of Physical Chemistry Letters* **2013**, *4* (3), 378-382. DOI: 10.1021/jz301965d.

(70) Baldelli, S. Surface Structure at the Ionic Liquid−Electrified Metal Interface. *Accounts of Chemical Research* **2008**, *41* (3), 421-431. DOI: 10.1021/ar700185h.

(71) Zhang, M.; Duan, S.; Luo, S.; Zhong, Y.; Yan, J.; Liu, G.; Mao, B.; Tian, Z. Structural Exploration of Multilayered Ionic Liquid/Ag Electrode Interfaces by Atomic Force Microscopy and Surface-Enhanced Raman Spectroscopy. *ChemElectroChem* **2020**, *7* (24), 4936-4942. DOI: 10.1002/celc.202001294.

(72) Santos, V. O., Jr.; Alves, M. B.; Carvalho, M. S.; Suarez, P. A.; Rubim, J. C. Surface-enhanced Raman scattering at the silver electrode/ionic liquid (BMIPF6) interface. *Journal of Physical Chemistry B* **2006**, *110* (41), 20379-20385. DOI: 10.1021/jp0643348.

(73) Kiefer, J.; Fries, J.; Leipertz, A. Experimental Vibrational Study of Imidazolium-Based Ionic Liquids: Raman and Infrared Spectra of 1-Ethyl-3-methylimidazolium Bis(Trifluoromethylsulfonyl)imide and 1-Ethyl-3-methylimidazolium Ethylsulfate. *Applied Spectroscopy* **2007**, *16* (12), 1306-1311. DOI: 10.1366/00037020778329200.

(74) Schrekker, H. S.; Gelesky, M. A.; Stracke, M. P.; Schrekker, C. M.; Machado, G.; Teixeira, S. R.; Rubim, J. C.; Dupont, J. Disclosure of the imidazolium cation coordination and stabilization mode in ionic liquid stabilized gold(0) nanoparticles. *Journal of Colloid and Interface Science* **2007**, *316* (1), 189-195. DOI: 10.1016/j.jcis.2007.08.018.

(75) Nanbu, N.; Kato, T.; Sasaki, Y.; Kitamura, F. *In Situ* SEIRAS Study of Room-Temperature Ionic Liquid | Gold Electrode Interphase. *Electrochemistry* **2005**, *73* (8), 610-613. DOI: 10.5796/electrochemistry.73.610.

(76) Tsori, Y.; Tournilhac, F.; Leibler, L. Demixing in simple fluids induced by electric field gradients. *Nature* **2004**, *430* (6999), 544-547. DOI: 10.1038/nature02758.

(77) Tsori, Y.; Leibler, L. Phase-separation in ion-containing mixtures in electric fields. *Proceedings of the National Academy of Science* **2007**, *104* (18), 7348-7350. DOI: 10.1073/pnas.0607746104.

(78) Lahiri, A.; Behrens, N.; Pulletikurthi, G.; Yochelis, A.; Kroke, E.; Cui, T.; Endres, F. Electrochemically induced phase separation and in situ formation of mesoporous structures in ionic liquid mixtures. *Science Advances* **2018**, *4* (10), eaau9663. DOI: 10.1126/sciadv.aau9663.

(79) De Yoreo, J. J.; Gilbert, P. U. P. A.; Sommerdijk, N. A. J. M.; Penn, R. L.; Whitelam, S.; Joester, D.; Zhang, H.; Rimer, J. D.; Navrotsky, A.; Banfield, J. F.; et al. Crystallization by particle attachment in synthetic, biogenic, and geologic environments. *Science* **2015**, *349* (6247), aaa6760. DOI: doi:10.1126/science.aaa6760.

(80) Resasco, J.; Chen, L. D.; Clark, E.; Tsai, C.; Hahn, C.; Jaramillo, T. F.; Chan, K.; Bell, A. T. Promoter Effects of Alkali Metal Cations on the Electrochemical Reduction of Carbon Dioxide. *Journal of the American Chemical Society* **2017**, *139* (32), 11277-11287. DOI: 10.1021/jacs.7b06765.

Chapter 5. Assessing the role of the C2 carbene in imidazolium-mediated ionic liquid using diamondoid substituents[3]

5.1. Introduction

As global anthropogenic carbon emissions continue to rise, the devastating effects of increased atmospheric CO_2 concentrations have led to a multitude of ongoing environmental and socioeconomic concerns. Electrocatalysis offers a promising avenue for mitigating carbon emissions by incentivizing the development of technologies that convert CO_2 into value-added chemicals using sustainable electricity.[1-3] Products such as CO, CH_4, methanol, and hydrocarbons can be directly used as chemical feedstock in existing chemical manufacturing infrastructure with the ultimate goal of directly producing hydrocarbon fuels as CO_2 electrocatalysis technologies mature.[4]

The reduction of CO_2 can be represented by a substantial reaction network, the first step of which is often the two-proton, two-electron reaction to convert CO_2 into CO, which requires the formation of an unstable negatively-charged radical $CO_2^{\bullet-}$ intermediate.[5, 6] From there, the CO can be used as a chemical feedstock for existing industrial reactions like the water-gas shift reaction or further electrochemically converted into more complex products. Therefore, understanding how to promote this reaction is significant for its relevance to fundamental science and technological advancement.

$$CO_2 + 2H^+ + 2e^- \rightarrow CO + H_2O \qquad \text{(Equation 5.1)}$$

Ionic liquids, a class of salts composed of an organic cation paired with an organic or inorganic anion,[7, 8] have been identified as promising electrolyte additives for promoting CO_2 reduction.[2, 9-11] Rosen and coworkers reported the first instance of ionic liquid-mediated CO_2 reduction using 1-ethyl-3-methyl-imidazolium tetrafluoroborate ([EMIm][BF_4]), showing that the addition of [EMIm][BF_4] lowers the onset

[3] Manuscript in preparation.; Supplemental information is presented in the Appendix.

potential of CO_2 reduction to CO.[2] Since then, imidazolium-based ionic liquids have stood out among other types of ionic liquids for their ability to efficiently mediate CO_2 reduction in a variety of systems.

The exact mechanism by which imidazolium cations facilitate CO_2 reduction, however, remains unclear. In their work, Rosen and colleagues hypothesized that the presence of the positively-charged $[EMIm]^+$ cations at the electrode-electrolyte interface stabilized the negatively-charged $CO_2^{\bullet-}$ intermediate.[2, 12] Others in the field have since suggested that the ability of the imidazolium cation to form a carbene at the C2 position, generating N-heterocyclic carbenes, imparted a unique reactivity to the imidazolium class of ionic liquids through the formation of an imidazolium-CO_2 adduct.[13, 14] Methylating the C2 position and blocking carbene formation, however, unexpectedly enhanced reactivity, which led some to suggest that C4 and C5 hydrogen bonding acted as the primary method of stabilization of the $CO_2^{\bullet-}$ intermediate and that the imidazolium-CO_2 adduct was instead an undesirable byproduct.[15]

Previous work from our group has shown that the methylated imidazolium ionic liquid is not a practical electrolyte additive due to the formation of surface-blocking (bi)carbonate precipitates under CO_2 electrolysis conditions.[16] Additionally, the ability of the C2 position of the imidazolium cation to bind (bi)carbonate species preserves strong local electric fields and mitigates deleterious (bi)carbonate precipitate formation.[17] Further, C2-site methylation greatly affects the interfacial behavior of the imidazolium cation, as computational studies have shown significant structural differences between methylated and unmethylated imidazoliums.[18] In this light, these alternative impacts of imidazolium cations at the electrochemical interface are negated upon methylating the C2 position. Hence in this work, we sought to investigate the role of the C2 position by modifying the N1 and N3 substituents as a way to stabilize the N-heterocyclic carbene.

N-heterocyclic carbenes have appeared frequently in other fields due to their reactivity and role in many synthetic pathways.[19-21] First introduced in the late 19th and early 20th centuries,[22-24] carbenes have been introduced as catalysts or ligands in fields ranging from organometallics to biology. For much of the 20th century, however, carbenes were too reactive to isolate and hence characterization remained difficult.

The first persistent carbene was synthesized in 1991 by Arduengo and coworkers, in which the C2 position of an imidazolium cation with bulky adamantyl groups on the N1 and N3 atoms of the ring structure was chemically deprotonated, leading to the formation of a persistent carbene that was stable enough to be isolated.[25] The use of bulky, sterically-blocking substituent groups to stabilize carbenes in catalysis has since become a frequent theme in homogeneous catalysis, where the carbenes are used as ligands in organometallic complexes for various chemical reactions.[26] By themselves, N-heterocyclic carbenes have been used as catalysts for transesterification reactions and polymerization.[27]

In this work, we sought to directly evaluate the role of the C2 carbene by drawing inspiration from the field of persistent carbenes by tethering bulky and molecularly rigid substituents to imidazolium cations to stabilize the C2 carbene. We chose to use diamondoid substituents, named so because the diamondoid groups represent the smallest building block of diamond, due to their bulky and modular nature.[28-30] Gorodetsky and coworkers have previously shown that N-heterocyclic carbenes can be electrochemically generated by applying reductive potentials[31] and work by Feroci et al demonstrated their stability in a variety of solvents.[32] We therefore sought to study the electrochemical generation of carbenes and their role in imidazolium-mediated CO_2 electroreduction.

We hypothesized that diamondoid-substituted imidazoliums, with their sterically-blocking substituents, would more readily stabilize the C2 carbene and block unwanted side reactions, such as the dimerization of two N-heterocyclic carbenes or decomposition of solvent molecules. Diamondoid groups offer further advantages, as they are hydrophobic in nature[33, 34] and are more surface active due to the lower entropic penalty for confinement at electrochemical interfaces.[35] We predicted that ionic liquids with diamondoid substituents would form more selective electric double layers, as the formation of a compact and hydrophobic double layer would promote CO_2 electroreduction.

To study this, we conducted electrochemical and kinetic studies of three diamondoid-substituted ionic liquids: 1-adamantyl-3-methylimidazolium bis(trifluoromethanesulfonyl)imide ([AdMIm][TFSI]), 1-diamantyl-3-methylimidazolium bis(trifluoromethanesulfonyl)imide ([DiamMIm][TFSI]), and 1-(3,5-

dimethyladamantyl)-3-methylimidazolium bis(trifluoromethanesulfonyl)imide ([Me_2AdMIm][TFSI]). Although we ideally would have studied the bis-substituted ionic liquid used in the Arduengo work, we found that solubility limitations in acetonitrile could not be overcome. However, the diamondoid ionic liquids that we examine in this work offer unique insights into how asymmetry affects carbene formation and CO_2 electroreduction. Finally, we used 1-decyl-3-methylimidazolium bis(trifluoromethanesulfonyl)imide ([C_{10}MIm][TFSI]) to study the effects of molecular rigidity and hydrophobicity, as well as a more common ionic liquid, 1-butyl-3-methylimidazolium bis(trifluoromethanesulfonyl)imide ([BMIm][TFSI]) as a benchmark.

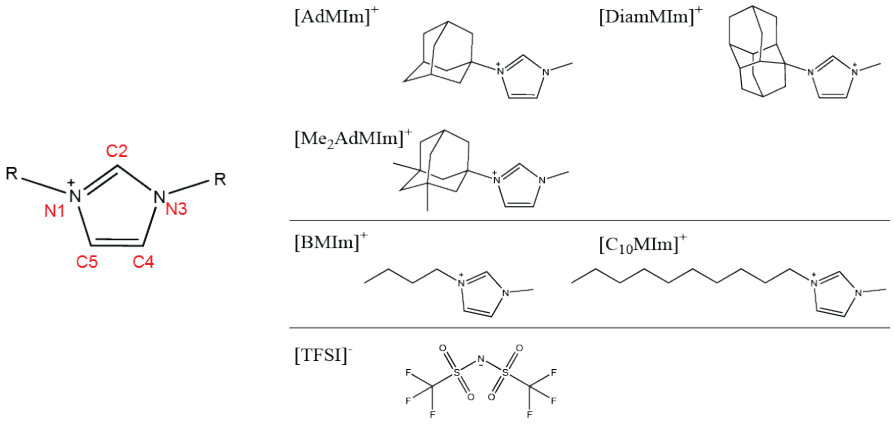

Figure 5.1 Chemical structures of the (top) diamondoid-substituted cations, the (middle) alkyl-substituted cations, and (bottom) the anion used in this work.

Contrary to our hypothesis, however, our results indicate the diamondoid ionic liquids perform worse than [C_{10}MIm][TFSI] and [BMIm][TFSI] in terms of both short term and steady-state electrolysis. Kinetic studies show the presence of higher order effects in the diamondoid ionic liquids, likely due to the steric hindrance of the diamondoid groups. Combined with chemical deprotonation studies, we conclude that the diamondoid groups provide an additional barrier to carbene formation. This is likely due to a combination of steric effects and the electronic stabilization of the C2 site, as the negative electron affinity of the diamondoid groups[28, 36] causes the diamondoids to act as electron donating moieties to the aromatic imidazolium ring. The diminished ability of the diamondoid-substituted ionic liquids to form carbenes

therefore leads to later onset potentials and poor faradaic efficiencies for CO. Hence, our work suggests that the C2 carbene may still be beneficial for CO_2 electroreduction, as preventing carbene formation yields decreased overall performance for the reaction.

5.2. Materials and Methods

Chemicals. 1-Butyl-3-methylimidazolium bis(trifluoromethanesulfonyl)imide ([BMIm][TFSI], >98% purity, Iolitec) and 1-decyl-3-methylimidazolium bis(trifluoromethanesulfonyl)imide ([BMIm][TFSI], >98% purity, Iolitec) were used as purchased. The water content of HPLC grade acetonitrile used for the electrolytes (>99.9%, Sigma-Aldrich) was adjusted to 900-1000 ppm using Karl Fischer titration to ensure that protons derived from water were available for the reaction.

The bromide versions of the diamondoid ionic liquids were synthesized by the Schreiner group at Justus Liebig University Giessen. Anion metathesis was used to substitute the bromide anion with a bis(trifluoromethanesulfonyl)imide anion. The ionic liquids and LiTFSI (>98%, TCI) were added to a round bottom flask in a 1:2 molar ratio and fully dissolved in Milli-Q water. The mixture was stirred at room temperature for 3 hours, during which the $[TFSI]^-$-substituted diamondoid ionic liquids precipitated out of the aqueous phase. The aqueous layer was decanted and the resulting ionic liquid was washed with Milli-Q water. After several washes, the decanted aqueous phase was tested with the silver nitrate halide test to confirm the removal of halides.

Ag-NHC complexes were synthesized according to prior literature.[37] Briefly, Ag_2O was synthesized by dissolving $AgNO_3$ (0.0425 mol, 7.2110 g) in 20 mL Milli-Q water in an Erlenmeyer flask. Once fully dissolved, NaOH (0.0425 mol, 1.700 g) was added to the Erlenmeyer flask under constant stirring. The solution was stirred at room temperature for 3 hours, during which Ag_2O particles precipitated out of solution. The Ag_2O was filtered out and washed with water. The Ag_2O was then dried *in vacuo* at 80°C for 24 hours.

The ionic liquid (10 mmol) was added to a small round bottom flask and dissolved in HPLC grade CH_2Cl_2 (>99.8%, Sigma-Aldrich) under stirring.[38] Once fully dissolved, Ag_2O (6.25 mmol) was added to the flask. Then, KOH (25 mmol) was dissolved in Milli-Q water and added drop-wise to the round bottom flask. The solution was stirred at room temperature for 24 hours, during which the Ag-NHC complex formed in the CH_2Cl_2 layer. The aqueous layer was decanted and washed with CH_2Cl_2. The resulting CH_2Cl_2 layer was collected and combined with the CH_2Cl_2 layer containing the Ag-NHC complex. The solids were then separated by vacuum filtration and dried using a rotary evaporator (BUCHI R-300M Rotavapor) followed by drying for 3 days *in vacuo* at 40°C.

Electrochemical Studies. A BioLogic VSP potentiostat was used for all electrochemical measurements. The working electrodes in these experiments were 3 mm polycrystalline Ag electrode (geometric surface area of 0.071 cm^2) (BASi) polished to a mirror finish using 15 μm, 3 μm, and 1 μm diamond polish followed by 0.05 um alumina (BASi) before ultrasonication in Milli-Q water. The reference electrode was a Ag/Ag^+ non-aqueous reference electrode containing 0.01 M $AgNO_3$ and 0.1 M tetrabutylammonium tetrafluoroborate ([TBA][BF_4])[39] in acetonitrile and the counter electrode was a polished and coiled platinum wire.

All electrolytes were purged with either Ar or CO_2 (Airgas) prior to electrochemical measurements. Cyclic voltammetry (CV) measurements were conducted in one-compartment borosilicate vials with a 3D-printed cap to ensure consistent electrode placement. All presented CV data were collected at a scan rate of 100 mV/s and are presented in their raw form. Chronoamperometry (CA) and chronopotentiometry (CP) studies were conducted in custom two-compartment H-cells, in which the catholyte and anolyte were separated using a Nafion 117 membrane. The catholyte chamber contained the electrolyte of choice while the anolyte chamber contained 125 mM [TBA][BF_4]. The Nafion 117 membranes were activated according to previously established protocols and stored in solutions of 0.1 M [TBA][BF_4] when not in use.[40, 41] The cells were continuously stirred with Teflon stir bars (VWR) throughout CA and CP experiments.

Product Analysis. The outlet gas during CA and CP experiments was fed into a gas chromatograph (Multiple Gas Analyzer #5, SRI Instruments) equipped with a flame-ionization detector (FID) coupled with a methanizer and a thermal conductivity detector (TCD). The gas chromatograph columns were a HayeSep D and Molesieve 5A column (Restek) leading to the FID while a HayeSep D column led to the TCD. The carrier gas was ultrahigh purity grade Ar (Airgas). Reported steady-state results and standard deviations were calculated by averaging current densities and faradaic efficiencies after 8 minutes of applying the potential.

NMR spectroscopy using a BBFO probe (400 MHz, Bruker Avance) was used to identify the products in the catholyte and to assess the stability of the electrolyte. Since there is the possibility of H-D exchange in deuterated solvents interfering with the detection of the C2 proton, 0.4 mL of the sample of interest was first introduced into the NMR tubes without the addition of deuterated solvent. A capillary tube containing 0.3 mL of deuterated solvent was then added to the NMR tube for the analysis.

Kinetic Studies. Tafel and reaction order studies were conducted using CA or CP techniques and each data point was collected with a different sample.

For Tafel analysis, CV experiments were initially used to assess the current density and potential range of interest. CP experiments of 20 minutes were used to maintain steady current densities and the resulting potentials were averaged for each point. Faradaic efficiencies were used to calculate the partial current density to CO, which was used as the current density value for Tafel experiments.

For reaction order studies, CA experiments were used to hold a potential of -2.5 V vs. Ag/Ag^{+} for 20 minutes. The partial pressure of CO_2 was varied by mixing CO_2 with Ar in different ratios using mass flow controllers (Cole Parmer) to maintain a total gas flow of 10 sccm. Faradaic efficiencies were used to calculate the partial current to CO, which was used in reaction order analysis.

5.3. Results and Discussion

5.3.1. Diamondoid Groups Impair CO_2 Electroreduction Rates

We began by evaluating the ability of the diamondoid ionic liquids to facilitate CO_2 electroreduction to CO using electrochemical methods. Polycrystalline Ag working electrodes were used due to the high selectivity for CO.

Under CO_2-sparged conditions, we found that on the whole, the diamondoid ionic liquids exhibited lower current densities and more cathodic onset potentials than the alkyl-substituted ionic liquids (Fig. 5.2), which suggests that the presence of the bulky diamondoid substituents kinetically hinder the electrochemical reaction and therefore a stronger driving force is required to facilitate the reaction. This same trend of delayed onset potentials for electrochemical processes is also reflected in Ar-sparged conditions (Fig. A3.1), where the reductive current is typically associated with the onset of solvent breakdown as well as the electrochemical deprotonation of the imidazolium cation. Notably, [DiamMIm][TFSI] exhibited significantly more cathodic onset potentials and lower current densities.

Although we initially hypothesized that the ionic liquids that could impart greater hydrophobicity to the electrochemical interface would favor CO_2 electroreduction, we did not observe a significant difference in either onset potential or steady state current density between [BMIm][TFSI] and the more hydrophobic [C_{10}MIm][TFSI]. It is when molecular rigidity is introduced that we observe noticeable differences between [C_{10}MIm][TFSI] and its diamondoid analogue, [AdMIm][TFSI], suggesting that it is the structure of the diamondoids rather than hydrophobicity that dictates the diminished performance.

The onset potential for electrochemical reactions is dependent on a variety of factors and is more broadly associated with the kinetics of an electrochemical reaction, as a larger overpotential indicates a higher activation energy barrier that must be overcome to achieve a desired reaction. The factors that govern onset potential include kinetic and thermodynamic barriers, both of which may play a role in the more cathodic onset potentials exhibited by the diamondoid ionic liquids, as the imidazolium cation has long

been thought to play an important role in facilitating the CO_2 electroreduction reaction by stabilizing the key intermediate, $CO_2^{\bullet-}$. Although the CVs do not show signs of significant mass transport limitations, in the case of the diamondoid-substituted imidazolium, the relative bulk of the substituents may hinder not just CO_2 transport to the interface, but also the ability of the imidazolium to reorient at interfaces, which can affect both intermediate stabilization and carbene formation, ultimately convoluting the interpretation of the CV results. This is especially apparent when comparing the [C_{10}MIm][TFSI] results with [AdMIm][TFSI], as both the adamantyl and C_{10} groups consist of 10 carbons and hence the only difference is that the substituent is molecularly rigid in [AdMIm][TFSI].

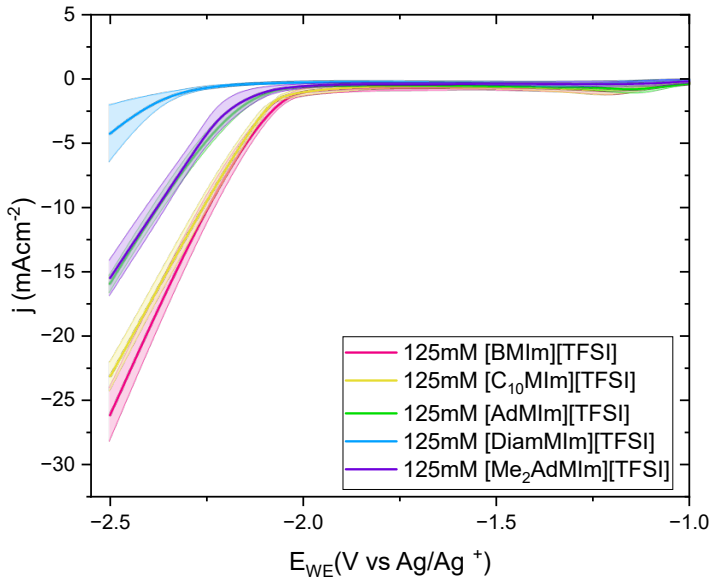

Figure 5.2 Cyclic voltammetry results show the difference between alkyl chain (pink, yellow) and diamondoid (green, blue, purple) substituents. The diamondoid ionic liquids all display later onset potentials and lower current densities for CO_2 electroreduction than both [C_{10}MIm][TFSI] and [BMIm][TFSI]. Each CV curve is the average of 2 cycles across three different samples. The shaded region represents the standard deviation for each of the curves.

Chronoamperometry studies also displayed a marked difference between the alkyl-substituted and diamondoid-substituted ionic liquids (Fig. 5.3). Both [BMIm][TFSI]- and [C_{10}MIm][TFSI]-containing electrolytes were able to maintain relatively stable current densities and faradaic efficiencies for CO of

about 80%. In diamondoid ionic liquids, these faradaic efficiencies for CO were generally lower than 80% and current densities over one hour of electrolysis were consistently 5 $mAcm^{-2}$ lower than the alkyl-substituted ionic liquids. Of note is the case of the [DiamMIm][TFSI] electrolytes, which demonstrated both larger current density deviations in CV experiments and much lower current densities in CA experiments. The cause for such deviations was the formation of electrochemically-driven phase separation in both Ar- and CO_2-sparged [DIamMIm][TFSI] electrolytes (Fig. A3.2). Under CO_2, this phase separation is likely due to the formation of (bi)carbonate salts while the formation of solid precipitates in Ar-sparged conditions appears to be a form of potential-induced phase separation, which has been previously demonstrated to be possible in complex electrolytes.[42-44]

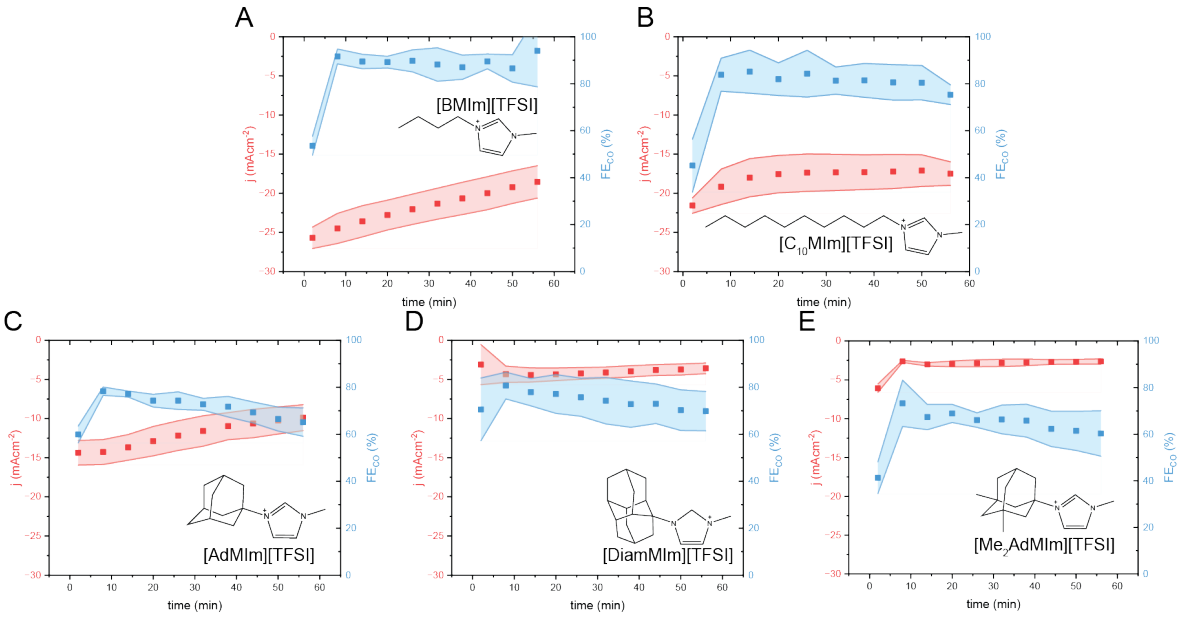

Figure 5.3 Chronoamperometry data over the course of 1 hour of electrolysis at -2.5 V vs. Ag/Ag^+. Compared to (A) [BMIm][TFSI] and (B) [C_{10}MIm][TFSI], the (C-E) diamondoid ionic liquids perform worse both in terms of steady state current density and faradaic efficiency. This is likely due to the bulky nature of the diamondoid substituents, which lack the molecular flexibility of the alkyl chains and can therefore impede imidazolium cation reorientation at the interface. Data points represent the average values from three separate trials and the shaded regions represent standard deviations.

5.3.2. Reaction Kinetics are Hindered by Bulky Substituents

To further investigate the impact of the rigid diamondoid substituents, we conducted Tafel analysis on the different ionic liquid electrolytes to understand whether different reaction mechanisms are the main cause for the disparity in onset potentials and reaction rates.

Briefly, Tafel experiments provide insight into the possible mechanisms of an electrochemical reaction and entails plotting the applied potential versus the partial current density for a desired product on a logarithmic scale.[45, 46] The Tafel slope can then be extracted from the linear region of the graph and denotes how much more potential must be applied to the system to cause a logarithmic increase in partial current density. Possible reaction steps can therefore be ruled out or confirmed as the rate-limiting step by comparing experimental Tafel slopes with the hypothetical Tafel slope for each possible rate-limiting step.

In practical applications, Tafel analysis is not so straightforward. Extra care must be made to ensure that the current density used in Tafel graphs are partial current densities for the desired product, CO, as the presence of other reduction products and competition with the hydrogen evolution reaction can also contribute to the total current density. Furthermore, although the CO_2 reduction reaction to CO is a two-electron process, there are many more possible reaction pathways dictating the transfer of each electron and the overall reaction sequence cannot be as neatly described as with HER. Hence, deciphering the complete reaction mechanism remains a challenge[47, 48] even with the aid of computational methods,[49] as a single Tafel slope could correspond with several different rate-determining steps, and different steps before or after the rate-determining step could also lead to the same Tafel slope.

In CO_2 electrocatalysis literature, it is typical to assume a Butler-Volmer-type relationship between potential and current density, with a symmetry factor of 0.5.[49] In these cases, “cardinal” Tafel slopes of 120, 60, and 40 mV/dec can be derived by considering the total number of electrons transferred prior to the rate-determining step and how many electrons are transferred during the rate-determining step. Oftentimes, experimentally-determined Tafel slopes fall somewhere within the range of these possible Tafel slopes and it is common to attribute these middling Tafel slopes to a combination of the mechanisms described by the

cardinal Tafel slopes. This analysis must be done carefully, as different interpretations of the Tafel slopes can ultimately lead to different reaction schemes. Although not prescriptive of a specific set of reaction sequences, Tafel analysis can still provide useful kinetic insight when combined with additional evaluation methods.

By conducting Tafel analysis on the electrolytes described in this work, we aimed to understand whether the difference in onset potentials and reaction rates was due to differences in reaction mechanisms (Fig. 5.4). Our results indicate a significant difference in Tafel slopes between the alkyl- and diamondoid-substituted imidazoliums. In fact, [BMIm][TFSI] and [C_{10}MIm][TFSI] exhibited Tafel slopes of 136 mV/dec and 92 mV/dec, respectively, which is often associated with the initial electron transfer step to form the $CO_2^{\bullet-}$ intermediate (120 mV/dec), or a mixture of the initial electron transfer and a chemical step (60 mV/dec). These conclusions are indeed aligned with the conventional understanding of CO_2 reduction.[50-52]

In diamondoid ionic liquid electrolytes, however, the measured Tafel slopes were all greater than 200 mV/dec, which does not fall in line with typical Tafel slopes and is often associated with mass transport limitations or higher-order electrolyte effects.[53, 54] We note that at the chosen electrolyte concentration of 125 mM, the CO_2 solubility is primarily dictated by the solubility of CO_2 in acetonitrile and is therefore most likely very similar across the different electrolytes we tested and hence it is unlikely the cause of the difference between alkyl-substituted ionic liquids and diamondoid-substituted ones. Moreover, neither the CV nor the CA results exhibited signs of mass transport limitations and the CA experiments took place under sparged and mixed conditions.

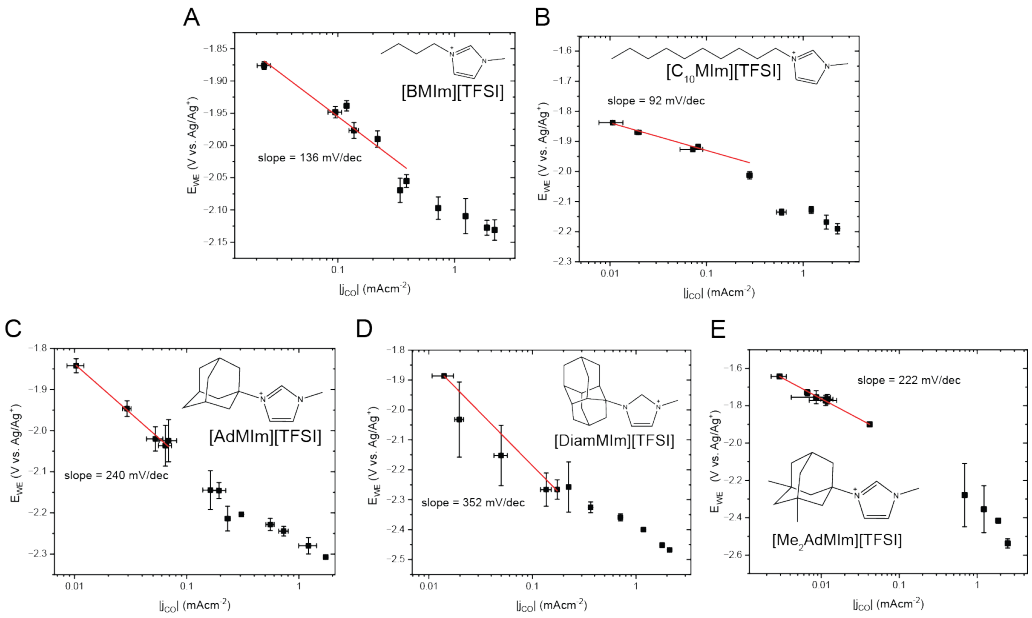

Figure 5.4 Tafel slope experiments comparing (A, B) alkyl-substituted and (C-E) diamondoid-substituted imidazolium ionic liquids. The Tafel slopes for CO_2 reduction to CO fall within the range of cardinal Tafel slope values in the alkyl-substituted ionic liquids, suggesting that the rate-determining step in these systems is the 1-electron transfer step to form $CO_2^{\bullet-}$ or a mixture of the 1-electron transfer step with a chemical step. Tafel slopes for the diamondoid ionic liquids, however, all remain greater than 200, which indicates that the reaction mechanism is subject to higher-order influences and cannot be simply described by a single rate-limiting electron transfer step. Data points represent one trial, during which the current density, working electrode potential, and faradaic efficiencies over the course of 8-20 minutes of electrolysis are obtained and averaged.

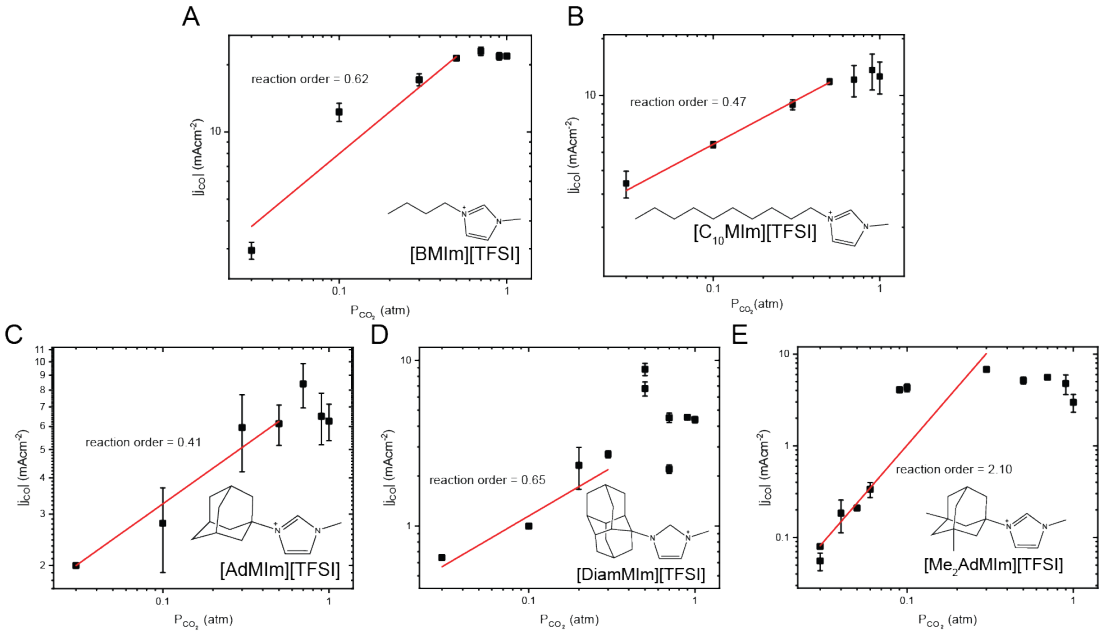

Figure 5.5 Reaction order studies for (A, B) alkyl-substituted and (C-E) diamondoid-substituted ionic liquid electrolytes. Under varying CO_2 partial pressures, alkyl-substituted ionic liquid electrolytes exhibit a reaction order <1. Among the diamondoid-substituted ionic liquids, the reactions orders for [AdMIm][TFSI] and [DiamMIm][TFSI] were similar to those of [BMIm][TFSI] and [C_{10}MIm][TFSI], suggesting that the concentration of CO_2 does not play a defining role in dictating reaction rates. For [Me_2AdMIm][TFSI], however, the reaction order is approximately 2, suggesting a strong relationship between CO_2 concentration and overall reaction rates until a partial pressure of 0.3 atm is reached. Data points represent one trial, during which the current density and faradaic efficiencies over the course of 8-20 minutes of electrolysis is obtained and averaged.

To investigate this further, we conducted reaction order experiments to study the relationship between CO_2 concentration and current densities (Fig. 5.5). We found that, with the exception of [Me_2AdMIm][TFSI], the reaction orders for both the alkyl- and diamondoid-substituted ionic liquids were <1, which agrees with prior literature.[55-57] In the case of [Me_2AdMIm][TFSI], the experimentally determined reaction order of 2.1 suggests a more complicated relationship between partial current densities for CO and bulk CO_2 concentration.

A fractional reaction order suggests a possible mixture of reaction mechanisms, as previous work by others in the field have identified reaction orders between 0 and 1 with respect to CO_2 partial pressure.[57] Work by the Surendranath group attributed a reaction order of 1 to a single electron transfer step to CO_2

rate-determining step.[55] In ionic liquids, it is common to observe reaction orders closer to 0, which is attributed to the reordering of the imidazolium cations at the interface in order to stabilize the $CO_2^{\bullet-}$ intermediate.[57] It is likely that both reaction mechanisms are at play in electrolytes containing [BMIm][TFSI], [C_{10}MIm][TFSI], [AdMIm][TFSI], and [DiamMIm][TFSI], which indicates that the imidazolium cation overall plays the same role in these systems. The case of the high reaction order in [Me_2AdMIm][TFSI] may indicate a less significant role for the imidazolium ring, but further investigation would be required to determine the difference imparted by the methylation of the adamantyl group.

Reaction order studies show a similar mechanism facilitated by the imidazolium cations through intermediate stabilization while the larger Tafel slopes suggest that the ionic liquid restructuring process needed to stabilize the intermediate may be affected by the substituents and hence contribute to the higher-order electrolyte effects. Taken together, Tafel and reaction order studies appear to implicate higher-order electrolyte effects that likely arise from the nature of the substituents, which could hinder the ability of the diamondoid imidazoliums to stabilize the $CO_2^{\bullet-}$ intermediate, thus leading to more cathodic onset potentials and larger Tafel slopes.

5.3.3. Diamondoid Substituents Prevent Carbene Formation

Given that the presence of the diamondoid groups could affect carbene formation and hence adduct formation, we then sought to assess carbene formation through chemical deprotonation. Electrochemical carbene formation and subsequent imidazolium-CO_2 adduct formation have been reported previously in literature.[31, 32] However, due to the instability of the N-heterocyclic carbene, it is very difficult to isolate and identify the carbene after -electrolysis. Hence, identification of the N-heterocyclic carbene often comes through indirect means by identifying other byproducts such as dimerization products or imidazolium-CO_2 adducts. We sought to understand whether the diamondoid groups affected electrochemical generation of carbenes through steric effects or whether the carbene generation was prohibited through chemical means as well.

Our NMR experiments post-electrolysis showed imidazolium-CO_2 adduct formation in the alkyl-substituted ionic liquids but not in diamondoid-substituted ones (Fig. A3.3-A3.8), which suggests that the diamondoid substituents either limits carbene formation or limits adduct formation. We therefore turned to chemical deprotonation to assess carbene formation in these ionic liquids. Due to the fleeting nature of the carbene, we chose to use Ag^+ ions as trapping agents as described in previous literature,[38] which bind to the carbenes to form Ag-NHC complexes and prevent unwanted side reactions caused by the reactive carbene. For ^{1}H-NMR experiments, the disappearance of the C2-H signal therefore signifies complex formation while a slight diminishing of the C2-H signal accompanied by peak splitting of the C4,5-H and substituent protons demonstrates partial deprotonation.[58]

We found that full deprotonation is readily achieved with the alkyl-substituted ionic liquids, as NMR experiments show the complete disappearance of the C2-H signal while the other proton signals remained largely unaffected (Fig. 5.6). The same preparation methods, however, yielded partial adduct formation in the diamondoid-substituted imidazoliums as evidenced by the peak splitting of the signals associated with the protons on the imidazolium ring and on the substituents (Fig. 5.7). Of the diamondoid-substituted ionic liquids, [Me_2AdMIm][TFSI] showed the largest decrease in the C2-H proton signal relative to the C4, C5 protons, indicating that in [Me_2AdMIm][TFSI], the carbene is more readily formed than in either [AdMIm][TFSI] or [DiamMIm][TFSI].

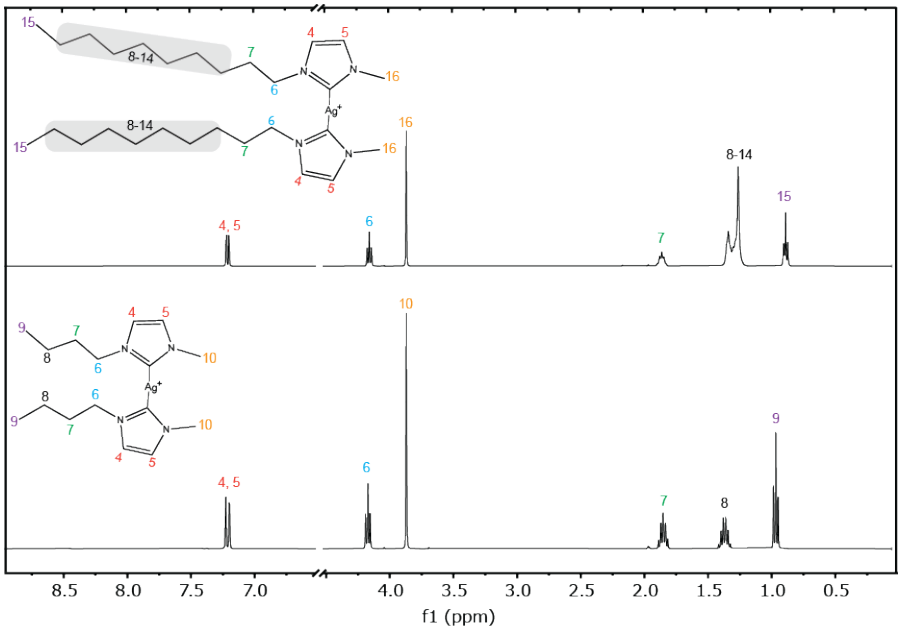

Figure 5.6 ^{1}H-NMR spectra of chemically deprotonated alkyl-substituted imidazolium cations, which form complexes with Ag^{+}. For both (top) [C_{10}MIm][TFSI] and (bottom) [BMIm][TFSI], the signal associated with the C2-H disappears, indicating full deprotonation and subsequent complex formation.

Evidence of only partial adduct formation suggests that the deprotonation does occur but that the diamondoid substituents may serve to hinder carbene formation. Diamondoid groups are also known to have negative electron affinity and can serve as electron donating groups to the aromatic imidazolium ring structure. The enhanced electron donating ability of the diamondoid can be observed using ^{13}C NMR, as electron donating groups would cause subtle upfield shifts of the C2 position carbon atom, indicating more shielding. This is indeed what we observe, as the C2 peaks in the diamondoid ionic liquids appeared to be shifted upfield of the C2 carbon of [C_{10}MIm][TFSI] by 2.28, 1.47, and 2.21 ppm for [AdMIm][TFSI], [DiamMIm][TFSI], and [Me_2AdMIm][TFSI], respectively (Fig. A3.9, A3.10, Table A3.1). While steric effects cannot be discounted as a potential factor behind the limited carbene formation in diamondoid ionic liquids, this electron donating capability of the diamondoid groups to stabilize the C2 position is likely the primary cause behind the diminished carbene formation observed in the diamondoid ionic liquids, as steric effects would still allow for chemical deprotonation to occur. Hence, chemical deprotonation and NMR

experiments show that rather than facilitating the formation of and stabilizing the carbene, diamondoid substituents actually hinder deprotonation processes.

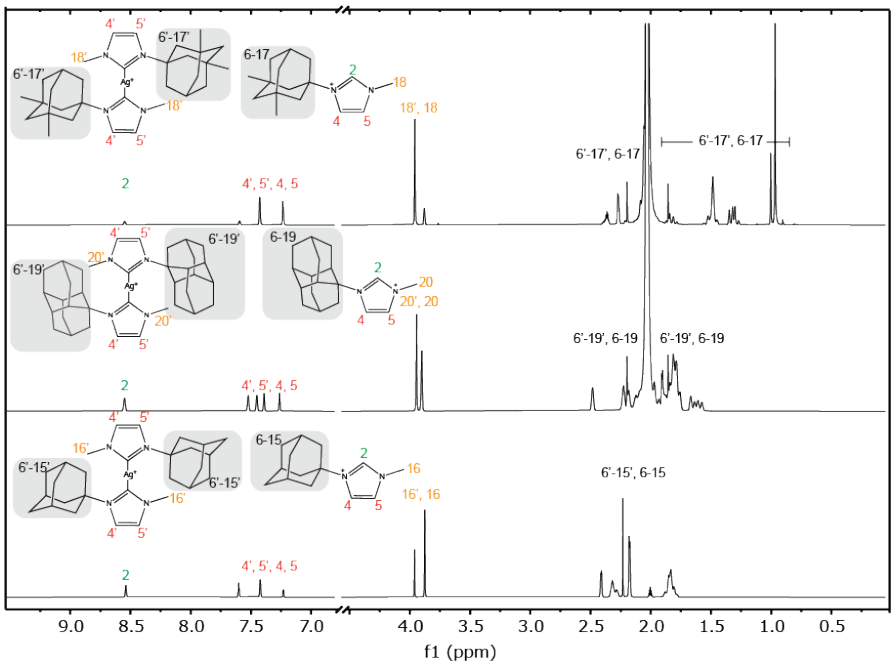

Figure 5.7 ^{1}H-NMR spectra showing partial deprotonation of diamondoid-substituted imidazolium cations, as evidenced by peak splitting on the C4 and C5 protons as well as the substituent protons. Among the diamondoids, (top) [Me_2AdMIm][TFSI] was more prone to deprotonation than (middle) [DiamMIm][TFSI] or (bottom) [AdMIm][TFSI], suggesting that steric hindrance hinders carbene and complex formation.

5.3.4. Carbene Formation Still Plays Valuable Role in Imidazolium-Mediated CO_2 Reduction

The role of the C2 carbene in imidazolium-mediated CO_2 electrocatalysis has long been discussed in the ionic liquids community.[9, 10] Although a popular motif in early mechanistic studies, more recent works have widened the possible mechanisms to include themes like hydrogen bonding,[15] hydrophobicity,[59] solvation,[60] and longer range interactions leading to electric double layer effects.[16] As a result, the C2 carbene has taken a backseat considering these multitude of other potential mechanisms.

Yet, it is undeniable that under electroreduction potentials, the 1 electron transfer to the imidazolium cation can lead to the formation of the carbene,[31] which would result in the consumption of imidazolium cations through imidazolium-CO_2 adduct formation. Introducing sterically blocking substituents like diamondoid moieties should in theory stabilize the C2 carbene and prevent unwanted side reactions like adduct formation or dimerization, but in reality greatly hinders CO_2 electroreduction. Our results show that the slow reaction kinetics manifest as more cathodic onset potentials as well as poor performance during steady state electrolysis.

The earlier onset potential in imidazolium-mediated CO_2 electroreduction is often attributed to the ability of the imidazolium to stabilize the $CO_2^{\bullet-}$ intermediate. In diamondoid-substituted ionic liquids, the later onset potential suggests an impaired ability to stabilize the intermediate. Within the crowded environment of the electric double layer, the added steric hindrance could prevent the reorientation of the imidazolium cation that would be needed to stabilize the intermediate either through C4 and C5 hydrogen bonding or through interactions with the C2 position.

Furthermore, the electron donating nature of the diamondoid groups also prevents carbene formation, as the increased electron density on the imidazolium ring stabilizes the positive charge and lowers the activity of the C2 proton. This is supported by NMR results of the neat ionic liquids, which demonstrated increased shielding of the C2-site of the imidazolium ring, suggesting that the diamondoid groups act as electron donating group and decreases the activity of the C2-site. This aligns well with computational studies, which have previously demonstrated a high C2-site pKa in imidazoliums with admantyl groups.[61] As a result, we observe decreased carbene formation in diamondoid-substituted ionic liquids through both electrochemical and chemical means.

The increased electron density around the imidazolium ring also has electrostatic implications for double layer formation, as a cation with higher electron density experiences weaker electrostatic attraction to a negatively-charged electrode surface. In electrochemical deprotonation, the combination of steric hindrance and weaker electrostatic interactions could mean that the imidazoliums cannot reach the

proximity required for the electron transfer to occur. The increased electron density would also have compounding effects, as it would also diminish the stabilizing interactions between the electron dense imidazolium cation and the negatively-charged $CO_2^{\bullet-}$ intermediate. In cases in which the proton is sourced from water, it is also less energetically favorable for the imidazolium to capture resulting $[OH]^-$ or (bi)carbonates to form a neutral zwitterion due to the lower activity of that C2 site. It is therefore important to consider whether the onset potential corresponds to strictly CO_2 reduction or whether it is also related to the formation of the carbene which stabilizes the intermediate, maintains local electric fields, and ultimately allows for the reaction to occur at lower onset potentials.

During steady state electrolysis, these problems are exacerbated by the crowded electric double layer, which can serve as an additional impediment to the movement of ions as well as CO_2 across the electrochemical interface. This is what ultimately leads to the large Tafel slopes exhibited in the diamondoid ionic liquids, which suggest higher order effects governing reaction mechanisms, as imidazolium reorientation and structure formation in response to applied potential stabilizes the intermediate. We found that the diamondoid groups prevent carbene formation by comparing NMR after electrolysis with chemically deprotonated imidazoliums using Ag^+ ions as trapping agents. Under the same electrolysis conditions, we therefore found that the diamondoid-substituted ionic liquids were unable to form the imidazolium-CO_2 adduct, which is a symptom of its diminished ability to form a carbene.

In sum, our experiments suggest that the C2 carbene may in fact play an important role in ionic liquid-mediated CO_2 reduction. When carbene formation is blocked using the diamondoid substituents, we found that overall performance greatly suffered. Therefore, the imidazolium-CO_2 adduct formation might be a byproduct of a necessary component of the reaction rather than a completely deleterious process. This outlook aligns with our recent work examining the role of the C2 carbene in modulating local electric fields, which found that the imidazolium-CO_2 adduct was formed when the proton donor for the reaction was the C2-H of the imidazolium and that the adduct acted as a neutral conjugate base that sustained the local electric field unlike interfacial $[OH]^-$, which was generated when water was the primary proton donor. Our

results suggest that additionally, the formation of the carbene itself may be necessary to lower onset potentials and maintain high faradaic efficiencies for CO production.

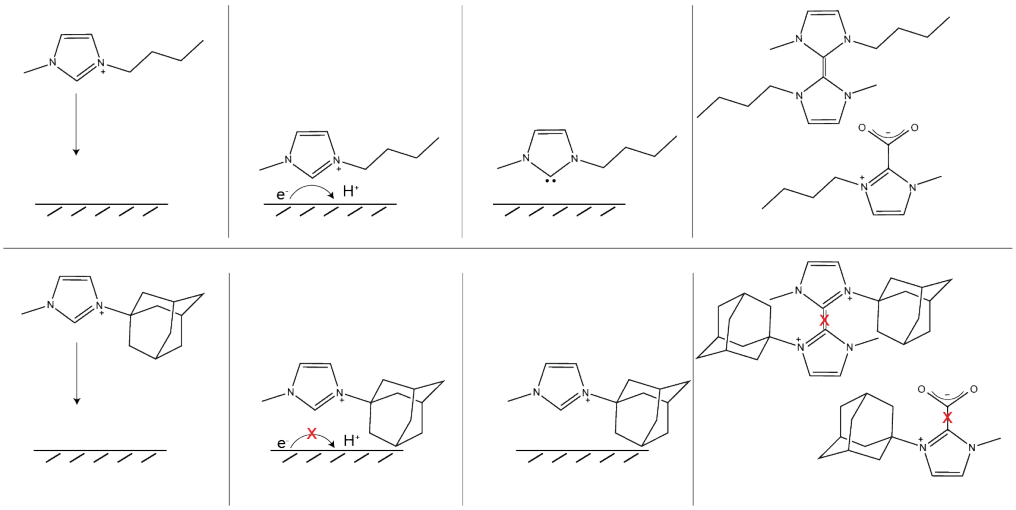

Figure 5.8 Diamondoid substituents prevent the formation of C2 carbenes. In (top) alkyl-substituted ionic liquids, the C2 carbene approaches the electrode surface. Subsequent electron transfer results in deprotonation, leaving a carbene at the C2 position of the imidazolium ring. The reactive nature of the carbene can lead to byproducts through dimerization or imidazolium-adduct formation. When one of the substituents is a (bottom) diamondoid group however, the bulky diamondoid prevents the approach of the imidazolium ring through steric hindrance, which ultimately means that dimerization and adduct formation do not occur either. Consequently, this also means that the $CO_2^{\bullet-}$ stabilization mechanism is hindered, as the imidazolium ring cannot reorient relative to the surface.

5.4. Conclusion

In this work, we investigated the role of the C2 carbene in facilitating CO_2 electroreduction by examining how the introduction of diamondoid substituents affects carbene formation under potentials relevant to electroreduction. Contrary to our initial hypothesis, our data demonstrates that the bulky diamondoid substituents inhibit electrochemical carbene formation, which negatively impacts CO_2 electroreduction rates and kinetics.

We find that the introduction of the diamondoid substituents caused a significant delay in CO_2 reduction onset potential. Current densities and selectivity during chronoamperometry studies were similarly affected, as the diamondoid-substituted ionic liquids consistently performed worse than alkyl-substituted ones. In particular, Tafel and reaction order analyses showed significant higher-order effects for the diamondoid-substituted ionic liquids but reaction mechanisms may not be greatly affected. As demonstrated by chemical deprotonation comparisons, the diamondoid substituents hinder carbene formation which, combined with the formation of a highly crowded and structured electric double layer under reactive conditions, inhibits CO_2 electroreduction. We attribute these differences to the negative electron affinity and hence electron donating capabilities of the diamondoid groups, which lower the activity of the C2-H and prevents carbene formation.

We find that the carbene indeed has an important role in imidazolium-mediated electrocatalysis, as preventing its formation leads to poor reaction kinetics and long-term performance. More broadly, we conclude that the diamondoid groups act as interesting electron donor species and allows us to modify electron density without necessarily tuning polarity. Although poor facilitators of CO_2 electrocatalysis, the use of diamondoid groups to protect the imidazolium ring from electrochemical reduction may open up new avenues for their use in applications such as energy storage, where electrolyte stability is of paramount importance. Hence our work emphasizes the importance of this C2 position and may reopen investigations into how the tuning carbene formation via substituents can yield new insights into the role of the imidazolium in electrocatalytic reactions.

5.5. References

(1) Seh, Z. W.; Kibsgaard, J.; Dickens, C. F.; Chorkendorff, I. B.; Nørskov, J. K.; Jaramillo, T. F. Combining Theory and Experiment in Electrocatalysis: Insights into Materials Design. *Science* **2017**, *355* (6321), 146. DOI: 10.1126/science.aad4998.

(2) Rosen, B. A.; Salehi-Khojin, A.; Thorson, M. R.; Zhu, W.; Whipple, D. T.; Kenis, P. J. A.; Masel, R. I. Ionic Liquid-Mediated Selective Conversion of CO_2 to CO at Low Overpotentials. *Science* **2011**, *334* (6056), 643-644. DOI: 10.1126/science.1209786.

(3) De Luna, P.; Hahn, C.; Higgins, D.; Jaffer, S. A.; Jaramillo, T. F.; Sargent, E. H. What Would it Take for Renewably Powered Electrosynthesis to Displace Petrochemical Processes? *Science* **2019**, *364* (6438), 350. DOI: 10.1126/science.aav3506.

(4) Shin, H.; Hansen, K. U.; Jiao, F. Techno-economic assessment of low-temperature carbon dioxide electrolysis. *Nature Sustainability* **2021**, *4* (10), 911-919. DOI: 10.1038/s41893-021-00739-x.

(5) Kortlever, R.; Shen, J.; Schouten, K. J. P.; Calle-Vallejo, F.; Koper, M. T. M. Catalysts and Reaction Pathways for the Electrochemical Reduction of Carbon Dioxide. *Journal of Physical Chemistry Letters* **2015**, *6* (20), 4073-4082. DOI: 10.1021/acs.jpclett.5b01559.

(6) Shin, S. J.; Choi, H.; Ringe, S.; Won, D. H.; Oh, H. S.; Kim, D. H.; Lee, T.; Nam, D. H.; Kim, H.; Choi, C. H. A unifying mechanism for cation effect modulating C1 and C2 productions from CO_2 electroreduction. *Nature Communications* **2022**, *13* (1). DOI: 10.1038/s41467-022-33199-8.

(7) Seddon, K. R. Ionic liquids for clean technology. *Journal of Chemical Technology and Biotechnology* **1997**, *68* (4), 351-356. DOI: Doi 10.1002/(Sici)1097-4660(199704)68:4<351::Aid-Jctb613>3.0.Co;2-4.

(8) Welton, T. Room-Temperature Ionic Liquids. Solvents for Synthesis and Catalysis. *Chemical Reviews* **1999**, *99* (8), 2071-2084. DOI: DOI 10.1021/cr980032t.

(9) Fortunati, A.; Risplendi, F.; Fiorentin, M. R.; Cicero, G.; Parisi, E.; Castellino, M.; Simone, E.; Iliev, B.; Schubert, T. J. S.; Russo, N.; et al. Understanding the role of imidazolium-based ionic liquids in the electrochemical CO_2 reduction reaction. *Communications Chemistry* **2023**, *6* (1). DOI: 10.1038/s42004-023-00875-9.

(10) Neyrizi, S.; Kiewiet, J.; Hempenius, M. A.; Mul, G. What It Takes for Imidazolium Cations to Promote Electrochemical Reduction of CO_2. *ACS Energy Letters* **2022**, *7* (10), 3439-3446. DOI: 10.1021/acsenergylett.2c01372.

(11) Golru, S. S.; Biddinger, E. J. Effect of anion in diluted imidazolium-based ionic liquid/buffer electrolytes for CO_2 electroreduction on copper. *Electrochimica Acta* **2020**, *361*. DOI: 10.1016/j.electacta.2020.136787.

(12) Rosen, B. A.; Haan, J. L.; Mukherjee, P.; Braunschweig, B.; Zhu, W.; Salehi-Khojin, A.; Dlott, D. D.; Masel, R. I. In Situ Spectroscopic Examination of a Low Overpotential Pathway for Carbon Dioxide Conversion to Carbon Monoxide. *Journal of Physical Chemistry C* **2012**, *116* (29), 15307-15312. DOI: 10.1021/jp210542v.

(13) Gu, L. Q.; Zhang, Y. G. Unexpected CO_2 Splitting Reactions To Form CO with N-Heterocyclic Carbenes as Organocatalysts and Aromatic Aldehydes as Oxygen Acceptors. *Journal of the American Chemical Society* **2010**, *132* (3), 914-915. DOI: 10.1021/ja909038t.

(14) Hollóczki, O.; Firaha, D. S.; Friedrich, J.; Brehm, M.; Cybik, R.; Wild, M.; Stark, A.; Kirchner, B. Carbene Formation in Ionic Liquids: Spontaneous, Induced, or Prohibited? *Journal of Physical Chemistry B* **2013**, *117* (19), 5898-5907. DOI: 10.1021/jp4004399.

(15) Motobayashi, K.; Maeno, Y.; Ikeda, K. In Situ Spectroscopic Characterization of an Intermediate of CO_2 Electroreduction on a Au Electrode in Room-Temperature Ionic Liquids. *Journal of Physical Chemistry C* **2022**. DOI: 10.1021/acs.jpcc.2c03012.

(16) Liu, B.; Guo, W.; Gebbie, M. A. Tuning Ionic Screening To Accelerate Electrochemical CO_2 Reduction in Ionic Liquid Electrolytes. *ACS Catalysis* **2022**. DOI: 10.1021/acscatal.2c021549706.

(17) Guo, W. X.; Liu, B. C.; Gebbie, M. A. Suppressing Co-Ion Generation Cationic Proton Donors to Amplify Driving Forces for Electrochemical CO_2 Reduction. *Journal of Physical Chemistry C* **2023**, *127* (29), 14243-14254. DOI: 10.1021/acs.jpcc.3c04004.

(18) Hunt, P. A. Why does a reduction in hydrogen bonding lead to an increase in viscosity for the 1-butyl-2,3-dimethyl-imidazolium-based ionic liquids? *Journal of Physical Chemistry B* **2007**, *111* (18), 4844-4853. DOI: 10.1021/jp067182p.

(19) Bellotti, P.; Koy, M.; Hopkinson, M. N.; Glorius, F. Recent advances in the chemistry and applications of N-heterocyclic carbenes. *Nature Reviews Chemistry* **2021**, *5* (10), 711-725. DOI: 10.1038/s41570-021-00321-1.

(20) Herrmann, W. A. N-heterocyclic carbenes: A new concept in organometallic catalysis. *Angewandte Chemie-International Edition* **2002**, *41* (8), 1290-1309. DOI: 10.1002/1521-3773.

(21) Enders, D.; Niemeier, O.; Henseler, A. Organocatalysis by N-heterocyclic carbenes. *Chemical Reviews* **2007**, *107* (12), 5606-5655. DOI: 10.1021/cr068372z.

(22) Staudinger, H.; Kupfer, O. On reactions of methylene. III. Diazomethane. *Berichte Der Deutschen Chemischen Gesellschaft* **1912**, *45*, 501-509. DOI: DOI 10.1002/cber.19120450174.

(23) Bourissou, D.; Guerret, O.; Gabbaï, F. P.; Bertrand, G. Stable carbenes. *Chemical Reviews* **2000**, *100* (1), 39-91. DOI: DOI 10.1021/cr940472u.

(24) Buchner, E.; Curtius, T. Ueber die Einwirkung von Diazoessigäther auf aromatische Kohlenwasserstoffe. *Berichte Der Deutschen Chemischen Gesellschaft* **1885**, *18* (2), 2377-2379. DOI: 10.1002/cber.188501802119.

(25) Arduengo, A. J.; Harlow, R. L.; Kline, M. A Stable Crystalline Carbene. *Journal of the American Chemical Society* **1991**, *113* (1), 361-363. DOI: DOI 10.1021/ja00001a054.

(26) Agnew-Francis, K. A.; Williams, C. M. Catalysts Containing the Adamantane Scaffold. *Advanced Synthesis & Catalysis* **2016**, *358* (5), 675-700. DOI: 10.1002/adsc.201500949.

(27) Korotkikh, N. I.; Saberov, V. S.; Glinyanaya, N. V.; Marichev, K. A.; Kiselyov, A. V.; Knishevitsky, A. V.; Rayenko, G. F.; Shvaika, O. P. Catalysis of Organic Reactions by Carbenes and Carbene Complexes. *Chemistry of Heterocyclic Compounds* **2013**, *49* (1), 19-38. DOI: 10.1007/s10593-013-1230-4.

(28) Schwertfeger, H.; Fokin, A. A.; Schreiner, P. R. Diamonds are a Chemist's Best Friend: Diamondoid Chemistry Beyond Adamantane. *Angewandte Chemie International Edition* **2008**, *47* (6), 1022-1036. DOI: 10.1002/anie.200701684

(29) Fort, R. C.; Schleyer, P. v. R. Adamantane: Consequences of the Diamondoid Structure. *Chemical Reviews* **1964**, *64* (3), 277-300. DOI: 10.1021/cr60229a004.

(30) Richter, H.; Schwertfeger, H.; Schreiner, P. R.; Fröhlich, R.; Glorius, F. Thieme Chemistry Journal Awardees - Where are They Now? Synthesis of Diamantane-Derived N-Heterocyclic Carbenes and Applications in Catalysis. *Synlett* **2009**, (2), 193-197. DOI: 10.1055/s-0028-1087676.

(31) Gorodetsky, B.; Ramnial, T.; Branda, N. R.; Clyburne, J. A. C. Electrochemical reduction of an imidazolium cation: a convenient preparation of imidazol-2-ylidenes and their observation in an ionic liquid. *Chemical Communications* **2004**, (17), 1972-1973. DOI: 10.1039/b407386j.

(32) Feroci, M.; Chiarotto, I.; D'Anna, F.; Forte, G.; Noto, R.; Inesi, A. Stability and organocatalytic efficiency of N-heterocyclic carbenes electrogenerated in organic solvents from imidazolium ionic liquids. *Electrochimica Acta* **2015**, *153*, 122-129. DOI: 10.1016/j.electacta.2014.11.135.

(33) Maciel, C.; Malaspina, T.; Fileti, E. E. Prediction of the Hydration Properties of Diamondoids from Free Energy and Potential of Mean Force Calculations. *Journal of Physical Chemistry B* **2012**, *116* (45), 13467-13471. DOI: 10.1021/jp3079474.

(34) Noh, H.; Myung, S.; Kim, M. J.; Yang, S. K. Stimuli-responsive supramolecular assemblies via self-assembly of adamantane-containing block copolymers. *Polymer* **2019**, *175*, 65-70. DOI: 10.1016/j.polymer.2019.05.011.

(35) King, E. M.; Gebbie, M. A.; Melosh, N. A. Impact of Rigidity on Molecular Self-Assembly. *Langmuir* **2019**, *35* (48), 16062-16069. DOI: 10.1021/acs.langmuir.9b01824.

(36) Sakai, Y.; Nguyen, G. D.; Capaz, R. B.; Coh, S.; Pechenezhskiy, I. V.; Hong, X. P.; Wang, F.; Crommie, M. F.; Saito, S.; Louie, S. G.; et al. Intermolecular interactions and substrate effects for an adamantane monolayer on a Au(111) surface. *Physical Review B* **2013**, *88* (23). DOI: 10.1103/PhysRevB.88.235407.

(37) Janssen, D. E.; Wilson, C. V. 4-Iodoveratrole. *Organic Syntheses* **1956**, *36* (46). DOI: 10.15227/orgsyn.036.0046.

(38) Hintermair, U.; Englert, U.; Leitner, W. Distinct Reactivity of Mono- and Bis-NHC Silver Complexes: Carbene Donors versus Carbene-Halide Exchange Reagents. *Organometallics* **2011**, *30* (14), 3726-3731. DOI: 10.1021/om101056y.

(39) Pavlishchuk, V. V.; Addison, A. W. Conversion constants for redox potentials measured versus different reference electrodes in acetonitrile solutions at 25°C. *Inorganica Chimica Acta* **2000**, *298* (1), 97-102. DOI: Doi 10.1016/S0020-1693(99)00407-7.

(40) Sheng, H.; Hermes, E. D.; Yang, X.; Ying, D.; Janes, A. N.; Li, W.; Schmidt, J. R.; Jin, S. Electrocatalytic Production of H_2O_2 by Selective Oxygen Reduction Using Earth-Abundant Cobalt Pyrite (CoS_2). *ACS Catalysis* **2019**, *9*, 8433-8442. DOI: 10.1021/acscatal.9b02546.

(41) Chae, K. J.; Choi, M.; Ajayi, F. F.; Park, W.; Chang, I. S.; Kim, I. S. Mass Transport through a Proton Exchange Membrane (Nafion) in Microbial Fuel Cells. *Energy Fuels* **2008**, *22* (1), 169-176. DOI: 10.1021/ef700308u.

(42) Lahiri, A.; Behrens, N.; Pulletikurthi, G.; Yochelis, A.; Kroke, E.; Cui, T.; Endres, F. Electrochemically induced phase separation and in situ formation of mesoporous structures in ionic liquid mixtures. *Science Advances* **2018**, *4* (10), eaau9663. DOI: 10.1126/sciadv.aau9663.

(43) Tsori, Y.; Leibler, L. Phase-separation in ion-containing mixtures in electric fields. *Proceedings of the National Academy of Science* **2007**, *104* (18), 7348-7350. DOI: 10.1073/pnas.0607746104.

(44) Tsori, Y.; Tournilhac, F.; Leibler, L. Demixing in simple fluids induced by electric field gradients. *Nature* **2004**, *430* (6999), 544-547. DOI: 10.1038/nature02758.

(45) Fletcher, S. Tafel slopes from first principles. *Journal of Solid State Electrochemistry* **2009**, *13* (4), 537-549. DOI: 10.1007/s10008-008-0670-8.

(46) Lee, C. W.; Cho, N. H.; Im, S. W.; Jee, M. S.; Hwang, Y. J.; Min, B. K.; Nam, K. T. New challenges of electrokinetic studies in investigating the reaction mechanism of electrochemical CO_2 reduction. *Journal of Materials Chemistry A* **2018**, *6* (29), 14043-14057. DOI: 10.1039/c8ta03480j.

(47) Watkins, N. B.; Schiffer, Z. J.; Lai, Y. C.; Musgrave, C. B.; Atwater, H. A.; Goddard, W. A.; Agapie, T.; Peters, J. C.; Gregoire, J. M. Hydrodynamics Change Tafel Slopes in Electrochemical CO_2 Reduction on Copper. *ACS Energy Letters* **2023**, *8* (5), 2185-2192. DOI: 10.1021/acsenergylett.3c00442.

(48) van der Heijden, O.; Park, S.; Vos, R. E.; Eggebeen, J. J. J.; Koper, M. T. M. Tafel Slope Plot as a Tool to Analyze Electrocatalytic Reactions. *ACS Energy Letters* **2024**, *9* (4), 1871-1879. DOI: 10.1021/acsenergylett.4c00266.

(49) Limaye, A. M.; Zeng, J. S.; Willard, A. P.; Manthiram, K. Bayesian data analysis reveals no preference for cardinal Tafel slopes in CO_2 reduction electrocatalysis. *Nature Communications* **2021**, *12* (1). DOI: 10.1038/s41467-021-20924-y.

(50) Li, T. F.; Yang, C.; Luo, J. L.; Zheng, G. F. Electrolyte Driven Highly Selective CO_2 Electroreduction at Low Overpotentials. *ACS Catalysis* **2019**, *9* (11), 10440-10447. DOI: 10.1021/acscatal.9b02443.

(51) Verma, S.; Hamasaki, Y.; Kim, C.; Huang, W. X.; Lu, S.; Jhong, H. R. M.; Gewirth, A. A.; Fujigaya, T.; Nakashima, N.; Kenis, P. J. A. Insights into the Low Overpotential Electroreduction of CO_2 to CO on a Supported Gold Catalyst in an Alkaline Flow Electrolyzer. *ACS Energy Letters* **2018**, *3* (1), 193-198. DOI: 10.1021/acsenergylett.7b01096.

(52) Zhan, T. R.; Kumar, A.; Sevilla, M.; Sridhar, A.; Zeng, X. Q. Temperature Effects on CO_2 Electroreduction Pathways in an Imidazolium-Based Ionic Liquid on Pt Electrode. *Journal of Physical Chemistry C* **2020**, *124* (48), 26094-26105. DOI: 10.1021/acs.jpcc.0c06065.

(53) Parada, W. A.; Vasilyev, D. V.; Mayrhofer, K. J. J.; Katsounaros, I. CO_2 Electroreduction on Silver Foams Modified by Ionic Liquids with Different Cation Side Chain Length. *ACS Applied Materials & Interfaces* **2022**, *14* (12), 14193-14201. DOI: 10.1021/acsami.1c24386.

(54) Bhargava, S. S.; Proietto, F.; Azmoodeh, D.; Cofell, E. R.; Henckel, D. A.; Verma, S.; Brooks, C. J.; Gewirth, A. A.; Kenis, P. J. A. System Design Rules for Intensifying the Electrochemical Reduction of CO_2 to CO on Ag Nanoparticles. *Chemelectrochem* **2020**, *7* (9), 2001-2011. DOI: 10.1002/celc.202000089.

(55) Wuttig, A.; Yaguchi, M.; Motobayashi, K.; Osawa, M.; Surendranath, Y. Inhibited proton transfer enhances Au-catalyzed CO_2-to-fuels selectivity. *Proceedings of the National Academy of Sciences of the United States of America* **2016**, *113* (32), E4585-E4593. DOI: 10.1073/pnas.1602984113.

(56) Liu, S.; Yang, H. B.; Hung, S. F.; Ding, J.; Cai, W. Z.; Liu, L. H.; Gao, J. J.; Li, X. N.; Ren, X. Y.; Kuang, Z. C.; et al. Elucidating the Electrocatalytic CO_2 Reduction Reaction over a Model Single-Atom Nickel Catalyst. *Angewandte Chemie-International Edition* **2020**, *59* (2), 798-803. DOI: 10.1002/anie.201911995.

(57) Noh, S.; Cho, Y. J.; Zhang, G.; Schreier, M. Insight into the Role of Entropy in Promoting Electrochemical CO_2 Reduction by Imidazolium Cations. *Journal of the American Chemical Society* **2023**, *145* (50), 27657-27663. DOI: 10.1021/jacs.3c09687.

(58) Sun, L. Y.; Ramesha, G. K.; Kamat, P. V.; Brennecke, J. F. Switching the Reaction Course of Electrochemical CO_2 Reduction with Ionic Liquids. *Langmuir* **2014**, *30* (21), 6302-6308. DOI: 10.1021/la5009076.

(59) Cheng, B. G.; Du, J. H.; Yuan, H. Q.; Tao, Y.; Chen, Y.; Lei, J. X.; Han, Z. J. Selective CO_2 Reduction to Ethylene Using Imidazolium-Functionalized Copper. *ACS Applied Materials & Interfaces* **2022**, *14* (24), 27823-27832. DOI: 10.1021/acsami.2c03748.

(60) Lim, H. K.; Kwon, Y.; Kim, H. S.; Jeon, J.; Kim, Y. H.; Lim, J. A.; Kim, B. S.; Choi, J.; Kim, H. Insight into the Microenvironments of the Metal-Ionic Liquid Interface during Electrochemical CO_2 Reduction. *ACS Catalysis* **2018**, *8* (3), 2420-2427. DOI: 10.1021/acscatal.7b03777.

(61) Das, S.; Sinha, S.; Roymahapatra, G.; De, G. C.; Giri, S. Ligand effect on the stability, reactivity, and acidity of imidazolium systems. *Journal of Physical Organic Chemistry* **2023**, *36* (12). DOI: 10.1002/poc.4331.

Chapter 6. Conclusions and Future Directions

6.1. Conclusions

This dissertation aims to establish the importance of the electric double layer in electrocatalytic reactions by demonstrating its role in governing local reaction environments using CO_2 electroreduction as a model reaction. We show how long range interactions control interfacial electric field strengths, the composition of the local electrolyte, and how understanding electric double layer formation can help us understand specific reaction mechanisms. Certainly, many more questions remain to be asked and much more work is needed to reconcile the role of the electric double layer with electrocatalytic reaction pathways and performance, but the work described herein attempts to make some headway in the development of a larger framework of knowledge on how to control electrochemical interfaces for electrocatalysis.

In Chapter 3, we used electrolyte concentration as a proxy for controlling double layer thickness to demonstrate its impact on CO_2 reduction. Our work showed that contrary to common assumptions, systematically tuning concentration yielded non-monotonic reaction rates and selectivity for CO. Electrolytes of intermediate concentrations performed better than either the dilute or neat ionic liquid cases, an observation that cannot be explained by CO_2 solubility or solution conductivity. Even more importantly, non-monotonic reaction trends apply to a range of ionic liquids, suggesting an aspect of universality that cannot be attributed to the chemical structure of any one ionic liquid. Indeed, *in situ* SERS results indicate that intermediate concentrations create more compact double layers, which screen the applied potential over a shorter distance, hence increasing the strength of local electric fields. Tuning electric field strength has long been an approach used in biological systems,[1] and it is the strong local electric field that stabilizes the negatively charged $CO_2^{\bullet-}$ in ionic liquid electrolytes. This effect explains why other ionic liquid-based electrolytes also exhibited non-monotonic reaction rate enhancements, as electric double layer formation occurs at all electrochemical interfaces. More crucially, this work bridged findings from the surface forces

and colloids fields with electrocatalysis, demonstrating the importance of long range interactions and self assembly in understanding and controlling reactions like CO_2 electroreduction.

We then probe how electric double layers form in Chapter 4, aiming to differentiate between entropic and electrostatic driving forces that govern its formation. To pursue this question, we synthesized and compared a dicationic ionic liquid, [BisMImO][TFSI]$_2$, with its monovalent counterpart, [BMIm][TFSI]. While we originally hypothesized that [BisMImO][TFSI]$_2$ would yield more compact double layers due to the lower entropic penalty for confinement at the interface on a per charge basis, we instead found that it performed worse in all reaction metrics than [BMIm][TFSI]. Using *in situ* SERS, we concluded that there is a difference in electrolyte structuring under reactive and non-reactive conditions, which has important implications for the future development of electric double layer models. Our spectroscopy results, in combination with our observations of reactivity in mixed electrolytes containing both $[BisMImO]^{2+}$ and $[BMIm]^{+}$, showed that the $[BisMImO]^{2+}$ cations preferentially accumulated at the interface and governed overall performance. However, the added entropic constraint introduced through the covalent link tethering two imidazolium cations around also profoundly impacted the behavior of the $[BisMImO]^{2+}$ cations, as its accumulation and interaction with interfacially-generated (bi)carbonate species caused substantial phase separation to occur, which blocked the electrode surface and stunted CO_2 reduction performance. Notably, this electrochemically-driven phase separation displayed unique nonclassical nucleation behavior in mixed electrolytes akin to those described in biological fields,[2, 3] which could point towards techniques to either prevent this from occurring or use phase separation to concentrate desirable molecules to the interface for more selective reductions.

In Chapter 5, we examined the carbene hypothesis through the lens of double layer formation in electrocatalytic environments. While previous attempts to assess the role of carbenes in ionic liquid-mediated electrocatalysis involved methylating the C2-site and concluded that C4/C5 hydrogen bonding was the key stabilization mechanism,[4] others have pointed out that methylating all the imidazolium carbon sites still yield enhanced reactivity.[5] We intended to use diamondoid groups as substituents on core

imidazolium structures to stabilize the C2-site carbene, allowing us to investigate the role of carbenes without methylating the C2 position. Instead, we found that the inclusion of the bulky and rigid diamondoid groups hindered CO_2 electroreduction, leading to both low reaction rates and selectivity. Rather than stabilizing the carbene, the negative electron affinity of the diamondoid groups instead caused these substituents to act as electron donors, stabilizing the C2-site and making carbene formation less favorable. Extra electron density around the imidazolium ring makes electrostatic interactions with the electrode surface weaker and the added steric hindrance of the diamondoid groups meant that interfacial cation orientation is less responsive to applied potentials. This manifests in the more cathodic onset potentials as well as a decreased ability to form the C2-site carbene through electrochemical or chemical deprotonation. An inability to form the C2-site carbene not only hinders possible stabilization mechanisms, but also prevents the imidazolium from forming adducts with interfacial (bi)carbonate species and preserving local electric fields. Our diamondoid work thus leads us to conclude that the carbene does play a role in facilitating the CO_2 reduction reaction, as preventing carbene formation leads to worse reaction kinetics and overall performance.

6.2. Future directions and outlook:

Many more questions must be answered before we can truly understand the extent to which the electric double layer governs electrocatalytic reactions and interfacial reactions influence double layer structure. As the work presented here suggests, controlling the electric double layer can have as great an effect on reaction metrics as changing the composition of the electrolyte itself, offering us new opportunities to control electrochemical interfaces and sculpt reaction environments. Several questions that arise from this dissertation include:

- What do direct methods of probing double layer structure like ec-AFM and SFA tell us about the interface under reactive and non-reactive conditions?
- How well do these findings translate to other electrochemical reactions? What new aspects of the double layer would we need to consider in these reactions?

- What can computational studies, like molecular dynamics simulations, tell us about these experimental interfaces? How can experimental findings help improve computational or theoretical models of electric double layers?
- To what extent can these findings be scaled up to more complex electrolyzer architectures?

The most immediate and logical follow up to the work presented here is to understand the structure of the electric double layer using direct methods of probing double layer thicknesses. Techniques like electrochemical atomic force microscopy (ec-AFM) or surface forces apparatus (SFA) could be used to measure double layer thicknesses and understand ion layering at the interface.[6] SFA in particular is suited for the study of double layer thicknesses, as this technique was previously used to demonstrate that the screening lengths in neat ionic liquids are several times longer than predicted values using dilute electrolyte theory,[7] and that there is a non-monotonic relationship between concentration and screening length.[8] In parallel, studies using ec-AFM can be useful for understanding more specific layering of the local electrolyte structure in different concentrations.[9] While these experiments have been performed before on neat ionic liquids, the choice of solvent in particular may prove to be crucial, as volatile solvents like acetonitrile may complicate the experimental setup. Furthermore, complications arising from the formation of gaseous products like CO under CO_2-saturated conditions may require additional modifications to existing systems. Still, the insight garnered from this kind of study would greatly inform the development of more refined and nuanced electric double layer models.

Since electric double layers form at all electrochemical interfaces, the findings from this dissertation are largely applicable to other electrolyte and reaction systems. The electroreduction of CO_2 in particular makes a compelling model reaction, as properties like the local electric field can have a significant impact on the stability of the polar and negatively-charged intermediate. Reactions involving polar and charged intermediates may be similarly affected by interfacial electric fields, and tuning these electric fields could affect more specific reaction pathways by favoring or disfavoring the formation of certain intermediates. Beyond CO_2 electroreduction, several electrochemical reactions are of relevance for their

potential impact on sustainable technologies. The hydrogen evolution reaction can be used to produce hydrogen fuels[10] while nitrate electroreduction can aid in wastewater remediation as well as the selective production of ammonia for fertilizers needed in the global agriculture industry.[11] These reactions, however, are often performed in aqueous solutions. Indeed, water is seen as a sustainable solvent when compared to acetonitrile so significant effort is being made to conduct reactions like CO_2 reduction in aqueous systems. The primary issue with aqueous systems, however, is the competing hydrogen evolution reaction, which decreases electrolyzer efficiency and could lead to increased separations costs if the desired product is also gaseous.[12] Hence, for aqueous systems, it is crucial to understand how to not only enhance reaction rates, but to also prevent unwanted reactions like hydrogen production from occurring. The electric double layer, if controlled, can offer ways to craft more selective reaction environments by creating hydrophobic interfaces or controlling local water structures to hinder hydrogen evolution while providing enough local protons to drive proton-demanding reactions.[13] Progress in any of these areas would lead to significant enhancements in reactor performance and are significant undertakings that could advance our knowledge of how to control electric double layers.

Due to the difficulty in directly probing electric double layers using experimental methods, computational studies would provide additional insight into interfacial reaction conditions and potentially enable high throughput screening of electrolyte compositions for different reactions. However, computational models of electrochemical interfaces involve assumptions and approximations that reduce the total computational cost. Often, this means that the nonclassical interactions and crowded environments cannot be fully captured by a single model alone at the time and length scales of electrochemical processes.[14, 15] Advances in computational and theoretical methods are important to develop an understanding of dynamic processes at interfaces, like the transport of reactants and (by)products across the double layer, which could yield important insight into how the double layer structure is structured in the presence of electrochemical reactions or how the interfacial electrolyte composition may be controlled to suit a specific application. Ultimately, the feedback loop between experimental and computational would

greatly aid in the development of sophisticated electric double layer models that go beyond dilute electrolyte theory, incorporating aspects of self assembly, long range interactions, and electrochemical reaction dynamics to explain interfacial processes.

The work presented in this dissertation is fundamental in nature, aimed at understanding how electric double layers form in simple reactors and with a relatively simple reaction. For these findings to have practical relevance, we need to understand how they scale up and fit in with the current frameworks for industrial scale electrolyzer designs. For instance, membrane electrode assemblies (MEAs)[16] utilize gas diffusion electrodes to introduce gaseous reactants directly to the electrode surface and complex membranes to modulate electrolyte properties like pH. Gas diffusion electrodes are fabricated by coating porous electrode frameworks with the desired catalyst so under operating conditions, a gas-liquid-solid interface forms, and more practical considerations involving the transport of reactants, electrode wetting, and changing local electrolyte properties must be considered. The membranes used in these MEA architectures could also drastically affect bulk electrolyte properties, as the difference between cation-exchange, anion-exchange, and bipolar membranes can lead to changes in electrolyte composition over time. In the case of bipolar membranes, the membrane itself develops an electric double layer as it splits water into protons and hydroxides. Developing a detailed knowledge of how our findings on electric double layer formation in simpler systems translate to these aspects of electrolyzer design could open the doors to more efficient reactors that operate on long timescales.

Understanding and controlling the electrochemical interface can ultimately lead to the development of reactor systems that would enable not just CO_2 reduction, but also more synthetically complex reactions that could sustainably replace existing chemical manufacturing methods. Even more importantly, the findings from these investigations into the role of the electric double layer could yield important insight into electrolyte design that would benefit electrocatalytic reactions and energy storage applications alike. In combination with significant progress in electrode design, we could envision a future in which electrode-

electrolyte systems are tailored for specific applications to create more stable batteries, more efficient fuel cells, and highly selective electrolyzers.

6.3. References

(1) Léonard, N. G.; Dhaoui, R.; Chantarojsiri, T.; Yang, J. Y. Electric Fields in Catalysis: From Enzymes to Molecular Catalysts. *ACS Catalysis* **2021**, *11* (17), 10923-10932. DOI: 10.1021/acscatal.1c02084.

(2) Du, J. S.; Bae, Y.; De Yoreo, J. J. Non-classical crystallization in soft and organic materials. *Nature Reviews Materials* **2024**, *9* (4), 229-248. DOI: 10.1038/s41578-023-00637-y.

(3) Jehannin, M.; Rao, A.; Cölfen, H. New Horizons of Nonclassical Crystallization. *Journal of the American Chemical Society* **2019**, *141* (26), 10120-10136. DOI: 10.1021/jacs.9b01883.

(4) Lau, G. P. S.; Schreier, M.; Vasilyev, D.; Scopelliti, R.; Gratzel, M.; Dyson, P. J. New Insights Into the Role of Imidazolium-Based Promoters for the Electroreduction of CO_2 on a Silver Electrode. *Journal of the American Chemical Society* **2016**, *138* (25), 7820-7823. DOI: 10.1021/jacs.6b03366.

(5) Sargeant, E.; Rodríguez, P. Electrochemical conversion of CO_2 in non-conventional electrolytes: Recent achievements and future challenges. *Electrochemical Science Advances* **2023**, *3* (4). DOI: 10.1002/elsa.202100178.

(6) Gebbie, M. A.; Liu, B. C.; Guo, W. X.; Anderson, S. R.; Johnstone, S. G. Linking Electric Double Layer Formation to Electrocatalytic Activity. *ACS Catalysis* **2023**, *13* (24), 16222-16239. DOI: 10.1021/acscatal.3c04255.

(7) Gebbie, M. A.; Smith, A. M.; Dobbs, H. A.; Lee, A. A.; Warr, G. G.; Banquy, X.; Valtiner, M.; Rutland, M. W.; Israelachvili, J. N.; Perkin, S.; et al. Long Range Electrostatic Forces in Ionic Liquids. *Chemical Communications* **2017**, *53*, 1214-1224. DOI: 10.1039/c6cc08820a.

(8) Smith, A. M.; Lee, A. A.; Perkin, S. The Electrostatic Screening Length in Concentrated Electrolytes Increases with Concentration. *Journal of Physical Chemistry Letters* **2016**, *7* (12), 2157-2163. DOI: 10.1021/acs.jpclett.6b00867.

(9) Li, H.; Wang, J. A.; Warr, G. G.; Atkin, R. Extremely slow dynamics of ionic liquid self-assembled nanostructures near a solid surface. *Journal of Colloid and Interface Science* **2023**, *630*, 658-665. DOI: 10.1016/j.jcis.2022.10.123.

(10) Cao, S.; Piao, L. Y.; Chen, X. B. Emerging Photocatalysts for Hydrogen Evolution. *Trends in Chemistry* **2020**, *2* (1), 57-70. DOI: 10.1016/j.trechm.2019.06.009.

(11) Wang, Y. T.; Wang, C. H.; Li, M. Y.; Yu, Y. F.; Zhang, B. Nitrate electroreduction: mechanism insight, characterization, performance evaluation, and challenges. *Chemical Society Reviews* **2021**, *50* (12), 6720-6733. DOI: 10.1039/d1cs00116g.

(12) Zhao, J. Y.; Liu, Y. W.; Li, W. J.; Wen, C. F.; Fu, H. Q.; Yuan, H. Y.; Liu, P. F.; Yang, H. G. A focus on the electrolyte: Realizing CO2 electroreduction from aqueous solution to pure water. *Chem Catalysis* **2023**, *3* (1). DOI: ARTN 100471

10.1016/j.checat.2022.11.010.

(13) Chen, J.; Qiu, H.; Zhao, Y.; Yang, H.; Fan, L.; Liu, Z.; Xi, S.; Zheng, G.; Chen, J.; Chen, L.; et al. Selective and stable CO_2 electroreduction at high rates via control of local H_2O/CO_2 ratio. *Nature Communications* **2024**, *15* (1), 5893. DOI: 10.1038/s41467-024-50269-1.

(14) Sundararaman, R.; Vigil-Fowler, D.; Schwarz, K. Improving the Accuracy of Atomistic Simulations of the Electrochemical Interface. *Chemical Reviews* **2022**, *122* (12), 10651-10674. DOI: 10.1021/acs.chemrev.1c00800.

(15) Sakong, S.; Huang, J.; Eikerling, M.; Gross, A. The structure of the electric double layer: Atomistic versus continuum approaches. *Current Opinion in Electrochemistry* **2022**, *33*. DOI: 10.1016/j.coelec.2022.100953.

(16) Zhang, Z.; Huang, X.; Chen, Z.; Zhu, J. J.; Endrődi, B.; Janáky, C.; Deng, D. H. Membrane Electrode Assembly for Electrocatalytic CO_2 Reduction: Principle and Application. *Angewandte Chemie-International Edition* **2023**, *62* (28). DOI: 10.1002/anie.202302789.

APPENDIX

Appendix for Chapter 3: Tuning Ionic Screening to Accelerate Electrochemical CO_2 Reduction in Ionic Liquid Electrolytes

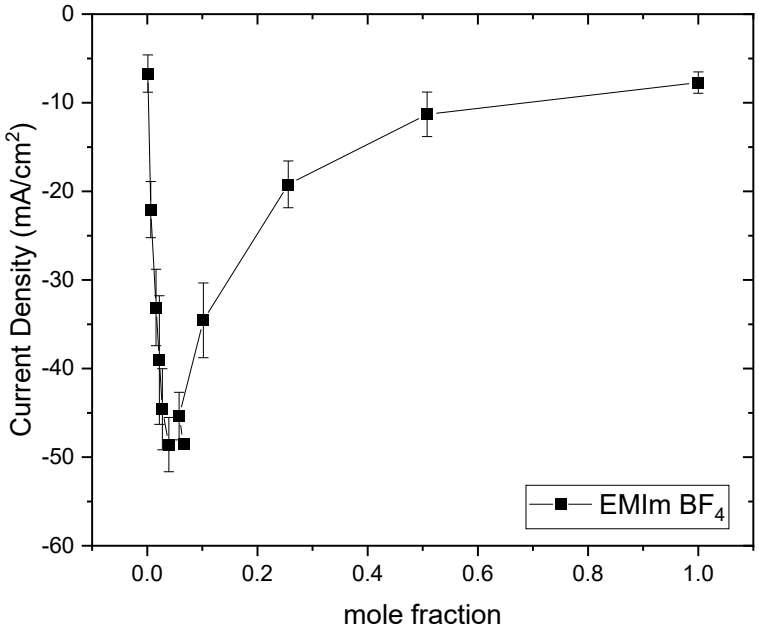

Figure A1.1 Non-monotonic behavior of current density as a function of mole fraction of EMIm BF_4.

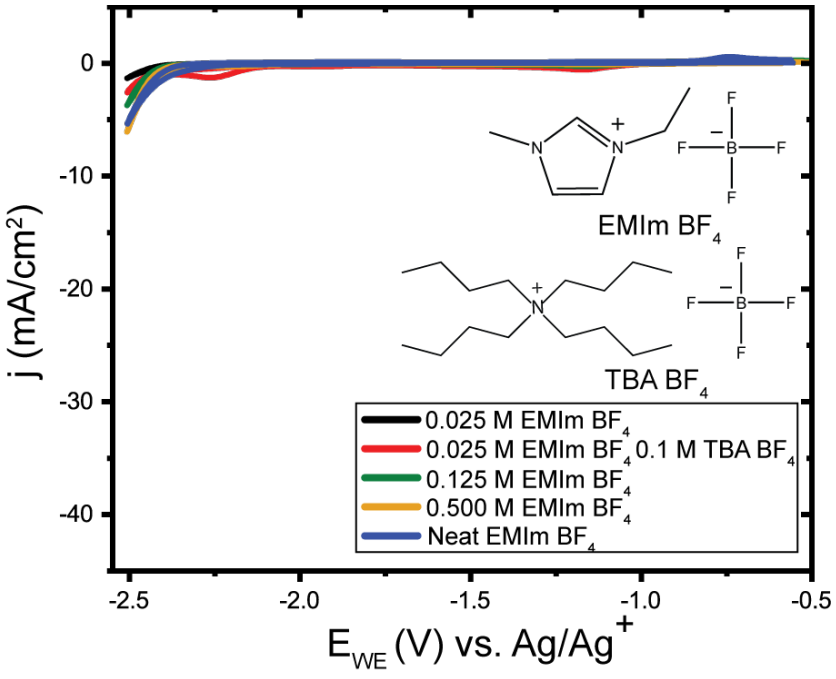

Figure A1.2 Representative cyclic voltammograms for varying concentrations of EMIm BF_4 in acetonitrile after saturating with argon on Ag electrodes using a scan rate of 100 mV/s. A slight increase in current densities was observed as concentration increased, but the rate enhancement effect at intermediate concentrations is much smaller. The current density that is observed is likely due to electrolyte decomposition.

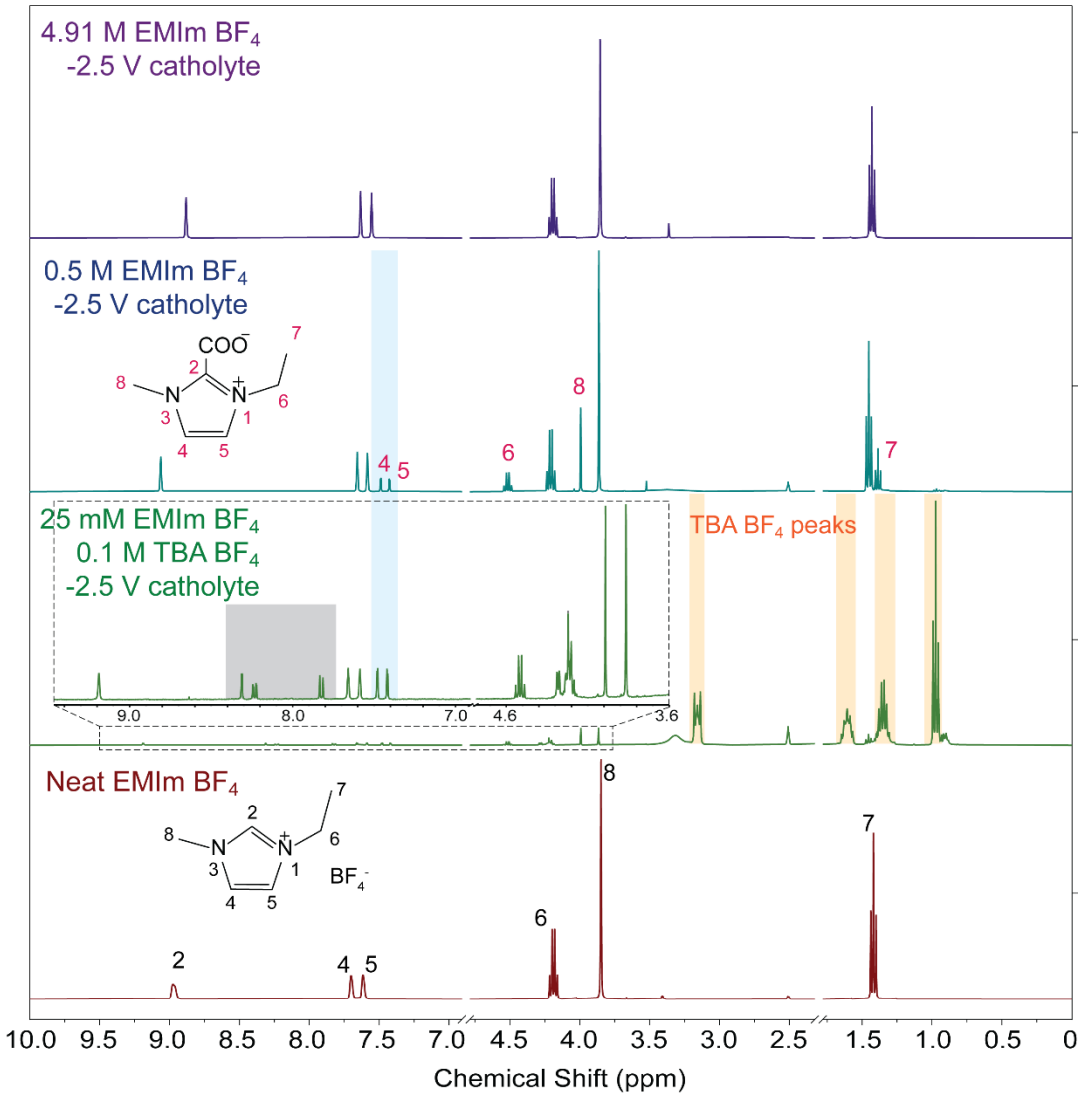

Figure A1.3 ^{1}H NMR results of catholytes containing EMIm BF_4 at different concentrations after 3 hours of electrolysis. An NMR spectrum from neat EMIm BF_4 (bottom panel) is provided with peak assignments for comparison. Only chemical shift regions with signals from EMIm BF_4 and TBA BF_4 are displayed. Peaks shaded in light blue correspond to protons on C4 and C5 in EMIm-COO adducts,[1] confirming the participation of C2 in EMIm-catalyzed CO_2 reduction. For the NMR spectrum from the catholyte containing 25 mM EMIm BF_4 and 0.1 M TBA BF_4 (green curve), signals from TBA BF_4 are shaded in light orange, and the chemical shift region with main peaks from EMIm BF_4 is enlarged for a clearer view. Peaks shaded in grey are suspected to originate from side products generated by solvent breakdown, as they are observed in NMR spectra for all catholytes after enlargement (data not shown). In the case of 25 mM EMIm BF_4 and 0.1 M TBA BF_4, these peaks become comparable to EMIm BF_4 peaks due to the low concentration of EMIm BF_4.

Concentration of EMIm BF_4 (M)	Averaged current density (mA/cm^2)	FE (%)	H4/5 NMR peak ratio between adduct and intact EMIm	Concentration of adduct (M)
0.025	-21.7	62.2	0.77	0.010
0.5	-48.5	89.8	0.28	0.102
4.91	-0.519	0	0	0.000

Table A1.1 Estimated concentration of carboxylate adduct in catholyte after 3-hour electrolysis from NMR spectra in Figure A1.2. The peak ratio between protons on C4 and C5 of carboxylate adduct and intact EMIm cations is used to estimate the final concentration of adduct in the catholytes. Clearly, the concentration of adducts scales with the current density toward CO formation and reaches the maximum in catholytes with intermediate concentration of EMIm BF_4.

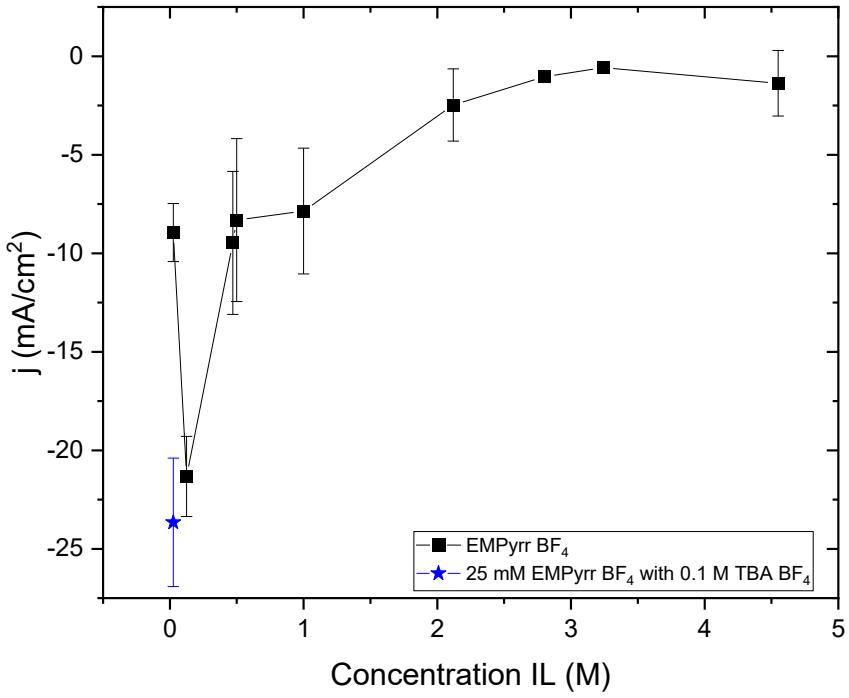

Figure A1.4 Concentration sweep for EMPyrr BF_4 using cyclic voltammetry data in which current densities at -2.5 V vs. Ag/Ag^+ are used. Each point represents three separate trials, in which two representative cyclic voltammograms were chosen for each sample for a total of at least six values per data point.

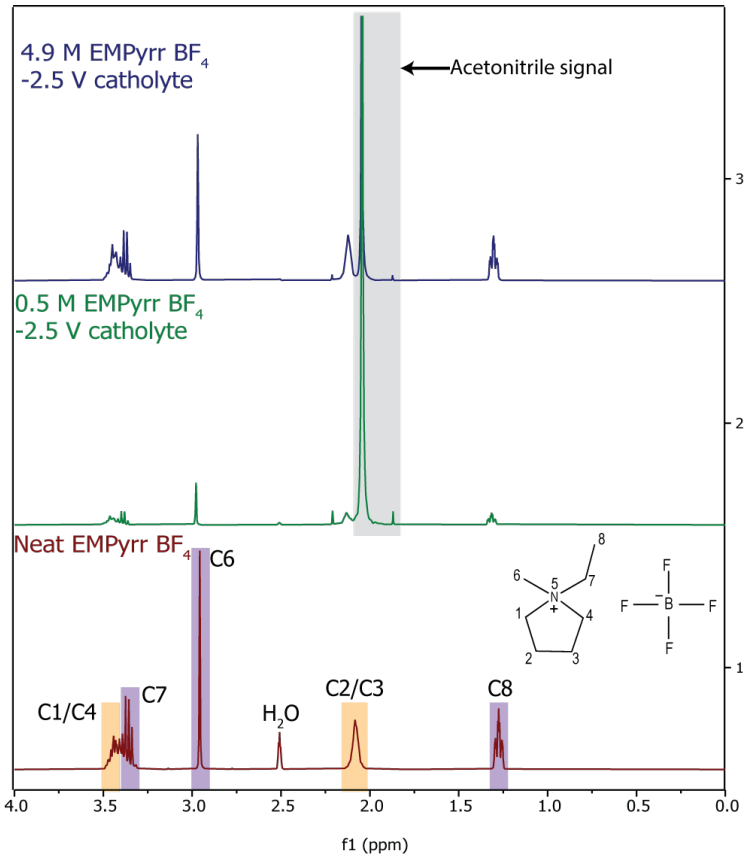

Figure A1.5 ^{1}H NMR results of catholytes containing EMPyrr BF_4 at different concentrations after 3 hours of electrolysis. An NMR spectrum from neat EMPyrr BF_4 (bottom panel) prior to electrolysis is provided for comparison. The peak from acetonitrile is shaded in grey.

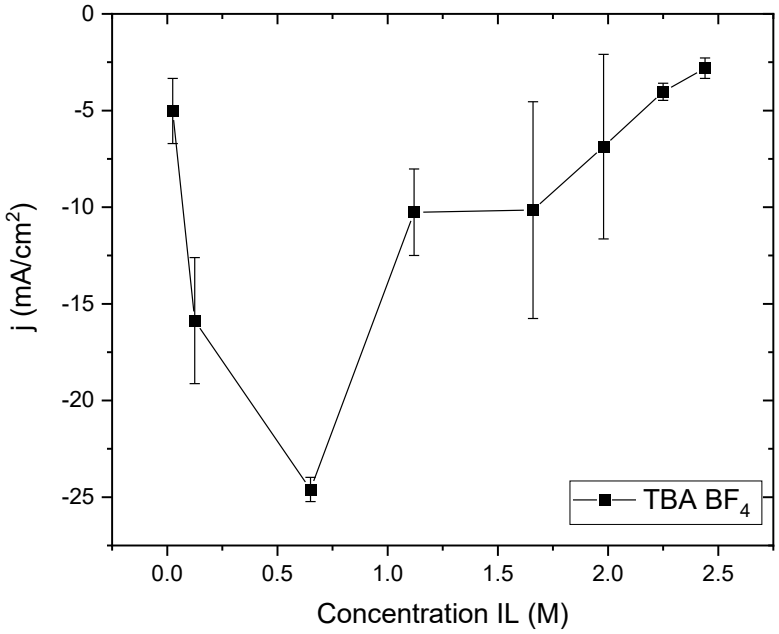

Figure A1.6 Concentration sweep for TBA BF_4 using cyclic voltammetry data in which current densities at -2.5 V vs. Ag/Ag^+ are used. Each point represents three separate trials, in which two representative cyclic voltammograms were chosen for each sample for a total of at least six values per data point.

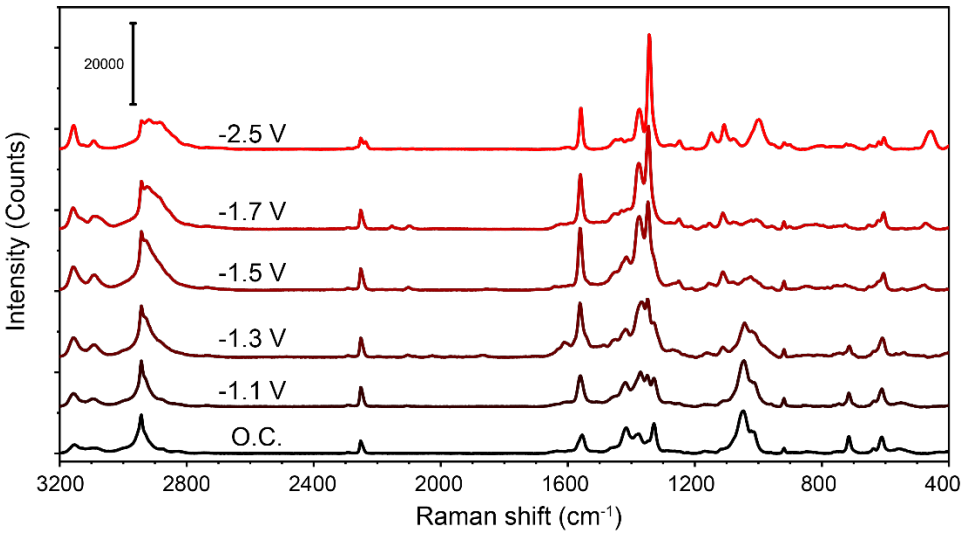

Figure A1.7 Full-range in situ SERS spectra of 0.5 M EMIm BF_4 without normalization. Using the acetonitrile peak at 2252 cm^{-1} as an internal standard, it can be seen that absolute intensities of peaks at 1560, 1375, and 1344 cm^{-1} gradually increase, and the peak at 1415 cm^{-1} gradually decreases when the potential is decreased from open-circuit potential to -2.5 V vs. Ag/Ag^+.

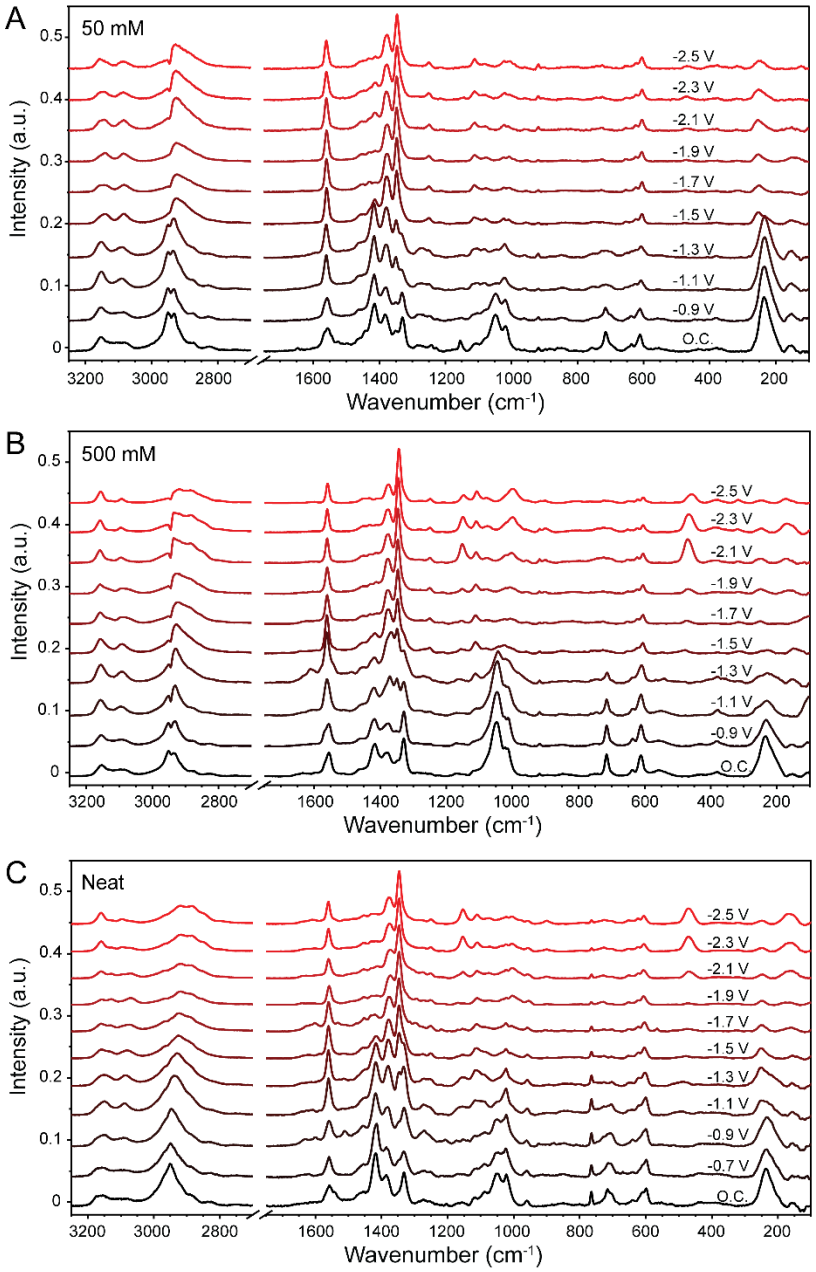

Figure A1.8 Full-range spectra of (A) 50 mM, (B) 500 mM, and (C) neat EMIm BF_4 solutions. Dips at 2943 cm^{-1} for spectra from 50 mM and 500 mM solutions result from the subtraction of acetonitrile background. Peak assignments are conducted based on prior studies.[2, 3] For all concentrations tested, significant spectral changes occur in both low-frequency and high-frequency regions. While a comprehensive interpretation of all spectral changes is beyond the scope of this study, we use changes in the ring deformation region (1200 to 1700 cm^{-1}) to represent the reorientation of EMIm cations.

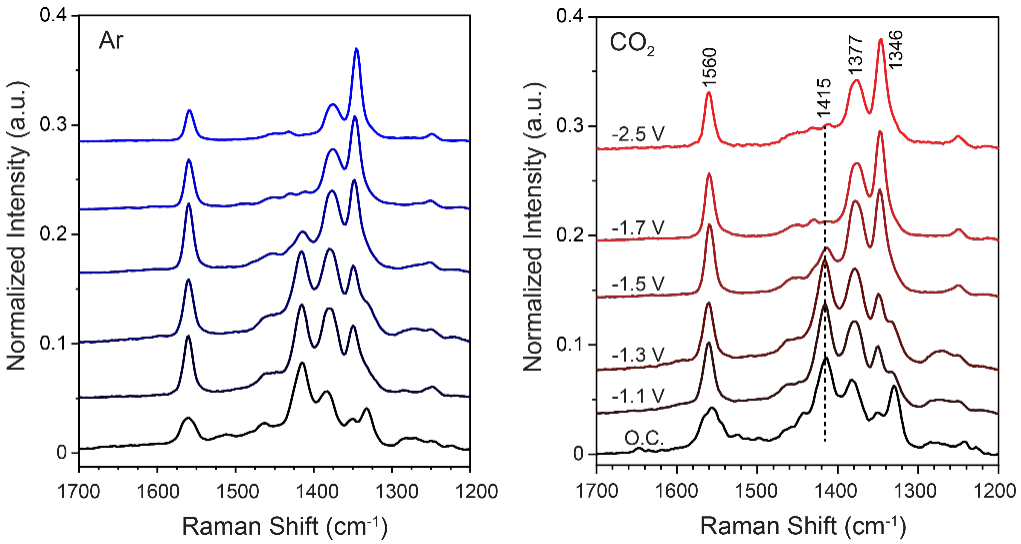

Figure A1.9 In situ SERS spectra of 0.05 M EMIm BF_4 solution under Ar (left) and CO_2 (right) conditions. Two sets of spectra show identical potential-dependent spectral changes, which indicate that the changes are not related to CO_2-related processes, such as the formation of EMIm-COO adducts. Meanwhile, the changes already become noticeable at -1.1 V vs Ag/Ag^+, which is positive to the onset potential for carbene formation. Therefore, we attribute the observed spectral changes the re-orientation of EMIm cations driven by applied negative potential.

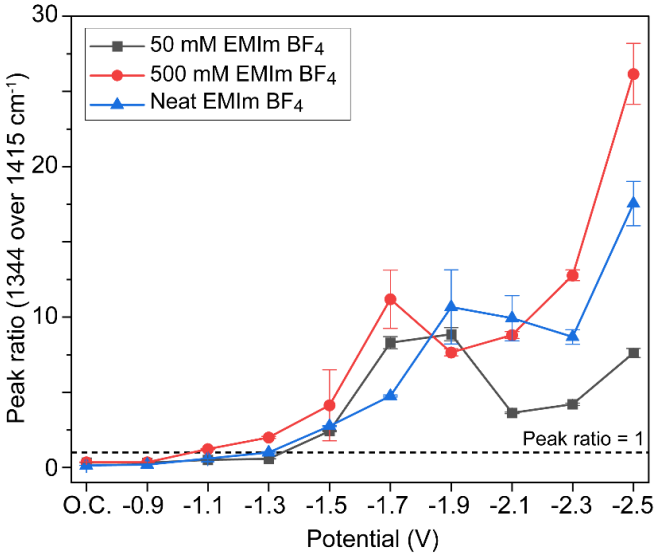

Figure A1.10 Intensity ratio of deconvoluted 1344 cm^{-1} peak over 1415 cm^{-1} peak as a function of applied potential for 50 mM, 500 mM, and neat EMIm BF_4 solutions. The ratio grows the fastest and exceeds 1 at the most anodic potential for 500 mM EMIm BF_4 solution, suggesting that the reorientation of EMIm cations as a result of near-surface potential gradient is the most efficient at intermediate concentrations.

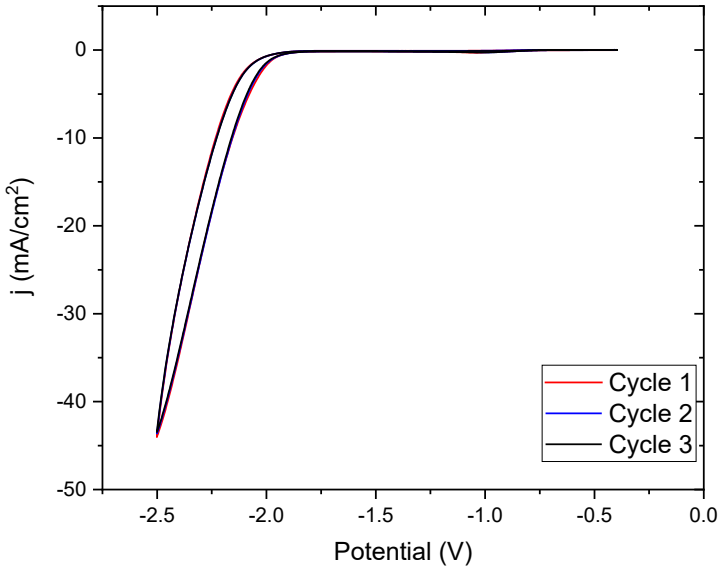

Figure A1.11 Representative CV for 500 mM EMIm BF_4, which shows that the same CV curve is observed for all 3 cycles. This repeatable behavior is observed for all scans for all EMIm BF_4 samples. Scan rate of 100 mV/s was used to collect the data for this CV.

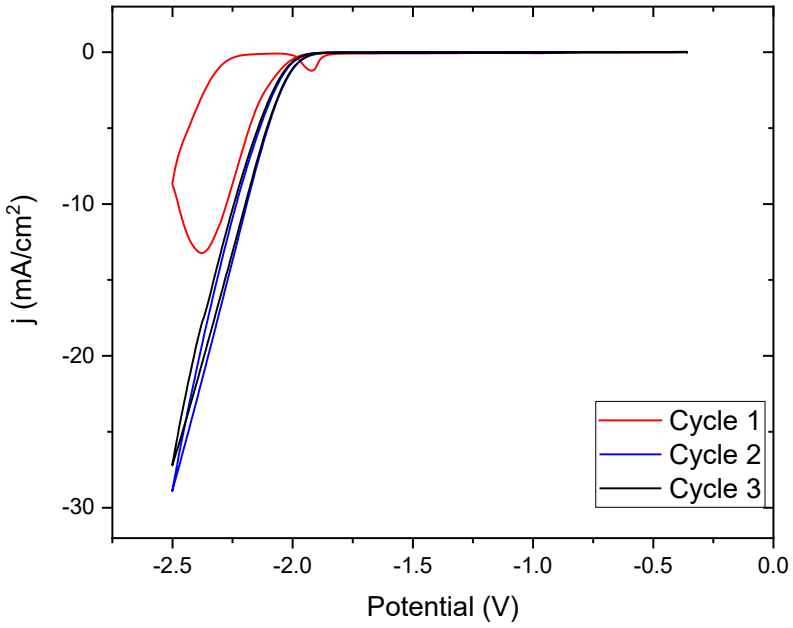

Figure A1.12 Representative CV for 125 mM EMMIm BF_4, which shows the difference between cycle 1 and cycles 2 and 3. Here, the very first cycle appears to be less active that the following cycles. Scan rate of 100 mV/s was used to collect the data for this CV.

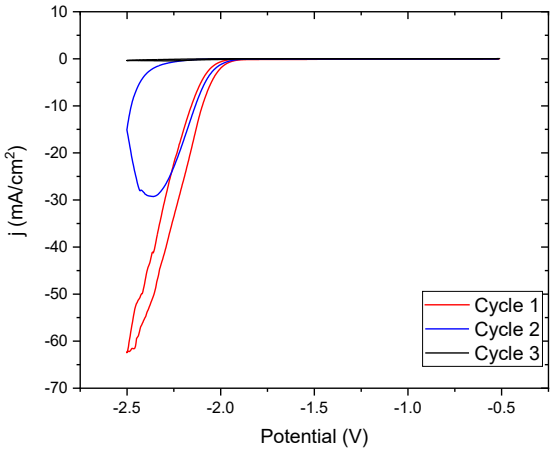

Figure A1.13 Representative CV for 0.5 M EMMIm BF_4, which shows the difference between cycle 1 and cycles 2 and 3. Here, cycle 1 displays the highest reactivity, but reactivity diminishes in the subsequent cycles. Scan rate of 100 mV/s was used to collect the data for this CV.

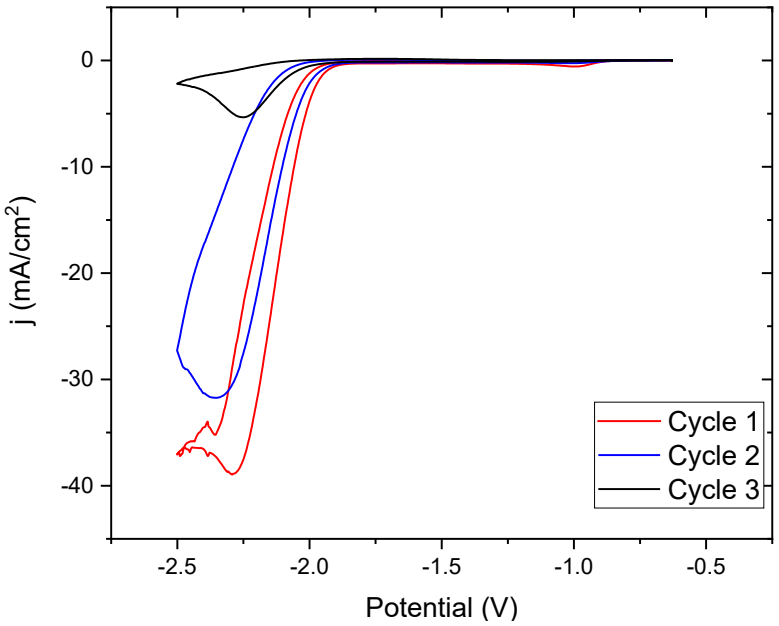

Figure A1.14 Representative CV for 1.4 M EMMIm BF_4, which shows the difference between cycle 1 and cycles 2 and 3. Here, cycle 1 displays the highest reactivity, but reactivity diminishes in the subsequent cycles. Scan rate of 100 mV/s was used to collect the data for this CV.

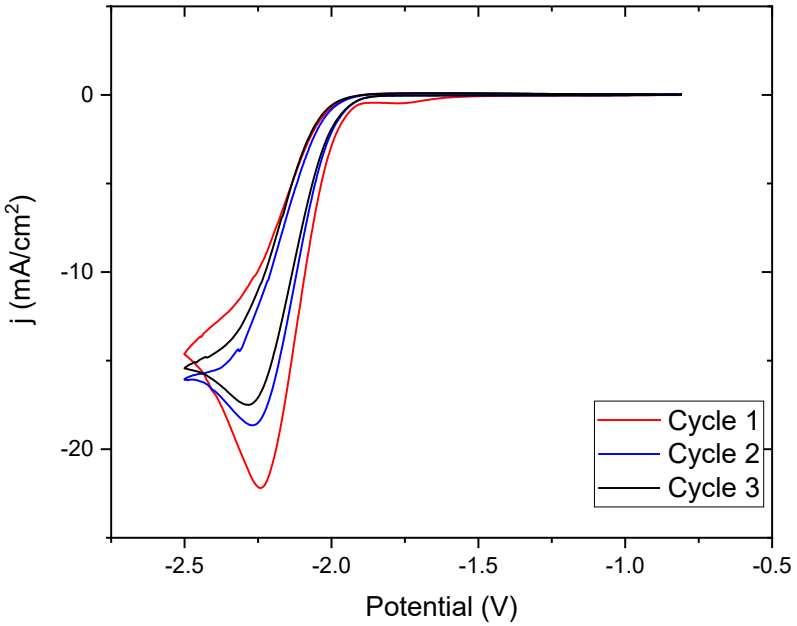

Figure A1.15 Representative CV for 3.16 M EMMIm BF_4, which shows the difference between cycle 1 and cycles 2 and 3. Here, cycle 1 displays the highest reactivity, but reactivity slightly decreases in the subsequent cycles rather than diminishing significantly. Scan rate of 100 mV/s was used to collect the data for this CV.

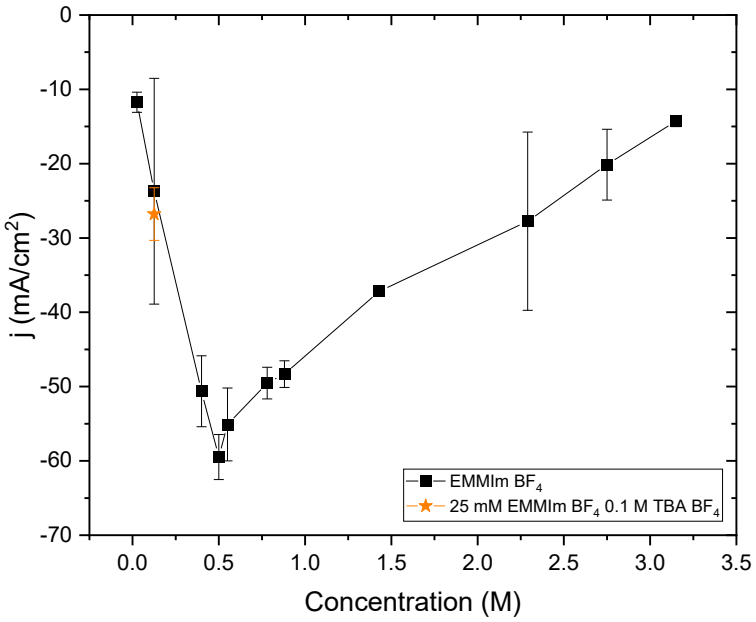

Figure A1.16 Concentration sweep for EMMIm BF_4 using cyclic voltammetry data in which current densities at -2.5 V vs. Ag/Ag^+ are used. The data associated with solutions containing 25 mM EMMIm BF_4 and 0.1 M TBA BF_4 is denoted by the orange star marker. Each point represents three separate trials, and only cycle 1 of the cyclic voltammograms.

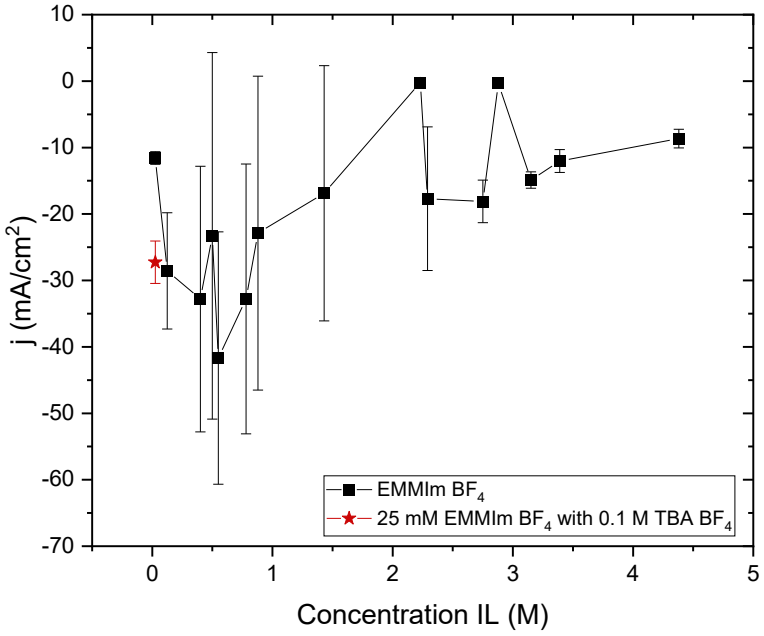

Figure A1.17 Concentration sweep for EMMIm BF_4 using cyclic voltammetry data in which current densities at -2.5 V vs. Ag/Ag^+ are used. The data associated with solutions containing 25 mM EMMIm BF_4 and 0.1 M TBA BF_4 is denoted by the red star marker. Each point represents three separate trials, in which two representative cyclic voltammograms were chosen for each sample for a total of at least 6 values per data point. The large error bars are a result of cycle-dependent reactivity, especially at intermediate concentrations.

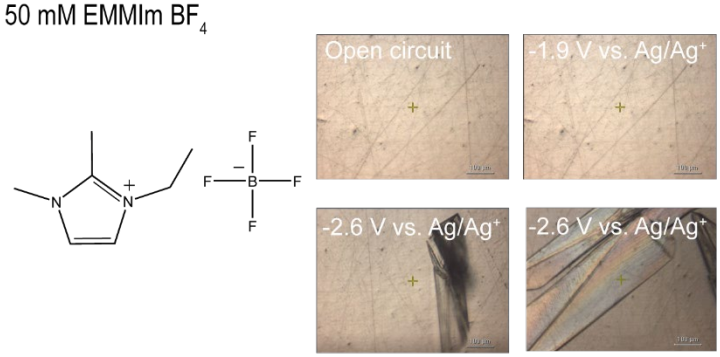

Figure A1.18 The potential-dependent formation of EMMIm BF_4 crystals at a silver electrode surface in a CO_2-saturated electrolyte containing 50 mM EMMIm BF_4. The onset potential for this crystallization process occurred at -2.6 V vs. Ag/Ag^+. Notably, crystal growth with EMMIm-containing ionic liquid solutions only occured in CO_2-saturated conditions, while Ar-purged solutions displayed no crystallization (data not shown), which suggests the strong correlation between the crystallization and CO_2 reduction.

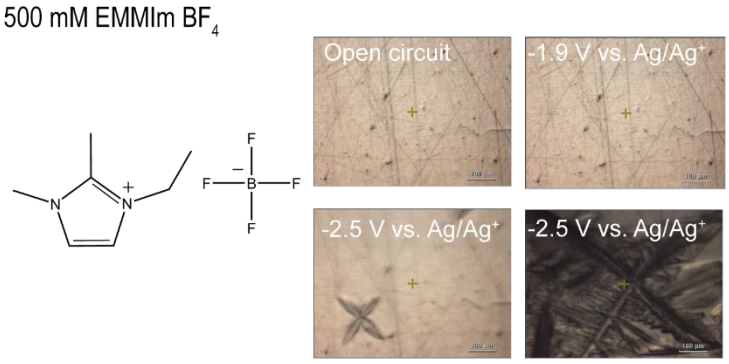

Figure A1.19 The potential-dependent formation of EMMIm BF_4 crystals at a silver electrode surface in a CO_2-saturated electrolyte containing 500 mM EMMIm BF_4. The onset potential for this crystallization process occurred at -2.5 V vs. Ag/Ag^+.

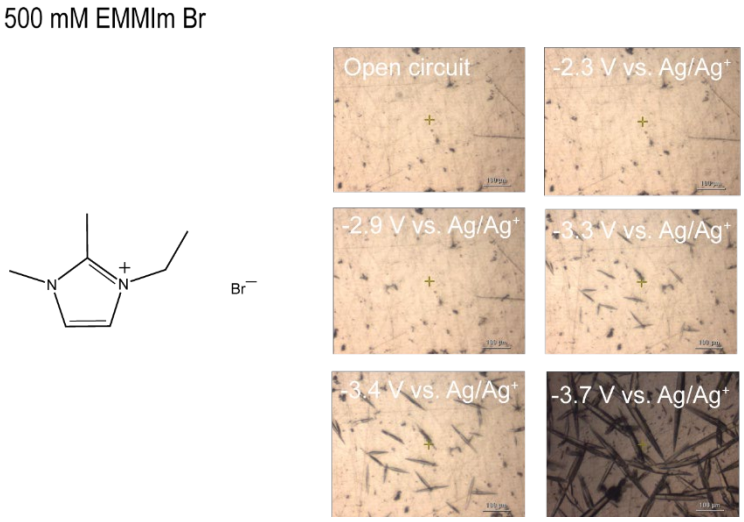

Figure A1.20 The potential-dependent formation of EMMIm Br crystals at a silver electrode surface in an CO_2-saturated electrolyte containing 500 mM EMMIm Br. The onset potential for this crystallization process occurred at -3.3 V vs. Ag/Ag^+, with the growth of crystal structures that are long, thin, and rod-like. It appears that the anion plays a significant role in controlling crystal nucleation and growth despite this process occurring at the cathode. It also suggests that the double layer structure is also highly dependent on both the cation and the anion.

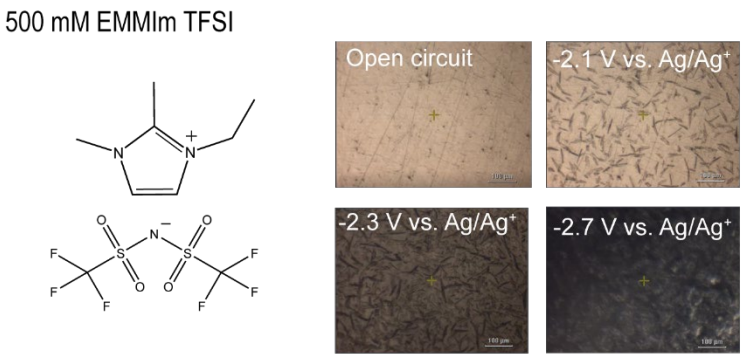

Figure A1.21 The potential-dependent formation of EMMIm TFSI crystals at a silver electrode surface in an CO_2-saturated electrolyte containing 500 mM EMMIm TFSI. The onset potential for this crystallization process occurred at -2.1 V vs. Ag/Ag^+, with the growth of crystal structures that are short and rod-like. It appears that the anion plays a significant role in controlling crystal nucleation and growth despite this process occurring at the cathode. Although a more mechanistic understanding of the impact of the anion on the double layer formation is required, these experiments suggest that larger anions may lower the onset potential of crystallization and can have significant impact on crystal morphology.

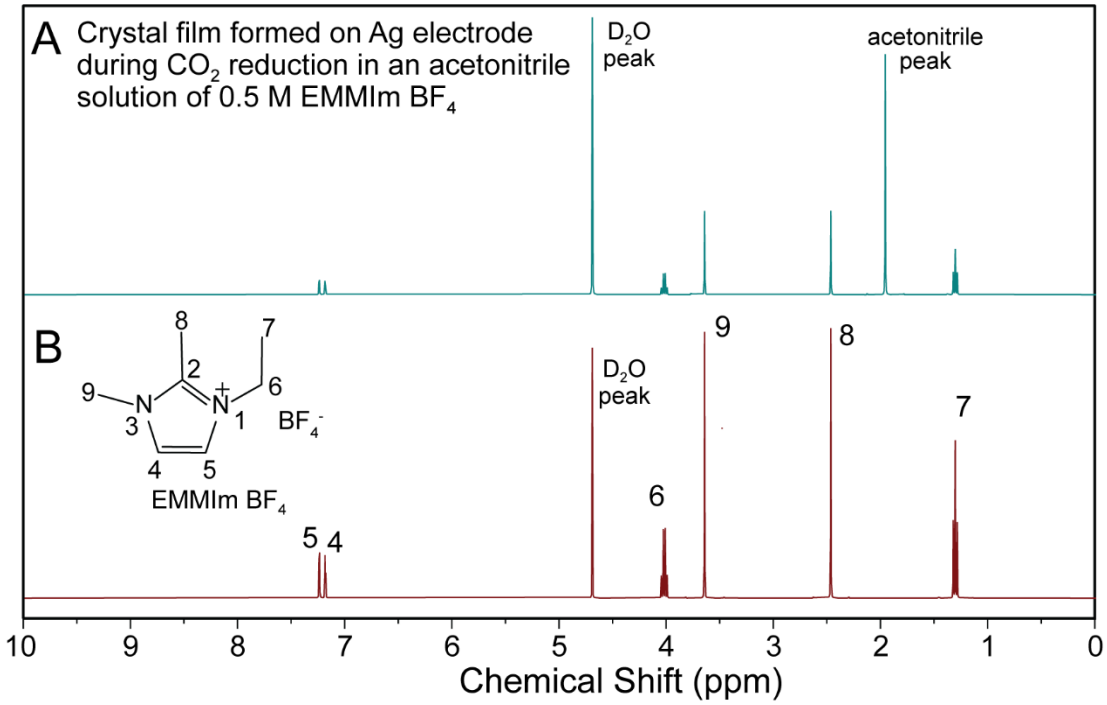

Figure A1.22 ^1H NMR results of (A) the crystal formed on the electrode surface and (B) EMMIm BF_4 in D_2O. The similarity between (A) and (B) indicates that EMMIm cations is a main composition of the crystal.

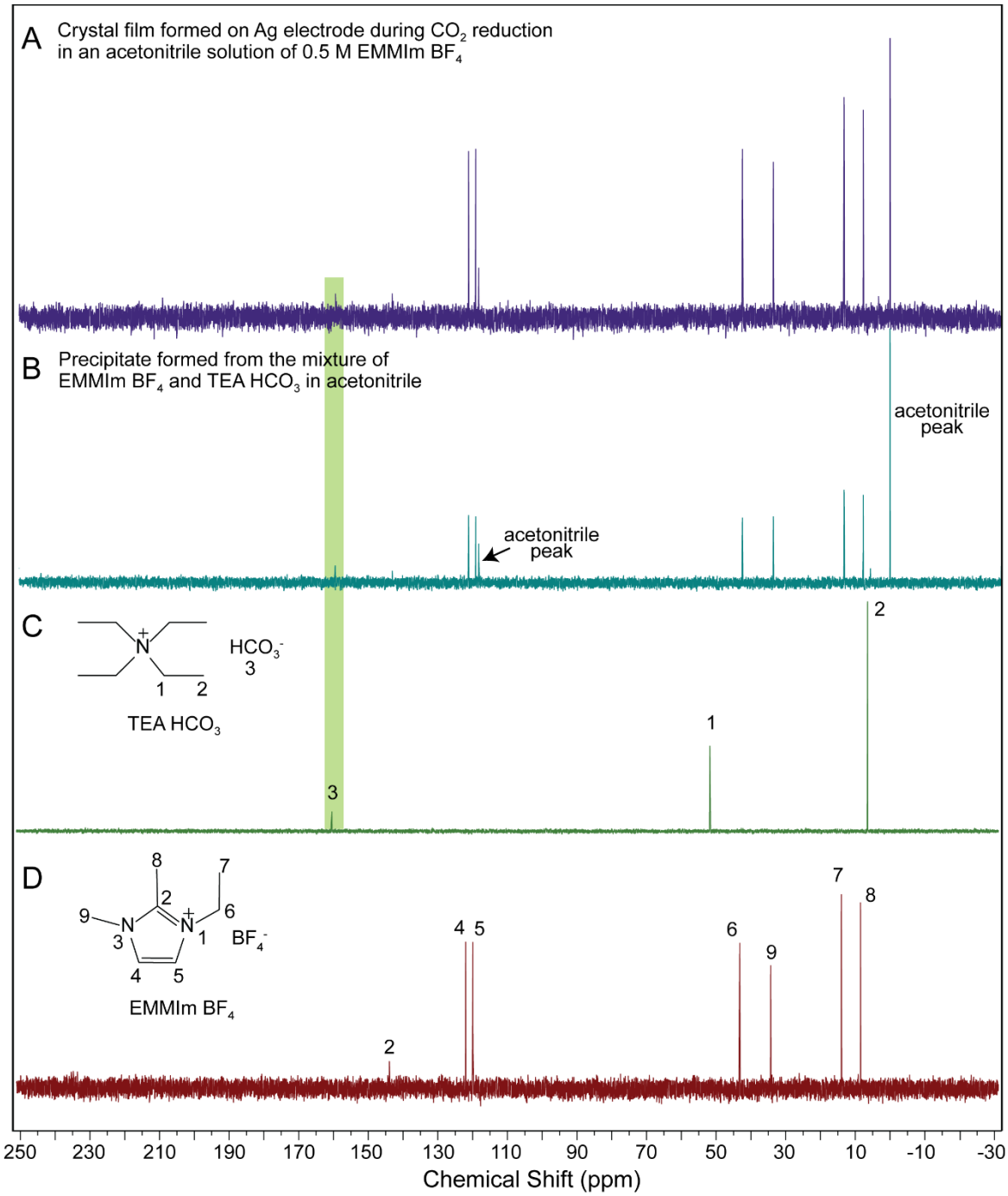

Figure A1.23 ^{13}C NMR spectra of (A) crystal formed on a Ag disk electrode during electrochemical reduction of CO_2 in an acetonitrile solution of 0.5 M EMMIm BF_4, (B) precipitate formed from the the mixture of acetonitrile solutions of 0.1 M EMMIm BF_4 and 0.1 M triethylammonium bicarbonate (TEA HCO_3^-), (C) neat TEA HCO_3, and (D) neat EMMIm BF_4 in D_2O. The presence of a peak from HCO_3^- (shaded in green at 160 ppm) in (B) indicates that EMMIm HCO_3 has low solubility in acetonitrile and would spontaneously form when $EMMIm^+$ cation and HCO_3^- coexist. The presence of the same HCO_3^- peak in (A) stronly suggested that the crystal film formed on Ag electrode during CO_2 reduction was EMMIm HCO_3. Assigments of peaks are shown in panel (D).

Scaling Theory Discussion

As discussed in the Chapter 3, a key assumption associated with defining the Debye length is to neglect attractive and repulsive ion-ion interactions, which drive aggregation into neutral clusters as concentration increases. Given the $\frac{1}{\sqrt{n}}$ dependence of the Debye length on ion concentration, this classical framework predicts that increasing the ion concentration of an electrolyte will always enhance screening efficiency. Yet, the predicted Debye screening length equation is developed for dilute electrolytes and is unable to capture experimental trends observed for concentrated electrolytes, where ion-ion interactions arise.

In fact, prior studies have demonstrated increasing deviations from the classical Debye screening length as ionic liquid concentration increases, where the deviations become pronounced at approximately 1 M for organic salts dissolved in propylene carbonate and inorganic salts dissolved in water.[4] Despite the presence of deviations at high concentrations, scaling theory analysis of the Debye screening length, in conjunction with experimental values of effective Debye screening length obtained from literature, can still yield valuable insight and guidance for electrolyte design.

For example, the classical Debye-Hückel model predicts the Debye screening length always decreases as concentration increases. Yet, as clustering emerges, many of the ions in solution become "bound" in neutral aggregates and no longer independently contribute to screening charged surfaces. However, classical Debye length calculations still include these bound ions in the overall concentration, leading to a discrepancy between the calculated Debye length and measured electrostatic screening length, where the measured screening length can be more than an order of magnitude larger than the calculated Debye length.

This disparity between the concentration of "free" ions at the surface and the total number of ions per unit volume after correlations emerge creates a scenario in which the Debye screening length initially decreases with concentration but then increases after a certain "crossover concentration." Prior to this point, the limiting factor is the concentration of ions available to screen the surface potential. Following the "crossover concentration," the formation of multi-ion clusters reduces the number of "free" ions available for electrostatic screening. Importantly, electrolytes are expected to exhibit the most efficient screening, as evidenced by thinnest electric double layers and largest local potential gradients, around this concentration where correlations begin to emerge.

While a general, quantitative prediction of the "crossover concentration" in electrolytes of different compositions remains subject to discussion, Fig. A1.24 shows a scaling analysis of the relationship between Debye screening length and concentration can be used to approximate the regime

where the concentration of maximum reactivity can be found. Previous reports of non-monotonic measured ionic screening lengths with concentration for a pyrrolidinium-based ionic liquid in propylene carbonate show good agreement between predicted and experimentally-determined Debye screening length up to approximately 1 M. Beyond 1 M, Smith et al. reported increasing Debye screening lengths with concentration.[4]

Indeed, the measured effective Debye screening length of EMIm TFSI, an analogue for EMIm BF_4, has been previously reported to be 7.5 nm and deviates drastically from the predicted Debye screening length of approximately 0.25 nm. In the limit of a neat ionic liquid, Debye length calculations, which assume all ions independently contribute to screening, differ from experimental values by more than a factor of 10. Given the fact that surfaces are not fully screened until several Debye lengths away from surfaces, the disparity between predicted and measured electric double layer thickness greatly exceeds an order of magnitude. We also find that most prior studies of ionic liquid-acetonitrile electrolytes of around 100 mM concentration likely exhibit screening lengths of around 0.6 nm, which is about the same of ionic dimensions for EMIm BF_4 but larger than its effective ion radius. At the concentrations of maximum reactivity, between 0.5 M and 1 M, the predicted Debye screening length ranges from 0.3 nm to 0.2 nm, which is on the order of, and can even be smaller than, ion radii. When compared to the surface forces results discussed in the main text, we conclude that this is a concentration range where correlations are key, meaning that further increases in concentration are expected to decrease screening efficiency and weaken interfacial potential gradients (Fig. 5). For example, the screening lengths of neat ionic liquids are measured to fall in the range of 5–10 nm, which is an order of magnitude larger than ion sizes.[4, 5] A decreased potential gradient due to the emergence of ion clustering is consistent with our reported reaction rate and spectroscopy results.

Overall, this scaling analysis, when compared to recent findings from the literature, enables us to identify a plausible region of concentration where we would expect to observe the highest reactivity by determining the concentration where the Debye screening length approaches ion sizes.

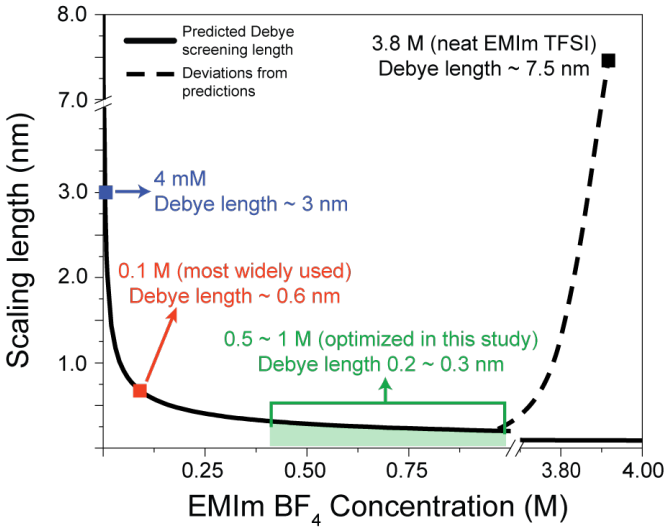

Figure A1.24 Debye-Hückel theory suggests that screening efficiency increases with concentration (solid line). As ion-ion interactions increase, however, the experimentally determined Debye screening length deviates from predictions (dashed line). As a result, there exists a concentration range at which the actual electrostatic screening length of an electrolyte achieves a minimum value.

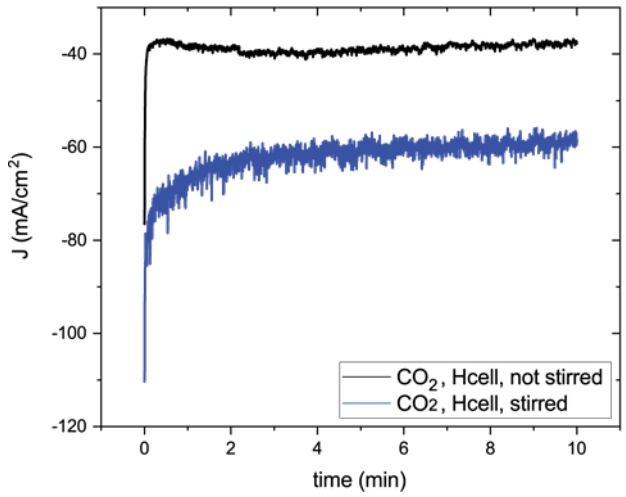

Figure A1.25 Comparison of steady-state current densities from a 1 M EMIm BF_4/acetonitrile electrolyte under continuous CO_2 purging with (blue line) and without (black line) stirring. When the electrolyte was not stirred, the current density significantly decreased due to transport limits. This comparison indicates that stirring can effectively eliminate transport effect, and the trends we observed from steady-state data was not from transport artifacts.

References

(1) Sun, L. Y.; Ramesha, G. K.; Kamat, P. V.; Brennecke, J. F. Switching the Reaction Course of Electrochemical CO_2 Reduction with Ionic Liquids. *Langmuir* **2014**, *30* (21), 6302-6308, Article. DOI: 10.1021/la5009076.

(2) Dhumal, N. R.; Noack, K.; Kiefer, J.; Kim, H. J. Molecular Structure and Interactions in the Ionic Liquid 1-Ethyl-3-methylimidazolium Bis(Trifluoromethylsulfonyl)imide. *The Journal of Physical Chemistry A* **2014**, *118* (13), 2547-2557. DOI: 10.1021/jp502124y.

(3) Sanchora, P.; Pandey, D. K.; Rana, D.; Materny, A.; Singh, D. K. Impact of Size and Electronegativity of Halide Anions on Hydrogen Bonds and Properties of 1-Ethyl-3-methylimidazolium-Based Ionic Liquids. *The Journal of Physical Chemistry A* **2019**, *123* (23), 4948-4963. DOI: 10.1021/acs.jpca.9b04116.

(4) Smith, A. M.; Lee, A. A.; Perkin, S. The Electrostatic Screening Length in Concentrated Electrolytes Increases with Concentration. *The Journal of Physical Chemistry Letters* **2016**, *7* (12), 2157-2163, Article. DOI: 10.1021/acs.jpclett.6b00867.

(5) Gebbie, M. A.; Smith, A. M.; Dobbs, H. A.; Lee, A. A.; Warr, G. G.; Banquy, X.; Valtiner, M.; Rutland, M. W.; Israelachvili, J. N.; Perkin, S.; et al. Long range electrostatic forces in ionic liquids. *Chemical Communications* **2017**, *53* (7), 1214-1224, Article. DOI: 10.1039/c6cc08820a.

Appendix for Chapter 4: Chapter 4. Exploring how cation entropy influences electric double layer formation and electrochemical reactivity

Synthesis of $[BisMImO][TFSI]_2$:

$[BisMImO][Br]_2$ Preparation:

10 g (0.055 moles) of 1-methylimidazole and 30 g (0.11 moles) of 1,8-dibromooctane were added to a round bottom flask and heated to 120 °C in a silicone oil bath for 48 hours under stirring. The resulting liquid is a light brown or yellow color. After cooling to room temperature, the ionic liquid can be crystallized by gently scraping the glass or cooling further in an ice bath, at which point the ionic liquid becomes light yellow or off-white in color as a solid. It is hygroscopic and will quickly absorb water, hence acetone is used to wash the $[BisMImO][Br]_2$ after breaking it up into smaller pieces. This washing step is performed 3 times, or until the acetone layer remains clear and colorless. The acetone is poured off and removed using a rotary evaporator. The resulting ionic liquid should be white/off-white powder.

$[BisMImO][TFSI]_2$ Preparation:

5 g (15.7) moles of $[BisMImO][Br]_2$ and 9.0 g (31.3 mmol) [Li][TFSI] are added to a clean round bottom flask. Approximately 30 mL of MilliQ water is added to the flask and the entire solution is stirred at room temperature for 3 hours. In this time, a separate phase containing $[BisMImO][TFSI]_2$ should form at the bottom of the flask. After allowing the ionic liquid phase to settle, the water layer is poured off, leaving the lightly colored, transparent $[BisMImO][TFSI]_2$. The ionic liquid is then washed with MilliQ water 5 times. The silver nitrate assay is used on the water supernatant after 5 washes to determine whether any halides remain. If the silver nitrate assay indicates the presence of $[Br]^-$, then the ionic liquid is washed another 3 times before further testing with the silver nitrate assay.

Once the ionic liquid is washed and no longer contains halides, the ionic liquid must be purified. To do this, acetonitrile is added to the ionic liquid to decrease the viscosity. Activated charcoal is added to decolorize the ionic liquid by stirring the charcoal in the ionic liquid-acetonitrile solution for 1 day, after which the charcoal is filtered out. The ionic liquid is then passed through an alumina column containing alumina oxide and acetonitrile to filter out remaining charcoal contaminants. What results should be a colorless and transparent solution. A rotary evaporator is then used to remove the acetonitrile and the ionic liquid is dried at 80 °C for 2 days in a vacuum oven.

^{1}H NMR (400 MHz, CD_3CN) δ 8.43 (s, 1H), 7.38 (dt, J = 14.8, 1.9 Hz, 2H), 4.14 (t, J = 7.3 Hz, 2H), 3.85 (s, 3H), 1.84 (p, J = 7.3 Hz, 2H), 1.34 (s, 3H), 1.31 (d, J = 8.7 Hz, 1H).

Table A2.1 Solution resistance values obtained from EIS for [BMIm][TFSI]

Concentration	Solution resistance 1	Solution resistance 2	Average Solution Resistance	Standard Deviation
M	Ohm	Ohm	Ohm	Ohm
0.025	350.30	345.70	348.00	2.30
0.125	78.02	87.34	82.68	4.66
0.5	31.75	38.67	35.21	3.46
1	32.90	34.02	33.46	0.56
1.65	30.02	29.54	29.78	0.24
1.74	28.27	30.23	29.25	0.98

Table A2.2 Solution resistance values obtained from EIS for [BisMImO][TFSI]$_2$

Concentration	Solution resistance 1	Solution resistance 2	Average Solution Resistance	Standard Deviation
M	Ohm	Ohm	Ohm	Ohm
0.025	273.70	228.80	251.25	22.45
0.125	23.75	23.50	23.625	0.125
0.5	36.44	36.18	36.31	0.13
1	67.46	68.54	68.00	0.54
1.65	770.40	774.70	772.55	2.15
1.74	935.3	943.30	939.30	4.00

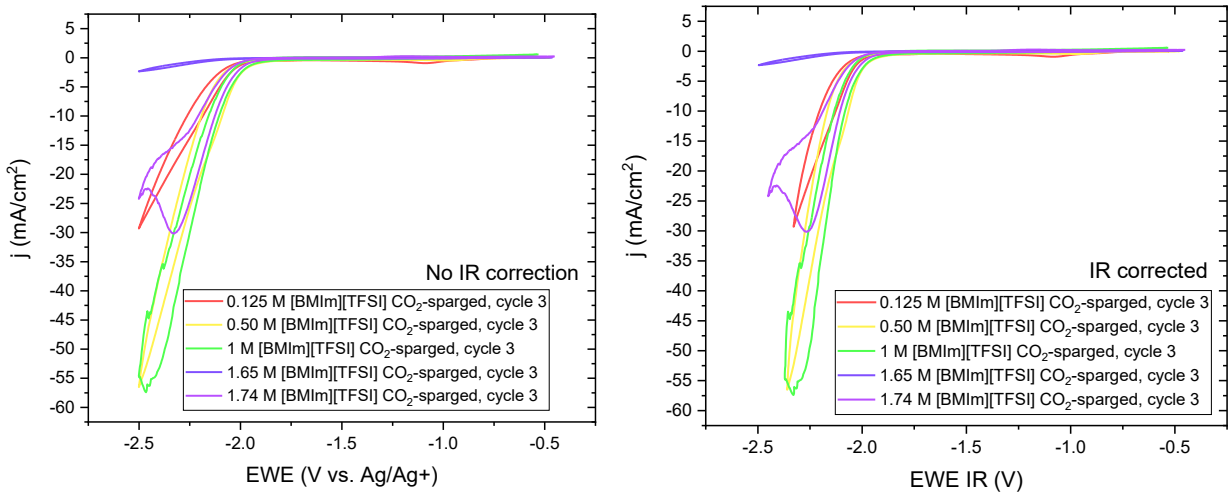

Figure A2.1 Representative cyclic voltammetry curves showing the results of no IR correction (left) and after IR correction (right).

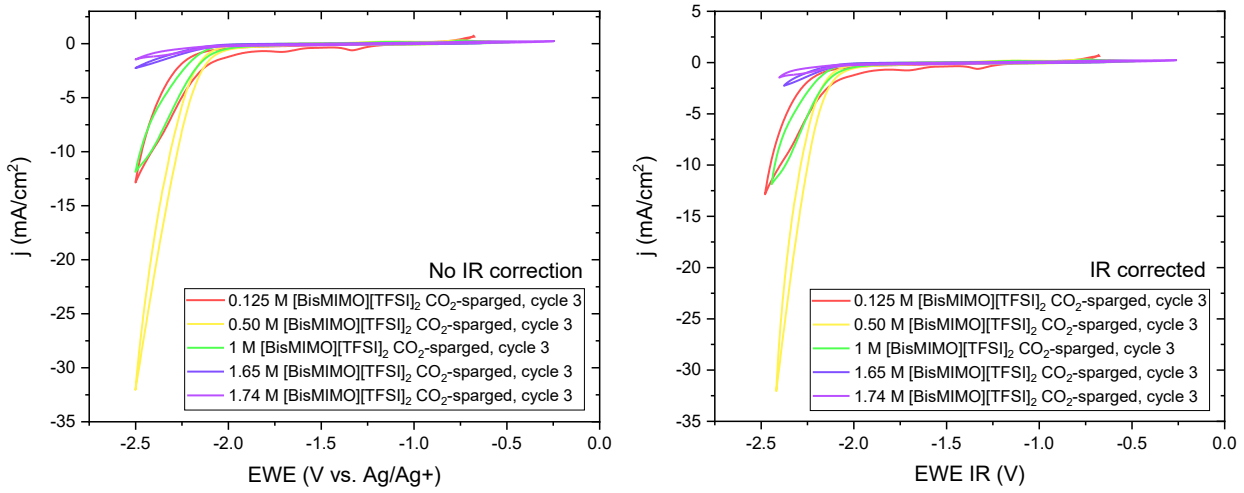

Figure A2.2 Representative cyclic voltammetry curves showing the results of no IR correction (left) and after IR correction (right).

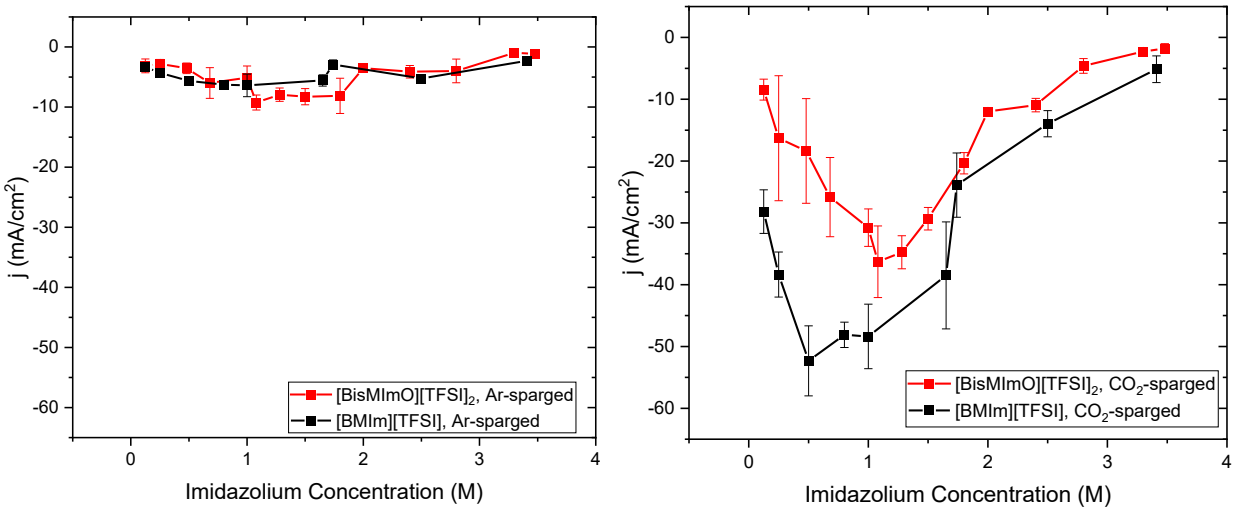

Figure A2.3 Ionic liquid decomposition does not account for the bulk of the current densities observed in CO_2-sparged electrolytes. Ar-sparged results (left) do not show the same non-monotonic reactivity trend nor the same current densities observed in CO_2-sparged electrolytes (right).

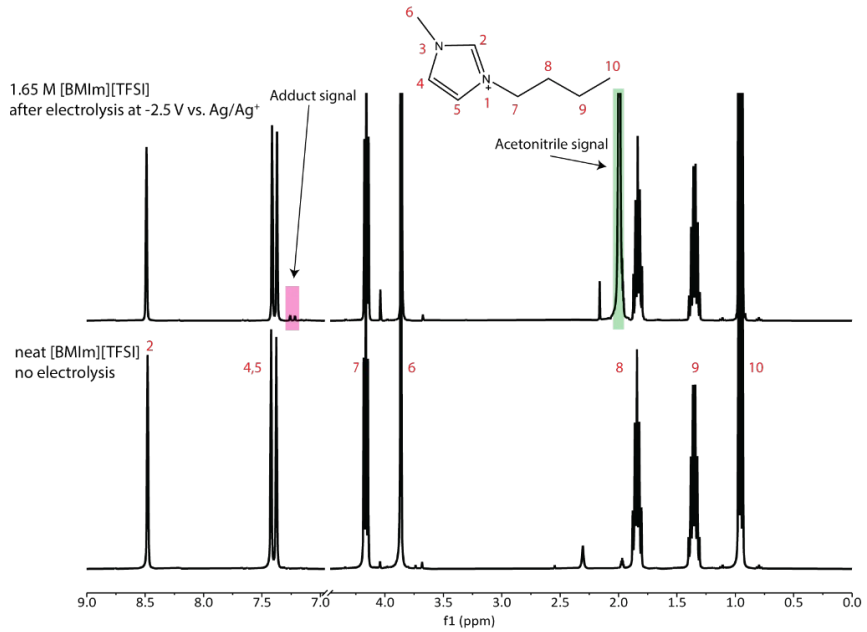

Figure A2.4 1H NMR results for 1.65 M [BMIm][TFSI] after electrolysis (top) compared to the pure ionic liquid (bottom). Other than the acetonitrile peak, the new peaks that are observed are due to the formation of imidazolium-CO_2 adduct, which causes peak splitting of the C4, C5, and C7 peaks. No peaks associated with imidazolium decomposition emerge after electrolysis.

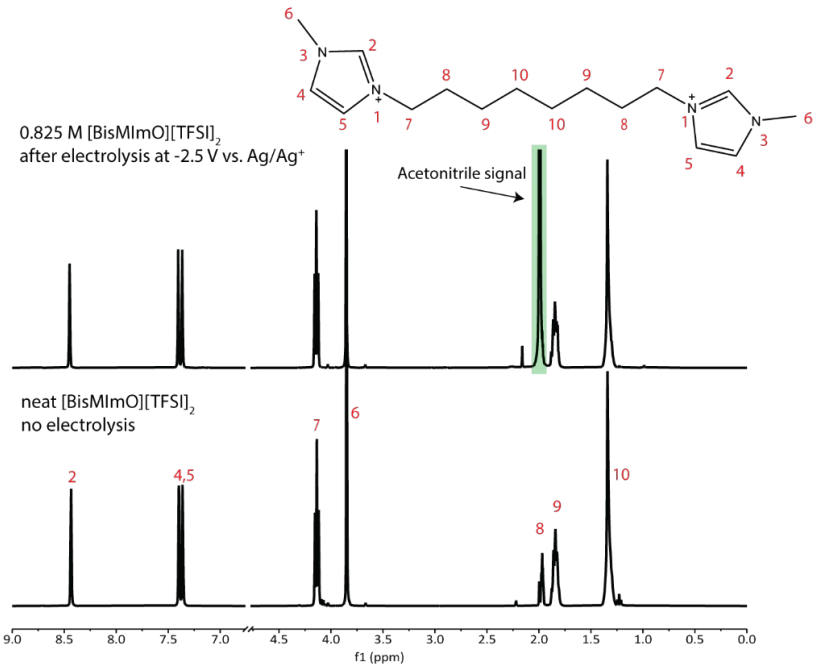

Figure A2.5 NMR results for 0.825 M [BisMImO][TFSI]$_2$ after electrolysis (top) compared to the pure ionic liquid (bottom). No new peaks emerge suggesting that ionic liquid does not decompose at -2.5 V vs. Ag/Ag$^+$. Rather, the relatively diminished intensity of the C2 peak relative to the C4, C5 peaks suggest that small amounts of the carbene at the C2 position may be formed. However, due to the low current densities in [BisMImO][TFSI]$_2$ electrolytes, isolating the carbene or ionic liquid decomposition products remains difficult.

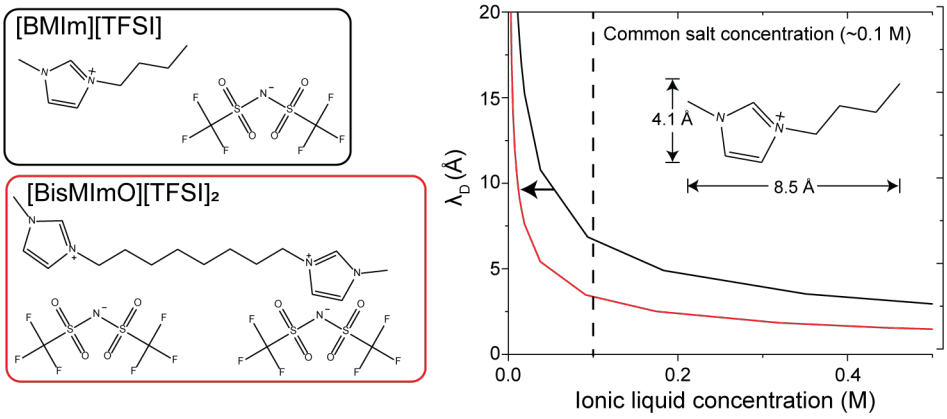

Figure A2.6 Predicted Debye lengths for [BMIm][TFSI] (black) and [BisMImO][TFSI]$_2$ (red) assuming the same dielectric permittivity values. At the same ionic liquid concentration Debye length is smaller for [BisMImO][TFSI]$_2$ due to the divalent nature of the cation. After approximately 0.4 M of ionic liquid, however, the predicted Debye screening length is smaller than two of the dimensions of the [BMIm]$^+$ cation.

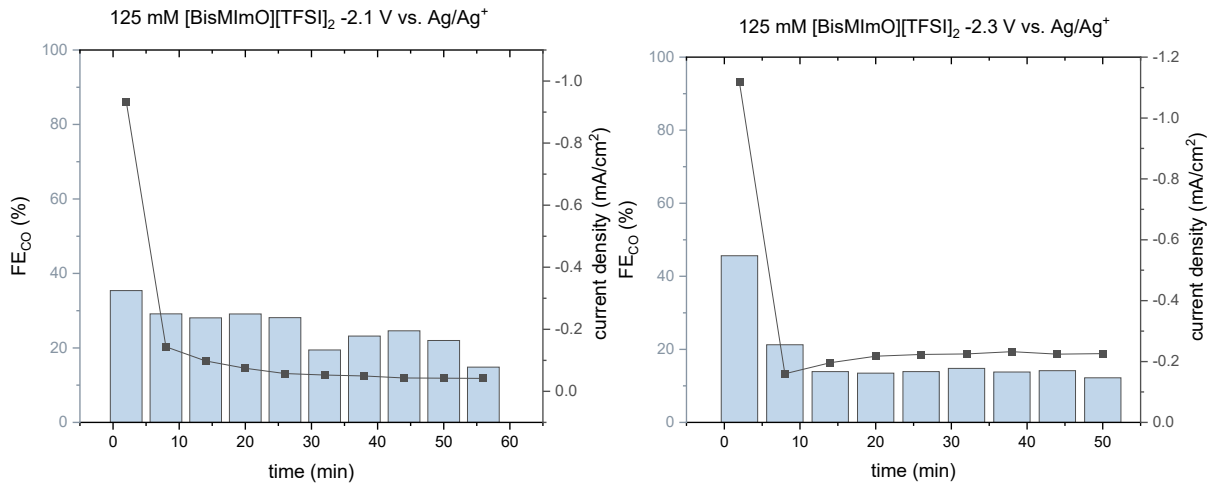

Figure A2.7 Potential-dependent CA results for 125 mM [BisMImO][TFSI]$_2$ held at -2.1 V vs. Ag/Ag$^+$ (left) and -2.3 V vs. Ag/Ag$^+$ (right). Within 10 minutes of applying a CO_2 reduction potential, the current density decreases dramatically due to the formation of a solid precipitate, which occludes the electrode surface.

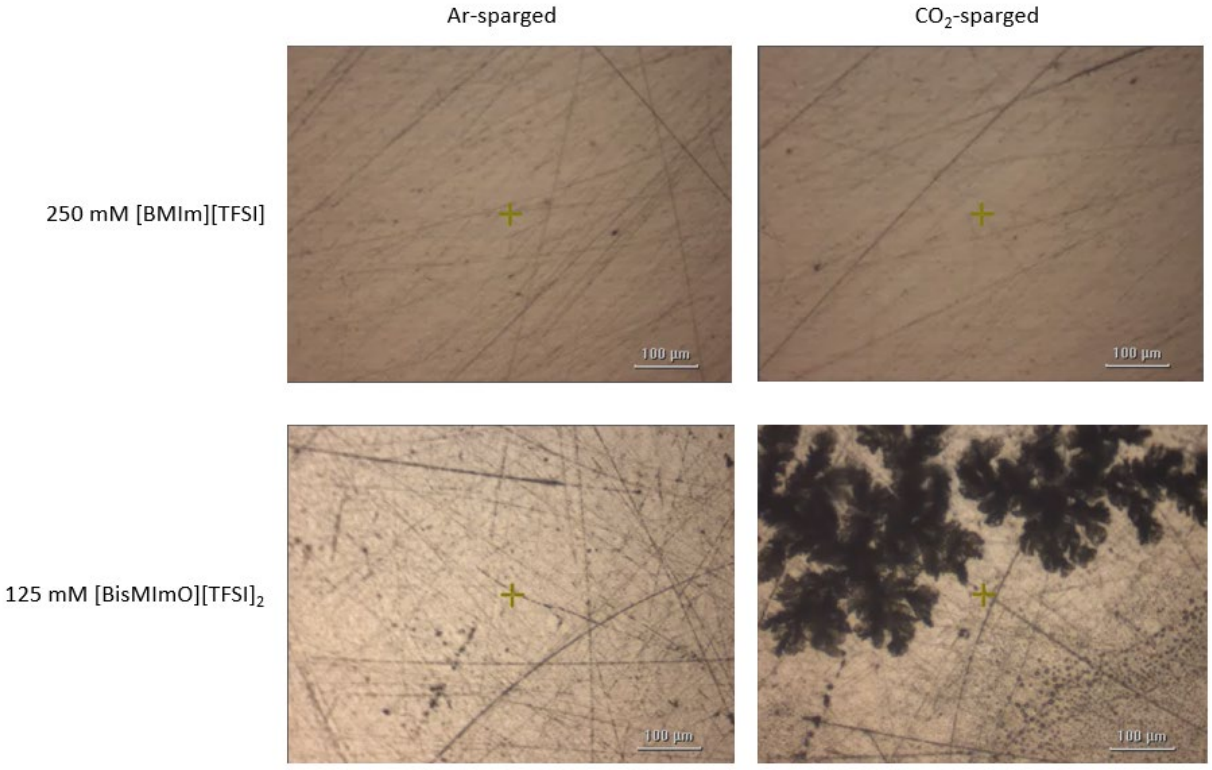

Figure A2.8 Images of 250 mM [BMIm][TFSI] (top row) and 125 mM [BisMImO][TFSI]$_2$ (bottom row) under Ar-sparged (left column) and CO_2-sparged (right column) conditions on a silver electrode surface at -2.5 V vs. Ag/Ag$^+$.

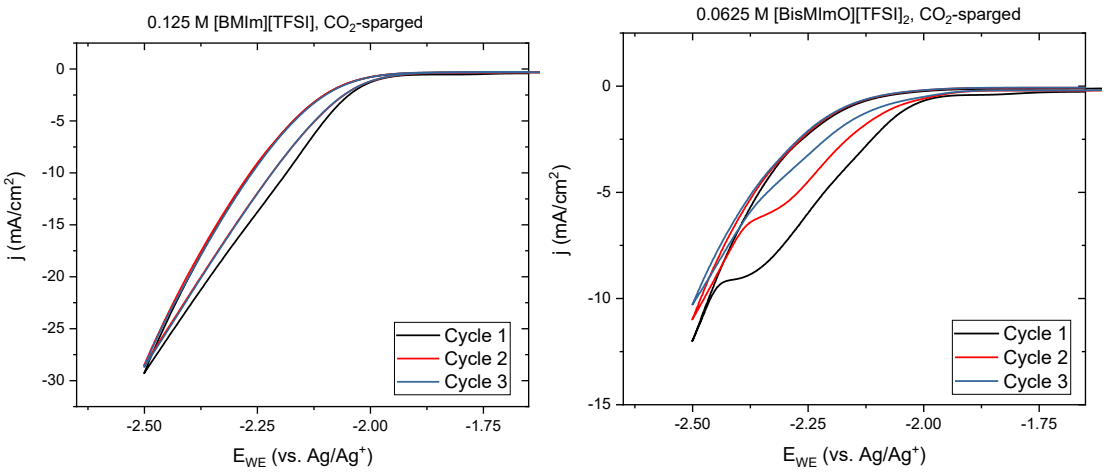

Figure A2.9 Cyclic voltammograms of 0.125 M [BMIm][TFSI] (left) and 0.0625 M [BisMImO][TFSI]$_2$ (right) under CO_2 sparged conditions. The voltammograms of 0.125 M [BMIm][TFSI] remain relatively constant over the course of 3 cycles while 0.0625 M [BisMImO][TFSI]$_2$ displays decreased current densities with each cycle due to the formation of small amounts of precipitates at the electrode surface.

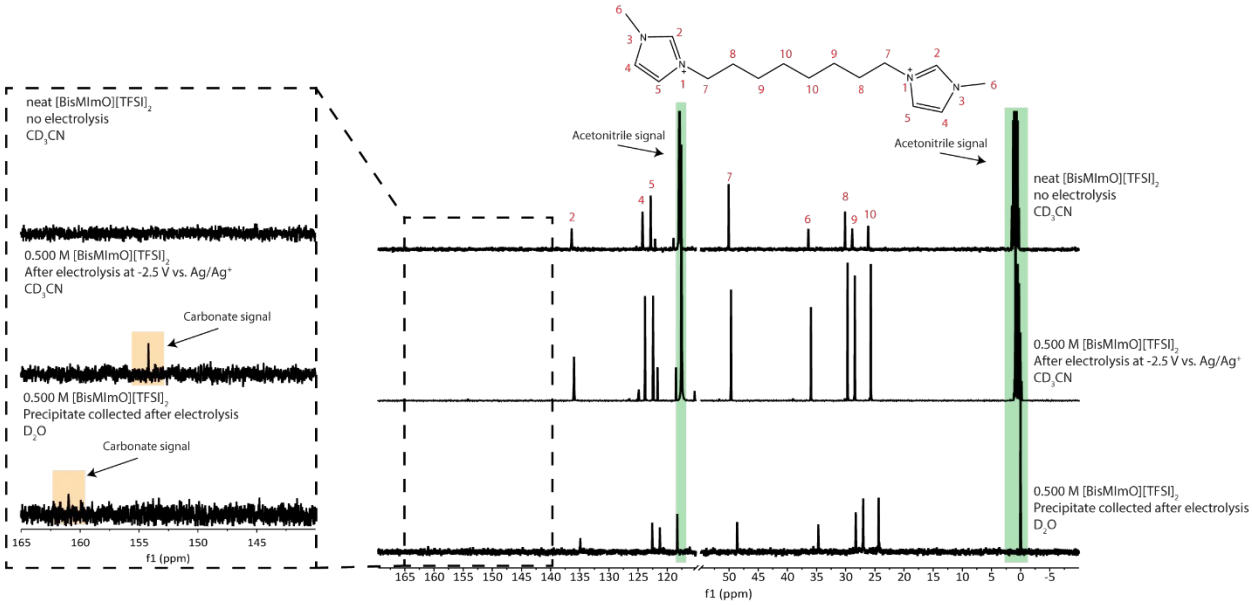

Figure A2.10 ^{13}C NMR results for pure [BisMImO][TFSI]$_2$ (top), 0.500 M [BisMImO][TFSI]$_2$ after electrolysis (middle), and the precipitate collected from electrolysis of [BisMImO][TFSI]$_2$ (bottom), with an inset that displays the carbonate region of the spectrum. The slight shift in the carbonate peak is attributed to the different deuterated solvents needed to solvate the analyte.

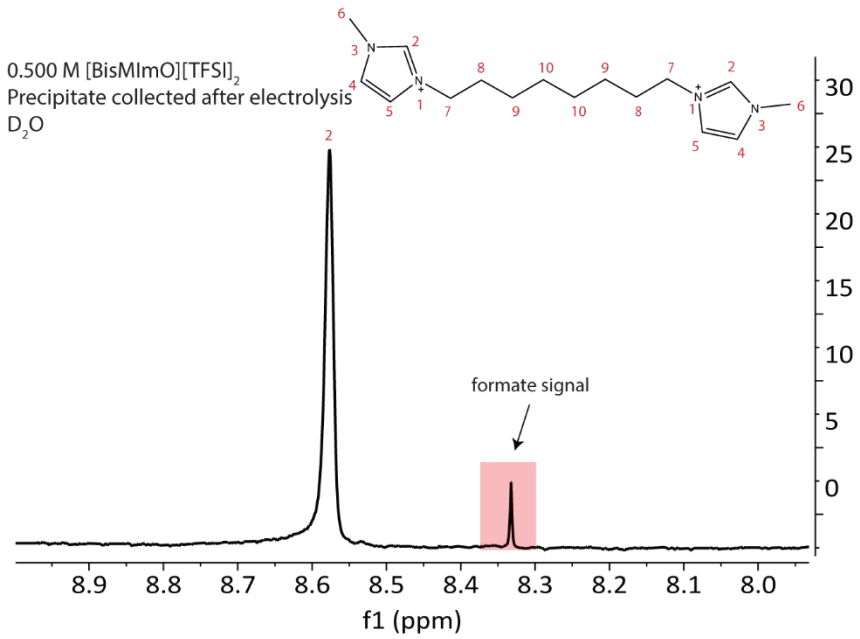

Figure A2.11 1H NMR results of the precipitate that forms in [BisMImO][TFSI]$_2$ electrolytes under CO_2-sparged conditions, indicating the formation of formate.

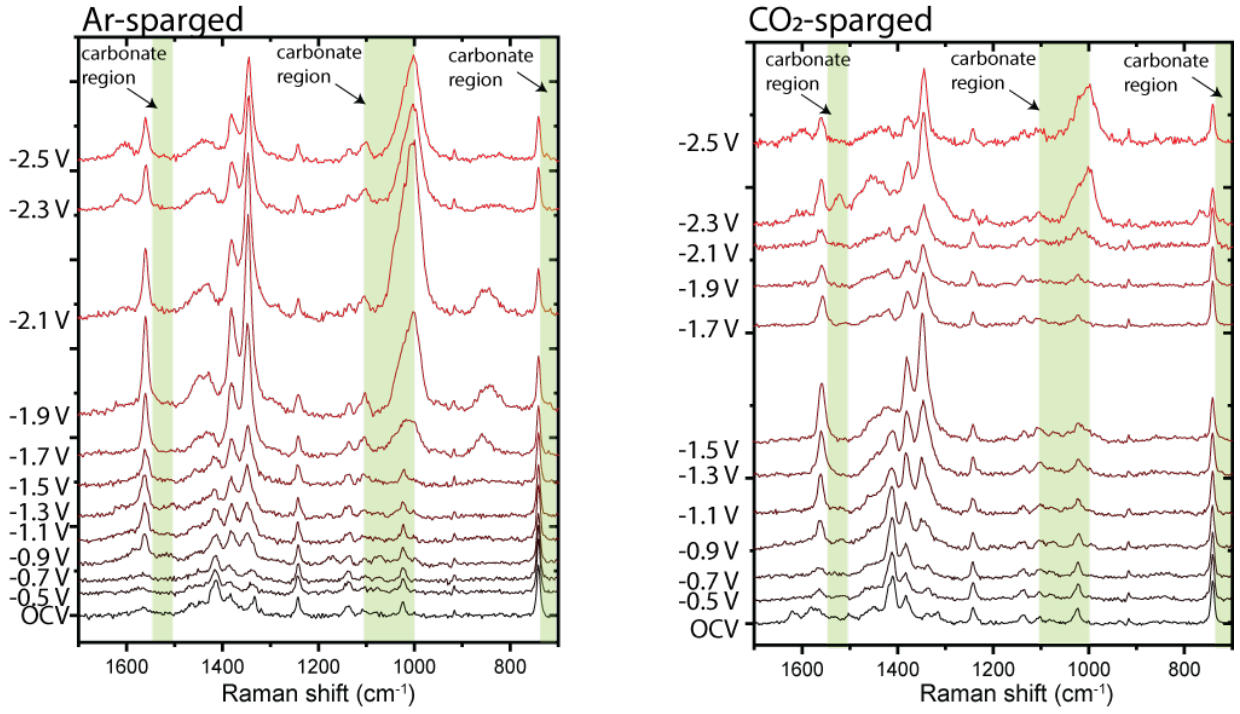

Figure A2.12 Representative Raman spectra of 0.825 M [BisMImO][TFSI]$_2$ under Ar-sparged (left) and CO_2-sparged (right) conditions. Regions associated with carbonate Raman modes are highlighted in green. The emergence of peaks in these regions associated with carbonate Raman modes under Ar-sparged conditions indicate that there is significant overlap between the carbonate and the imidazolium cation Raman modes, making carbonate identification difficult. These observations apply to both [BisMImO][TFSI]$_2$ and [BMIm][TFSI] electrolytes.

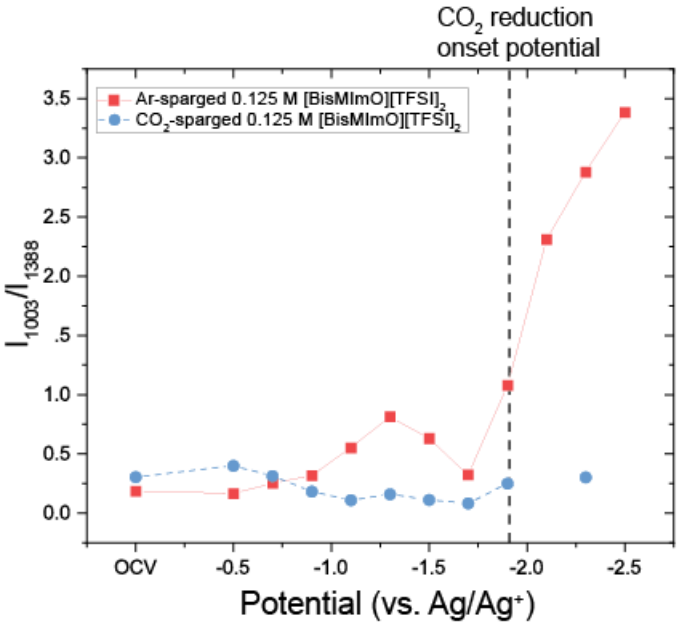

Figure 13 *In situ* SERS of 0.125 M [BisMImO][TFSI]$_2$ under Ar-sparged (red) and CO_2-sparged (blue) conditions. Peak ratios of 1003 cm^{-1} and 1388 cm^{-1} were taken to denote extent of alkyl chain organization. We note that the disappearance of the 1003 cm-1 peak under CO_2-sparged conditions indicates the alkyl chain aggregation behavior we observe under Ar is disrupted due to the dynamic nature of the CO_2 reduction double layer.

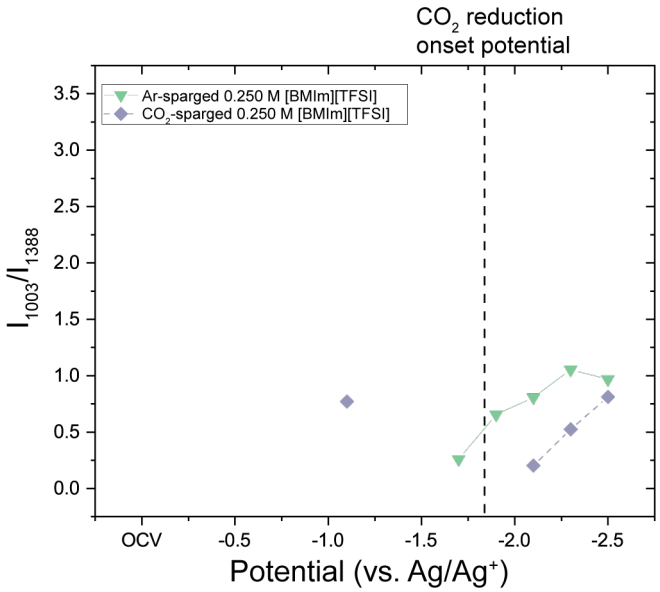

Figure A2.14 Potential-dependent *in situ* SERS of 0.250 M [BMIm][TFSI] under Ar- (green) and CO_2-sparged (purple) conditions. The noticeable lack of the 1003 cm^{-1} peak indicates that there is no significant aggregation of the alkyl chain in [BMIm][TFSI] electrolytes.

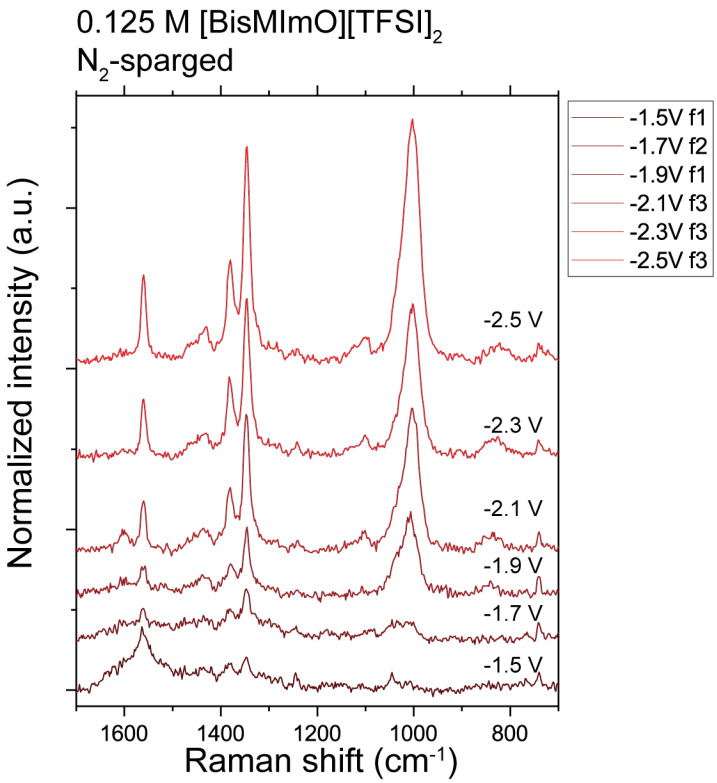

Figure A2.15 Potential-dependent *in situ* SERS of 0.125 M [BisMImO][TFSI]$_2$ under N_2-sparged conditions, which demonstrates the emergence of the 1003 cm^{-1} peak at -1.9 V vs. Ag/Ag^+ under inert conditions and suggests that there is a noticeable difference between interfaces in which a reaction such as CO_2 electroreduction occurs, and an inert interface.

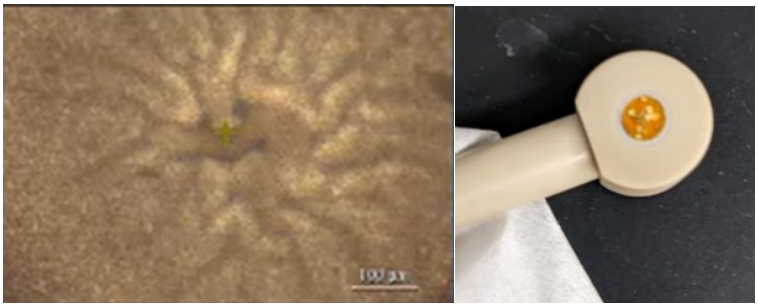

Figure A2.16 Picture of the electrode surface when a potential is stepped to -2.7 V vs. Ag/Ag^+ (left) showing the formation of solid precipitate that, when exposed to ambient humidity, forms an orange film (right).

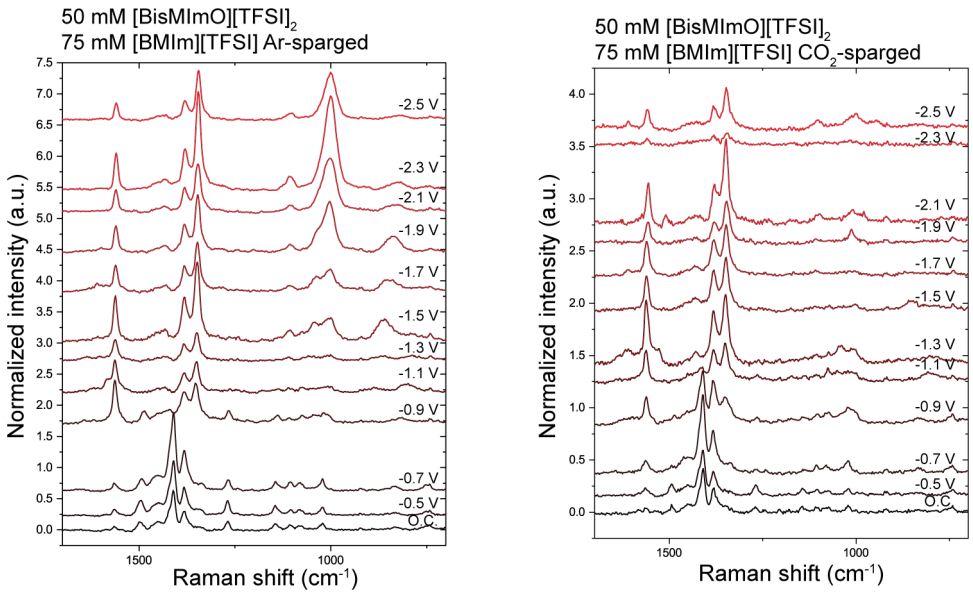

Figure A2.17 *In situ* SERS spectra of an electrolyte mixture containing 50 mM [BisMImO][TFSI]$_2$ and 75 mM [BMIm][TFSI] in acetonitrile either sparged with Ar (left) or CO_2 (right). In the Ar-sparged case, the emergence of a pronounced peak at 1003 cm^{-1} indicates the presence of [BisMImO][TFSI]$_2$, as the same peak is not observed in [BMIm][TFSI]-only solutions. In CO_2-sparged solutions, the peak does not appear, which aligns with observations made in CO_2-sparged [BisMImO][TFSI]$_2$-only electrolytes.

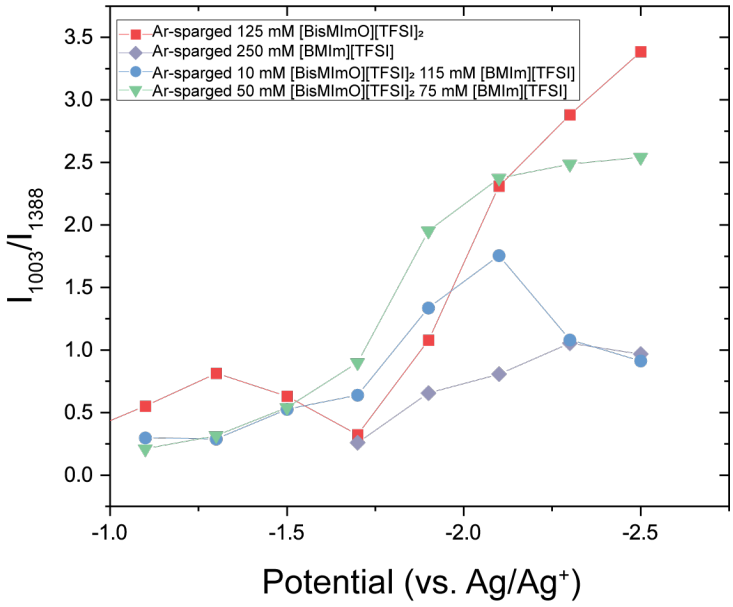

Figure A2.18 Peak ratios of 1003 cm^{-1} and 1388 cm^{-1} peaks of ionic liquid mixtures containing [BisMImO][TFSI]$_2$ under Ar-sparged conditions. Compared to 125 mM [BisMImO][TFSI]$_2$ (red) and 250 mM [BMIm][TFSI] (purple), electrolytes containing a mixture of the two show that as the concentration of [BisMImO][TFSI]$_2$ increases from 10 mM (blue) to 50 mM (green), the potential-dependent ratio of the two peaks becomes more like that of the [BisMImO][TFSI]$_2$-only electrolyte, suggesting enhanced accumulation of the [BisMImO][TFSI]$_2$ at the interface.

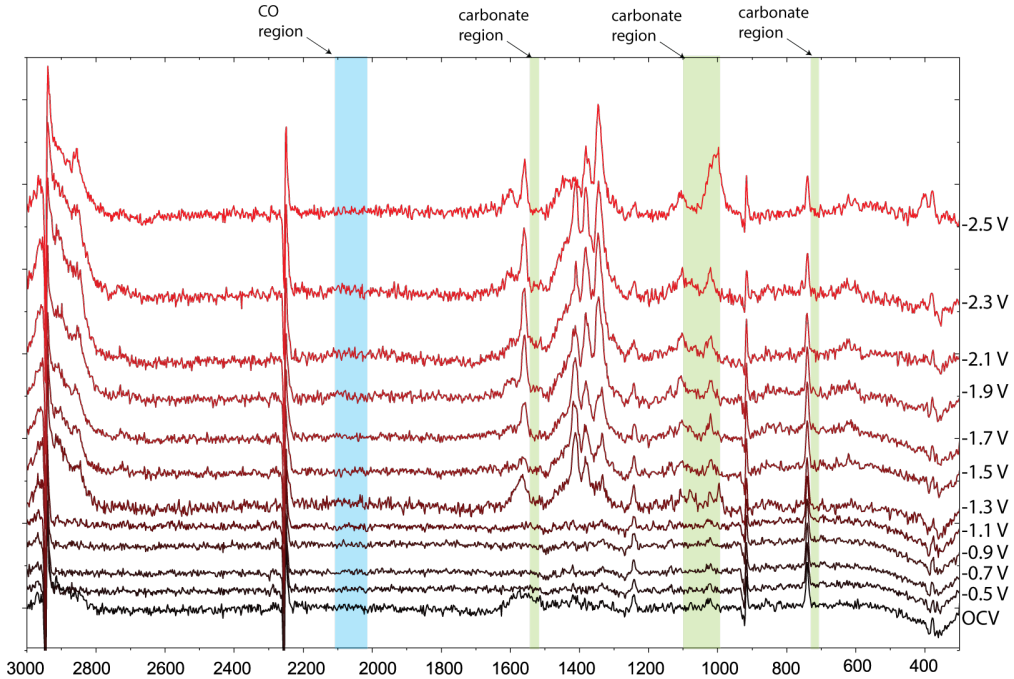

Figure A2.19 Full SERS spectra of CO_2-sparged 1.65 M [BMIm][TFSI] with regions where the carbonate (green) and CO (blue) Raman modes would appear.

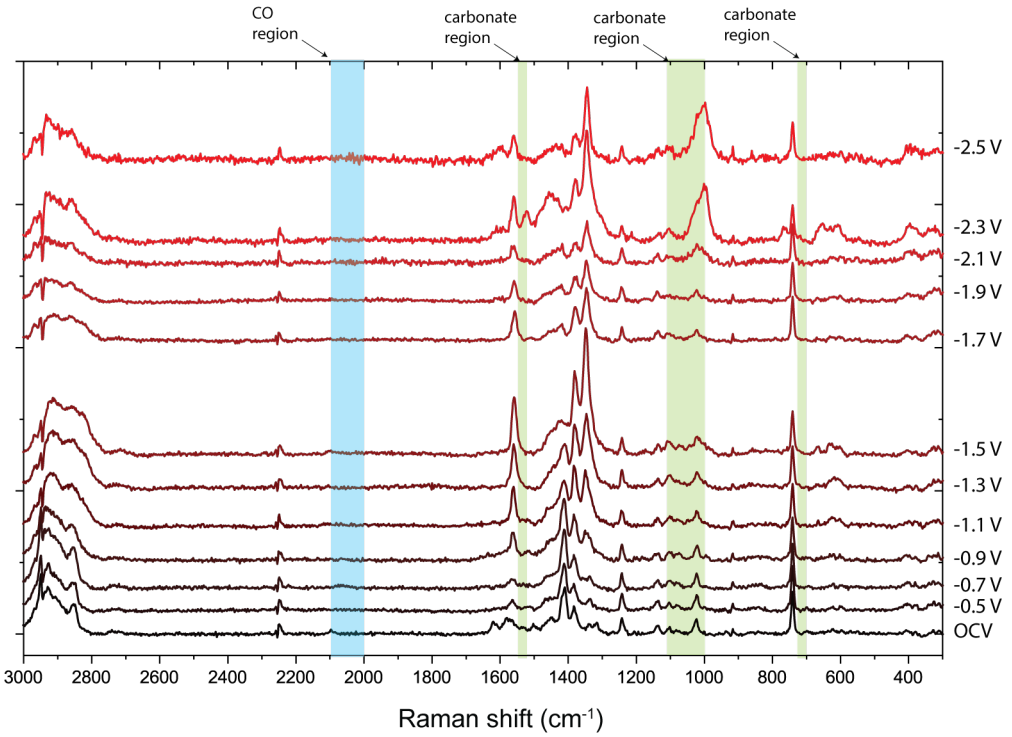

Figure A2.20 Full SERS spectra of CO_2-sparged 0.825 M [BisMImO][TFSI]$_2$ with regions where the carbonate (green) and CO (blue) Raman modes would appear.

Appendix for Chapter 5: Assessing the role of the C2 carbene in imidazolium-mediated ionic liquid using diamondoid substituents

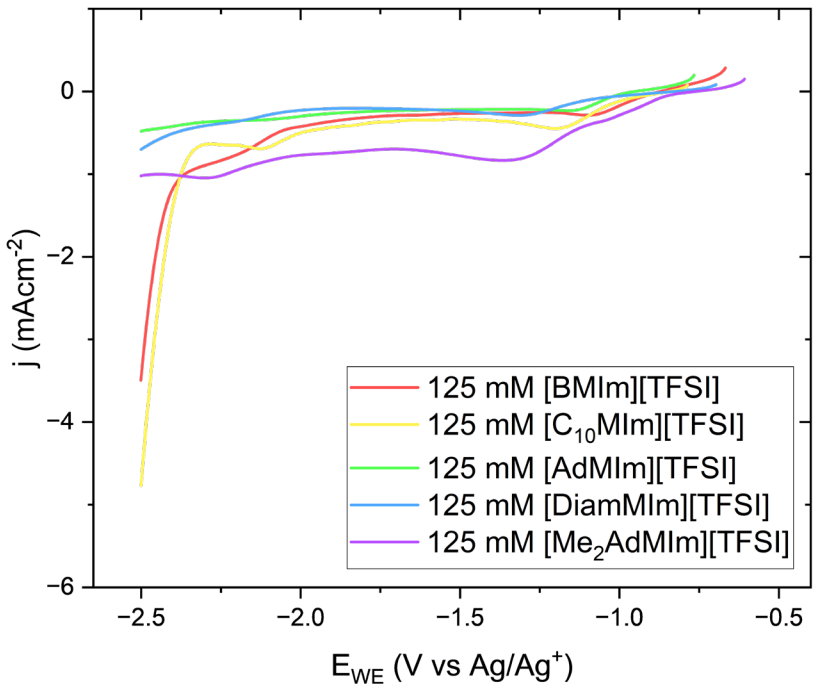

Figure A3.1 Ar-sparged CVs showing lower current densities for (green, blue, purple) diamondoid-substituted ionic liquids compared to (red, yellow) alkyl-substituted ionic liquids in the absence of CO_2.

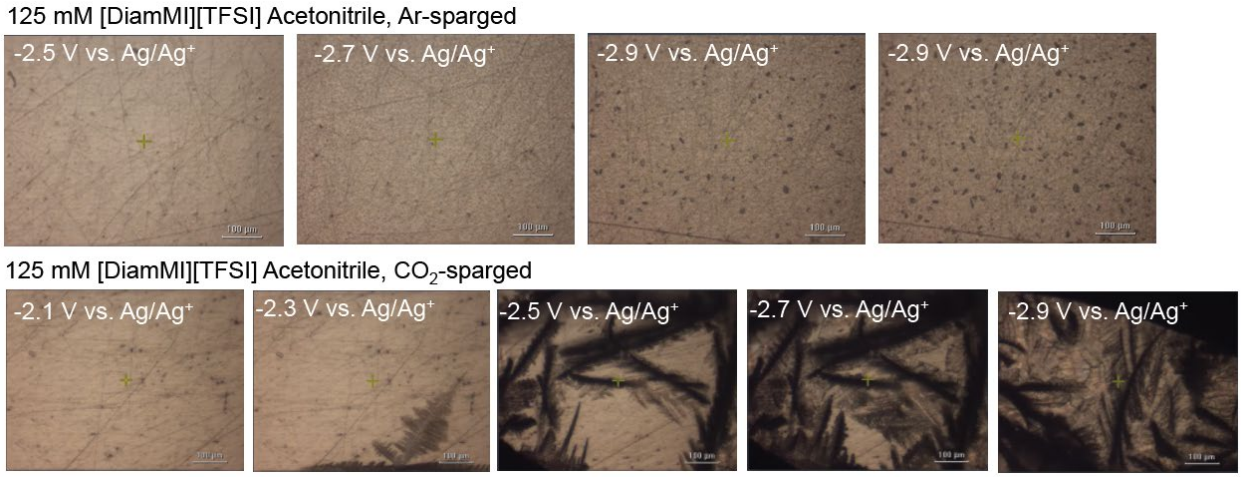

Figure A3.2 Precipitation on polycrystalline Ag electrode surfaces formed under (top) Ar-sparged conditions and (bottom) CO_2-sparged conditions. Under Ar-sparged conditions, solid precipitates begin to form at -2.5 V vs. Ag/Ag^+ but grows slowly until -2.9 V vs. Ag/Ag^+ is reached. Under CO_2-sparged

conditions, the formation of precipitates begins at -2.3 V vs. Ag/Ag^+ and continues to grow until the entire surface is covered. Precipitate growth rates appeared to increase as potential became more cathodic.

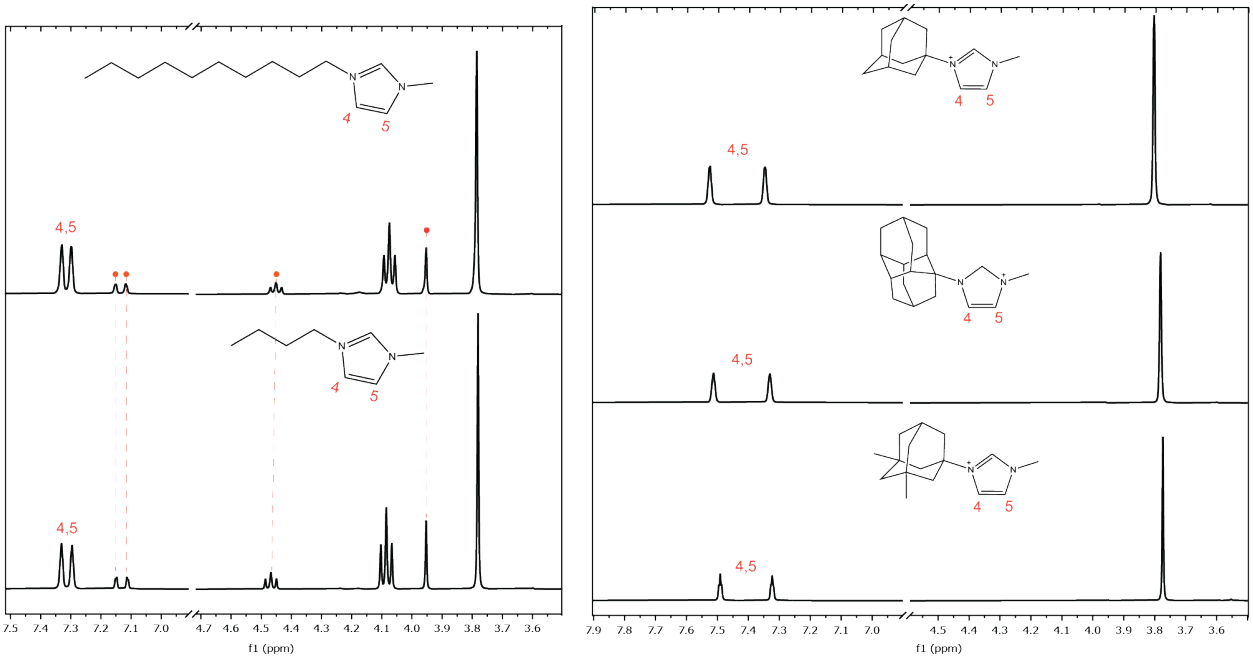

Figure A3.3 ^1H NMR results after CO_2 electrolysis at -2.5 V vs. Ag/Ag^+ show imidazolium-CO_2 adduct formation in the (left) alkyl-substituted ionic liquids but not in the (right) diamondoid-substituted ionic liquids. Imidazolium-CO_2 adduct formation is demonstrated by peak splitting of the C4 and C5 protons, as well as the appearance of a triplet at 4.47 ppm and a singlet at 3.95 ppm, denoted in the alkyl-substituted ionic liquid NMR spectra by a red dot, as identified by Michez and coworkers.[1] In diamondoid-substituted ionic liquids, these hallmarks of adduct formation are not observed. ^1H NMR data collected using CD_3CN.

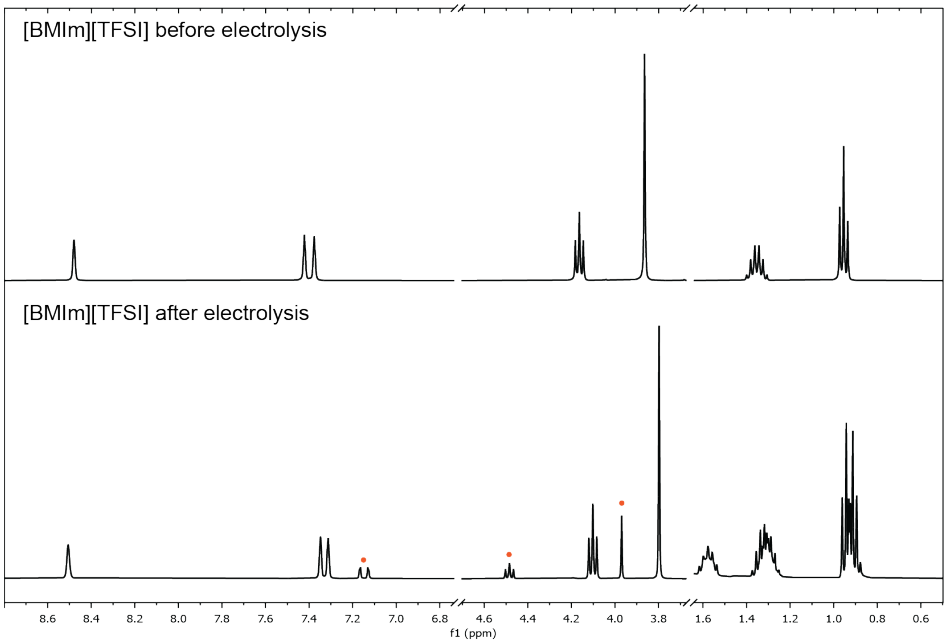

Figure A3.4 ^{1}H NMR results of [BMIm][TFSI] (top) before electrolysis and (bottom) after electrolysis showing peak splitting and the appearance of signals associated with imidazolium-CO_2 adduct formation. ^{1}H NMR data collected using CD_3CN.

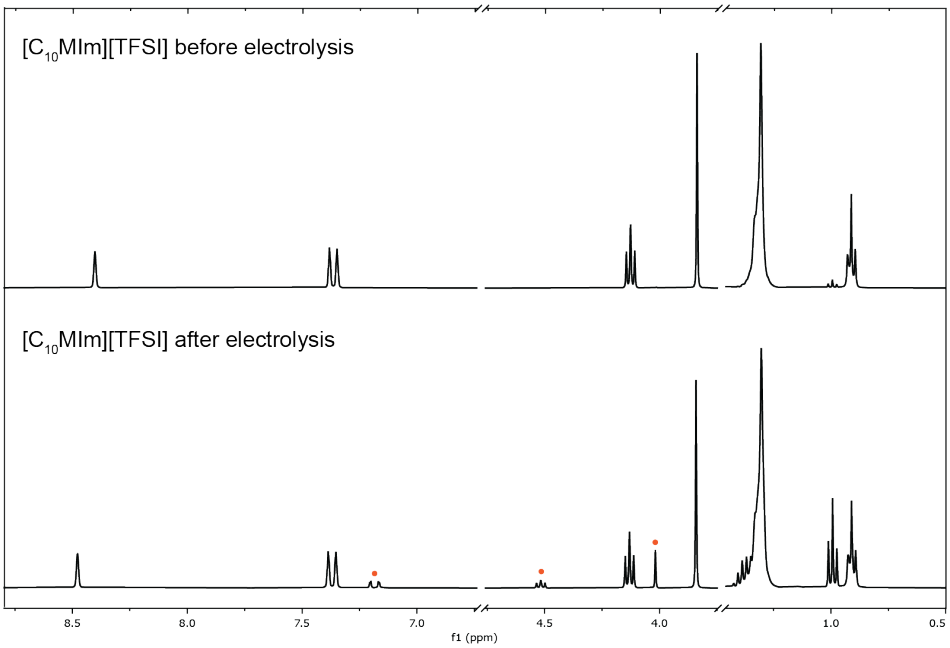

Figure A3.5 ^{1}H NMR results of [BMIm][TFSI] (top) before electrolysis and (bottom) after electrolysis showing peak splitting and the appearance of signals associated with imidazolium-CO_2 adduct formation. ^{1}H NMR data collected using CD_3CN.

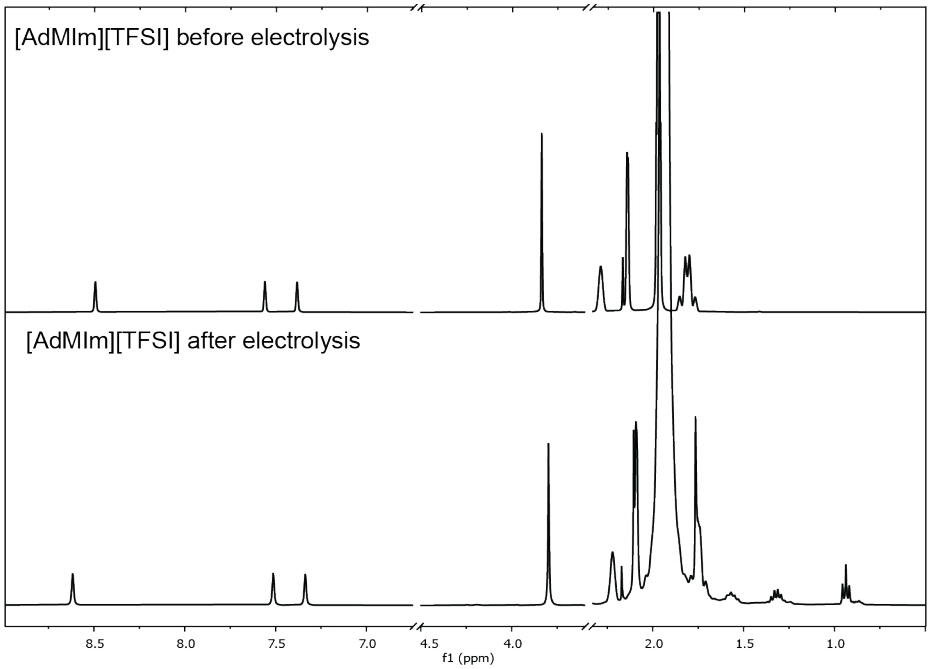

Figure A3.6 ^{1}H NMR results of [AdMIm][TFSI] (top) before electrolysis and (bottom) after electrolysis do not show significant peak formation or peak splitting. The additional peaks that appear at 1.55, 1.30, and 0.97 ppm are attributed to $[TBA]^{+}$ cations that were transported from the anolyte. ^{1}H NMR data collected using CD_3CN.

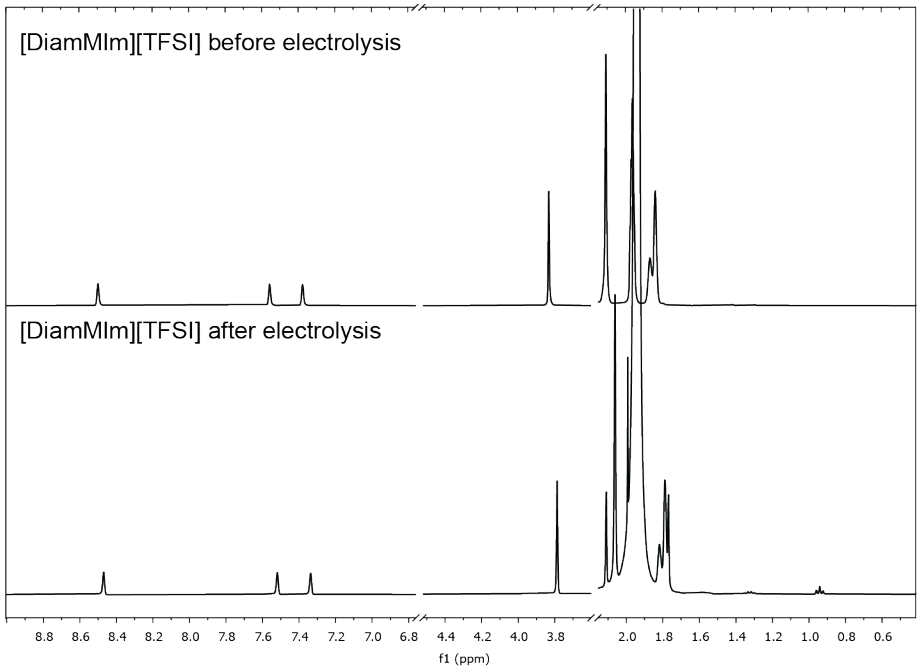

Figure A3.7 ^{1}H NMR results of [DiamMIm][TFSI] (top) before electrolysis and (bottom) after electrolysis do not show significant peak formation or peak splitting. The additional peaks that appear at 1.30 and 0.95 ppm are attributed to $[TBA]^{+}$ cations that were transported from the anolyte. ^{1}H NMR data collected using CD_3CN.

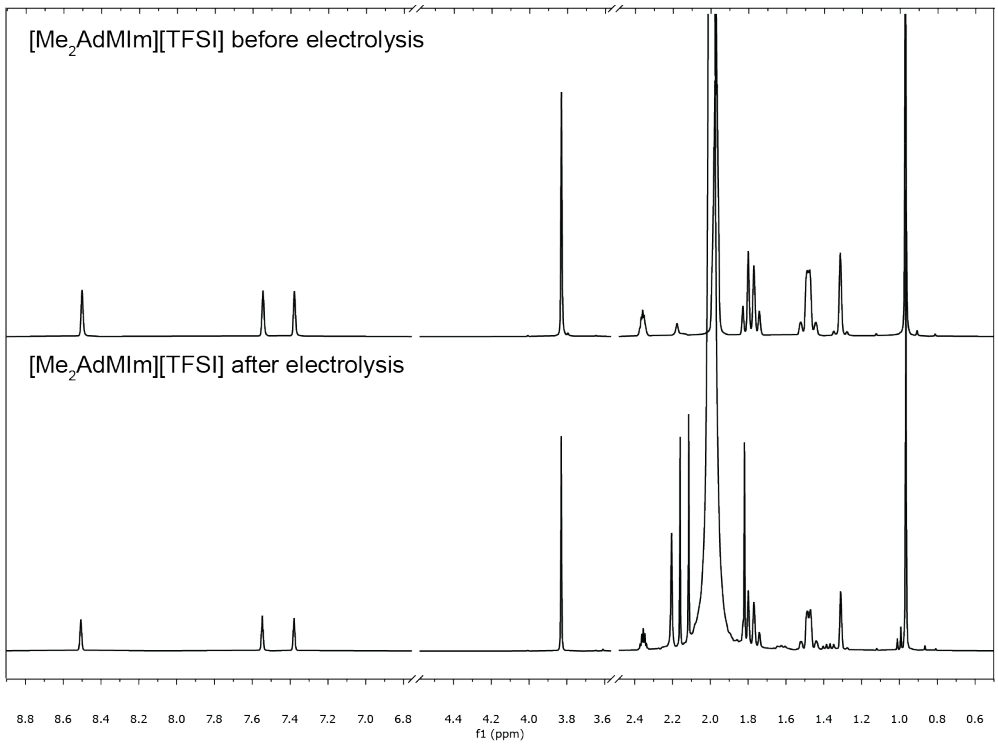

Figure A3.8 ^{1}H NMR results of [Me_2AdMIm][TFSI] (top) before electrolysis and (bottom) after electrolysis do not show significant peak formation or peak splitting. ^{1}H NMR data collected using CD_3CN.

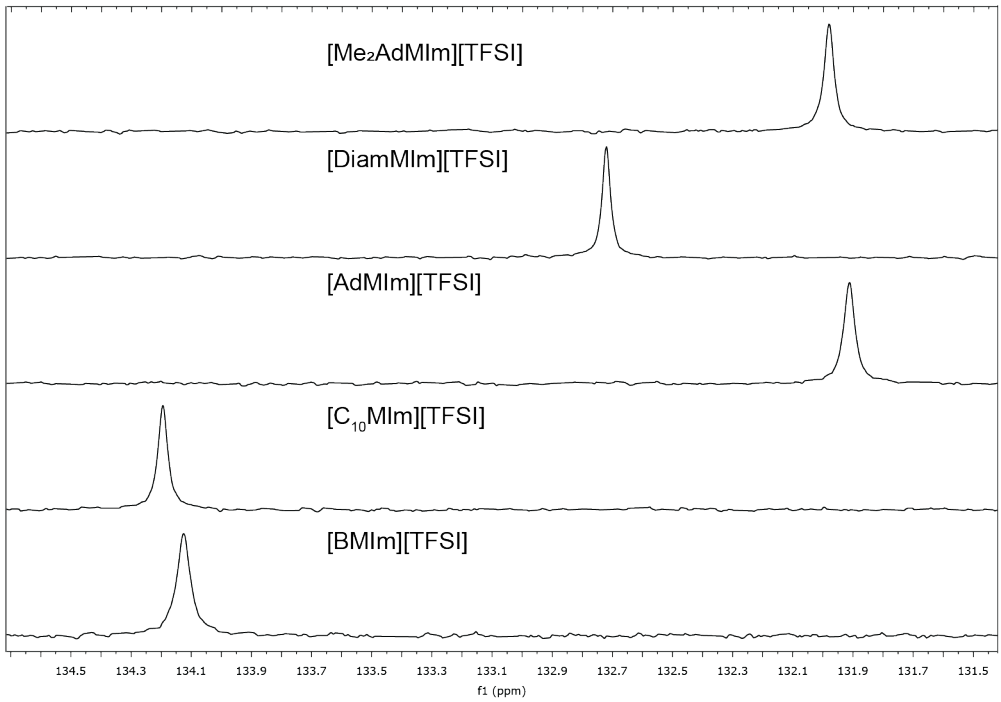

Figure A3.9 ^{13}C NMR results showing upfield shift of diamondoid-substituted ionic liquids compared to alkyl-substituted ones. Spectra were recorded in 0.5 M ionic liquid with 0.1 mL of acetonitrile in $CDCl_3$, referenced to the TMS peak.

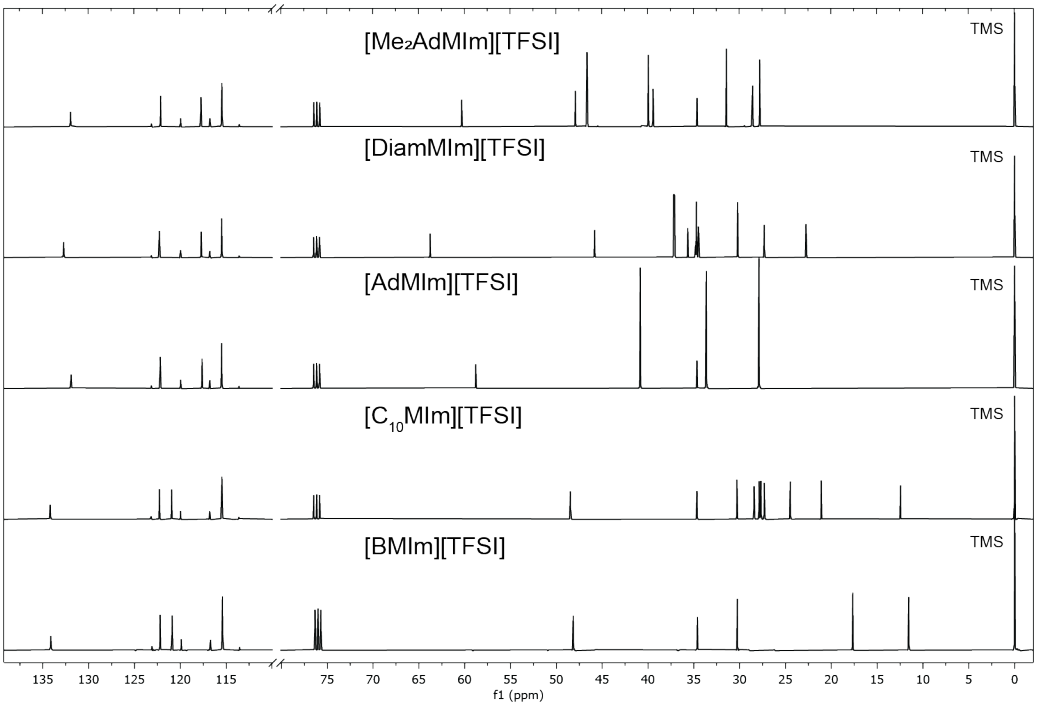

Figure A3.10 Full ^{13}C NMR of the diamondoid and alkyl-substituted ionic liquids. Spectra were recorded in 0.5 M ionic liquid with 0.1 mL of acetonitrile in $CDCl_3$, referenced to the TMS peak.

Table A3.1 Peak positions of C2 carbon in diamondoid vs. alkyl ionic liquids using ^{13}C NMR. Spectra were recorded in 0.5 M ionic liquid with 0.1 mL of acetonitrile in $CDCl_3$, referenced to the TMS peak.

Ionic Liquid	**C2 Carbon Peak Position (ppm)**
[BMIm][TFSI]	134.13
[C_{10}MIm][TFSI]	134.19
[AdMIm][TFSI]	131.91
[DiamMIm][TFSI]	132.72
[Me_2AdMIm][TFSI]	131.98

References

(1) Michez, R.; Doneux, T.; Buess-Herman, C.; Luhmer, M. NMR Study of the Reductive Decomposition of [BMIm] [NTf] at Gold Electrodes and Indirect Electrochemical Conversion of CO_2. *Chemphyschem* **2017**, *18* (16), 2208-2216. DOI: 10.1002/cphc.201700421.